

MATERIALS PHYSICS AND MECHANICS

Vol. 51, No. 5, 2023



MATERIALS PHYSICS AND MECHANICS

Principal Editors:

Alexander Belyaev

Andrei Rudskoi

Institute for Problems in Mechanical Engineering of the Russian Academy of Science (RAS), Russia

Peter the Great St.Petersburg Polytechnic University, Russia

Founder and Honorary Editor: Ilya Ovid'ko (1961-2017)

Institute for Problems in Mechanical Engineering of the Russian Academy of Sciences (RAS), Russia

Associate Editor:

Anna Kolesnikova

Artem Semenov

Institute for Problems in Mechanical Engineering of the Russian Academy of Sciences (RAS), Russia

Peter the Great St.Petersburg Polytechnic University, Russia

Editorial Board:

E.C. Aifantis

Aristotle University of Thessaloniki, Greece

K.E. Aifantis

University of Florida, USA

U. Balachandran

Argonne National Laboratory, USA

A. Bellosi

Research Institute for Ceramics Technology, Italy

S.V. Bobylev

Institute for Problems in Mechanical Engineering (RAS), Russia

A.I. Borovkov

Peter the Great St.Petersburg Polytechnic University, Russia

G.-M. Chow

National University of Singapore, Singapore

Yu. Estrin

Monash University, Australia

A.B. Freidin

Institute for Problems in Mechanical Engineering (RAS), Russia

Y. Gogotsi

Drexel University, USA

I.G. Goryacheva

Institute of Problems of Mechanics (RAS), Russia

D. Hui

University of New Orleans, USA

G. Kiriakidis

IESL/FORTH, Greece

D.M. Klimov

Institute of Problems of Mechanics (RAS), Russia

G.E. Kodzhaspirov

Peter the Great St.Petersburg Polytechnic University, Russia

S.A. Kukushkin

Institute for Problems in Mechanical Engineering (RAS), Russia

T.G. Langdon

University of Southampton, U.K.

V.P. Matveenko

Institute of Continuous Media Mechanics (RAS), Russia

A.I. Melker

Peter the Great St.Petersburg Polytechnic University, Russia

Yu.I. Meshcheryakov

Institute for Problems in Mechanical Engineering (RAS), Russia

N.F. Morozov

St.Petersburg State University, Russia

R.R. Mulyukov

Institute for Metals Superplasticity Problems (RAS), Russia

Yu.V. Petrov

St.Petersburg State University, Russia

N.M. Pugno

Politecnico di Torino, Italy

B.B. Rath

Naval Research Laboratory, USA

A.E. Romanov

Ioffe Institute (RAS), Russia

A.M. Sastry

University of Michigan, Ann Arbor, USA

B.A. Schrefler

University of Padua, Italy

N.V. Skiba

Institute for Problems in Mechanical Engineering (RAS), Russia

A.G. Sheinerman

Institute for Problems in Mechanical Engineering (RAS), Russia

R.Z. Valiev

Ufa State Aviation Technical University, Russia

K. Zhou

Nanyang Technological University, Singapore

"Materials Physics and Mechanics" Editorial Office:

Phone: +7(812)552 77 78, ext. 224 E-mail: mpmjournal@spbstu.ru Web-site: http://www.mpm.spbstu.ru

International scientific journal "Materials Physics and Mechanics" is published by Peter the Great St. Petersburg Polytechnic University in collaboration with Institute for Problems in Mechanical Engineering of the Russian Academy of Sciences in both hard copy and electronic versions.

The journal provides an international medium for the publication of reviews and original research papers written in English and focused on the following topics:

- Mechanics of composite and nanostructured materials.
- Physics of strength and plasticity of composite and nanostructured materials.
- Mechanics of deformation and fracture processes in conventional materials (solids).
- Physics of strength and plasticity of conventional materials (solids).
- Physics and mechanics of defects in composite, nanostructured, and conventional materials.
- Mechanics and physics of materials in coupled fields.

Owner organizations: Peter the Great St. Petersburg Polytechnic University; Institute of Problems of Mechanical Engineering RAS.

Materials Physics and Mechanics is indexed in Chemical Abstracts, Cambridge Scientific Abstracts, Web of Science Emerging Sources Citation Index (ESCI) and Elsevier Bibliographic Databases (in particular, SCOPUS).

© 2023, Peter the Great St. Petersburg Polytechnic University © 2023, Institute for Problems in Mechanical Engineering RAS



МЕХАНИКА И ФИЗИКА МАТЕРИАЛОВ

Materials Physics and Mechanics

Том 51, номер 5, 2023 год

Учредители:

Редакционная коллегия журнала Главные редакторы:

д.ф.-м.н., чл.-корр. РАН А.К. Беляев Институт проблем машиноведения Российской академии наук (РАН)

д.т.н., академик РАН А.И. Рудской Санкт-Петербургский политехнический университет Петра Великого

Основатель и почетный редактор: д.ф.-м.н. И.А. Овидько (1961-2017)

Институт проблем машиноведения Российской академии наук (РАН)

Ответственный редактор

д.ф.-м.н. А.Л. Колесникова

Институт проблем машиноведения Российской академии наук (РАН)

д.ф.-м.н. А.С. Семенов

Санкт-Петербургский политехнический университет Петра Великого

Международная редакционная коллегия:

д.ф.-м.н. С.В. Бобылев

Институт проблем машиноведения РАН, Россия

к.т.н., проф. А.И. Боровков

Санкт-Петербургский политехнический ун-т Петра Великого, Россия

д.ф.-м.н., проф. Р.З. Валиев

Уфимский государственный технический университет, Россия

д.ф.-м.н., академик РАН И.Г. Горячева Институт проблем механики РАН, Россия

д.ф.-м.н., академик РАН Д.М. Климов

Институт проблем механики РАН, Россия

д.т.н., проф. Г.Е. Коджаспиров

Санкт-Петербургский политехнический ун-т Петра Великого, Россия

д.ф.-м.н., проф. С.А. Кукушкин

Институт проблем машиноведения РАН, Россия

д.ф.-м.н., академик РАН В.П. Матвеенко

Институт механики сплошных сред РАН, Россия

д.ф.-м.н., проф. А.И. Мелькер

Санкт-Петербургский политехнический ун-т Петра Великого, Россия

д.ф.-м.н., проф. Ю.И. Мещеряков

Институт проблем машиноведения РАН, Россия

д.ф.-м.н., академик РАН Н.Ф. Морозов

Санкт-Петербургский государственный университет, Россия

д.ф.-м.н., чл.-корр. РАН Р.Р. Мулюков

Институт проблем сверхпластичности металлов РАН, Россия

д.ф.-м.н., чл.-корр. РАН Ю.В. Петров

Санкт-Петербургский государственный университет, Россия

д.ф.-м.н., проф. А.Е. Романов Физико-технический институт им. А.Ф. Иоффе РАН, Россия

д.ф-м.н. Н.В. Скиба

Институт проблем машиноведения РАН, Россия

д.ф.-м.н., проф. А.Б. Фрейдин

Институт проблем машиноведения РАН, Россия

д.ф-м.н. А.Г. Шейнерман

Институт проблем машиноведения РАН, Россия

Prof., Dr. E.C. Aifantis

Aristotle University of Thessaloniki, Greece

Dr. K.E. Aifantis

University of Florida, USA

Dr. U. Balachandran

Argonne National Laboratory, USA

Dr. A. Bellosi

Research Institute for Ceramics Technology, Italy

Prof., Dr. G.-M. Chow

National University of Singapore, Singapore

Prof., Dr. Yu. Estrin

Monash University, Australia

Prof., Dr. Y. Gogotsi

Drexel University, USA

Prof., Dr. D. Hui

University of New Orleans, USA

Prof., Dr. G. Kiriakidis

IESL/FORTH, Greece

Prof., Dr. T.G. Langdon

University of Southampton, UK

Prof., Dr. N.M. Pugno

Politecnico di Torino, Italy

Dr. B.B. Rath

Naval Research Laboratory, USA

Prof., Dr. A.M. Sastry

University of Michigan, Ann Arbor, USA

Prof., Dr. B.A. Schrefler

University of Padua, Italy

Prof. Dr. K. Zhou

Nanyang Technological University, Singapore

Тел.: +7(812)552 77 78, доб. 224 E-mail: mpmjournal@spbstu.ru Web-site: http://www.mpm.spbstu.ru

Тематика журнала

Международный научный журнал "Materials Physics and Mechanics" издается Санкт-Петербургским политехническим университетом Петра Великого в сотрудничестве с Институтом проблем машиноведения Российской академии наук в печатном виде и электронной форме. Журнал публикует обзорные и оригинальные научные статьи на английском языке по следующим тематикам:

- Механика композиционных и наноструктурированных материалов.
- Физика прочности и пластичности композиционных и наноструктурированных материалов.
- Механика процессов деформации и разрушения в традиционных материалах (твердых телах).
- Физика прочности и пластичности традиционных материалов (твердых тел).
- Физика и механика дефектов в композиционных, наноструктурированных и традиционных материалах.
- Механика и физика материалов в связанных полях.

Редколлегия принимает статьи, которые нигде ранее не опубликованы и не направлены для опубликования в другие научные издания. Все представляемые в редакцию журнала "Механика и физика материалов" статьи рецензируются. Статьи могут отправляться авторам на доработку. Не принятые к опубликованию статьи авторам не возвращаются.

Журнал "Механика и физика материалов" ("Materials Physics and Mechanics") включен в систему цитирования Web of Science Emerging Sources Citation Index (ESCI), SCOPUS и РИНЦ.

> © 2023, Санкт-Петербургский политех нический университет Петра Великого © 2023, Институт проблем машиноведения Российской академии наук

Contents

On the exact solution of mixed problems for multicomponent multilayer materials V.A. Babeshko, O.V. Evdokimova, O.M. Babeshko
Molecular dynamics study of the dissolution of titanium nanoparticles in aluminum 9-1 G.M. Poletaev, Y.V. Bebikhov, A.S. Semenov, A.A. Sitnikov, V.I. Yakovlev
A model of the formation of serrated deformation and propagation of Luders bands during the Portevin-Le Chatelier effect in alloys G.F. Sarafanov, Yu.G. Shondin, S. I. Kuznetsov
Influence of material anisotropy on the interaction between cracks under tension and shear 24-3 A.V. Savikovskii, A.S. Semenov
On the crack evolutional in human dentin under uniaxial compression imaged by high resolution tomography D. Zaytsev, A. Funk
Estimation of breakdown pressure in laboratory experiments on hydraulic fracturing 52-6 E.V. Novikova, M.A. Trimonova, N.V. Dubinya, S.B. Turuntaev, E.V. Zenchenko
Prediction of mechanical properties of elastomeric materials using neural networks S.V. Fomin, V.S. Rostovtsev, V.U. Meltsov, E.S. Shirokova
The numerical simulation of the post-welding stress-strain state of thin-sheets 79-8 welded joints of EP718 alloy A.Yu. Medvedev, A.E. Medvedev, A.F. Shaikhulova, R.V. Nikiforov, O.V. Murugova, V.R. Galimo
Simplistic model for the investigation of mechanical stability parameters of pyrochlore structured solids R. Bhati, D.S. Yadav, R.C. Gupta, A.S. Verma
Effect of cobalt and tungsten carbide particles inclusions into the aluminium composite on the hardness and wear properties U.B. Gopal Krishna, B. Vasudeva, V. Auradi, M. Nagaral
Effect of Al addition on the mechanical properties of Zr₅₀Cu₅₀-xAlx (0≤x≤50) 107-11 bulk metallic glass V. Guder
Effect of the parameters affecting the properties during friction stir welding of AA 5083 H111 alloy M. Merzoug, A. Ghazi, A. Lousdad, N. Benamara, A. Miloudi, A. Boulenouar
Structure and properties of porous glass ceramics from siliceous rocks with the addition of Mg(OH) ₂ A.I. Rodin, A.A. Ermakov, I.V. Erofeeva, V.T. Erofeev

Surface morphology of InGaAs and InP layers after local Zn diffusion	142-151
from the vapor phase in the MOCVD reactor	

S.A. Blokhin, R.V. Levin, V.S. Epoletov, A.G. Kuzmenkov, A.A. Blokhin, M.A. Bobrov, Y.N. Kovach, N.A. Maleev, N.D. Prasolov, M.M. Kulagina, Yu.A. Guseva, Yu.M. Zadiranov, E.V. Nikitina, V.V. Andryushkin, A.P. Vasil'ev, K.O. Voropaev, V.M. Ustinov

Features of the properties of steel with the trip effect under various types of deformation loading

A.E. Gulin, A.G. Korchunov, D.V. Konstantinov, M.A. Sheksheev, M. Polyakova

On the exact solution of mixed problems for multicomponent multilayer materials

Submitted: May 3, 2023 Approved: September 19, 2023

Accepted: October 9, 2023

V.A. Babeshko 📵 🖾, O.V. Evdokimova 📵, O.M. Babeshko 📵

Kuban State University, Krasnodar, Russia

☐ babeshko41@mail.ru

Abstract. For the first time, an accurate analytical solution of mixed or contact problems for multicomponent multilayer materials has been constructed. It is assumed that the contact problem is formulated at the boundary of a multilayer multicomponent material in a semi-infinite region. These can be contact problems for a multilayer medium that simultaneously includes thermoelectroelastic, magnetoelastic, piezoelastic, water-saturated, nanomaterials and other layers described by linear partial differential equations. In the contact area, there can be any conditions of mechanical, physical or chemical properties that lead the boundary problem to a system of arbitrary finite number of Wiener-Hopf integral equations with a meromorphic matrix in the core. The article uses a new universal modeling method that allowed factorizing the operator of an infinite system of linear algebraic equations.

Keywords: multicomponent materials, mixed, contact problems, system of Wiener-Hopf integral equations, Galerkin transformation, factorization.

Acknowledgements. The work was carried out with the financial support of the Russian Science Foundation, project 22-21-00129.

Citation: Babeshko VA, Evdokimova OV, Babeshko OM. On the exact solution of mixed problems for multicomponent multilayer materials. *Materials Physics and Mechanics*. 2023;51(5): 1-8. DOI: 10.18149/MPM.5152023 1.

Introduction

Mixed, including contact tasks for multicomponent layered media play an important role in a wide variety of practice areas. They arise in the problem of assessing the strength of structures [1–3], the dynamic behavior of deformable bodies [4,5], wave scattering by defects [6], ultrasonic testing [7], the study of semiconductor properties [8,9], the wave phenomena in liquid media [10], seismology [11], evaluation of useful signals [12–15], in banking [16], in probability theory [17–19], in the theory of resonances and localization of processes [20] in the development of block element theory in differential and integral equations [21] and in other fields. As a rule, they are reduced to solving systems of Wiener-Hopf integral equations. In the case of a multicomponent layered medium of finite thickness, these systems of integral equations they have a matrix kernel, which has the following property. Fourier transforms of elements of the matrix kernel of integral equations are meromorphic functions. As described in article [22], methods for the exact solution of such a system of integral equations have not been developed. In this article, thanks to the development of the factorization method in the form of the sum of the operator of an infinite system, it is possible to accurately solve infinite systems of integral equations, and with them, the systems of integral equations themselves. This work should be considered as a development of the previously described approach [22] to the study of the properties of multicomponent materials. A special case of the problem under consideration for a two-component material is considered in [23].

© V.A. Babeshko, O.V. Evdokimova, O.M. Babeshko, 2023.

Publisher: Peter the Great St. Petersburg Polytechnic University

This is an open access article under the CC BY-NC 4.0 license (https://creativecommons.org/li-censes/by-nc/4.0/)

Problem statement

The contact problem for a semi-infinite stamp on a multicomponent multilayer medium is investigated. It is assumed that the layers consist of various materials, the thickness of the multilayer medium has a finite value. In the area of contact of the stamp with the base, all types of permissible mechanical, physical, chemical, biological boundary conditions can be set with the requirement that they lead to a system of Wiener-Hopf integral equations of the order N. It is required that the Fourier transform of the kernel matrix of this system of integral equations has meromorphic functions as its elements. Here is the parameter N is an arbitrary bounded integer. Similarly, a semi-infinite Griffiths crack in the described layered medium can be considered. Mixed problems by known methods [2,4,5,22] are reduced to a system of integral equations of the form:

$$\int_{0}^{\infty} \mathbf{k}(x-\xi) \mathbf{\phi}(\xi) d\xi = \mathbf{f}(x), \quad 0 \le x < \infty ,$$

$$\mathbf{k}(x) = \frac{1}{2\pi} \int_{\Gamma} \mathbf{K}(\alpha) e^{-i\alpha x} d\alpha, \quad \mathbf{K}(\alpha) = ||K_{mr}(\alpha)||, \quad m, r = 1, 2, ..., N,,$$

$$\mathbf{\phi} = \{\phi_{1}, \phi_{2}, ..., \phi_{N}\}, \quad \mathbf{f} = \{f_{1}, f_{2}, ..., f_{N}\}, \quad f_{s}(x) = A_{s}(\eta) e^{-i\eta x},$$
(1)

where the vector $\mathbf{\phi}$ is the desired one, and the vector $\mathbf{f}(x)$ is the specified one.

We assume that the elements $K_{mp}(\alpha)$, m, p = 1, 2, ..., N of the matrix-function $\mathbf{K}(\alpha)$ in (1) are generally meromorphic functions of the variable α . In mixed problems of mechanics and mathematical physics, meromorphic functions $K_{mp}(\alpha)$ and the determinant $\det \mathbf{K}(\alpha)$ have the following representation and asymptotic behavior [2,5]:

$$K_{mp}(\alpha) = D^{-1}(\alpha)L_{mp}(\alpha) , det \mathbf{K}(\alpha) = D^{-N}(\alpha)\Delta(\alpha), \Delta(\alpha) = det \|L_{mp}(\alpha)\|.$$

$$K_{mp}(\alpha) = T_{mp} |\alpha|^{-1} (1 + o(\alpha)), m = p, K_{mp}(\alpha) = T_{mp}\alpha^{-1} (1 + o(\alpha)),$$

$$m \neq p, |\alpha| >> 1, p = 1, 2, ..., N.$$

Here, the functions $L_{mp}(\alpha)$, $D(\alpha)$, $\Delta(\alpha)$ are integer functions of first order and finite type, that is, exponential type, in particular, polynomials. It is assumed that integer functions $D(\alpha)$, $\Delta(\alpha)$ vanish on sets of values $\pm \zeta_n$ and $\pm z_n$, accordingly, having condensation points at infinity in some wedge-shaped regions of the upper, plus, and lower, minus, parts of the complex plane, as a rule, in the vicinity of the imaginary axis. For the sake of simplicity, we will not complicate the properties of matrix functions that have zero general and partial indices, and the system of integral equations is uniquely solvable in some L_p , p > 1. The properties of the matrix-function elements are described in more detail in [2,5] and here we repeat only the following. The determinant $\Delta(\alpha)$ of the matrix-function is an even whole function of type $N\sigma$ [24] and has a countable set of single zeros z_m going to infinity in the upper half-plane. Let 's denote this set W. The denominator $D(\alpha)$ is an even whole function of type σ and has a countable set of zeros ξ_m . Whole functions $L_{mn}(\alpha)$ have a type σ . Let 's construct N aggregates W_p containing zeros z_{mp} , which are selected from the number of zeros $z_{\scriptscriptstyle m}$ of the determinant $\Delta(\alpha)$. Each aggregate $W_{\scriptscriptstyle p}$ will have a countable number of them. When forming them, it is required that each zero z_{mp} number m, from the aggregate W_p , corresponds to the zero number ξ_m of the denominator, such that when $m \to \infty$, the behavior took place $|\xi_m z_{mp}^{-1}| \to v = const$. This requirement is met in most practically important tasks if the following rule applies. When constructing W_p , as the first zeros from the upper half-plane $Rez_{mp} \geq 0$ of the specified aggregates W_p , a sequence of the first zeros z_m of the determinant $\Delta(\alpha)$ is taken in ascending order of modules, or when counting counterclockwise, that is $z_{1p} = z_p$, p = 1, 2, ..., N. In the future, each subsequent zero z_{np} of the aggregate W_p will be taken from among all the zeros z_m of the determinant $\Delta(\alpha)$ according to the rule m = p + (n-1)N, $n \to \infty$ for each. Obviously, the collections W_p , p = 1, 2, ..., N of infinite sets of zeros z_{mp} constructed in this way, are independent, non-intersecting and their union contains the entire set of zeros z_m of the determinant $\Delta(\alpha)$, i.e., $W = \cup W_p$. We construct whole functions $M_p(\alpha, z_p)$ in the form of infinite products [2,5,24] with the help of the zeros included in W_p the number N [2,5,24], taking $\pm z_{sp} = z_{sp}^{\pm}$.

$$M_{p}(\alpha, z_{p}) = M_{pm}(\alpha, z_{p}^{\pm}) M_{p\pm}(\alpha, z_{p}^{m}),$$

$$M_{pm}\left(\alpha, z_{p}^{\pm}\right) = T_{pm}e^{mi\alpha} \prod_{s=1}^{\infty} \left(1 - \frac{\alpha}{z_{sp}^{\pm}}\right) e^{\frac{\alpha}{z_{sp}^{\pm}}}, \tag{2}$$

$$T_{p\mp} = const, \quad p = 1, 2, ..., N,$$

which, after dividing by $D(\alpha)$, will give meromorphic functions denoted by $M_p(\alpha)$. Their zeros are $\pm z_{mp}$. We take the components of the vector of the right part $\mathbf{f}(x)$ of the system of integral equations (1) in the form $A_p(\eta)e^{-i\eta x}$, p=1,2,...,N, $Im \eta=0$. Such component values make it possible to obtain arbitrary right-hand sides of a system of integral equations using Fourier transforms, in the form

$$f_p(x) = \frac{1}{2\pi} \int_{-\infty}^{\infty} A_p(\eta) e^{-i\eta x} d\eta, \quad p = 1, 2, ...N.$$
 (3)

Solution method

To attract to the study a new universal modeling method [21] based on the ideas of fractals, we present a system of Wiener-Hopf integral equations, taking into account the properties of matrix-function elements, in coordinate form:

$$\frac{1}{2\pi} \sum_{p=1}^{N} \int_{-\infty}^{\infty} K_{mp}(\alpha) \Phi_{p}(\alpha) e^{-i\alpha x} d\alpha = A_{m}(\eta) e^{-i\eta x}, 0 \le x < \infty,$$

$$\Phi_{p}(\alpha) = \int_{0}^{\infty} \varphi_{p}(x) e^{i\alpha x} dx, p = 1, 2, ..., N.$$
(4)

Then, taking into account the properties of whole functions having countable numbers of zeros, we have [24]:

$$k_{mp}(x) = \frac{1}{2\pi} \int_{-\infty}^{\infty} K_{mp}(\alpha) e^{-i\alpha x} d\alpha, \quad K_{mp}(\alpha) = \frac{L_{mp}(\alpha)}{D(\alpha)}, \quad f = \left\{ f_1, f_2, \dots f_N \right\},$$

$$L_{mp}(\alpha) = \prod_{n=1}^{\infty} L_{mpn}(\alpha), \qquad K_{mp}(\alpha) = \frac{L_{mp}(\alpha)}{D(\alpha)} = \prod_{n=1}^{\infty} \frac{L_{mpn}(\alpha)}{D_n(\alpha)},$$

$$L_{mpn}(\alpha) = (\alpha^2 - \tau_{mpn}^2), \quad D_n(\alpha) = (\alpha^2 - \xi_n^2).$$

$$(5)$$

Here τ_{mpn} are the zeros of whole functions representing the numerators of the matrix elements, which may not coincide with the zeros of the determinant. The system of Wiener-Hopf integral equations (1) can, taking into account (5), be represented using a system of differential equations in the form:

$$\sum_{p=1}^{N} \prod_{n=1}^{\infty} L_{mpn} (i\frac{\partial}{\partial x}) \varphi_{p}(x) = \prod_{s=1}^{N} D_{s} (i\frac{\partial}{\partial x}) f_{m}(x), \quad m = 1, 2, ..., N,$$

$$p = 1 \sum_{n=1}^{\infty} L_{mpn} (i\frac{\partial}{\partial x}) = \frac{\partial^{2}}{\partial x^{2}} + \tau_{mpn}^{2}, \quad D_{p} (i\frac{\partial}{\partial x}) = \frac{\partial^{2}}{\partial x^{2}} + \xi_{r}^{2}.$$

$$(6)$$

Taking into account (3), we limit ourselves to the representations of the right part of the functions $B_n e^{-i\eta x}$:

$$\prod_{s=1}^{N} D_s(i\frac{\partial}{\partial x}) f_s(x) = Be^{-i\eta x} . \tag{7}$$

Thus, assuming that the parameter η does not coincide with any of the poles ξ_r , we conclude that the differential operators leave the exponential function unchanged on the right, only changing the coefficient in front of it.

We apply the transformation of Galerkin [21]. to a system of the differential equations (6), (7). To do this, we will construct determinants containing new unknown functions χ_p and operators.

$$\Phi_{p}(\mathbf{x}) = \mathbf{E}_{p}(\mathbf{X}), \quad \mathbf{X} = \left\{ \boldsymbol{\chi}_{1}, \boldsymbol{\chi}_{2}, \dots, \boldsymbol{\chi}_{N} \right\}, \quad \Phi_{p} = \left\{ \boldsymbol{\varphi}_{1}, \boldsymbol{\varphi}_{2}, \dots, \boldsymbol{\varphi}_{N} \right\},$$

$$\mathbf{E}_{1}(\mathbf{X}) = \begin{vmatrix} \boldsymbol{\chi}_{1} & L_{12} & \cdots & L_{1N} \\ \boldsymbol{\chi}_{2} & L_{22} & \cdots & L_{2N} \\ \vdots & \vdots & \dots & \vdots \\ \boldsymbol{\chi}_{N} & L_{N2} & \cdots & L_{NN} \end{vmatrix}, \quad \mathbf{E}_{2}(\mathbf{X}) = \begin{vmatrix} L_{11} & \boldsymbol{\chi}_{1} & \cdots & L_{1N} \\ L_{21} & \boldsymbol{\chi}_{2} & \cdots & L_{2N} \\ \vdots & \vdots & \dots & \vdots \\ L_{N1} & \boldsymbol{\chi}_{N} & \cdots & L_{NN} \end{vmatrix}, \dots,$$

$$\mathbf{E}_{N}(\mathbf{X}) = \begin{vmatrix} L_{11} & L_{12} & \cdots & \boldsymbol{\chi}_{1} \\ L_{21} & L_{22} & \cdots & \boldsymbol{\chi}_{2} \\ \vdots & \vdots & \dots & \vdots \\ L_{N1} & L_{N2} & \cdots & \boldsymbol{\chi}_{N} \end{vmatrix}.$$

$$\mathbf{E}_{N}(\mathbf{X}) = \begin{vmatrix} L_{11} & L_{12} & \cdots & \boldsymbol{\chi}_{1} \\ L_{21} & L_{22} & \cdots & \boldsymbol{\chi}_{2} \\ \vdots & \vdots & \dots & \vdots \\ L_{N1} & L_{N2} & \cdots & \boldsymbol{\chi}_{N} \end{vmatrix}.$$

As a result of calculations and simplifications in (8), the following system of N independent differential equations is obtained to determine the functions χ_n :

$$L\chi_p = B_p e^{-i\eta x}, \quad L = \det \|L_{mr}\| \quad m, r = 1, 2, ..., N.$$
 (9)

Having opened the determinant (9), and having carried out possible transformations, we obtain differential equations. They do not depend on the order of calculation of the determinant, since all elements are differential operators with constant coefficients and are commuting. We obtain N infinite systems of differential equations with constant coefficients described by a single differential operator arising from the determinant (9) of the entire system of Wiener-Hopf integral equations. Thus, we obtain an entire function, the arguments

of which will be, in accordance with the conditions of the problem, the products of secondorder differential operators of the form:

$$\Delta(i\frac{\partial}{\partial x}) = \prod_{n=1}^{\infty} G_n, \quad G_n(i\frac{\partial}{\partial x}) = \frac{\partial^2}{\partial x^2} + z_n^2 \quad . \tag{10}$$

It follows that the homogeneous equation (11) for each function χ_p has the form:

$$\prod_{n=1}^{\infty} G_n(i\frac{\partial}{\partial x})\chi_p = 0, \quad p = 1, 2, ..., N.$$

Since the equation $L = \prod_{n=1}^{\infty} G_n$ has constant coefficients, the characteristic equation for homogeneous solutions of a differential equation is an integer function $\Delta(\alpha)$. As a result, a homogeneous solution for each χ_n is represent able in the form:

$$\chi_p = \sum_{m=1}^{\infty} \chi_m e^{iz_m x}, \quad p = 1, 2, ..., N.$$

The solutions of each equation $G_m(i\frac{\partial}{\partial x})\chi_p = 0$ are taken here. The presence of right-

hand sides in a system of integral equations leads systems of differential equations to inhomogeneous ones. To search the general solution of each inhomogeneous differential equation we will look for them in the following form.

The presence of right-hand sides in a system of integral equations leads systems of differential equations to inhomogeneous ones. Taking into account the fact that the general solutions of differential equations must also satisfy the inhomogeneous conditions of the system of integral equations, we will define the parameter B_p from this condition later. To search the general solution of each inhomogeneous differential equation (7) we will look for them in the following form:

$$\chi_{p\eta}(x) = B_p e^{-i\eta x} + \sum_{m=1}^{\infty} y_m e^{iz_m x}, \quad p = 1, 2, ..., N.$$
 (11)

Here B_p , y_m are independent of x and are unknown. Thus, all functions $\chi_{p\eta}(x)$ in (11) have the same decomposition, but with different coefficients B_p .

For mathematically rigorous finding of its expansion terms $y_{pm}e^{iz_{mp}x}$ for each function $\chi_{p\eta}(x)$, a new, previously unknown, factorization method has been developed in the form of the sum of the operator of an infinite system of linear algebraic equations, which is a discrete analog of continuous factorization used in the Wiener-Hopf method.

Solution of the Galerkin equation

A new universal modeling method is applicable for the solution [21]. Unlike traditional finite systems of Galerkin differential equations, in the case of differential equation (9) generated by a system of integral equations (1), a differential equation of infinite order is obtained. For it, it is necessary to construct linearly independent, complete solutions of this equation. Linear independence refers to the absence of identical exponential harmonics in these solutions. Completeness refers to the use of solutions N of all exponential harmonics contained in the characteristic equation in the aggregate $\Delta(\alpha) = 0$. The coefficients of the solutions constructed in this way must be uniquely determined from the requirement of satisfying the system of integral equations (1).

The developed method for solving such infinite systems of linear algebraic equations, technically quite complex, allowed us to obtain the result set out below.

Let the system of integral equations (1) be uniquely solvable in some Banach space [2,5] and the rank of the matrix $||K_{nr}(z_m)||$ is equal to N-1. Let's introduce notation using previously accepted parameters:

$$\begin{split} \mathbf{A} &= \left\| (\xi_k - z_m)^{-1} \right\|, \quad \mathbf{A}^{-1} &= \left\| \tau_{gr} \right\|, \quad \tau_{gr} = \frac{1}{\Delta_+ '(-z_g)(\xi_r - z_g) \left[D_+^{-1}(-\xi_r) \right]'}, \\ \mathbf{A}_p &= \left\| (\xi_k - z_{mp})^{-1} \right\|, \mathbf{A}_p^{-1} &= \left\| \tau_{pgr} \right\|, \quad \tau_{pgr} = \frac{1}{M_{p+} '(-z_{gp})(\xi_r - z_{gp}) \left[D_+^{-1}(-\xi_r) \right]'}, \\ , \quad \mathbf{C}_p &= \left\| K_{nr}(z_{mp}) \right\| \quad n, r = 2, 3, \dots, \\ N_{1p}(\alpha) &= \prod_{s=1}^{N} ' \mathbf{M}_s \left(\alpha, z_{ms} \right) + \mathbf{M}_p \left(\alpha, z_{mp} \right), \\ N_{2p}(\alpha) &= N_{1p}(\alpha) - 2 \mathbf{M}_p \left(\alpha, z_{mp} \right), \quad N_p(\alpha) = N_{2p}^{-1}(\alpha) N_{1p}(\alpha), \\ N_p(\alpha) &= \left\| N_p(\alpha) \right\|. \end{split}$$

The factorization of the following functions is used here $\Delta(\alpha) = \Delta_+(\alpha)\Delta_-(\alpha)$, $D(\alpha) = D_+(\alpha)D_-(\alpha)$, $M_p(\alpha) = M_{p+}(\alpha)M_{p-}(\alpha)$. In the course of the study, the lemma is proved.

Lemma. Let det $\mathbb{C} \neq 0$. Then the complete set of linearly independent solutions of the inhomogeneous Galerkin equation for the right - hand sides $B_p(\eta)e^{-i\eta x}$ is given by the relations:

$$\begin{split} \mathbf{X}_p &= \left\{ \chi_{p\eta} \right\}, \quad \mathbf{Y}_p = \left\{ y_{pm} \right\}, \\ \chi_{p\eta}(x) &= G^{-1}(\eta) B_p(\eta) e^{-i\eta x} + \sum_{m=1}^{\infty} y_{pm} e^{iz_{mp} x}. \end{split}$$

The designations are accepted here:

$$\mathbf{Y}_{1} = \mathbf{A}_{1}^{-1} \left\langle \mathbf{F}_{1} - \frac{1}{2} \sum_{p=2}^{N} \left[\mathbf{G}_{p} + \mathbf{G}_{1} \right] \right\rangle, \quad p=1$$

$$\mathbf{Y}_{p} = \mathbf{A}_{p}^{-1} \left\langle \frac{1}{2} [\mathbf{G}_{p} + \mathbf{G}_{1}] \right\rangle, \quad p = 2, 3, ..., N, \quad \mathbf{F}_{p} = \left\{ -\frac{G^{-1}(\eta)B_{p}}{\eta + \xi_{r}} \right\}$$

$$\mathbf{G}_1 = \mathbf{F}_1, \quad \mathbf{G}_p = \mathbf{A}\mathbf{N}_p(z_{mp})\mathbf{C}_p^{-1}\mathbf{A}^{-1}\mathbf{F}_p, \quad p=2,3,...,N,$$

To obtain a vector $\mathbf{\varphi}(x) = \{\varphi_1, \varphi_2, ..., \varphi_N\}$ representing the solution of the Wiener-Hopf system of integral equations (1), we use the Galerkin transformation formulas (8). The constructed system of solutions $\mathbf{X}(x)$ to the Galerkin differential equation (9) is complete, exhaustive of all harmonics of the zeros of the characteristic equation $\Delta(\alpha) = 0$, which is required when applying the Galerkin transformation. Therefore, to determine the vector $\mathbf{\varphi} = \{\varphi_1, \varphi_2, ..., \varphi_N\}$ of the solution of the integral equation (1), it is necessary to use the formulas (8). The complete system of solutions of the Galerkin equation (9), functions $\chi_{p\eta}(x)$, are introduced into the determinants (8) and, after their disclosure and performing the necessary differential operations, give an exact solution to the system of integral equations (1).

The theorem. Under the conditions of the lemma, the exact solution of the system of integral equations (1) for the right parts $A_n(\eta)e^{-i\eta x}$ has the form:

$$\Phi_{p}(x) = \mathbf{E}_{p}(\mathbf{X}), \quad \mathbf{X}(x) = \left\{ \boldsymbol{\chi}_{1\boldsymbol{\eta}}, \boldsymbol{\chi}_{2\boldsymbol{\eta}}, ..., \boldsymbol{\chi}_{p\boldsymbol{\eta}} \right\},
\mathbf{X}(x) = \mathbf{K}^{-1}(\boldsymbol{\eta})\mathbf{f} + \mathbf{Z}(x), \quad \mathbf{Z}(x) = \left\{ \sum_{m=1}^{\infty} y_{pm} e^{iz_{mp}x} \right\},
\mathbf{f} = \left\{ f_{1}, f_{2}, ..., f_{N} \right\}, \quad \mathbf{F} = -\frac{\mathbf{K}^{-1}(\boldsymbol{\eta})\mathbf{f}}{\boldsymbol{\eta} + \boldsymbol{\xi}_{r}}, \quad \mathbf{F} = \left\{ \mathbf{F}_{p} \right\}.$$

The validity of both the lemma and the theorem can be verified by directly substituting the corresponding solutions into systems of differential and integral equations.

In the event that the matrix-function $K(\alpha)$ continuously transitions into a functional-commutative one, the constructed solution passes into the solution obtained by simple handling of a system with functionally commutative matrix functions for a particular case. From this formula, as a special case, the result of a two-dimensional problem of the work [24] is obtained.

Conclusions

For the first time, an accurate analytical solution of mixed or contact problems for multicomponent multilayer materials has been constructed.

The article uses a new universal modeling method, [21] which made it possible to overcome the problem of factorization of the operator of an infinite system of linear algebraic equations. The exact solution is given in the form of formulas and accompanying parameters that allow the result to be applied in research. The considered contact problem is formulated on the boundary of a multilayer multicomponent material in a semi-infinite region. These can be contact problems for a multilayer medium, which simultaneously includes thermoelectroelastic, magnetoelastic, piezoelastic, water-saturated, nanomaterials and other layers described by linear partial differential equations. In the contact area, there can be any conditions of a mechanical, physical or chemical nature that lead the boundary problem to a system of arbitrary finite number of Wiener-Hopf integral equations with a meromorphic matrix in the core. This method is applicable to solving a mixed problem about the behavior of a semi-infinite crack in a multicomponent multilayer foundation. Unlike other approaches, the proposed method allows you to obtain the desired solution in an analytical form without requiring additional research.

Referensces

- 1. Freund L. B. Dynamic Fracture Mechanics. Cambridge, UK: Cambridge University Press; 1998.
- 2. Vorovich II, Alexandrov VM, Babeshko VA. *Nonclassical mixed problems of elasticity theory*. Moscow; 1974. (In-Russian)
- 3. Khrapkov AA. Solutions of closed-form problems on the elastic equilibrium of an infinite wedge with an asymmetric notch at the top. *PMM*. 1971;35: 1009–1016. (In-Russian)
- 4. Achenbach JD. Wave propagation in Elastic Solids. Amsterdam: North-Holland; 1973.
- 5. Vorovich II, Babeshko VA. Dynamic mixed problems of elasticity theory for nonclassical domains. Moscow: Nauka; 1979. (In-Russian)
- 6. Abrahams ID, Wickham GR. General Wiener-Hopf factorization matrix kernels with exponential phase factors. *SIAM J. Appl. Math.* 1990;50: 819–838.
- 7. Norris AN, Achenbach JD. Elastic wave diffraction by a semi infinite crack in a transversely isotropic material. Q. J. Apple. Math. Mech. 1984;37(4): 565–580.
- 8. Sautbekov S, Nilsson B. Electromagnetic scattering theory for gratings based on the Wiener-Hopf method. *AIP Conf. Proc.* 2009;1106(1): 110–117.

- 9. Noble B. Wiener-Hopf method. Moscow: ILL; 1962. (In-Russian).
- 10. Chakrabarti A, George AJ. Solution of a singular integral equation involving two intervals arising in the theory of water waves. *Appl. Math. Lett.* 1994;7(5): 43–47.
- 11. Davis AMJ. Continental shelf wave scattering by a semi-infinite coastline. *Geophys. Astrophys. Fluid Dyn.* 1987;39(1-2): 25–55.
- 12. Payandeh Najafabadi AT, Kucerovsky D. Exact solutions for a class matrix Riemann-Hilbert problems. *IMA Journal of Applied Mathematics*. 2014;79(1): 109–123.
- 13. Anderson BD, Moore JB. *Optimal Filtering*. New York: SDover Publications; 2005.
- 14. Litvinchuk GS, Spitkoskii IM. Factorization of Measurable Matrix Functions. Boston: Birkhäuser Verlag Basel; 1987.
- 15. Adukov VM. Wiener-Hopf factorization of meromorphic matrix-functions. *Algebra and Analysis*. 1992;4(1); 54–74. (In-Russian)
- 16. Fusai G, Abrahams ID, Sgarra C. An exact analytical solution for discrete barrier options. *Finance Stoch.* 2006;10: 1–26.
- 17. Najafabadi ATP, Kucerovsky D. On distribution of extrema for a class of Lévy processes. To be published in: *J. Probab. Statist. Sci.* [Preprint] 2011;9: 127–138.
- 18. Brockwell PJ, Davis RA. Introduction to Time Series and Forecasting. New York: Springer; 2002.
- 19. Dym H, McKean HP. Fourier Series and Integrals. Probability and Mathematical Statistics. New York: Academic Press; 1972.
- 20. Vorovich II, Babeshko VA, Pryakhina OD. *Dynamics of massive bodies and resonant phenomena in deformable media*. Moscow: Nauka; 1999. (In-Russian)
- 21. Babeshko VA, Evdokimova OV, Babeshko OM. Fractal properties of block elements and a new universal modeling method. *DAN*. 2021;499: 21–26.
- 22. Babeshko VA, Evdokimova OV, Babeshko OM. On the problem of evaluating the behavior of multicomponent materials in mixed boundary conditions in contact problems. *Materials Physics and Mechanics*. 2022;48(3): 379–385.
- 23. Babeshko VA, Evdokimova OV, Babeshko OM. The Hilbert-Wiener factorization problem and the block-element method. *Dokl. Phys.* 2014;59: 591–595.
- 24. Markushevich AI. Theory of analytic functions. Moscow; 1968. (In-Russian)

THE AUTHORS

Babeshko V.A.

e-mail: babeshko41@mail.ru

Evdokimova O.V.

e-mail: evdokimova.olga@mail.ru

Babeshko O.M. @

e-mail: babeshko49@mail.ru

Molecular dynamics study of the dissolution of titanium nanoparticles in aluminum

Submitted: March 10, 2023

Approved: July 4, 2023

Accepted: July 13, 2023

G.M. Poletaev (1) 1 2, Y.V. Bebikhov (1) 2, A.S. Semenov (1) 2,

A.A. Sitnikov (1) 1, V.I. Yakovlev (1) 1

¹ Polzunov Altai State Technical University, Barnaul, Russia ² Polytechnic Institute of North-Eastern Federal University, Mirny, Russia ☐ gmpoletaev@mail.ru

Abstract. The dissolution of a titanium particle in aluminum under the conditions of the crystalline and amorphous state of aluminum and titanium was studied by the molecular dynamics method. It is shown that the state of the aluminum structure has little effect on the intensity of titanium dissolution. This is due to the formation around a crystalline titanium particle, regardless of the initial aluminum structure, of a crystalline layer of aluminum with a thickness of about 1 nm, which repeats the titanium lattice. This layer affects the mechanism and intensity of mutual diffusion near the Ti–Al interface. In the case of the amorphous state of the titanium particle and the aluminum matrix, the dissolution occurred several times faster than in the crystalline state of titanium. That is, the reduction in the ignition temperature of the reaction of high-temperature synthesis in the Ti–Al system is much more efficiently achieved not by amorphization of aluminum, but by amorphization of titanium.

Keywords: molecular dynamics; diffusion; interphase boundary; titanium, aluminum

Acknowledgements. Poletaev G.M., Sitnikov A.A. and Yakovlev V.I. thank the Ministry of Science and Higher Education of the Russian Federation for financial support (project FZMM-2023-0003). Bebikhov Y.V. and Semenov A.S. are grateful for the financial support of the Russian Science Foundation (RSF project No. 22-22-00810).

Citation: Poletaev GM, Bebikhov YV, Semenov AS, Sitnikov AA, Yakovlev VI. Molecular dynamics study of the dissolution of titanium nanoparticles in aluminum. *Materials Physics and Mechanics*. 2023;51(5): 9-15. DOI: 10.18149/MPM.5152023_2.

Introduction

Intermetallic compounds of the Ti–Al system have a significant potential for their use as high-temperature structural materials for the aerospace and automotive industries. They have a combination of such properties as a high yield strength at elevated temperatures and good resistance to oxidation and corrosion, along with a relatively low density [1–7]. In practice, coarse-grained powders with grain sizes on the order of micrometers are usually used for the reaction synthesis of aluminides [8–10]. Currently, one of the promising methods for their preparation is preliminary mechanical activation treatment, which makes it possible to achieve the limiting degree of grain refinement in a mixture before the main synthesis reaction [11–13]. In the process of mechanoactivation, so-called mechanocomposites are formed, which are a matrix of a more plastic component (aluminum), in the volume of which there are nanosized particles of a more brittle component of the mixture (in this case, titanium) [12,13]. Such a system is characterized by a high degree of nonequilibrium due to

© G.M. Poletaev, Y.V. Bebikhov, A.S. Semenov, A.A. Sitnikov, V.I. Yakovlev, 2023.

Publisher: Peter the Great St. Petersburg Polytechnic University

the high concentration of defects, interfaces, internal stresses, and the presence of an amorphous phase. It is noted that the onset of the combustion reaction in such a nonequilibrium system begins at temperatures significantly below the melting temperature of aluminum [12,13].

Earlier, in [14], using the molecular dynamics method, we studied the dependence of the melting temperature of titanium nanoparticles, as well as Ti₃Al, TiAl, and TiAl₃ particles, on their diameter in vacuum and in liquid aluminum. It has been shown that the melting point decreases as the particle size decreases in proportion to the ratio of the surface area of the particle to its volume. However, the decrease in the ignition temperature of the high-temperature synthesis reaction in mechanocomposites is obviously not associated with a decrease in the melting temperature of titanium nanoparticles, but is apparently due to the presence of internal stresses and an amorphous phase in the mixture, which can contribute to the intensification of mutual diffusion and the release of additional energy. To verify this, in the present work, a study was carried out using molecular dynamics simulation of the dissolution of titanium nanoparticles of different sizes in aluminum under the conditions of crystalline and amorphous states of aluminum and titanium.

Description of the model

The computational cell in the molecular dynamics model had the shape of a rectangular parallelepiped. Periodic boundary conditions were used along two axes, and free (or open) conditions were used along the third. The presence of an open surface allowed the computational cell to freely change the volume during the melting of aluminum or as a result of other processes during mutual diffusion. A round titanium particle was placed in the aluminum matrix at the center of the computational cell (Fig. 1). Aluminum and titanium were initially created in the crystalline state. Particles of three diameters were considered: 5, 7, and 9 nm. In our previous work [14], it was shown that the greatest influence of the particle size on its melting point is observed at a diameter less than about 7 nm. The number of atoms in the computational cell was 32427, 82401, or 179725, depending on the considered particle size. After introducing a titanium particle into an aluminum matrix and removing excess aluminum atoms, the structure was relaxed at a starting temperature of 0 K. After stabilization of the structure and temperature of the computational cell, it was again cooled to 0 K.

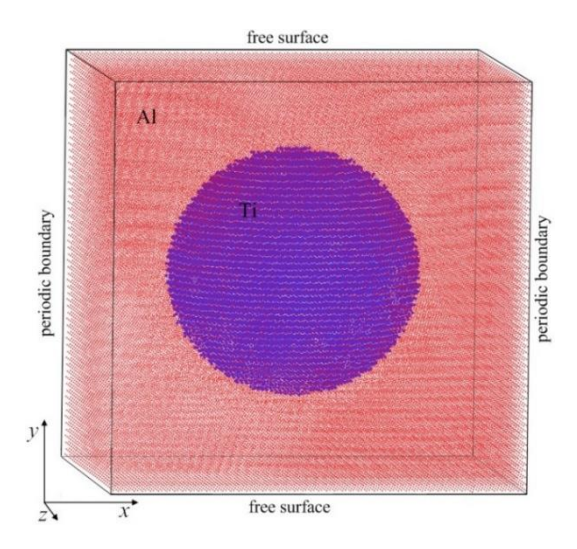


Fig. 1. Computational cell with the round titanium particle in aluminum

To describe interatomic interactions in the Ti–Al system, EAM potentials from [15] were used, where they were obtained based on comparison with experimental data and ab initio calculations for various properties and structures of metals Ti, Al and intermetallic compounds Ti₃Al and TiAl. These potentials have proven themselves well in various studies and have been successfully tested in a wide range of mechanical and structural-energy properties of alloys of the Ti–Al system [14–19]. In particular, the potentials used quite well describe the melting points of Ti and Al: in our molecular dynamics model, they turned out to be 1995 and 990 K, respectively (reference values: 1943 and 933 K).

In addition to the crystalline state of aluminum and titanium, in this work we considered the cases of dissolution of crystalline titanium in amorphous aluminum and amorphous titanium in amorphous aluminum. The amorphous structure of aluminum or titanium was created by heating in the model of the corresponding phase to a temperature significantly higher than the melting point of the metal, holding for some time for the final destruction of the crystalline structure, and subsequent rapid cooling, during which crystallization did not have time to occur. In carrying out this procedure, we sought to minimize the initial mutual diffusion of titanium and aluminum. The quality of the amorphous structure was verified not only by the diagrams of the radial distribution of atoms, but also by the absence of crystallization during the subsequent simulation in the considered phase. For the occurrence of homogeneous crystallization in the molecular dynamics model, as a rule, longer computer experiments were required to be compared to those considered in the present work [18–22].

The temperature in the main computer experiments was set in terms of the initial velocities of the atoms according to the Maxwell distribution. A Nose-Hoover thermostat was used to keep the temperature constant during the simulation. The time integration step in the molecular dynamics method was 2 fs.

Results and discussion

To analyze the intensity of the dissolution of titanium atoms in aluminum, a special characteristic was used – the difference in the number of dissolved titanium atoms ΔN at the current and initial moments of time. A Ti atom was considered dissolved if the number of Al atoms in its nearest environment (within a radius of 3.7 Å) exceeded 50 %. Figure 2(a) shows the time dependences of the percentage of dissolved titanium atoms for particles with a diameter of 5, 7, and 9 nm at a constant temperature of 1200 K, that is in molten aluminum. In all cases, as can be seen in the figure, the dissolution at first proceeded intensively, then the rate decreased and subsequently remained approximately constant. The same character of particle dissolution was noted by other researchers, for example, in [23,24], and is apparently explained by the formation at the first stage of a diffusion zone saturated with atoms of both components.

The ratio of the surface area of a particle to its volume increases as the particle diameter decreases. In this regard, the proportion of dissolved titanium atoms is higher for particles of smaller size than for particles with a large diameter (Fig. 2(a)). Next, we used a value that is universal for particles of different sizes – the specific number of dissolved atoms $\Delta N/S$, which was defined as the ratio of the number of dissolved atoms to the surface area of a particle. Figure 2(b) shows the dependences of $\Delta N/S$ on time at a constant temperature of 800 K for the considered particles in the cases of crystalline Ti and Al, crystalline Ti and amorphous Al, and amorphous Ti and Al.

The first thing that attracts attention is the coincidence of the graphs obtained for the crystalline and amorphous states of aluminum (lower graphs in Fig. 2(b)). The titanium particle in both cases was crystalline. This is an interesting result, indicating that the intensity of titanium dissolution in aluminum is almost independent of the state, crystalline or amorphous, of the aluminum structure. Here it should be emphasized that we are talking about

dissolution at a constant temperature below the melting point of aluminum. Structural transformations and partial crystallization of amorphous aluminum can lead to the release of additional heat in real materials, which can accelerate dissolution. However, at a constant temperature, as the simulation showed, there is almost no difference for the crystalline and amorphous states of aluminum. Small differences in the values of $\Delta N/S$ for particles of different sizes are due to the fact that the interphase boundary has a certain effective thickness, which was also discussed in [14] when studying the effect of particle diameter on their melting temperature.

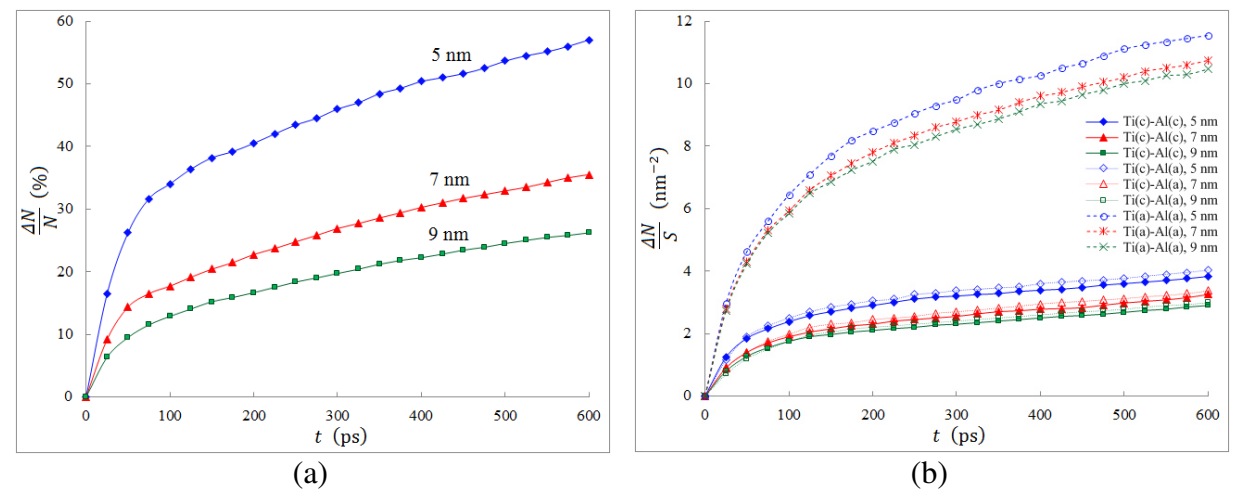
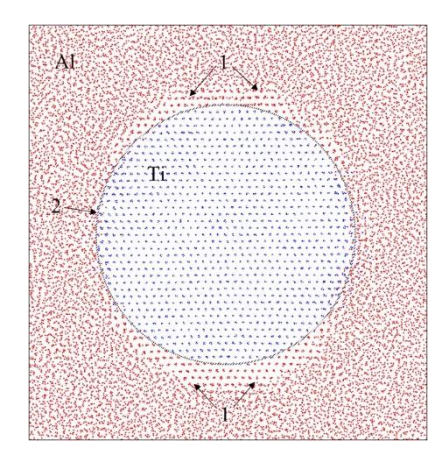
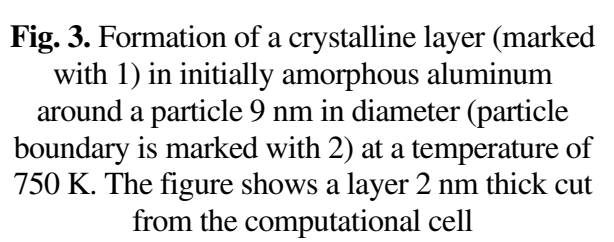


Fig. 2. Dissolution of Ti particles in Al at a constant temperature: (a) time dependence of the percentage of dissolved Ti atoms at a temperature of 1200 K for particles with a diameter of 5, 7, and 9 nm; (b) time dependences of the specific amount of dissolved Ti atoms at a temperature of 800 K for the considered particles in the cases of crystalline Ti and Al, crystalline Ti and amorphous Al, and amorphous Ti and Al

The fact is that, as we noted earlier in [19], when studying the effect of the orientation of the interphase boundary on the intensity of mutual diffusion, regardless of the type of aluminum structure and its orientation, a crystalline aluminum layer several atomic planes thick is formed on the Ti–Al interphase boundary, repeating the crystal lattice of titanium. This layer was observed by us in [19] even at temperatures above the melting point of aluminum and had a significant effect on the mechanism of mutual diffusion at the Ti–Al interface. Figure 3 shows an example of the formation of a crystalline layer in initially amorphous aluminum around a titanium particle 9 nm in diameter. It should be noted that further crystallization of aluminum during the modeling process, as a rule, did not occur, mainly due to the mismatch between the parameters and types of titanium and aluminum crystal lattices. The formation of a crystalline layer of aluminum near the interface with a titanium particle primarily depended on the orientation of the titanium crystal lattice. The thickness of this layer was not the same in different areas of the particle surface (Fig. 3).

When modeling the dissolution of an amorphous titanium particle in amorphous aluminum, the situation changed drastically and, in contrast to the cases with a crystalline titanium particle, the dissolution proceeded much faster (upper plots in Fig. 2(b)). The specific amount of dissolved atoms $\Delta N/S$ for amorphous titanium was several times greater than for a particle with a crystalline structure at the same temperature. Thus, the decrease in the ignition temperature is achieved much more efficiently not by aluminum amorphization, but by titanium amorphization.





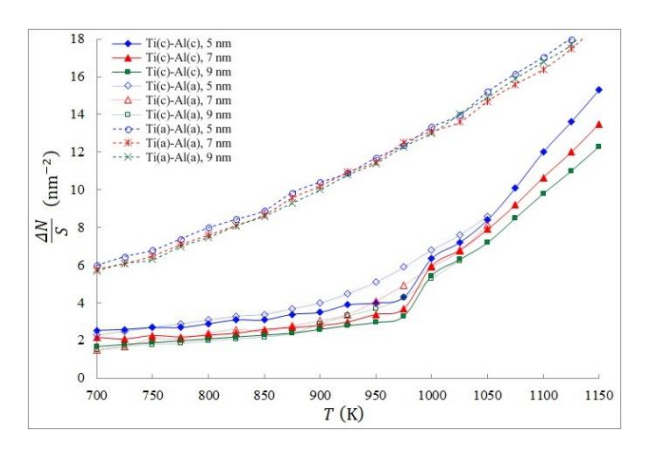


Fig. 4. Temperature dependences of the specific amount of dissolved Ti atoms after simulation for 200 ps for particles 5, 7, and 9 nm in diameter in the cases of crystalline Ti and Al, crystalline Ti and amorphous Al, and amorphous Ti and Al

To further confirm this thesis, we studied the dependence of the specific amount of dissolved Ti atoms on temperature for the same duration of a computer experiment of 200 ps. Figure 4 shows the dependences obtained for the three considered particle sizes and the cases of crystalline Ti and Al, crystalline Ti and amorphous Al, and amorphous Ti and Al.

On Fig. 4 for the case of crystalline Ti and Al, the "ignition temperature" is well identified by a sharp increase in the value of $\Delta N/S$ at a temperature coinciding with the melting point of aluminum. For the potentials used, it is slightly higher than the reference value of 933 K and is approximately 990 K. In addition, it can be seen that the diameter of the particle does not affect the position of the jump in the value of $\Delta N/S$ and coincides for all considered particles. Thus, another important result is the absence of an effect of the titanium nanoparticle diameter on the ignition temperature of the high-temperature synthesis reaction in the Ti–Al system. It should be emphasized that this refers specifically to the temperature at which there is a sharp acceleration of mutual diffusion, and not to the intensity of dissolution, which is proportional to the total area of the interphase boundary and will obviously be higher with a smaller diameter of titanium particles.

In the amorphous state of aluminum, no jumps were observed in the dependences of the $\Delta N/S$ value in the region of the melting temperature. However, these dependences otherwise coincided with the dependences obtained for the case of crystalline aluminum. The absence of a jump in the dependences was obviously due to the absence of a phase transition in aluminum – aluminum in this case was initially amorphous.

In the amorphous state of the titanium particle and the aluminum matrix, the dissolution occurred much more intensively (upper graphs in Fig. 4). In this case, the dependences of the $\Delta N/S$ value did not contain any breaks or jumps. In the entire considered temperature range, the behavior of the dependences had the classical form of the Arrhenius temperature dependence.

Conclusion

The dissolution of a titanium particle in aluminum under the conditions of the crystalline and amorphous state of aluminum and titanium was studied by the molecular dynamics method. It is shown that the state of the aluminum structure has practically no effect on the intensity of titanium dissolution. This is due to the formation around a crystalline titanium particle,

regardless of the initial aluminum structure, of a crystalline layer of aluminum with a thickness of about 1 nm, which repeats the titanium lattice. This layer affects the mechanism and intensity of mutual diffusion near the Ti–Al interface.

In the case of an amorphous state of a titanium particle and an aluminum matrix, the dissolution occurs much more intensively than in the crystalline state of titanium. The intensity of dissolution in the first case already at a temperature of 700 K corresponds to the melting temperature of aluminum in the case of a crystalline titanium particle. That is, a decrease in the ignition temperature of the high-temperature synthesis reaction in the Ti–Al system is achieved much more effectively not by aluminum amorphization, but by titanium amorphization.

The diameter of titanium nanoparticles, as was found in the work, affects the intensity of dissolution of titanium in aluminum, but does not affect the ignition temperature of the high-temperature synthesis reaction.

References

- 1. Tetsui T. Manufacturing technology for gamma-TiAl alloy in current and future applications. *Rare Metals*. 2011;30: 294–299.
- 2. Lapin J. TiAl-based alloys: Present status and future perspectives. *Proceedings of the Metal.* 2009;19: 2019–2031.
- 3. Voisin T, Monchoux J-P, Couret A. Near-net shaping of titanium-aluminum jet engine turbine blades by SPS. In: *Spark Plasma Sintering of Materials*. Cham: Springer; 2019. p.713–737.
- 4. Wu H, Zhang Sh, Hu H, Li J, Wu J, Li Q, Wang Zh. Concentration-dependent diffusion kinetics of Ti-Al binary system at elevated temperatures: experiments and modeling. *Intermetallics*. 2019;110: 106483.
- 5. Thiyaneshwaran N, Sivaprasad K, Ravisankar B. Nucleation and growth of TiAl₃ intermetallic phase in diffusion bonded Ti/Al Metal Intermetallic Laminate. *Scientific Reports*. 2018;8: 16797.
- 6. Grigorenko SG, Grigorenko GM, Zadorozhnyuk OM. Intermetallics of titanium. peculiar features, properties, application (review). *Sovremennaya Electrometallurgiya*. 2017;128: 51–58. (In-Russian)
- 7. Wu Q, Wang J, Gu Y, Guo Y, Xu G, Cui Y. Experimental diffusion research on BCC Ti-Al-Sn ternary alloys. *Journal of Phase Equilibria and Diffusion*. 2018;39: 724-730.
- 8. Lee S-H, Lee J-H, Lee Y-H, Shin DH, Kim YS. Effect of heating rate on the combustion synthesis of intermetallics. *Materials Science and Engineering:* A. 2000;281: 275–285.
- 9. Bertolino N, Monagheddu M, Tacca A, Giuliani P, Zanotti C, Tamburini UA. Ignition mechanism in combustion synthesis of Ti–Al and Ti–Ni systems. *Intermetallics*. 2003;11: 41–49.
- 10. Adeli M, Seyedein SH, Aboutalebi MR, Kobashi M, Kanetake N. A study on the combustion synthesis of titanium aluminide in the self-propagating mode. *Journal of Alloys and Compounds*. 2010;497(1-2): 100–104.
- 11. Boldyrev VV, Tkacova K. Mechanochemistry of solids: past, present, and prospects. *Journal of Materials Synthesis and Processing*. 2000;8: 121–132.
- 12. Filimonov VY, Loginova MV, Ivanov SG, Sitnikov AA, Yakovlev VI, Sobachkin AV, Negodyaev AZ, Myasnikov AY. Peculiarities of phase formation processes in activated Ti+Al powder mixture during transition from combustion synthesis to high-temperature annealing. *Combustion Science and Technology*. 2020;192(3): 457–470.
- 13. Loginova MV, Yakovlev VI, Filimonov VY, Sitnikov AA, Sobachkin AV, Ivanov SG, Gradoboev AV. Formation of structural states in mechanically activated powder mixtures Ti+Al exposed to gamma irradiation. *Letters on Materials*. 2018;8(2): 129–134.
- 14. Poletaev GM, Sitnikov AA, Yakovlev VI, Filimonov VY. Melting point of Ti, Ti₃Al, TiAl, and TiAl₃ nanoparticles versus their diameter in vacuum and liquid aluminum: molecular dynamics investigation. *Journal of Experimental and Theoretical Physics*. 2022;134(2): 183–187.

- 15. Zope RR, Mishin Y. Interatomic potentials for atomistic simulations of the Ti-Al system. *Physical Review B*. 2003;68(2): 024102.
- 16. Kim Y-K, Kim H-K, Jung W-S, Lee B-J. Atomistic modeling of the Ti–Al binary system. *Computational Materials Science*. 2016;119: 1–8.
- 17. Pei Q-X, Jhon MH, Quek SS, Wu Z. A systematic study of interatomic potentials for mechanical behaviours of Ti-Al alloys. *Computational Materials Science*. 2021;188: 110239.
- 18. Poletaev GM. Self-diffusion in liquid and solid alloys of the Ti-Al system: molecular-dynamics simulation. *Journal of Experimental and Theoretical Physics*. 2021;133(4): 455–460.
- 19. Poletaev GM, Bebikhov YV, Semenov AS, Sitnikov AA. Molecular dynamics investigation of the effect of the interface orientation on the intensity of titanium dissolution in crystalline and amorphous aluminum. *Journal of Experimental and Theoretical Physics*. 2023;136(4): 477–483.
- 20. Poletaev GM, Novoselova DV, Kaygorodova VM. The causes of formation of the triple junctions of grain boundaries containing excess free volume in fcc metals at crystallization. *Solid State Phenomena*. 2016;249: 3–8.
- 21. Poletaev GM, Rakitin RY. Molecular dynamics study of stress-strain curves for γ -Fe and Hadfield steel ideal crystals at shear along the <111> direction. *Materials Physics and Mechanics*. 2021;47(2): 237–244.
- 22. Poletaev GM, Rakitin RY. Molecular dynamics simulation of severe plastic deformation of nanotwinned Hadfield steel. *Materials Physics and Mechanics*. 2022;50(1): 118–125.
- 23. Levchenko EV, Evteev AV, Lorscheider T, Belova IV, Murch GE. Molecular dynamics simulation of alloying in an Al-coated Ti nanoparticle. *Computational Materials Science*. 2013;79: 316–325.
- 24. Cherukara MJ, Weihs TP, Strachan A. Molecular dynamics simulations of the reaction mechanism in Ni/Al reactive intermetallics. *Acta Materialia*. 2015;96: 1–9.

THE AUTHORS

Poletaev G.M.

e-mail: gmpoletaev@mail.ru

Semenov A.S. (D)

e-mail: as.semenov@s-vfu.ru

Yakovlev V.I. @

e-mail: yak1961@yandex.ru

Bebikhov Y.V.

e-mail: bebikhov.yura@mail.ru

Sitnikov A.A.

e-mail: sitalan@mail.ru

A model of the formation of serrated deformation and propagation of Luders bands during the Portevin-Le Chatelier effect in alloys

Submitted: June 1, 2023

Approved: July 20, 2023

Accepted: August 1, 2023

G.F. Sarafanov ^{1 ⊠}, Yu.G. Shondin ^{10 2}, S.I. Kuznetsov ³

¹ Institute of mechanical engineering problems RAS – branch of the Federal State Budgetary Scientific

Institution "Federal Research Center Institute of Applied Physics of the Russian Academy of Science", Nizhny

Novgorod, Russia

Abstract. A distributed autowave model of the Portevin-Le Chatelier effect has been developed for the region of medium and elevated temperatures in alloys. The model was converted into dimensionless form and the mechanisms of serrated deformation and localization of plastic flow were studied using analytical and numerical approaches. An instability region is found for the rate of plastic deformation and temperature, in the vicinity of which the Portevin-Le Chatelier effect is realized. The critical dimensionless parameters responsible for the variety of spatial-wave solutions of the initial system of equations are determined: the shapes of the load oscillations representing a quasi-periodic sequence of oscillating wave packets; bursts of plastic deformation velocity. The bursts are strictly correlated and form distinct Portevin-Le Chatelier bands under the stochastic deformation regime. Portevin-Le Chatelier bands extend from one end of the crystal to the other, where the reverse band is formed. This process of propagation of deformation bands is periodically repeated.

Keywords: Portevin-Le Chatelier effect; alloys; serrated deformation; high temperatures; stochastic self – oscillation; Luders and Portevin-Le Chatelier bands

Acknowledgements. The Russian Science Foundation supported this work, project No. 22-22-00749.

Citation: Sarafanov GF, Shondin YG, Kuznetsov SI. A model of the formation of serrated deformation and propagation of Luders bands during the Portevin-Le Chatelier effect in alloys. *Materials Physics and Mechanics*. 2023;51(5): 16-23. DOI: 10.18149/MPM.5152023_3.

Introduction

Plastic deformation processes are among the most complex processes in materials science, since they lead to various features of the microstructure of the resulting materials and their behavior under loading.

One of such features of metal alloys in the region of medium and elevated temperatures is the instability of plastic deformation in the form of the serrated flow [1–7] known as the Portevin-Le Chatelier effect (PLC), named after French researchers who first observed this phenomenon in 1923 [8].

The PLC effect consists in the irregular repetition of the load jumps σ_d and the rate of plastic deformation [4,5,9], which correspond to the localization of plastic flow in the form of deformation bands of the Luders type [10,11]. The oscillations of the deformable crystal occur due to the elastic response of the machine-sample system [12,13] and have the form of stochastic relaxation self-oscillations (Fig. 1).

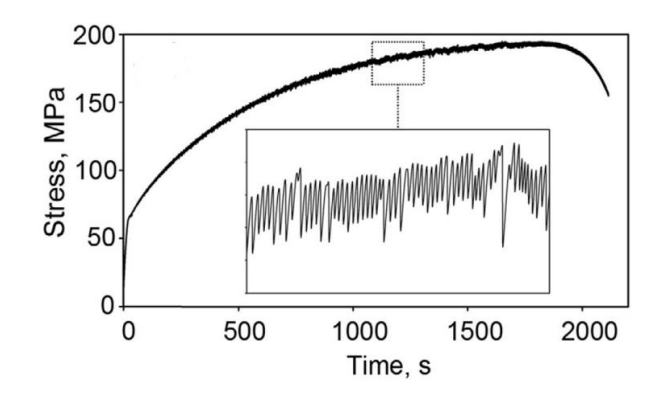


Fig. 1. A typical stress-time curve showing type *B* stress jumps at a given rate of plastic deformation $\dot{\epsilon}_0 = 1.4 \cdot 10^{-4} \, s^{-1} [12]$

There are usually five types of basic jumps of the deforming stress [14,15], but three [13,16] of them are distinguished, which correspond to various features of the occurrence and propagation of deformation bands [4,5].

Jumps of the A type occur above a certain average level of deforming stresses at relatively low temperatures. Jumps of the B type are irregular in nature and characterized by the relay propagation of deformation bands and their spatial correlation. Jumps of the C type occur at elevated temperatures, are located below the average level of deforming stresses and are characterized by high randomness. Jumps of other types are usually less common [14].

In the articles [17,20], an autowave model of the Portevin-Le Chatelier effect has been proposed. The model is described by a system of differential equations for deforming stress, dislocation velocity, concentration of dissolved impurity atoms interacting with moving dislocations and forming a cloud of impurity atoms around them, which is called the Cottrell atmosphere [3]. At low velocities of dislocations the Cottrell atmosphere brakes them strongly. However, as the dislocation velocity increases, the atmosphere decreases, which leads to a weakening of the braking force (there is a negative sensitivity to strain rate) and instability, which is the cause of various spatial-wave solutions.

In [20], within the framework of this model, in the dislocation sliding plane, the formation of a switching wave of the plastic deformation rate was described, interpreted as a Luders band. In the article [17], a solution was obtained in the form of relaxation self-oscillations of the deforming stress and the plastic deformation rate, which can be considered as a manifestation of the Portevin-Le Chatelier effect. However, in [17], the oscillatory process is considered in a homogeneous approximation, which does not allow for the localization of sliding in the form of deformation bands.

In this paper, the PLC autowave model is generalized to the case of deformation propagation along the sample and investigated numerically for spatial wave solutions, namely stochastic load dynamics and plastic deformation rate.

Note that there are other models for describing the phenomenon of PLC [12,13], the so-called Dynamic Strain Ageing (DSA) models [14]. However, they are mainly phenomenological in nature, unlike our approach.

PLC effect model

Consider the behavior of an ensemble of dislocations in a slip band of width w. Let's choose the direction of dislocation sliding to the 0x' axis at some angle to the 0x axis of sample stretching. Usually this angle is approximately $\pi/3$ [2]. Let the dislocation distribution in the slip band be considered homogeneous $\rho = \rho_0$. Denote by v(t,x') the velocity of dislocations in the transverse sliding plane. Accordingly, the rate of plastic deformation in the slip band is determined by the Orovan's formula as $\dot{\gamma}(t,x') = b\rho_0 v(t,x')$ (b is the modulus of the Burgers vector). Then the dislocation velocity and the rate of plastic deformation along the loading axis can be approximately written as $v(t,x) \approx \phi v(t,x')$ and $\dot{\varepsilon}(t,x) \approx \dot{\phi}\dot{\gamma}(t,x')$, where $\phi = 1/2 \div 1/3$ is the orientation factor.

In this case, the process of plastic deformation in the loading regime with a given rate of plastic deformation $\dot{\epsilon}_0$ can be described along the loading axis by the following system of equations [17]

$$m^* \frac{\partial v}{\partial t} = b(\sigma + \sigma^{int}) - F(v), \tag{1}$$

$$\frac{\partial \sigma^{int}}{\partial t} = -\frac{\sigma^{int}}{t_a} + \gamma_1 \frac{\partial^2 \dot{\varepsilon}}{\partial x^2},\tag{2}$$

$$\frac{\partial \sigma}{\partial t} = G^* [\dot{\varepsilon}_0 - \frac{b\rho_0}{L} \int_0^L v(x, t) dx]. \tag{3}$$

Here we neglect the orientation factor ϕ , since it has little effect on the nature and shape of the space-wave solutions, making only small corrections to the numerical results.

Equation (1) is the equation of dislocation motion, m^* is the effective mass of a dislocation (per unit length), $\sigma(t)$ is the external stress minus dry friction stresses (which we consider constant) such as Hall-Petch stresses and substructural hardening, σ^{int} is an internal stress field from a system of dislocation charges induced by plastic deformation at grain boundaries, F(v) is a viscous N-shaped braking force per unit dislocation length due to the interaction of dislocations with impurity atoms [3].

Equation (2) takes account for the role of boundaries in the formation and propagation of deformation bands. Due to the elastic correlation of the grains, stresses $\sigma^{int} = \gamma_1 \partial_{xx}^2 \varepsilon$ [14, 18] arise, which relax due to accommodation mechanisms [19]. The parameter $\gamma_1 \approx \alpha_g GD^2$ serves as a measure of elastic correlation of grains ($\alpha_g \approx 1$, D is the grain size), t_a is characteristic time of plastic accommodation [20].

Equation (3) is the Gilman-Johnston equation for the active loading mode [21], which takes account for the dynamics of the load change σ under the condition that the strain rate of the crystal sample is constant. Here $\dot{\epsilon}_0$ is the specified rate of plastic deformation in the slip band, $G^* = \kappa h_0/\zeta S$ is the effective modulus of elasticity, κ is the rigidity of the "machine-sample" system, h_0 and S are the height and cross-section area of the sample, L is the length of the sample, ζ is geometric factor of the order one.

In equation (1) the function
$$F(v) = F_1(v) + F_2(v)$$
 (4)

consists of two terms. The force $F_1(v)$ is due to the interaction of impurity atoms with a dislocation moving at some speed v and is determined by the formula [3]

$$F_1(v) = -\int_{-\infty}^{\infty} c \frac{\partial W}{\partial x'} dx', \tag{5}$$

where c is the concentration of impurity atoms, which is determined from the stationary diffusion equation [17]

$$D_{c} \frac{\partial^{2} c}{\partial x'^{2}} + \frac{D_{c}}{kT} \frac{\partial}{\partial x'} (c \frac{\partial W}{\partial x'}) + v \frac{\partial c}{\partial x'} = 0.$$
 (6)

Here D_c is the diffusion coefficient of dissolved atoms,

$$W = \frac{\beta}{(b^2 + x'^2)^{1/2}} \tag{7}$$

is the energy of interaction of dislocations with impurity atoms in the one-dimensional approximation, similar to the interaction energy in the two-dimensional case in the Cottrell theory [1, 3].

Analysis of solution for the braking force F(v) shows that the deceleration force first increases, reaching a maximum at a certain value $b\sigma_{max}$ at a speed $v_a = D_c kT/\beta$ [22], and then decreases. This is due to the fact that as the velocity increases, the dislocation gradually loses the atmosphere of dissolved atoms and at some critical velocity [3]

$$v_c = D_c \beta / k T b^2 \tag{8}$$

the atmosphere disappears and the braking is caused only by statistically distributed atoms of the dissolved substance. In this region $(v > v_c)$ the deforming stress linearly depends on the velocity [3, 22], i.e. $F_2 = Bv$, where the mobility is defined as $B = \alpha c_0 \beta^2 / (D_c bkT)$ [22]. Here, parameter $\alpha < 1$ takes account for the features of the movement of dislocations in the field of uniformly distributed impurity atoms.

Analyzing the mathematical structure of the equation (6), it can be seen that its solution is determined by two dimensionless quantities: velocity $u = bv/D_c$ and parameter $a = W_c/kT$, which is inversely proportional to temperature. Here $W_c = \beta/b$ is the maximum binding energy of the dislocation with impurity atoms [3].

Numerical solution for F(u) by taking account for equations (4)-(6) and $F_2 = B'u$ (where $B' = \alpha c_0 W_c a$), leads to the dependency shown in Fig. 2.

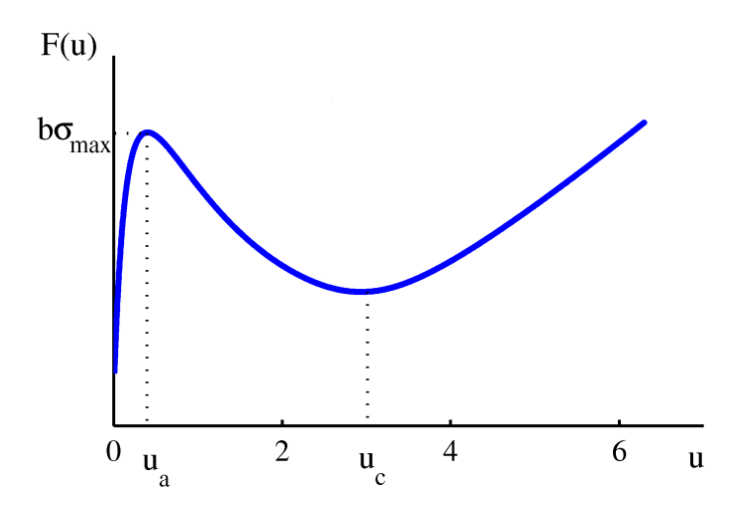


Fig. 2. Dependence of the N – shaped braking force F(u) on the dimensionless dislocation velocity $u = vb/D_c$, where $b\sigma_{max} = 3ac_0\beta$. The calculations were performed at the values of the parameters a = 3 and $\alpha = 0.7$

It can be seen that $u_c = v_c b/D_c = a$ and $u_a = v_a b/D_c = a^{-1}$. Since a typical value of the binding energy is $W_c = 0.1 \,\text{eV}$, then at room temperature T = 300 K (temperature kT in energy units is 0.025 eV) parameter a = 4, the value a = 3 corresponds to the temperature T = 400 K.

Let us determine the region of instability of plastic deformation at which F'(u) < 0. By analyzing the curve F(u) we find that the condition F'(u) < 0 is satisfied for the velocity interval in the range $[a^{-1},a]$. For example, at temperature T=400K, this is [0.33,3].Cottrell noticed [1] that the Portevin-Le Chatelier effect is experimentally observed at $(D_c/\dot{\epsilon}_0)^{1/2} \approx 10^{-5} \, \mathrm{cm}$.

If $u = bv/D_c$ is converted to the form $bv\rho_0/D_c = \dot{\epsilon}_0/D_c$, then the above mentioned instability region for $(\dot{\epsilon}_0/D_c)^{1/2}$ takes the form 0.57 $< \rho^{1/2} < 1.73$, i.e. approximately $(D_c/\dot{\epsilon}_0)^{1/2} \approx \rho^{-1/2}$. If we take the typical value $\rho = 10^{10} \, \mathrm{cm}^{-2}$, then we get Cottrell's experimental result.

Numerical study of the PLC effect

In [17], a regular self-oscillating solution of $\sigma(t)$ was obtained for the homogeneous case. Such solution, however, does not correspond to experimental results, because the load fluctuations have a pronounced stochastic character.

To identify the spatial-wave solutions of the original model, a numerical study of the original system of equations (1)–(3) was carried out. At the same time, the system of equations was transformed to a dimensionless form. It was found out that solutions of the system are controlled by temperature via the parameter $a = W_c/kT$ and a given plastic deformation rate $\dot{\epsilon}_0$. In addition, dimensionless parameters play an essential role:

$$\kappa = \frac{G^*b\rho_0 v_a t_0}{\sigma_{\text{max}}}, \quad K = \frac{\gamma_1 b\rho_0 t_0 v_a}{L^2 \sigma_{\text{max}}}, \quad \gamma_a = t_0 / t_a, \tag{9}$$

which characterize, respectively, the rigidity of the sample-machine system, the elastic correlation of grains and the intensity of plastic accommodation. Here $t_0 = v_a m^* / b \sigma_{max}$.

The analysis shows that the parameters (9) have a large range of possible values. Therefore, in this paper we will limit ourselves to the following values: the length of the plastic zone is chosen equal to L = 20cm, grain size $D = 10\mu$ m, and

$$\kappa = 1, \quad \gamma_a = 0.01, \quad a = 3, \quad \dot{\varepsilon}_0 = 10^{-4} \, \text{s}^{-1}.$$
(10)

The parameters κ , K and γ_a characterize, respectively the rigidity of the sample-machine system, the elastic correlation of grains and the intensity of plastic accommodation.

For small values of $K < 10^{-6}$, a regular mode is realized in the system. In this case, there is a in-phase mode of velocity fluctuations in the areas of the plastic flows (along the x coordinate), but already at $K = 10^{-5}$, the deformation process acquires an irregular stochastic character (Fig. 3).

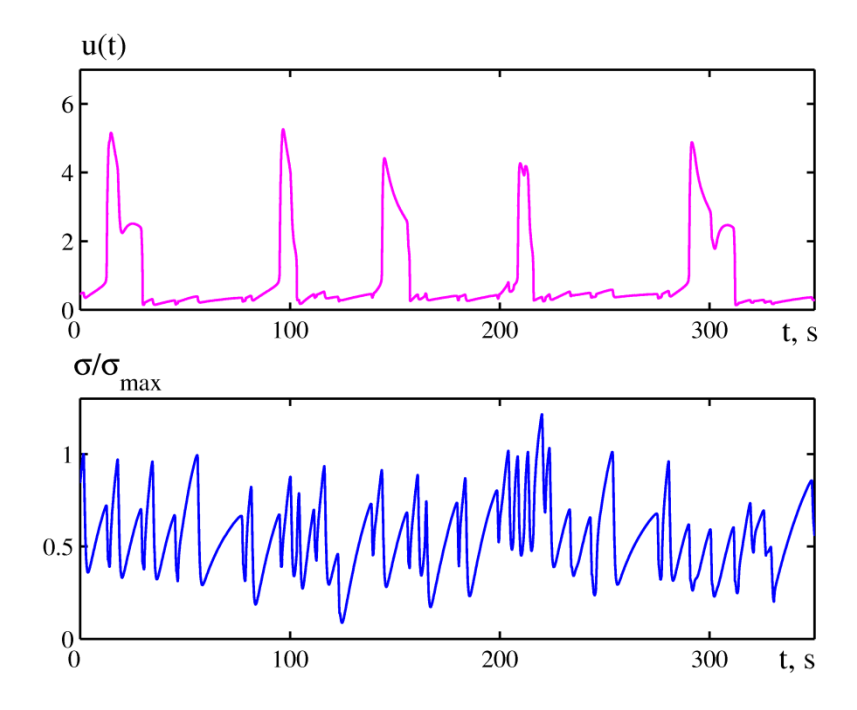


Fig. 3. Change of dislocation velocity u(t,x) (in section x = 10 cm) and load $\sigma(t)$ depending on time. Numerical results are obtained at a temperature of 400 K and the values of the parameters given in (10) and $K = 10^{-5}$

At the same time, the pulses of the plastic deformation rate are strictly correlated and form clear Portevin-Le Chatelier bands, which are shown in Fig. 4. This figure shows the wave pattern of the propagation velocity of dislocations u(t,x) in a crystal sample.

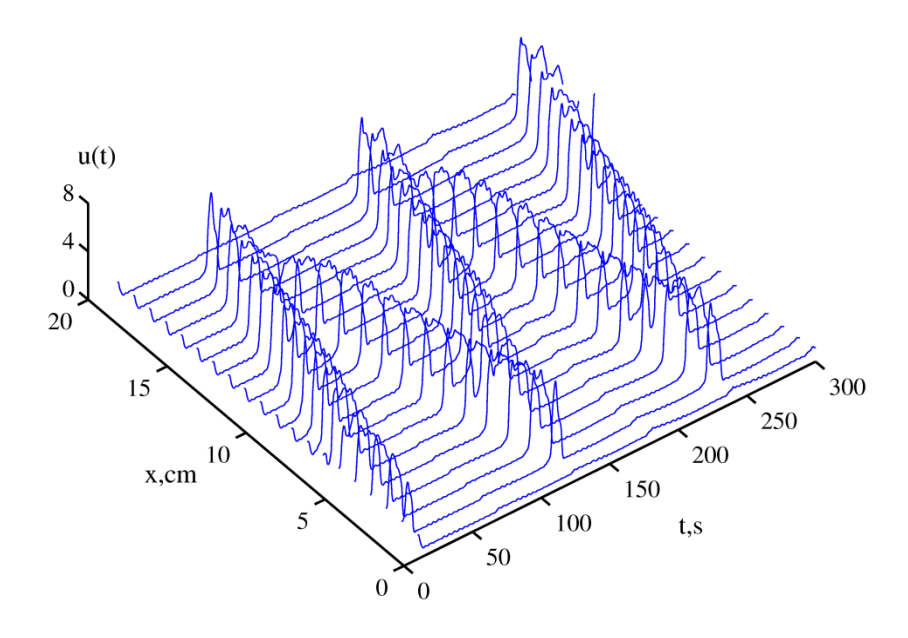


Fig. 4. Wave pattern of propagation of dislocation velocity disturbances u(t,x) in a crystalline sample in the form of PLC bands under stochastic deformation mode

It can be noticed that the PLC deformation bands, which are pulses of plastic deformation, they originate at one of the ends of the crystal and move at a certain speed to the other, where the reverse band is formed. This deformation process is periodically repeated.

Under the given deformation conditions, the PLC bands are strictly correlated. When conditions change, oncoming bands may occur, propagating simultaneously from opposite ends of the crystal. In this case, the bands can annihilate, break up into parts, reappear in other parts, etc. It is necessary at the same time that the total rate of plastic deformation is equal to the specified speed $\dot{\epsilon}_0$.

In conclusion, we will make some remarks about the Luders bands and PLC bands. In many respects, the mathematical description of these deformation bands differs little, however, the Luders band is a single wave front [20] and occurs above a certain critical load value, while the Portevin-Le Chatelier bands are formed in the instability region $(F'(v)|_{v=v_0} \le 0$, where $v_0 = \dot{\epsilon}_0/b\rho_0$) as a quasi-periodic sequence of running waves.

Thus, the original model assumes a wide variety of space-wave solutions, which will be considered in the following work.

Resume

- 1. The mechanism of plastic deformation instability of crystalline alloys is considered in the autowave model of the Portevin-Le Chatelier effect. Within the framework of the model in the field of medium and elevated temperatures, the mechanisms of serrated deformation and localization of plastic flow in alloys have been studied.
- 2. An analytical and numerical study of the model was carried out after bringing it to a dimensionless form. An instability region is determined for the rate of plastic deformation and temperature, in the vicinity of which the Portevin-Le Chatelier effect is realized. The critical dimensionless parameters responsible for the variety of wave solutions of the initial system of equations are determined.
- 3. For given values of the model parameters, the form of stochastic load oscillations is determined, which is a quasi-periodic sequence of oscillating wave arcs, i.e. load surges, as well as bursts of plastic deformation rate, which are strictly correlated and form clear Porteyin-Le Chatelier bands under stochastic deformation mode.

References

- 1. Cotrell AH. Dislocations and Plastic Flow in Cryctals. London: Oxford University Press; 1953.
- 2. Friedel J. Dislocations. Oxford: Pergamon; 1964.
- 3. Hirth JP, Lothe J. Theory of dislocatons. New York John Wiley; 1968.
- 4. Chen H, Chen Z, Cui Y, Wang L, Wang M, Liu J, Zhong S, Wang H. The effect of TiB2 ceramic particles on Portevin–Le Chatelier behavior of TiB2/AlMg metal. *Journal of Materials Research and Technology*. 2021;14: 2302–2311.
- 5. Cui CY, Zhang R, Zhou YZ, Sun X. Portevin-Le Chatelier effect in wrought Ni-based superalloys: Experiments and mechanisms. *Journal of Materials Science & Technology*. 2020;51: 16–31.
- 6. Geng YX, Zhang D, Zhang JS, Zhuang L. Zn/Cu regulated critical strain and serrated flow behavior in Al-Mg alloys. *Mater. Sci. Eng. A.* 2020;795: 1391–1397.
- 7. Wang XG, Wang L, Huang MX. Kinematic and thermal characteristics of Luders and Portevin-Le Chatelier bands in a medium Mn transformation-induced plasticity steel. *Acta Materialia*. 2017; 124: 17–29.
- 8. Portevin A, Le Chatelier F. Sur un phenomene observe lors de l'essai de traction d'alliages en cours de transformation. *C.R. Acad. Sci.* 1923;176: 507–510.

- 9. Zhang F, Curtin WA. Atomistically informed solute drag in Al-Mg. *Model. Simul. Mater. Sci. Eng.* 2008;16(5): 055006.
- 10. Shariat BS, Li Y, Yang H, Wang Y, Liu Y. On the Luders band formation and propagation in NiTi shape memory alloys. *Journal of Materials Science and Technology*. 2022;116: 22–29.
- 11. J Zhang, M Huang, B Sun, B Zhang, R Ding, C Luo, Zeng W, Zhang C, Zhang Z, van der Zwaag S, Chen H. Critical role of Luders banding in hydrogen embrittlement susceptibility of medium Mn steels. *Scripta Materialia*. 2021;190: 32–37.
- 12. Lebyodkin MA, Zhemchuzhnikova DA, Lebedkina TA, Aifantis EC. Kinematics of formation and cessation of type B deformation bands during the Portevin-Le Chatelier effect in an AlMg alloy. *Results in Physics*. 2019;12: 867–869.
- 13. Kubin LP, Estrin Y. Strain nonunifomities and plastic instabilities. *Rev. Phys. Appl.* 1988;28(4): 573–583.
- 14. Rowlands B, Rae C, Galindo-Nava E. The Portevin-Le Chatelier effect in nickel-base superalloys: Origins, consequences and comparison to strain ageing in other alloy systems. *Progress in Materials Science*. 2023;132: 2–66.
- 15. Yilmaz A. The Portevin-Le Chatelier effect: a review of experimental findings. *Sci. Technol. Adv. Mater.* 2011;12(6): 063001.
- 16. Korbel A, Dybiec H. The problem of the negativ strain rate sensitiviti of metals under the Portevin-Le Chatelier deformation conditions. *Acta Metall.* 1981;29(1): 89–93.
- 17. Sarafanov GF, Shondin YG. Instability of plastic deformation in crystalline alloys: the Portevin-Le Chatelier effect. *Materials Physics and Mechanics*. 2022;50(1): 158–165.
- 18. Rybin VV. Regularities of Mesostructures Development in Metals in the Course of Plastic Deformation. *Problems of Material Science*. 2003;1(33): 9–28.
- 19. Perevezentsev VN, Sarafanov GF. The screening of mesodefects stress fields by dislocation ensemble and misorientation structure formation during plastic deformation. *Rev. Adv. Mater. Sci.* 2012;30: 73–89.
- 20. Sarafanov GF, Shondin YG. Deformation instability in crystalline alloys: Luders bands. *Materials Physics and Mechanics*. 2021;47(3): 431–437.
- 21. Johston WG, Gilman J. Dislocation velocities, dislocation densities and plastic flow in lithium fluoride crystals. *J. Appl Phys.* 1959;30: 129–143.
- 22. Suzuki T, Takeuchi S, Yoshinaga H. Dislocation Dynamics and Plasticity. NY: Springer; 1991.

THE AUTHORS

Sarafanov G.F.

e-mail: gf.sarafanov@yandex.ru

Shondin Yu.G. @

e-mail: yu.shondin@yandex.ru

Kuznetsov S. I.

e-mail: sergkuznet@hotmail.com

Influence of material anisotropy on the interaction between cracks under tension and shear

Submitted: March 6, 2023

Approved: September 17, 2023

Accepted: September 28, 2023

A.V. Savikovskii 📵 1,2 🖂, A.S. Semenov 🗓 1

¹ Peter the Great St. Petersburg Polytechnic University, St. Petersburg, Russia

² JSC «Power machines», St. Petersburg, Russia

⊠ savikovskii.artem@yandex.ru

Abstract. The fracture of anisotropic bodies with multiple macrocraks is analyzed by means of modeling interaction between cracks and interaction of crack with the free boundary. The influence of material anisotropy on cracks behavior is investigated for orthotropic material, material with cubic symmetry and isotropic material. Article deals with numerical computations of stress intensity factors of internal and edge cracks in the rectangular plate under uniaxial tension and pure shear loadings. The displacement extrapolation method is used for the computation of stress intensity factors for anisotropic materials. The effect of material anisotropy on stress intensity factors for different crack configurations (one, two and three cracks of different lengths) under various loading conditions (tension or shear) is investigated and discussed.

Keywords: linear elastic fracture mechanics; anisotropic material; stress intensity factor; finiteelement modeling; displacement extrapolation method; Lekhnitskii formalism, crack

Acknowledgements. The reported study was supported by The Government of the Russian Federation (State Assignment No. 0784-2020-0021).

Citation: Savikovskii AV, Semenov AS. Influence of material anisotropy on the interaction between cracks under tension and shear. *Materials Physics and Mechanics*. 2023;51(5): 24-37. DOI: 10.18149/MPM.5152023_4.

Introduction

Single-crystal nickel-based superalloys [1] are widely used for production of blades of gas turbine engines [2]. These materials have a pronounced anisotropy (cubic symmetry) and temperature dependence of mechanical properties [2]. Cracking of the gas turbine blades is caused by fatigue, creep and thermal fatigue and also corrosion [3–8]. The stress intensity factor (SIF) is the most widespread parameter in the linear fracture mechanics that defines stress state near the crack tip and is used for crack propagation prediction. Determination of SIF for the isotropic material is extensively studied in details theoretically and numerically [9–13] et al., while the study of cracks in anisotropic solids has received much less attention [14–16].

Effects of delay time, crystallographic orientation and mechanical properties of single-crystal anisotropic superalloys on the number of cycles to the main crack formation in thermal fatigue experiments were investigated in paper [17]. Effect of material anisotropy on the crack interaction with a free boundary for the central crack for I fracture mode and the central inclined crack in the finite plate under mixed mode was investigated in paper [18]. Effect of crack orientation with respect to material anisotropy axes on SIF for the anisotropic finite plane was studied in paper [19]. Effect of free edge and material axes orientation on SIF in anisotropic

CT-sample was studied in paper [20]. However, determination of SIF in conditions of mutual influence of cracks and material anisotropy is more complex and less studied. The paper deals with edge cracks in anisotropic bodies and consider the influence of (i) the material anisotropy, (ii) the number of cracks and (iii) the distance from the free boundary on SIFs.

The analytical solutions for SIFs concerning the *single internal inclined crack* in the infinite plane under uniaxial tension for both isotropic and anisotropic materials are defined by relations [14]:

$$K_{I} = \sigma_{\infty} \sqrt{\pi l} \sin^{2} \varphi, \qquad K_{II} = \sigma_{\infty} \sqrt{\pi l} \sin \varphi \cos \varphi,$$
 (1)

where σ_{∞} is the value of uniform tensile stress at infinity, l is the half-length of the crack, φ is the angle between the crack and of the uniaxial tensile stress direction. Note, that the analytical solution is the same for isotropic and anisotropic material. Handbook [12] points to the solutions for one, two and three edge cracks in the infinite isotropic half-plane under uniaxial tension.

SIFs for the *single edge crack* is defined by expressions:

$$K_{I} = 1.1215\sigma_{\infty}\sqrt{\pi l}, \qquad K_{II} = 0,$$
 (2)

where σ_{∞} is the value of tensile stress, l is the length of the crack. This solution is depended (in contrast to (1)) on material anisotropy even for infinite half-plane. Coefficients 1.1215 and 0 are valid for the isotropic material only. Due to the symmetry of the problem, a pure I mode with $K_{II} = 0$ is realized in the isotropic material.

SIFs for *two edge horizontal cracks* (of equal lengths l and with a distance between cracks also equal to l) in infinite isotropic half-plane are defined by relations:

$$K_I = 0.854\sigma_{\infty}\sqrt{\pi l} , \qquad K_{II} = 0.1333\sigma_{\infty}\sqrt{\pi l} . \tag{3}$$

This solution is depended on material anisotropic properties. Coefficients 0.854 and 0.1333 correspond to isotropic material only. The mutual influence of cracks gives rise to the appearance of a mixed fracture mode and the appearance of nonzero K_{π} .

SIFs for *three edge horizontal cracks* (of equal lengths *l* and with a distance between cracks also equal to *l*) in isotropic half-plane are defined by expressions (for outside cracks):

$$K_{I} = 0.815\sigma_{\infty}\sqrt{\pi l} , \qquad K_{II} = 0.590\sigma_{\infty}\sqrt{\pi l} . \tag{4}$$

Solution (4) is also sensitive to the material anisotropy. Specified coefficients 0.815 and 0.590 correspond to the isotropic material.

Studying of material anisotropy effect on the interaction between cracks for the finite bodies represents important problem for the reliability analysis of real industrial structures. Application of analytical methods for the general case of arbitrary configurations of multiple cracks is significantly limited, therefore, numerical methods for calculating the SIF are used.

Fracture problem formulations

The four problems with various crack configurations are considered: a single internal central crack in the rectangular plate (Fig. 1); a single edge crack in the rectangular plate (Fig. 2); two edge cracks in the rectangular plate (Fig. 3); three edge cracks in the rectangular plane (Fig. 4). In each of the four tasks listed above, two loading options were considered: uniaxial tension in vertical direction (Figs. 1(a), 2(a), 3(a), 4(a)); pure shear loading (Figs. 1(b), 2(b), 3(b), 4(b)).

The problems are solved in two-dimensional formulation under assumption of plane stress state. Isotropic and anisotropic materials are considered and compared. Anisotropy axes are parallel to edges of plate and global coordinate axes. Studying of material anisotropy effect is carried out using multivariant computations with varied sizes of the plate. Calculation of SIFs has been performed by means of the finite element program PANTOCATOR [21], which has the ability of automatized SIF calculations for isotropic and anisotropic materials based on various numerical methods. Thus anisotropy, dimensions of the plate and fracture modes are varied in the calculation process. In all computations tensile stress σ_{∞} is equal to 100 MPa and shear stress τ_{∞} is also equal to 100 MPa.

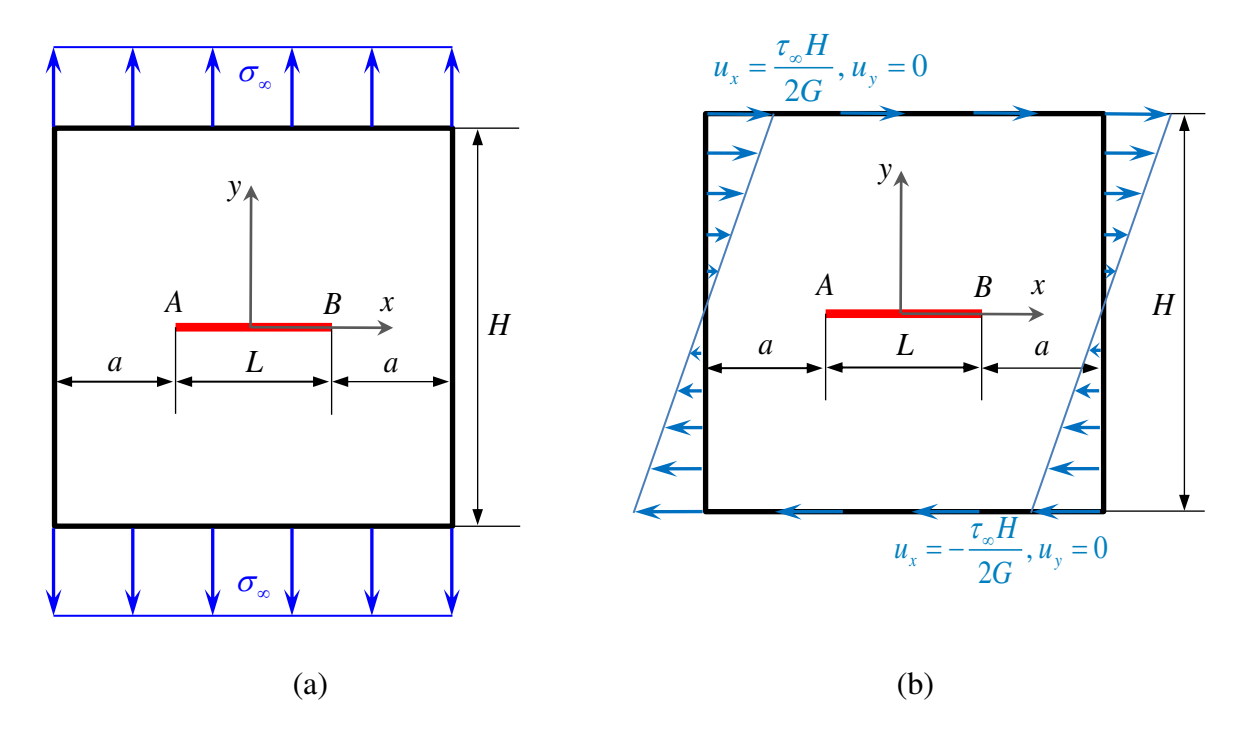


Fig. 1. Single internal central crack in the rectangular plate under (a) tension (I fracture mode), and (b) shear (II fracture mode)

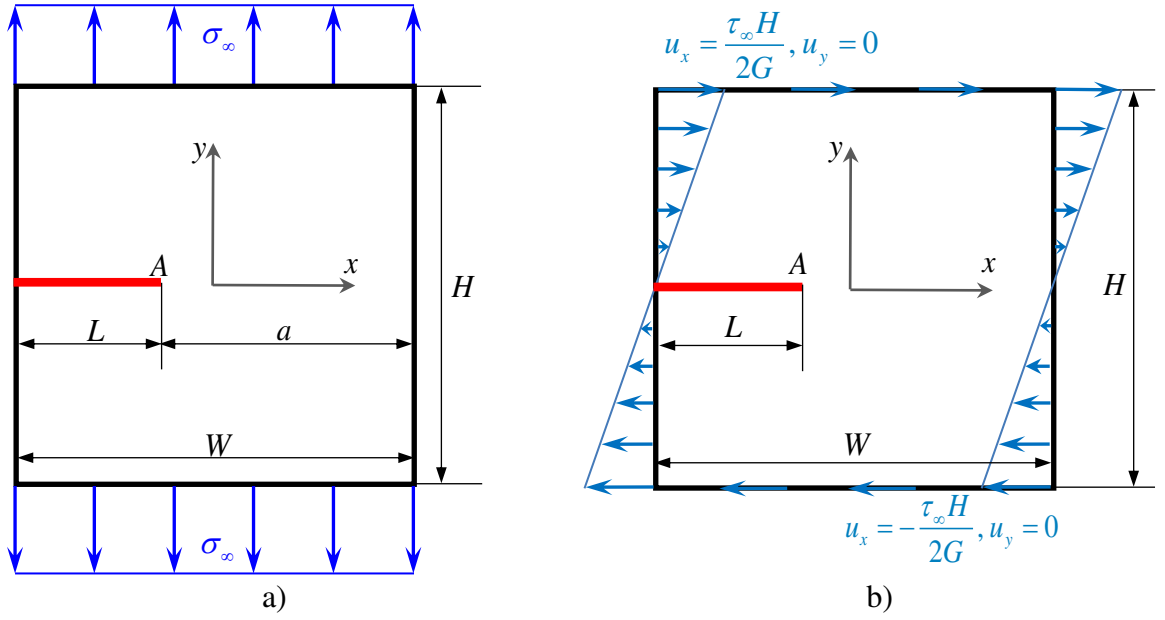


Fig. 2. Single edge crack in the rectangular plate under (a) tension (I fracture mode), (b) shear (II fracture mode)

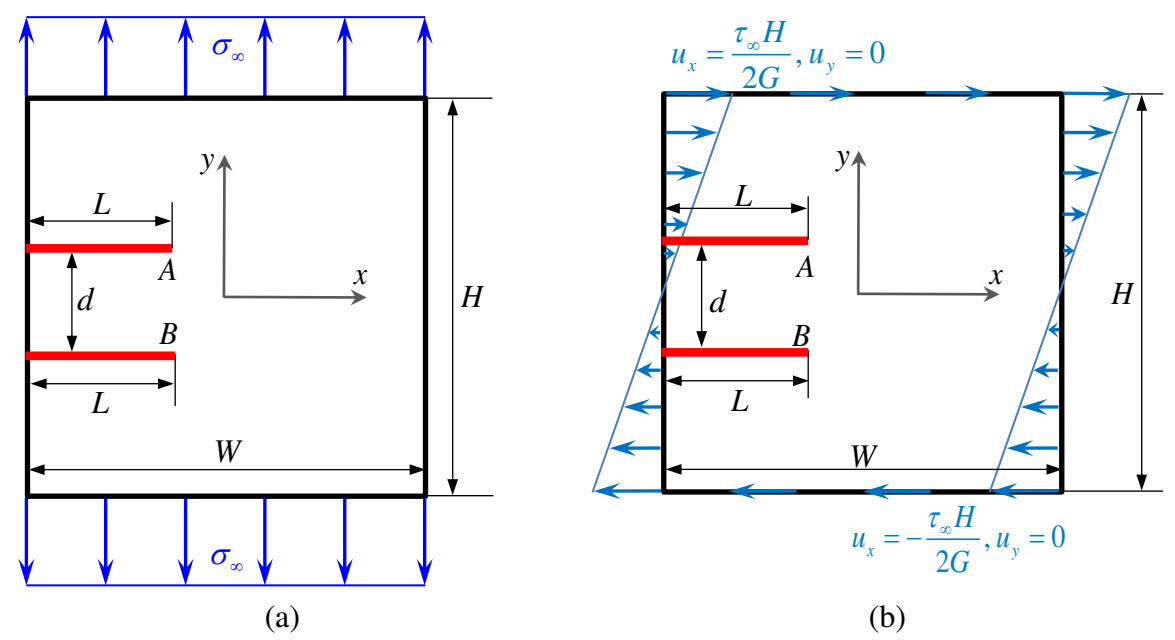


Fig. 3. Two edge cracks in the rectangular plate under (a) tension, and (b) shear

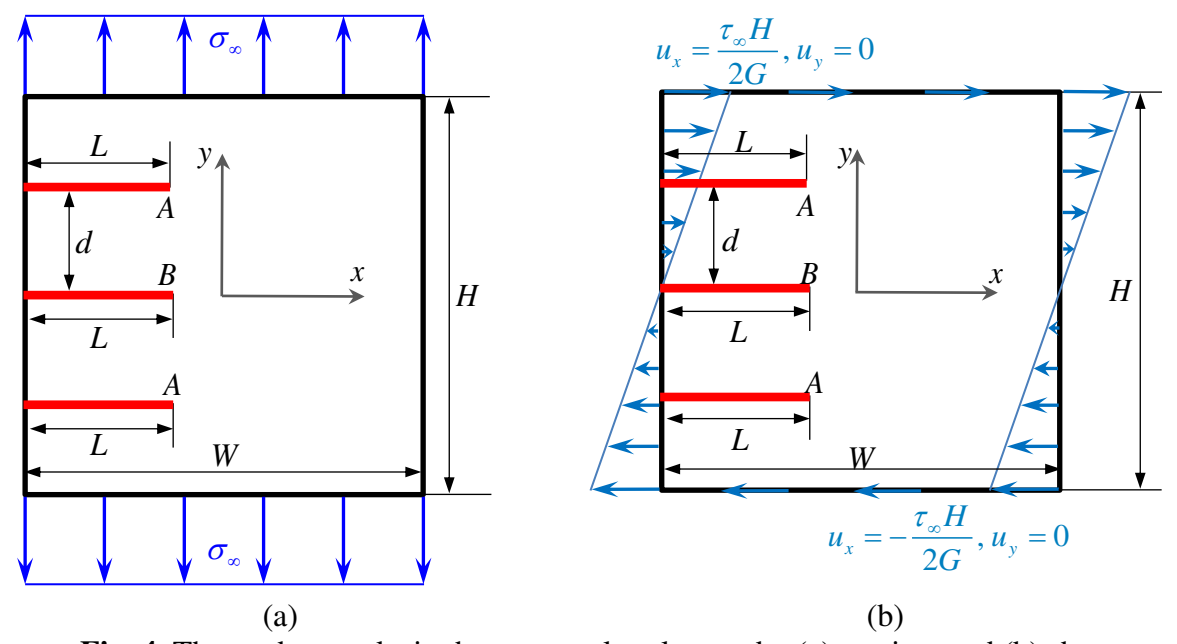


Fig. 4. Three edge cracks in the rectangular plate under (a) tension, and (b) shear

Table 1. Elastic moduli used in computations

Material	Young's modulus, MPa	Shear modulus, MPa	Poisson ratio
Isotropic material	E = 20000	G = 7692.3	v = 0.3
Cubic symmetry, $\rho = -0.25$	E = 20000	G = 200000	v = 0.3
Cubic symmetry, $\rho = -0.17$	E = 20000	G = 77000	v = 0.3
Cubic symmetry, $\rho = 0.37$	E = 20000	G = 15000	v = 0.3
Cubic symmetry, $\rho = 10$	E = 20000	G = 970.8	v = 0.3
Orthotropic material 1	$E_1 = 100000 E_2 = 20000$	$G_{12} = 970.8$	$v_{12} = 0.3$
Orthotropic material 2	$E_1 = 6000 E_2 = 20000$	$G_{12} = 970.8$	$v_{12} = 0.3$

For each of the four boundary value problems (see Figs. 1-4), three classes of anisotropy were considered to study the effect of anisotropy on crack behavior: isotropic material, material with cubic symmetry, and orthotropic material. Material properties used in computations are summarized in Table 1.

In Table 1 the parameter ρ characterized for the cubic symmetry (with three independent elastic moduli E, v, G) the deviation from isotropy:

$$\rho = \frac{E}{2G} - v \,. \tag{5}$$

For the isotropic material the parameter ρ equal to 1. In computations the value of G varied for fixed values of elastic modules E and v.

Displacement extrapolation method for stress intensity factors calculation

The crack-tip displacement fields in polar coordinates in the general three-dimensional case (nonzero K_I , K_{II} , K_{III}) for an *isotropic* material are given by relations [22]:

$$u_{x}(r,\alpha) = \frac{K_{I}}{G} \sqrt{\frac{r}{2\pi}} \cos \frac{\alpha}{2} \left(\frac{\kappa - 1}{2} + \sin^{2} \frac{\alpha}{2}\right) + \frac{K_{II}}{G} \sqrt{\frac{r}{2\pi}} \sin \frac{\alpha}{2} \left(\frac{\kappa + 1}{2} + \cos^{2} \frac{\alpha}{2}\right),$$

$$u_{y}(r,\alpha) = \frac{K_{I}}{G} \sqrt{\frac{r}{2\pi}} \sin \frac{\alpha}{2} \left(\frac{\kappa + 1}{2} - \cos^{2} \frac{\alpha}{2}\right) + \frac{K_{II}}{G} \sqrt{\frac{r}{2\pi}} \cos \frac{\alpha}{2} \left(\frac{\kappa - 1}{2} + \sin^{2} \frac{\alpha}{2}\right),$$

$$u_{z}(r,\alpha) = \frac{K_{III}}{G} \sqrt{\frac{r}{2\pi}} \sin \frac{\alpha}{2},$$
(6)

where $u_x(r,\alpha)$, $u_y(r,\alpha)$, $u_z(r,\alpha)$ are axial displacements in crack coordinate systems, K_I , K_{II} , K_{III} are SIFs for I, II and III fracture modes, the Kolosov's constant $\kappa = \frac{3-v}{1+v}$ in the case of plane stress state, G is the shear modulus, r is the distance from crack tip to considered point, α is the angle between point direction and crack axis, v is the Poisson's ratio.

Asymptotic expressions for displacements near the crack tip in the general three-dimensional case for *anisotropic* material obtained using the Lekhnitskii formalism have the following form [14, 23, 24]:

$$u_{x}(r,\alpha) = \frac{K_{I}\sqrt{2r}}{\sqrt{\pi}}\operatorname{Re}\left(\frac{1}{\mu_{1}-\mu_{2}}\left(\mu_{1}p_{2}\sqrt{\cos\alpha+\mu_{2}\sin\alpha}-\mu_{2}p_{1}\sqrt{\cos\alpha+\mu_{1}\sin\alpha}\right)\right) + \frac{K_{II}\sqrt{2r}}{\sqrt{\pi}}\operatorname{Re}\left(\frac{1}{\mu_{1}-\mu_{2}}\left(p_{2}\sqrt{\cos\alpha+\mu_{2}\sin\alpha}-p_{1}\sqrt{\cos\alpha+\mu_{1}\sin\alpha}\right)\right),$$

$$u_{y}(r,\alpha) = \frac{K_{I}\sqrt{2r}}{\sqrt{\pi}}\operatorname{Re}\left(\frac{1}{\mu_{1}-\mu_{2}}\left(\mu_{1}q_{2}\sqrt{\cos\alpha+\mu_{2}\sin\alpha}-\mu_{2}q_{1}\sqrt{\cos\alpha+\mu_{1}\sin\alpha}\right)\right) + \frac{K_{II}\sqrt{2r}}{\sqrt{\pi}}\operatorname{Re}\left(\frac{1}{\mu_{1}-\mu_{2}}\left(q_{2}\sqrt{\cos\alpha+\mu_{2}\sin\alpha}-q_{1}\sqrt{\cos\alpha+\mu_{1}\sin\alpha}\right)\right),$$

$$u_{z}(r,\alpha) = \frac{K_{III}\sqrt{2r}}{\sqrt{\pi}}\operatorname{Re}\left(\frac{\sqrt{\cos\alpha+\mu_{3}\sin\alpha}}{C_{45}+\mu_{3}C_{44}}\right),$$

$$(7)$$

where μ_1 and μ_2 are the complex-valued roots of the fourth degree equation (complex parameters of anisotropic material [25])

$$S'_{11}\mu^4 - 2S'_{16}\mu^3 + (2S'_{12} + S'_{66})\mu^2 - 2S'_{26}\mu + S'_{22} = 0$$
(8)

with positive imaginary part, S_{ij} are the elements of the elastic compliance matrix of the material in the crack coordinate system, $p_i = S_{11}^{'} \mu_i^{'2} + S_{12}^{'} - S_{16}^{'} \mu_i^{'}, q_i = S_{12}^{'} \mu_i^{'} + \frac{S_{22}^{'}}{\mu_i^{'}} - S_{26}^{'}, \mu_3^{'}$ is the root of equation $C_{44}^{'} \mu^2 - 2C_{45}^{'} \mu + C_{55}^{'} = 0$ with positive imaginary part, $C_{ij}^{'}$ are the constants of the matrix of elastic modules of the material in the crack coordinate system ($[C] = [S]^{-1}$).

In the case of an *isotropic* material, the displacements are related to SIFs by formulas (6). Substitution of $\alpha = \pm \pi$ in the equation (6) leads to the expression for the SIFs in terms of displacement jumps on the crack banks for the isotropic material:

$$K_{II} = \lim_{r \to 0} \left[\left[u_{y}(r, \pi) - u_{y}(r, -\pi) \right] \sqrt{\frac{2\pi}{r}} \frac{G}{1+\kappa} \right],$$

$$K_{II} = \lim_{r \to 0} \left[\left[u_{x}(r, \pi) - u_{x}(r, -\pi) \right] \sqrt{\frac{2\pi}{r}} \frac{G}{1+\kappa} \right],$$

$$K_{III} = \lim_{r \to 0} \left[\left[u_{z}(r, \pi) - u_{z}(r, -\pi) \right] \sqrt{\frac{2\pi}{r}} \frac{G}{1+\kappa} \right].$$

$$(9)$$

In the case of an *anisotropic* material, after substitution $\alpha = \pm \pi$ in the equation (7), we obtain the expressions for displacement jumps on the crack banks:

$$[[\mathbf{u}]] = \sqrt{\frac{2r}{\pi}} [\mathbf{B}] \{\mathbf{K}\}, \tag{10}$$

where
$$[[\mathbf{u}]] = \begin{cases} \begin{bmatrix} u_y(r,\pi) - u_y(r,-\pi) \end{bmatrix} \\ [u_x(r,\pi) - u_x(r,-\pi)] \\ [u_z(r,\pi) - u_z(r,-\pi)] \end{cases}$$
 is the displacement vector of crack banks, $\{\mathbf{K}\} = \begin{cases} K_I \\ K_{II} \\ K_{III} \end{cases}$

is the vector of SIFs,
$$[\mathbf{B}] = \begin{pmatrix} \operatorname{Re}\left(\frac{\mu_{1}p_{2} - \mu_{2}p_{1}}{\mu_{1} - \mu_{2}}i\right) & \operatorname{Re}\left(\frac{p_{2} - p_{1}}{\mu_{1} - \mu_{2}}i\right) & 0 \\ \operatorname{Re}\left(\frac{\mu_{1}q_{2} - \mu_{2}q_{1}}{\mu_{1} - \mu_{2}}i\right) & \operatorname{Re}\left(\frac{q_{2} - q_{1}}{\mu_{1} - \mu_{2}}i\right) & 0 \\ 0 & 0 & \frac{1}{\sqrt{C_{44}C_{55} - C_{45}^{'2}}} \end{pmatrix}$$
 is the 3×3

matrix of the mutual influence of three components of the vector of relative displacement of the crack banks on three stress intensity coefficients. The result of inversion (10) makes it possible to calculate the SIF through the displacement of the crack banks in the case of an anisotropic material [26]:

$$\{\mathbf{K}\} = \lim_{r \to 0} \left(\frac{1}{2} \sqrt{\frac{\pi}{2r}} [\mathbf{B}]^{-1} [[\mathbf{u}]] \right), \tag{11}$$

where

$$[\mathbf{B}]^{-1} = \begin{pmatrix} \frac{1}{\det[\mathbf{D}]} \operatorname{Re} \left(\frac{\mu_{1} p_{2} - \mu_{2} p_{1}}{\mu_{1} - \mu_{2}} i \right) & \frac{1}{\det[\mathbf{D}]} \operatorname{Re} \left(-\frac{p_{2} - p_{1}}{\mu_{1} - \mu_{2}} i \right) & 0\\ \frac{1}{\det[\mathbf{D}]} \operatorname{Re} \left(-\frac{\mu_{1} q_{2} - \mu_{2} q_{1}}{\mu_{1} - \mu_{2}} i \right) & \frac{1}{\det[\mathbf{D}]} \operatorname{Re} \left(\frac{q_{2} - q_{1}}{\mu_{1} - \mu_{2}} i \right) & 0\\ 0 & 0 & \sqrt{C_{44} C_{55} - C_{45}^{'2}} \end{pmatrix}, \tag{12}$$

$$\det[\mathbf{D}] = \begin{vmatrix} \operatorname{Re}\left(\frac{\mu_{1}p_{2} - \mu_{2}p_{1}}{\mu_{1} - \mu_{2}}i\right) & \operatorname{Re}\left(\frac{p_{2} - p_{1}}{\mu_{1} - \mu_{2}}i\right) \\ \operatorname{Re}\left(\frac{\mu_{1}q_{2} - \mu_{2}q_{1}}{\mu_{1} - \mu_{2}}i\right) & \operatorname{Re}\left(\frac{q_{2} - q_{1}}{\mu_{1} - \mu_{2}}i\right) \end{vmatrix}.$$
(13)

It should be noted, that if the crack coordinate system does not coincide with the axes of anisotropy of the material, then the constants of the compliance and stiffness matrix must be converted into the crack coordinate system. In the case of the coordinate system rotation, the

transition matrix in the plane by rotation on an angle
$$\varphi$$
 has the form: $Q = \begin{pmatrix} \cos \varphi & -\sin \varphi & 0 \\ \sin \varphi & \cos \varphi & 0 \\ 0 & 0 & 1 \end{pmatrix}$

and converting elements of the compliance and stiffness tensor from the global to the crack coordinate system is defined by relations: $S_{ijkl}^{'} = Q_{im}Q_{jn}Q_{ko}Q_{lp}S_{mnop}$, $C_{ijkl}^{'} = Q_{im}Q_{jn}Q_{ko}Q_{lp}C_{mnop}$. In equations (10) and (11) the displacements also should be converted to the coordinate system associated with the crack: $u_i^{'} = Q_{im}u_m$. Formulas (9)-(13) were implemented in the finite element program PANTOCRATOR [21].

Results of SIFs computations

The influence of various factors, such as: the material anisotropy, the number of edge cracks, and the distance from crack tip to the free boundary on SIFs is investigated. For this purpose, four boundary value problems with various crack configurations described in Section 2 (see Figs. 1-4) were considered.

In the *first* problem (Fig. 1) the relative distance from crack tip to free boundary a/L varied from 1 to 10.5, where L is the crack length, a is the distance from the left (right) crack tip to the left (right) plate boundary. The height of the plate H was chosen to be large enough to ignore the influence of the upper and lower boundaries. Figure 5 shows a finite element model for the problem with a single central horizontal crack for the case a/L = 4. The number of degrees of freedom is 185 000. The eight-node isoparametric finite elements with second order approximation are used in computations.

In order to validate the results, the finite element solution for the case a/L = 10.5 was compared with the analytical solution for an infinite plate (1). The practical convergence of the numerical solution on various nested meshes was investigated (for the isotropic material). When the number of degrees of freedom decreases by a factor of 2, the result changes by less than 1 %.

When varying the distance a from the crack tip to the free edge of the plate (jumper size), the finite element mesh around the crack tip was not changed, only the plate dimensions were changed. The enlarged sections were divided proportionally to the length.

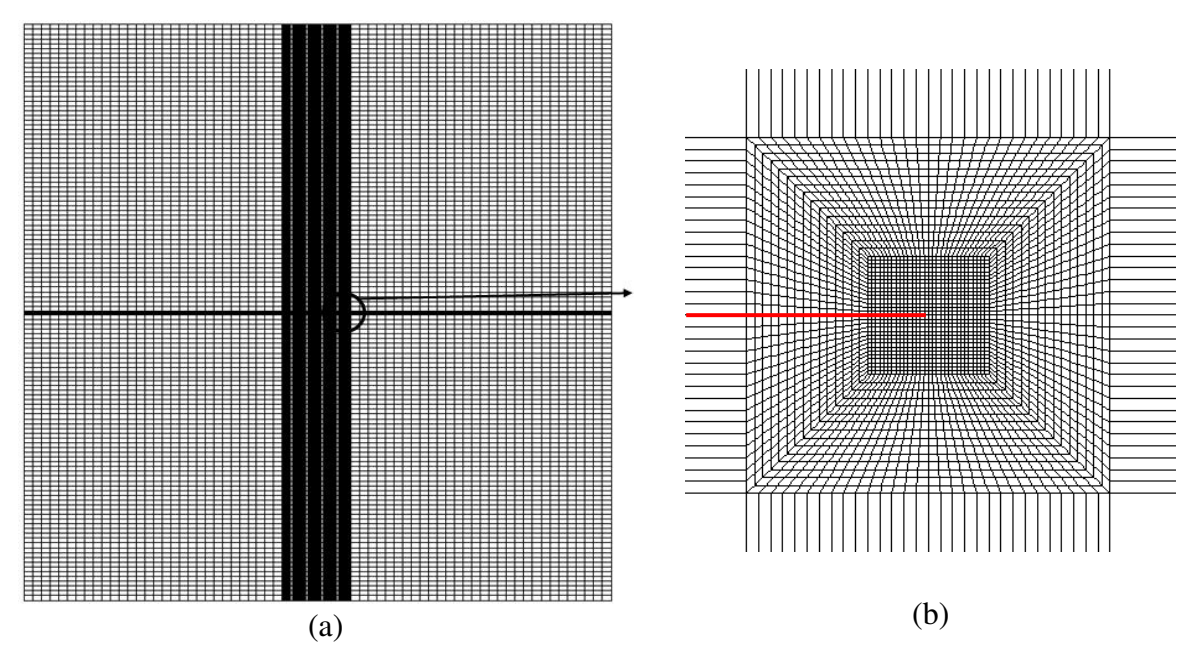


Fig. 5. Finite element model of (a) the plate with single internal horizontal crack (a/L = 4), (b) the vicinity of the right crack tip.

In the *second* (Fig. 2), *third* (Fig. 3) and *fourth* (Fig. 4) problems the relative distance from crack tip to free boundary a/L varied from 2 to 40, where L is the equal length of all cracks, a is the distance from the crack tip to the right boundary of plate. The plate has square shape for the problems with one and two edge cracks, whereas the plate was rectangular in the problem with three edge cracks. The distance between cracks d is equal to L. Finite element models for second, third and fourth boundary problems with edge cracks are shown in Fig. 6.

In order to validate the results, the finite element solution for the case with maximal relation a/L = 40 was compared with the analytical solution for single edge crack (2), two edge cracks (3) and three edge cracks (4) in an infinite plate under tension. The practical convergence of the numerical solution on various nested meshes for this problem was investigated (for the isotropic material). Difference between analytical and numerical solutions is less 0.6 % for all considered problems. Verification results are shown in Table 2.

Table 2. Verification of numerical results for the problems of uniaxial tension of plate with crack(s) from the isotropic material on the base of analytical solutions (1)-(4)

	Numerical value K_{IA} , $MPa\sqrt{m}$	Analytical value K_{IA} , $MPa\sqrt{m}$	Numerical value K_{IB} , $MPa\sqrt{m}$	Analytical value K_{IB} , $MPa\sqrt{m}$	Maximum error, %
Problem with single internal crack	124.80	125.30	124.80	125.30	0.56
Problem with single edge crack	198.57	198.51			0.03
Problem with two edge cracks	151.18	151.36	151.20	151.36	0.12
Problem with three edge cracks	143.71	144.45	104.08	104.57	0.50

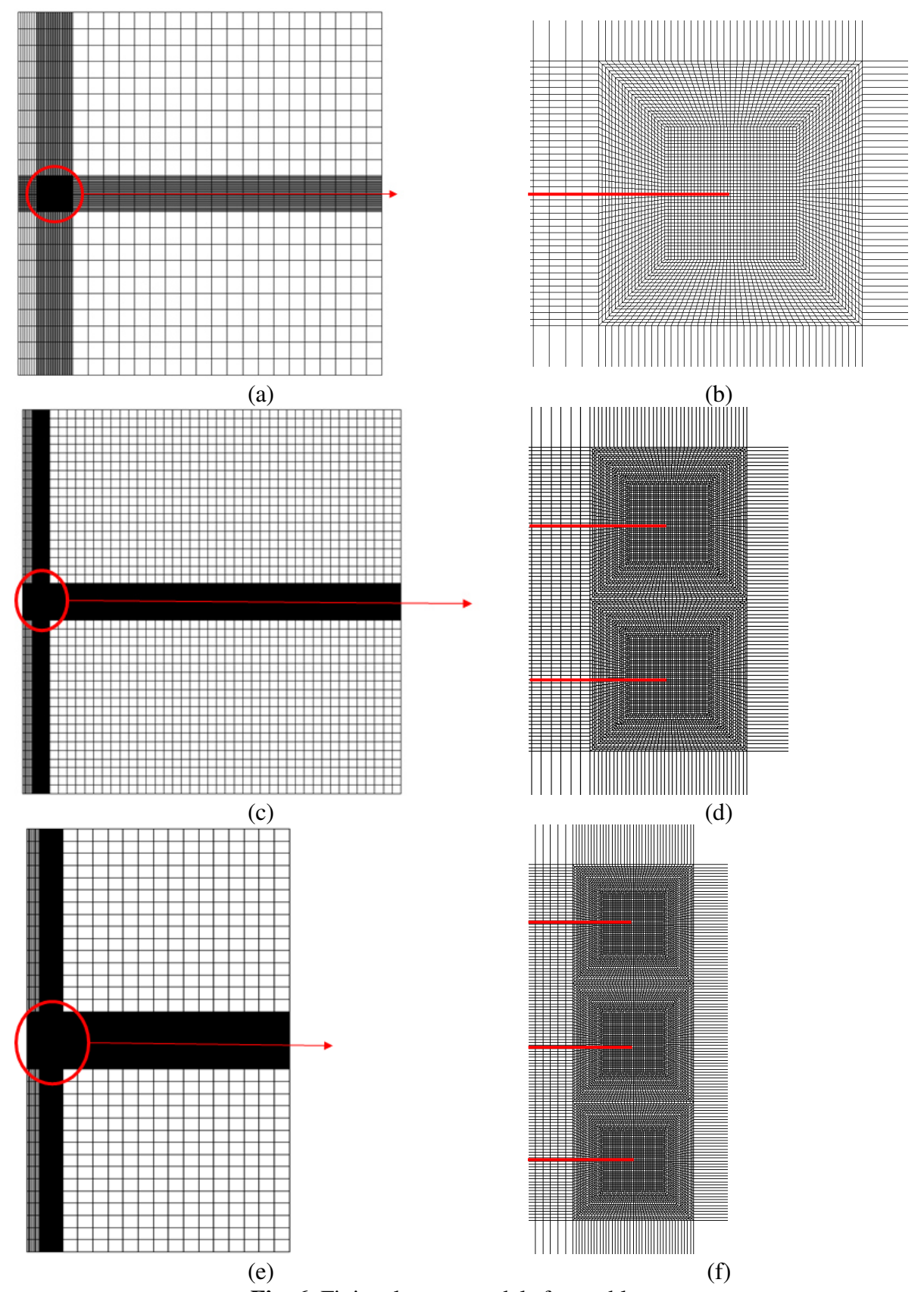


Fig. 6. Finite element models for problems:

- (a) single edge crack in a plate, (b) crack tip vicinity for single edge crack,
 - (c) two edge cracks in a plate, (d) crack tip vicinity for two edge cracks,
 - (e) three edge cracks in plate, (f) crack tip vicinity for three edge cracks

The numerical results of the anisotropy effect on the interaction of crack with the free boundary and interaction between cracks are presented below. Simulations has been performed for the case of the uniaxial tension (see Figs. 1(a), 2(a), 3(a), 4(a), σ_{∞} =100 MPa) and for the shear loading (Figs. 1(b), 2(b), 3(b), 4(b)). In the last case the displacements on the edges of the plate are chosen to make far shear stress τ_{∞} =100 MPa.

Figure 7 shows of the anisotropy influence on SIFs for the *first* problem concerning the *internal crack* in the plate under tension (Fig. 7(a)) and shear loading (Fig. 7(b)). In the first loading case, the pure I fracture mode is realized, and in the second case the pure II fracture mode takes place. For ease of comparison of results for cracks with different relative lengths, all curves are scaled to the isotropic solution.

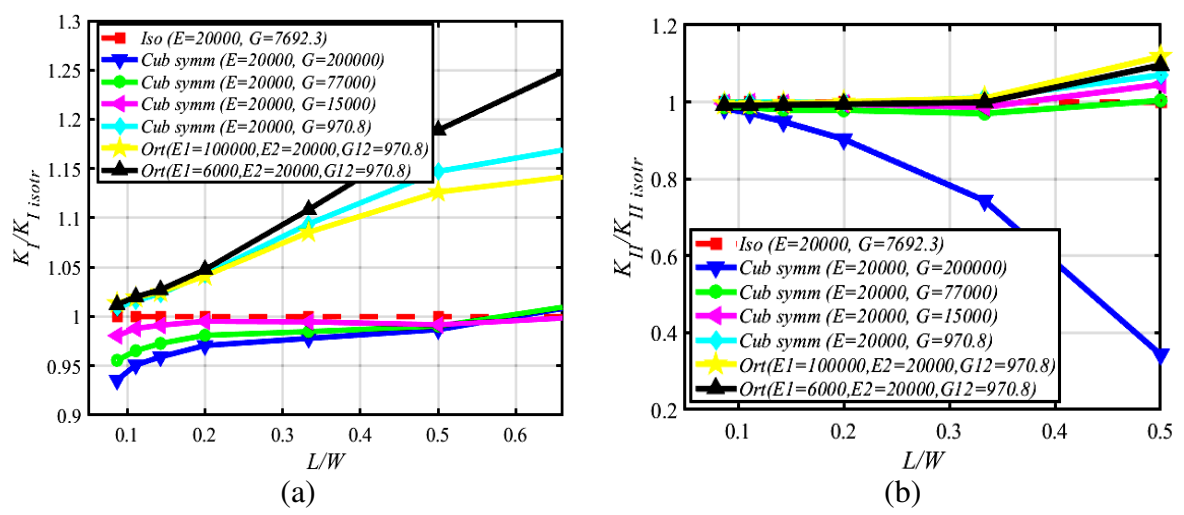


Fig. 7. Influence of anisotropy on SIF for internal crack in the plate under (a) tension (I fracture mode), and (b) shear (II fracture mode)

It should be noted that influence of anisotropy is higher when the internal crack is close to free boundaries. Influence for shear loading is stronger in several times than for the tension loading. A possible explanation is that the shear modulus G for an anisotropic material varies over a wide range. Note, that all curves are obtained at equal values of Young's modulus E = 20000 MPa in the vertical direction. Away from free edges (L/W < 0.1), the shear crack (unlike tensile crack) is almost insensitive to the type of anisotropy.

Note, depending on the elastic moduli, SIFs for an anisotropic material can be larger or smaller than the SIFs for an isotropic material.

Figure 8 shows the anisotropy influence on SIFs for the *second* problem concerning the *single edge crack* in the plate under tension (Fig. 8(a), pure I fracture mode) and shear loading (Fig. 8b, the pure II fracture mode).

The dependences of $K_{\rm I}(L/W)$ / $K_{\rm I\,isotr}$ under tension are not monotonic (Fig. 8(a)), while $K_{\rm II}(L/W)$ / $K_{\rm II\,isotr}$ under shear are monotonic (Fig. 8(b)). A possible explanation that dependence $K_{\rm II}(L/W)$ / $K_{\rm II\,isotr}$ under shear are monotonic is varied shear modulus G. A possible explanation that dependence $K_{\rm I}(L/W)$ / $K_{\rm I\,isotr}$ under tension for cubic symmetry and orthotropic materials are not monotonic, is that we varied plate dimensions over a wide range and influence of shear modulus G and effect of free boundary are competing effects.

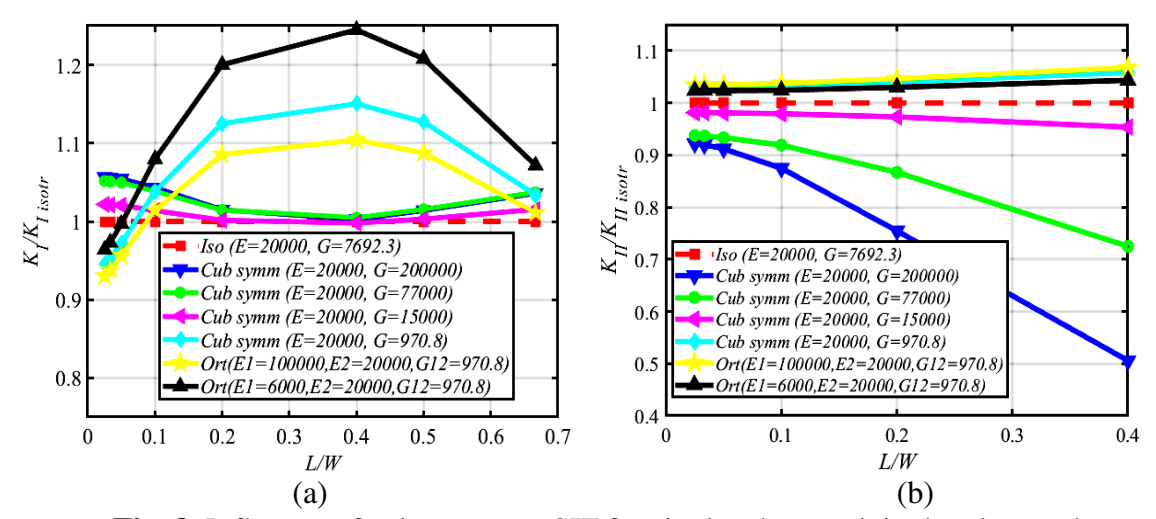


Fig. 8. Influence of anisotropy on SIF for single edge crack in the plate under (a) tension (I fracture mode), and (b) shear (II fracture mode)

However, the material anisotropy strongly affects the SIFs in all cases considered. Influence of material anisotropy is monotonously increase when closing to free boundary for II fracture mode. Also the influence for II fracture modes is stronger in several times than for I fracture modes. A possible explanation is that the shear modulus G for an anisotropic material varies over a wide range. The main difference between edge and internal cracks is the alternative nature of the effect of anisotropy away from the free edges (L/W<0.1). As the crack approaches the free surface $(L/W\rightarrow1)$, the same pattern of anisotropy effects is observed.

Figure 9 shows the anisotropy influence on SIFs for the *third* problem concerning the *two edge cracks* in the plate under tension (Fig. 9(a)) and shear loading (Fig. 9(b)). Due to the influence of cracks on each other, pure fracture modes (in contrast to the first and second problems) are not realized neither in tension nor in shear. Both $K_{\rm I}$ and $K_{\rm II}$ are different from zero and a mixed fracture mode is realized.

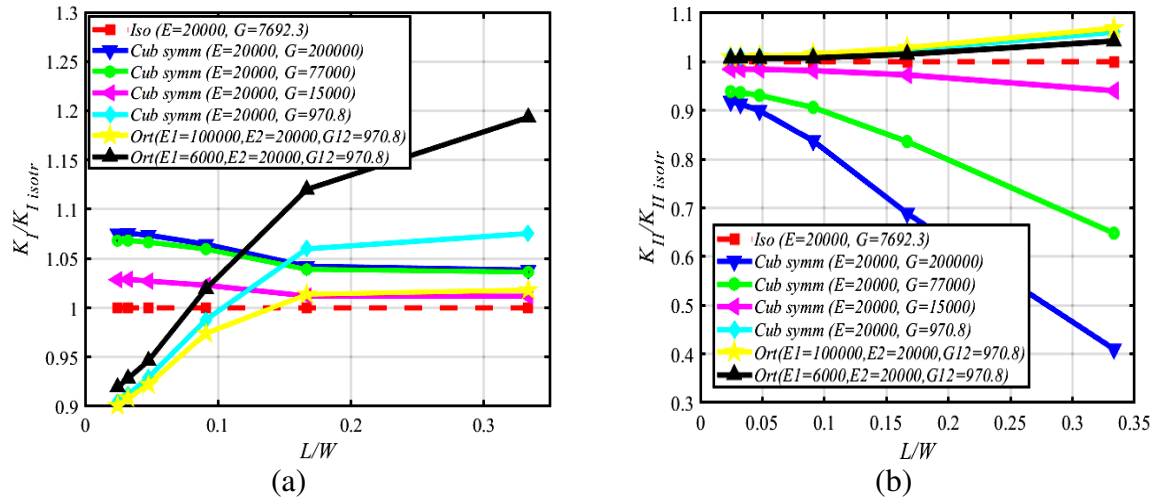


Fig. 9. Influence of anisotropy on SIF for two edge cracks in the plate under (a) tension, and (b) shear

Influence of material anisotropy is monotonously increase when closing to free boundary for shear loading (Fig. 9(b)), while this effect is not observed in tension (Fig. 9(a)). In general, in shear, the behavior of one and two edge cracks is quite similar (cf. Figs. 8(b) and 9(b)).

In tension, the behavior of one and two edge cracks for cubic symmetry is also very close (cf. Figs. 8(a) and 9(a)), while significant differences are observed for orthotropic material.

Figure 10 shows influence of anisotropy on SIFs for the *fourth* problem concerning the *three edge cracks* in the plate under tension (Fig. 10(a,b)) and shear loading (Fig. 10(c,d)). Due to the influence of cracks on each other, pure fracture modes are not realized neither in tension nor in shear loading. Both $K_{\rm I}$ and $K_{\rm II}$ are different from zero and a mixed fracture mode is observed. The SIFs for the central crack (with the crack tip at point B in Fig. 4) differ from the SIFs for the outermost cracks (with the crack tip at points A in Fig. 4).

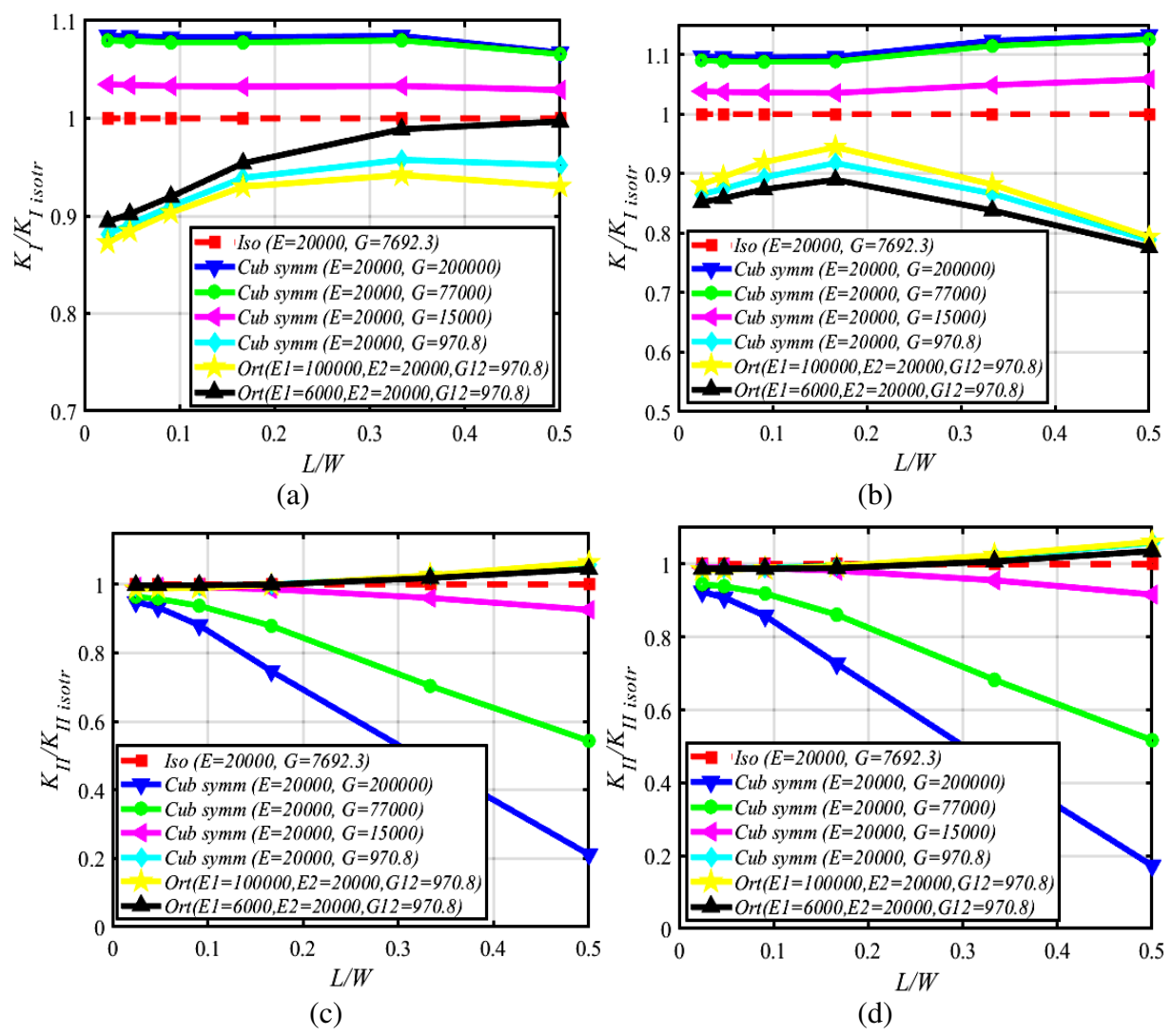


Fig. 10. Influence of anisotropy on SIFs for three edge cracks in the plate under (a) tension (Point A – outer crack), $K_{\rm I}$, (b) tension (Point B – central cracks), $K_{\rm I}$, (c) shear (Point A – outer crack), $K_{\rm II}$, (d) shear (Point B – central crack), $K_{\rm II}$

For the three edge cracks, the effect of anisotropy on the SIF is also very prominent. The character of dependences $K_{\rm I}(L/W)$ / $K_{\rm I \, isotr}$ add $K_{\rm II}(L/W)$ / $K_{\rm II \, isotr}$ for three cracks is close to the character of corresponding dependences for two cracks for cubic symmetry (cf. Figs. 10(a,b) with 9(a) and Figs. 10(c,d) with 9(b)), while significant differences are observed for orthotropic material. From the comparison of points A and B, it can be seen that the relative SIFs $K_{\rm I}(L/W)$ / $K_{\rm I \, isotr}$ in tension are larger for the internal crack with the tip at point B, while the absolute values $K_{\rm I}(L/W)$ are larger for the lateral cracks with the tip at point A, which reflects the shading effect.

Conclusions

The results of multivariant numerical experiments have demonstrated sensitivity of SIFs to material anisotropy for both internal and edge cracks under both tensile and shear loading. Depending on the elastic moduli, SIFs for an anisotropic material can be larger or smaller than the corresponding SIFs for an isotropic material. The effect of material anisotropy strongly depends on shear modulus value. For pure shear loading the influence of material anisotropy becomes stronger when the crack is approaching to the plate boundary. For uniaxial tension loading the effect of material anisotropy is approximately constant for different distances to the plate boundary in the problem of interaction of the cracks. The influence of material anisotropy in the problem with the three edge cracks is stronger than in the problem with one edge crack for purely shear loading (the increase in SIF reaches 80 %).

References

- 1. Shalin RE, Svetlov IL, Kachanov EB, Toloraiya VN, Gavrilin OS. *Single crystals of nickel heat-resistant alloys*. Moscow: Mashinostroenie; 1997. (In-Russian)
- 2. Getsov LB. *Materials and strength of gas turbine parts*. Rybinsk: Gazoturbinnye Tekhnologii; 2010. (In-Russian)
- 3. Dulnev RA, Kotov PI. *Thermal fatigue*. Moscow: Mashinostroenie; 1980. (In-Russian)
- 4. Getsov LB, Dobina NI, Rybnikov AI, Semenov AS, Staroselskii A, Tumanov NV. Thermal fatigue resistance of a monocrystalline alloy. *Strength of Materials*. 2008;40(5): 538–551.
- 5. Semenov AS, Semenov SG, Nazarenko AA, Getsov LB. Computer simulation of fatigue, creep and thermal fatigue cracks propagation in gas turbine blades. *Materials and Technology*, 2012; 3: 197–203.
- 6. Semenov AS, Semenov SG, Getsov LB. Methods for calculating the growth rate of fatigue cracks, creep and thermal fatigue in poly- and single-crystal gas turbine blades. *Journal of Strength Materials*. 2015; 2: 61–87.
- 7. Getsov LB, Semenov AS, Ignatovich IA. Thermal fatigue analysis of turbine discs on the base of deformation criterion. *International Journal of Fatigue*. 2017; 97: 8–97.
- 8. Getsov LB, Semenov AS. On the safety margins of gas turbine engine parts under thermal cyclic loading. *Aviation Engines*. 2023; 18(1): 79–98.
- 9. Liebowitz H. Fracture, an Advanced Treatise. Vols. I and II. NY: Academic Press; 1968.
- 10. Sih GC. (Ed.) *Mechanics of Fracture. Methods of analysis and solutions of crack problems*. Netherlands, Leyden: Noordhoff International Publishing; 1973.
- 11. Morozov NF. Mathematical Problems in the Theory of Cracks. Moscow: Nauka; 1984. (In-Russian)
- 12. Murakami Y. Stress Intensity Factors Handbook. Pergamon; 1987.
- 13. Kuna M. Finite Elements in Fracture Mechanics. New York: Springer; 2013.
- 14. Sih GC, Paris PC, Irwin GR. On cracks in rectilinearly anisotropic bodies. *International Journal of Fracture Mechanics*. 1965;1: 189–203.
- 15. Barnett DM, Asaro RJ. The fracture mechanics of slit-like cracks in anisotropic elastic media. *Journal of Mechanics and Physics of Solids*. 1972;20(6): 353–366.
- 16. Azhdari A, Nemat-Nasser S Experimental and computational study of fracturing in an anisotropic brittle solid. *Mechanics of Materials*. 1998;28(1-4): 247–262.
- 17. Savikovskii AV, Semenov AS, Getsov LB. Crystallographic orientation, delay time and mechanical constants influence on thermal fatigue strength of single-crystal nickel superalloys. *Materials Physics and Mechanics*. 2020;44(1): 125–136.
- 18. Savikovskii AV, Semenov AS, Kachanov ML. Influence of Material Anisotropy on the Interaction of a Crack with a Free Boundary. *Mechanics of Solids*. 2022;57: 2030–2037.
- 19. Yu H., Kuna M. Interaction integral method for computation of crack parameters K-T a review. *Engineering Fracture Mechanics*. 2021;249: 107722.
- 20. Ozkan U, Nied HF, Kaya AC. Fracture analysis of anisotropic materials using enriched crack tip elements. *Engineering. Fracture Mechanics*. 2010;77: 1191–1202.

- 21. Semenov AS. PANTOCRATOR finite-element program specialized on the solution of non-linear problems of solid body mechanics. In: *Proc. of the V-th International. Conf.* "Scientific and engineering problems of reliability and service life of structures and methods of their decision". SPb: Izd-vo SPbGPU; 2003. p.466–480. (In-Russian)
- 22. Kachanov LM. Osnovy mekhaniki razrusheniya. Moscow: Nauka; 1974. (In-Russian)
- 23. Banks-Sills L, Hershkovitz I, Wawrzynek PA, Eliasi R, Ingraffea AR. Methods for calculating stress intensity factors in anisotropic materials: Part I-z=0 is a symmetric plane. *Engineering. Fracture Mechanics*. 2005;72(15): 2328–2358.
- 24. Judt PO, Ricoeur A, Linek G. Crack path prediction in rolled aluminum plates with fracture toughness orthotropy and experimental validation. *Engineering Fracture Mechanics*. 2015;138: 33–48. 25. Lekhnitskiy SG. *Teoriya uprugosti anizotropnogo tela*. Moscow: Nauka; 1977. (In-Russian) 26. Ranjan S, Arakere NK. A Fracture-mechanics-based methodology for fatigue life prediction of single crystal nickel-based superalloys. *Journal of Engineering Gas Turbines Power*. 2008;130(3): 032501.

THE AUTHORS

Savikovskii A.V.

Semenov A. S. 🗓

e-mail: savikovskii.artem@yandex.ru

e-mail: Semenov.Artem@googlemail.com

On the crack evolutional in human dentin under uniaxial compression imaged by high resolution tomography

Submitted: April 25, 2023

Approved: July 3, 2023

Accepted: July 17, 2023

D. Zaytsev **1**,2 **3**, **A.** Funk **1**,3

¹ Ural State Mining University, Yekaterinburg, Russia.

² Ural Federal University, Yekaterinburg, Russia.

³ Federal Institute for Materials Research and Testing (BAM), Berlin, Germany

⊠ dmitry.zaytsev@urfu.ru

Abstract. An observation of the fracture process in front of the crack tip inside a dentin sample by means of ex-situ X-ray computed tomography after uniaxial compression at different deformation values was carried out in this work. This ex-situ approach allowed the microstructure and fracturing process of human dentin to be observed during loading. No cracks are observed up to the middle part of the irreversible deformation in the samples at least visible at $0.4\mu m$ resolution. First cracks appeared before the mechanical stress reached the compression strength. The growth of the cracks is realized by connecting the main cracks with satellite cracks that lie ahead of the main crack tip and parallel its trajectory. When under the stress load the deformation in the sample exceeds the deformation at the compression strength of dentin, an appearance of micro-cracks in front of the main cracks is observed. The micro-cracks are inclined ($\sim60^{\circ}$) to the trajectory of the main cracks. The further growth of the main cracks is not realized due to the junction with the micro-cracks; we assume that the micro-cracks dissipate the energy of the main crack and suppressed its growth. These micro-cracks serve as additional stress accommodations, therefore the samples do not break apart after the compression test, as it is usually observed under bending and tension tests.

Keywords: dentin; crack evolution; compression strength; mechanical properties; microstructure; ex-situ X-ray computed tomography

Acknowledgements. D. Zaytsev is grateful for the financial support of the Russian Science Foundation (RSF project No. 22-29-00268).

Citation: Zaytsev D, Funk A. On the crack evolutional in human dentin under uniaxial compression imaged by high resolution tomography. *Materials Physics and Mechanics*. 2023;51(5): 38-51. DOI: 10.18149/MPM.5152023 5.

Introduction

Human dentin is the hard base of the tooth. It is composed of an organic matrix that is reinforced by carbonated apatite [1]. The main mechanical function of dentin is to distribute mechanical loads within the tooth under mastication. Due to its unique hierarchical microstructure from macroscopic to microscopic length scales, dentin is able to endure both considerable elastic (~15%) and irreversible deformation (~15%) at high strength under uniaxial compression (~430 MPa) [2]. On the other hand, its deformation behavior is close to brittle solid under bending and tension. The total deformation of human dentin in three-point bending tests is considerably low (~1.5%) in comparison to uniaxial compression (~3%) [3]. The flexural strength (150-200 MPa) is also lower [3–5]. The ultimate tensile strength of dentin is

40-90 MPa, which is less than the flexural strength and the compression strength [6–8]. This dependence of the strength of dentin samples on the loading scheme is caused by the difference of stress distribution in samples that different mechanisms of deformation and fracture are activated under respective loads under compression, bending, and tension.

It is supposed that the crack growth in dentin is realized due to the junction of the primary or main crack with the secondary or satellite cracks ahead of the main crack tip [9,10]. At that, part of the satellite cracks can nucleate from tiny cracks in the highly mineralized cuff of peritubular dentin [11]. Therefore, the trajectory of the main crack preferably runs through the dentinal tubules [9]. Such a mechanism of crack growth is anticipated for high tensile stresses inside a dentin sample. However, tensile stresses in tensile and three-point bending tests are much higher than in compression tests. Therefore, the fracture process is different under compression test compared to tensile.

It has been shown that the compression strength decreases with an increase of the sample height or, in other words, with decreasing d/h ratio (the ratio between the diagonal d of the compressed sample surface and the sample height h) [2,12]. Samples with a low d/h ratio behave brittle-like while the deformation behavior of samples with a high d/h ratio is close to a ductile. The friction between the sample surfaces and the compression punches under uniaxial compression results in a dependence of the mechanical properties of dentin samples on its d/h ratio. If transverse or tensile deformation is suppressed in region compressed sample surfaces in a sample with a high d/h ratio, an inhomogeneous deformation will occur. As a result, the samples can possess a barrel-like shape after compression [2]. The crack growth in dentin is suppressed when the tensile and the shear stresses are minimized. Indeed, a sample with a high d/h ratio and already present cracks can be compressed several times without any fatal destruction and decreasing the ability to elastic deformation [13]. In this case, intensive deformation should occur ahead of the crack tip. Observations of samples surfaces after compression have shown that the quantity and the length of cracks are decreasing with decreasing of d/h ratio [3]. However, no differences between in profiles of cracks under tension or bending and under compression were observed. The specific reasons for the ability of human dentin to endure significant deformation under compression are still unknown. Is this the result of a decrease in the tensile stresses while compressing or something else? It is possible that the considerable deformation of dentin during compression is caused by the accumulation of microcracks in the sample, which do not lead to its destruction due to smaller tensile stresses.

Light microscopy and scanning electron microscopy allow only the sample surface to be observed and provide information about the appearance of cracks on the surface or the fracture surface of a sample. Based on this information, researchers interpret how a crack in the sample can grow. Transmission electron microscopy can estimate the crack growth in the whole volume of a sample but samples for this technique are very thin. Therefore, we obtain two-dimensional information about the crack growth, which is not the case for bulk samples under mechanical testing. However, the assessment of the crack growth within an appropriately large sample volume can be performed using non-destructive three-dimensional imaging techniques such as X-ray computed tomography enables the crack growth to be assessed within an appropriately large sample volume [14,15]. The high-resolution X-ray computed tomography employed in this work (with the resolution up to 0.4 µm) should reveal the relationship between the crack trajectory and the orientation of the dentinal tubules, as the diameter of a single dentin tubular is 1-3 µm [16]. An observation of the crack growth using X-ray computed tomography at different stages of loading will show how cracks nucleate and grow in a dentin sample under compression and may bring new insights as to understand why dentin is able to endure considerable deformation.

Thus, the aim of this work is the observation of the fracture process within dentin samples at different stages of loading by means of high-resolution ex-situ X-ray computed tomography

D. Zaytsev, A. Funk

under uniaxial compression. It is expected that the intensive deformation and fracture processes should occur in front of the main crack tip. The results of this work are potentially useful for the creation of new biomimetic materials, including materials for dental science.

Materials and Methods

Sample preparation. Five intact (caries-free), recently extracted human molars were used in this work. The teeth were obtained from male and female subjects aged 25 to 40 years living within the Ural region (Russia). The tooth extraction procedure was performed according to the Ethical Protocol of the Urals State Medical University in Yekaterinburg that is in accordance with all the requirements of the law. For mechanical testing, from the central part of the teeth crown five cuboid dentin samples were cut out by a diamond saw under continuous irrigation. After that, the surface of the samples was polished by means of the abrasive papers starting with grit 600 and finishing with grit 2000. The samples had a cuboid shape with the approximate size $2 \times 2 \times 0.9 \text{ mm}^3$. The deviation in size was no more than 23µm in height (Z-direction, Fig. 1) and no more than 18 µm in the face of the compression plane (X-Y plane, Fig. 1). The measurement accuracy was 5 µm. The quality of sample surface preparation was controlled using light microscopy (Bresser advance ICD) with the magnification of 50x. There is no strict direction of the dentinal tubules in the samples since they have a large size relative to the tooth where tubules have a complex, sigmoid «S» curvature [14].

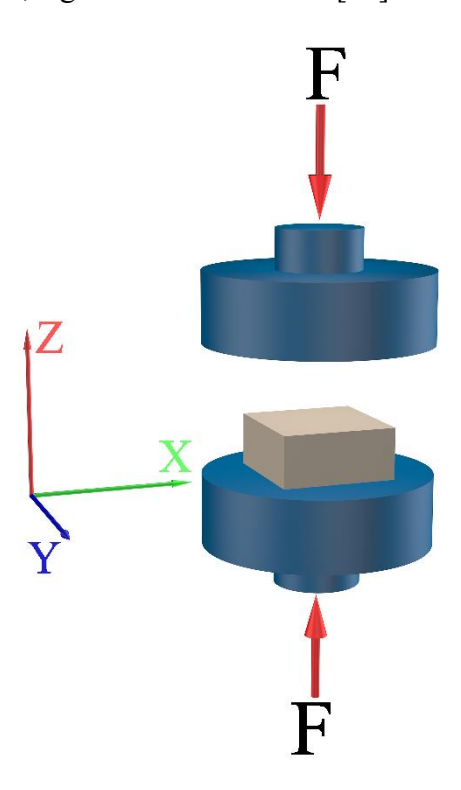


Fig. 1. The scheme of deformation for the dentin samples

Mechanical testing. Until testing the samples were stored in 0.9 % salt solution at ambient temperature before testing. Shimadzu AGX-50kN testing machine has been used for uniaxial compression of the dentin samples. The scheme of loading is given in fig. 1. The tests were carried out with the constant loading rate of 0.1 mm/min. The first sample was not subjected to loading, whereas the other samples 2-5 were loaded up to different deformation values, which are given in Table 1. The deformation values were chosen based on previously performed dentin compression tests, which allow the deformation and fracture process to be estimated during loading from elastic deformation to the start of the fracture process [2].

The deformation of the samples was determined by means of the movement of the traverse. Trapezium-X standard software for Shimadzu was used for processing the experimental data.

Table 1. Dentin sample testing conditions

Sample	Deformation, %	Condition		
1	0	initial state		
2	7	elastic mode		
3	15	irreversible mode		
4	25	pre-fracture mode		
5	35	after fracture		

Microstructure characterization. The observation of the microstructure and the defects within the samples was carried out by means of X-ray computed tomography employing a ZEISS Xradia 620 Versa device. While rotating a sample for 360° within the X-ray beam path, a set of radiographs is captured at discrete angular steps. Subsequently, a three-dimensional volume is reconstructed from the set of radiographs using the standard filtered back-projection algorithm for cone-beam setups [17]. Both data acquisition and reconstruction were performed with ZEISS software "Scout-and-Scan Control" and "Scout-and-Scan Reconstructor" (version 14). Details on the method can be found elsewhere [18].

Overview scans are taken for all five samples at low resolution. Interesting sample spots e.g., ahead of the main crack tips, are tested additionally at high resolution (detail scan). The scanning parameters are summarized in Table 2. Note that besides the voxel size resulting from the total magnification (geometrical and optical), the basic spatial resolution of the device and used objectives is limited. For the high-resolution scans, the total size of the investigated volume was a cylinder with a diameter of 360 μm and a height of 390 μm. ImageJ Fiji, Avizo 2019.4 (ThermoFischer Scientific) and VG Studio max 3.3 (Volume Graphics) were used for image analysis [19–21].

Table 2. Summary of X-ray computed tomography parameters.

	X-ray tube voltage, kV	X-ray tube power, W	Device spec. X-ray filter	Source- Object- Distance, mm	Object- Detector- Distance, mm	Geometrical magnification
Overview scan	50	4.5	LE3	17	17	2x
D	50	4.7	1.50	1.1		1.622
Detail scan	50	4.5	LE2	11	7	1.633x
	Optical magnification	Total magnification	Voxel size, µm	Basic spatial resolution, µm	Exposure time, sec	Set of radiographs
Overview scan	4x	8x	1.7	1.9	5	801
Detail scan	40x	65.32x	0.4	0.5	30	2401

Results

The deformation stress-strain curves of samples 2-5 under compression are shown in Fig. 2. The trend of deformation curves is similar for all compressed samples. The dependence of the stress on the strain of the samples at the initial stage of loading is linear, while under stress ~ 300 MPa and ~8 % deformation it changes to non-linear. The blue arrows in Fig. 2 points to the stress and the deformation at which the compression test was stopped for each sample.

D. Zaytsev, A. Funk

Sample 2 is compressed to the end of linear deformation (7 %) whereas sample 3 is compressed to the middle part of nonlinear deformation (15 %). The loading of sample 4 was stopped right before the maximum stress or compression strength (25 %) that corresponds to the state of prefracture. The deformation under compression of sample 5 was slightly larger than the deformation at which the compression strength was achieved during testing. The gradual stress drop is observed in sample 5 after reaching the compression strength. The stress drop on the deformation curve corresponds to the process of intense fracture or crack nucleation and growth in sample 5.

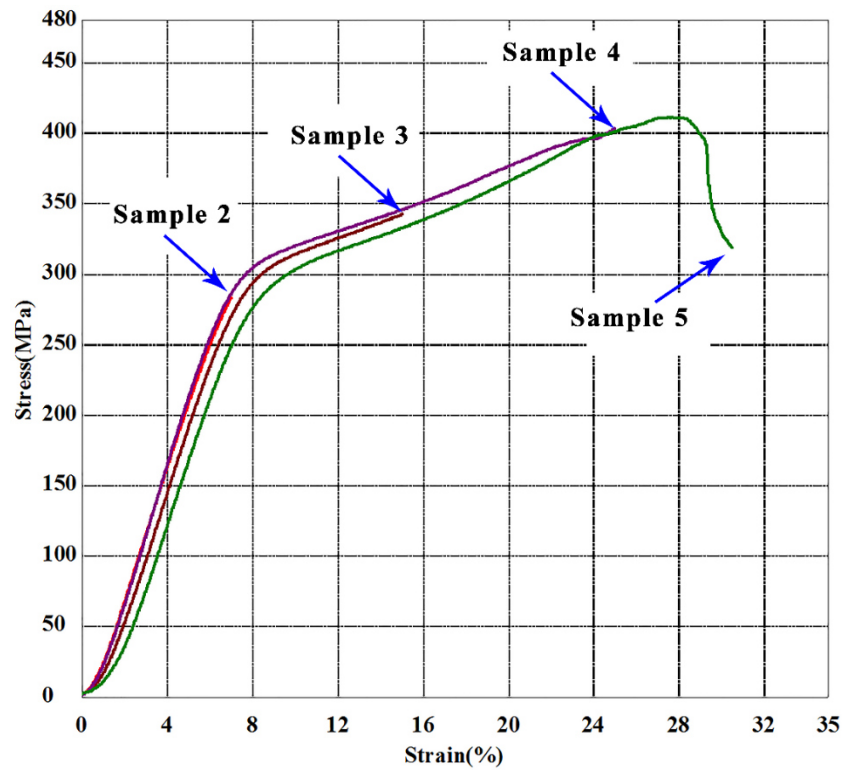


Fig. 2. Deformation curve of dentin sample under compression. Arrows are indicated at the end of the deformation curve for the samples

X-ray computed tomography at low resolution (1.7 μ m) of sample 1 and samples 2, 3, 4 and 5 after loading showed that the cracks appear only in samples 4 and 5. The cracks appear at the surface of the samples and penetrate the entire volume. The number of cracks in sample 5 is greater than in sample 4, both on the surface of the sample and inside the sample (Fig. 3). At that, the cracking pattern is similar in both samples. The cracks were almost parallel to the edge of the backside on the compression surface (X-Y plane, Fig. 1) and the cracks are tilted at an angle of 30° to the side surface (Z-Y plane, Fig. 1) for both samples, Fig. 3. In addition, there is a crack in sample 5 (Fig. 5(e)), which is inclined at an angle of 45° to the side surface (X-Y plane, Fig. 1). Besides, there is a secondary crack that begins to grow from the compression surface at the end of the primary crack and it is tilted at an angle of 60° to the side surface of the primary crack (Z-Y plane, Fig. 1) in sample 5. However, despite the similarity of the profiles of the cracks between samples 4 and 5, parallel micro-cracks are observed in the middle part of sample 5 in the area of the main crack tip. The micro-cracks are inclined (~ 60°) to the trajectory of the main crack (Fig. 3(f)). Also, similar micro-cracks are observed directly on the compression surface (X-Y plane, Fig. 1). On the contrary, there are no micro-cracks in the area of the main crack tip in sample 4 (Fig. 3(c)). Both samples 4 and 5 have a barrel-like shape (Fig. 5(c) and 5(f)). Dentin tubules are not viewed at this resolution.

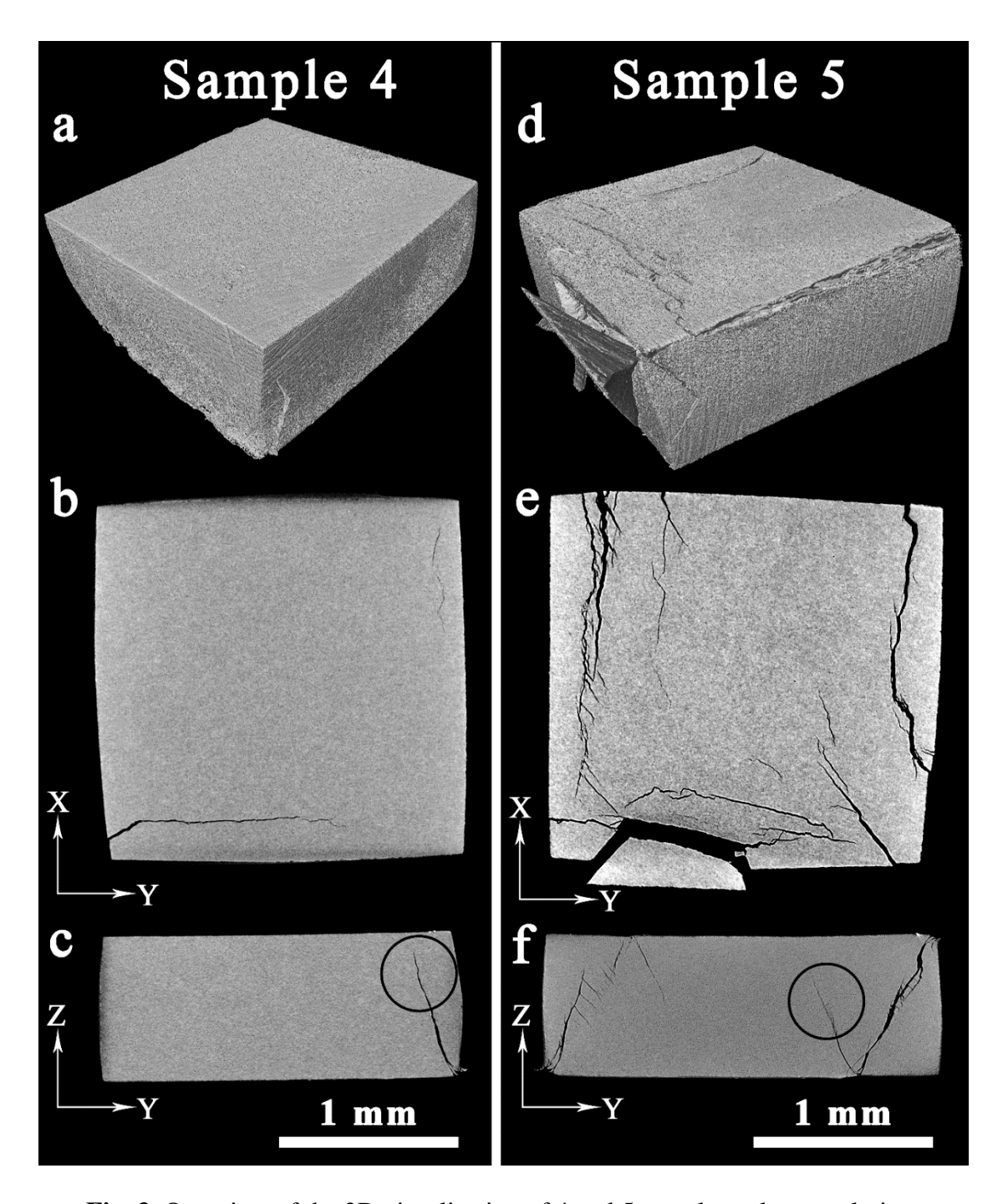


Fig. 3. Overview of the 3D visualization of 4 and 5 samples at low resolution: (a) the view of sample 4; (b) the reconstructed longitudinal slice in the middle part of sample 4; (c) the reconstructed cross-section slice in the middle part of sample 4; (d) the view of sample 5; (e) – the reconstructed longitudinal slice in the middle part of sample 5; (f) the reconstructed cross-section slice in the middle part of sample 5

X-ray computed tomography of samples 4 and 5 after loading at high resolution (0.4 µm) was performed in detail for the regions ahead of the main cracks tip (indicated by black circles in Fig. 3(c, f)). The trajectory of the main cracks is uneven, but despite this, the main cracks approximately lie in the planes (Figs. 4(a) and 5(a)). There are satellite cracks lying ahead of the main crack tip for both samples (Figs. 4(b) and 5(b)). The plane of the satellite crack is parallel to the plane of the main crack in sample 4 (Fig. 4(b)). On the contrary, the planes of the satellite cracks are almost perpendicular to the plane of the main crack into sample D. Zaytsev, A. Funk

5 (Fig. 5(b)). The number of the satellite cracks ahead of the main crack tip is greater in sample 5 (Fig. 5(b)). Dentin tubules are clearly visible at this resolution. Tubules appear as black dots by the overview and as a white line at the view where crack is highlighted (Figs. 4 and 5). In both cases, the trajectory of the main cracks was independent of the alignment of the dentinal tubules.

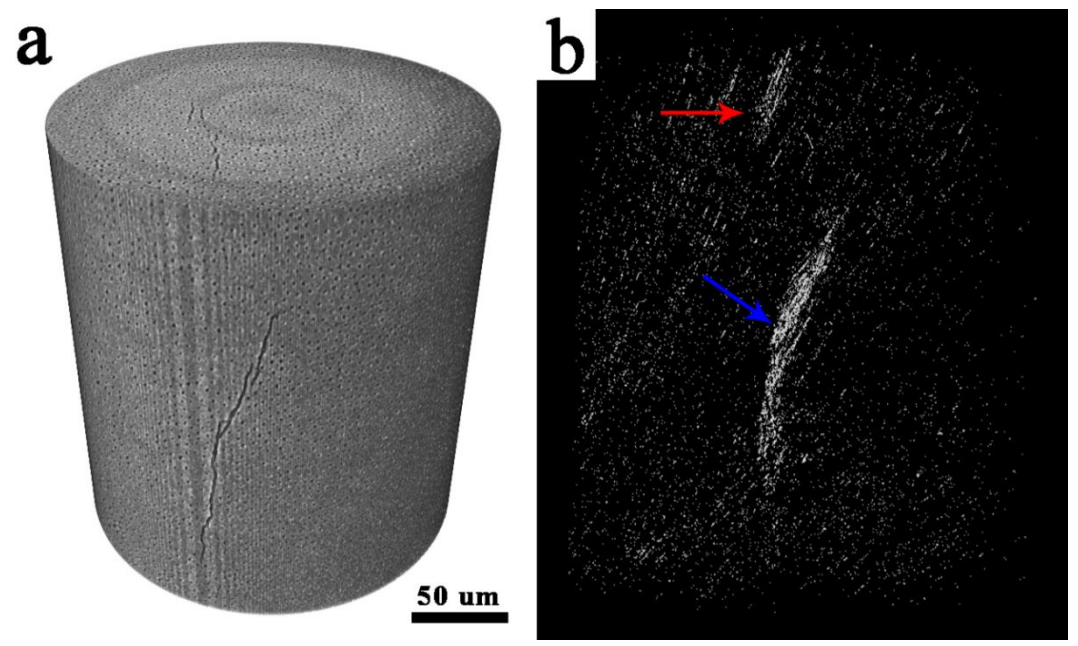


Fig. 4. The 3D visualization of the area of the main crack tip into sample 4 at high resolution (indicated black circle at Fig. 3(c)): (a) the overview; (b) the view where crack is highlighted. The red arrow indicates the satellite crack lying ahead of the main cracks that are indicated by the blue arrow

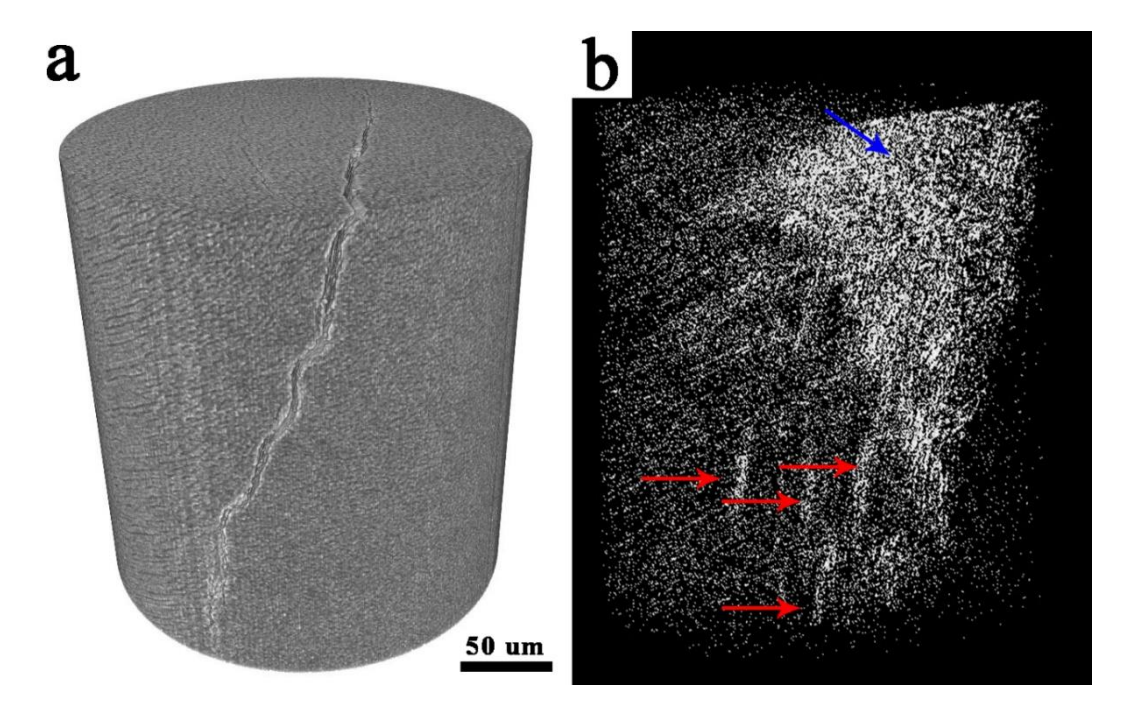


Fig. 5. The 3D visualization of the area of the main crack tip into sample 5 at high resolution (indicated black circle at Fig. 3(f)): (a) the overview; (b) – the view where crack is highlighted. The red arrows indicated the several micro-cracks ahead of the main cracks indicated by the blue arrow

The detailed study of the main crack tip region in sample 4 at high resolution has shown that there are satellite cracks ahead of the main crack tip (Fig. 6). The trajectory of the main crack and the satellite cracks pass through the dentinal tubules (Fig. 6). The trajectory of the main crack and satellite cracks are initially rectilinear but sometimes turn into a zigzag profile (Fig. 6(g)). Besides, tiny cracks inclined ($\sim 60^{\circ}$) to the main cracks are observed (Fig. 6(h)). The trajectory of the satellite cracks is parallel to the trajectory of the main cracks (Figs. 6(c,e)). At that, not all satellite cracks create a junction with the main crack (Fig. 6(f)). The tiny cracks in sample 5 also branch off from the main crack, but tilted at an angle 30° (Fig. 7(a)). The main crack in sample 5 grows due to the junction with the satellite cracks that lie along further on its growth path as it takes place into sample 4 (Figs. 6(b,c)). However, there are many parallel micro-cracks tilted at an angle 60° to the main crack in sample 5 (Fig. 7). The distance between micro-cracks varies from 16 to 3 µm. The main crack can pass through micro-cracks, but this does not change its trajectory (Fig. 7(e)). The long micro-cracks have a sigmoid "S" shape profile. Such profile of the long micro-cracks caused by the fact that the cracks started and stopped at the dentinal tubules due to the trajectory of the micro-crack has changed from a straight line to sigmoid "S" near the dentinal tubules (Fig. 7(e)).

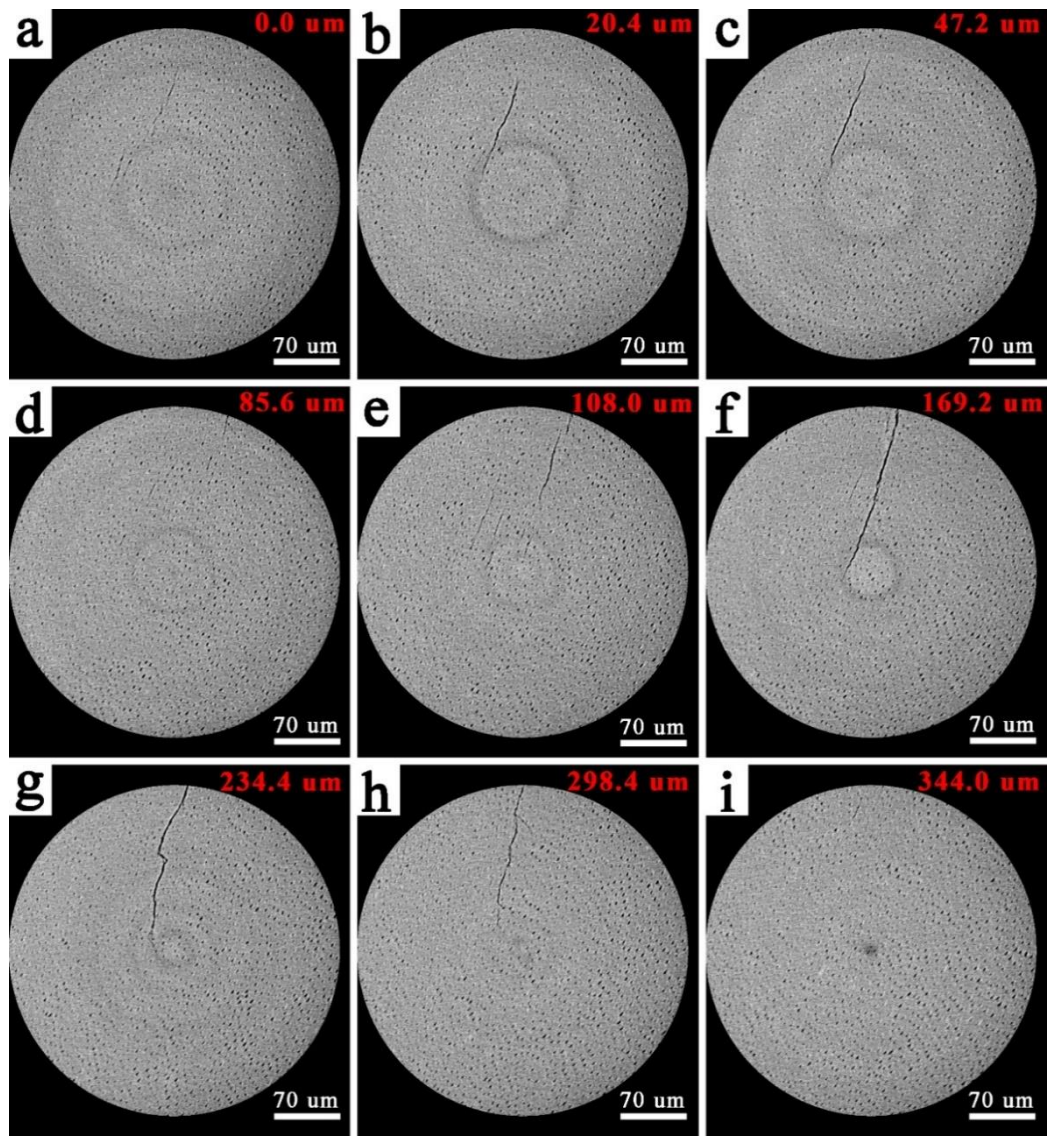


Fig. 6. The reconstructed cross-section slices of the main crack tip area of sample 4 at high resolution (indicated black circle at Fig. 3(c)). Red numbers indicate the layer depth: (a) 0; (b) 20.4 µm; (c) 47.2 um; (d) 85.6 µm; (e) 108.0 µm; (f) 169.2 µm; (g) 234.4 µm; (h) 298.4 µm; (i) 344.0 µm

D. Zaytsev, A. Funk

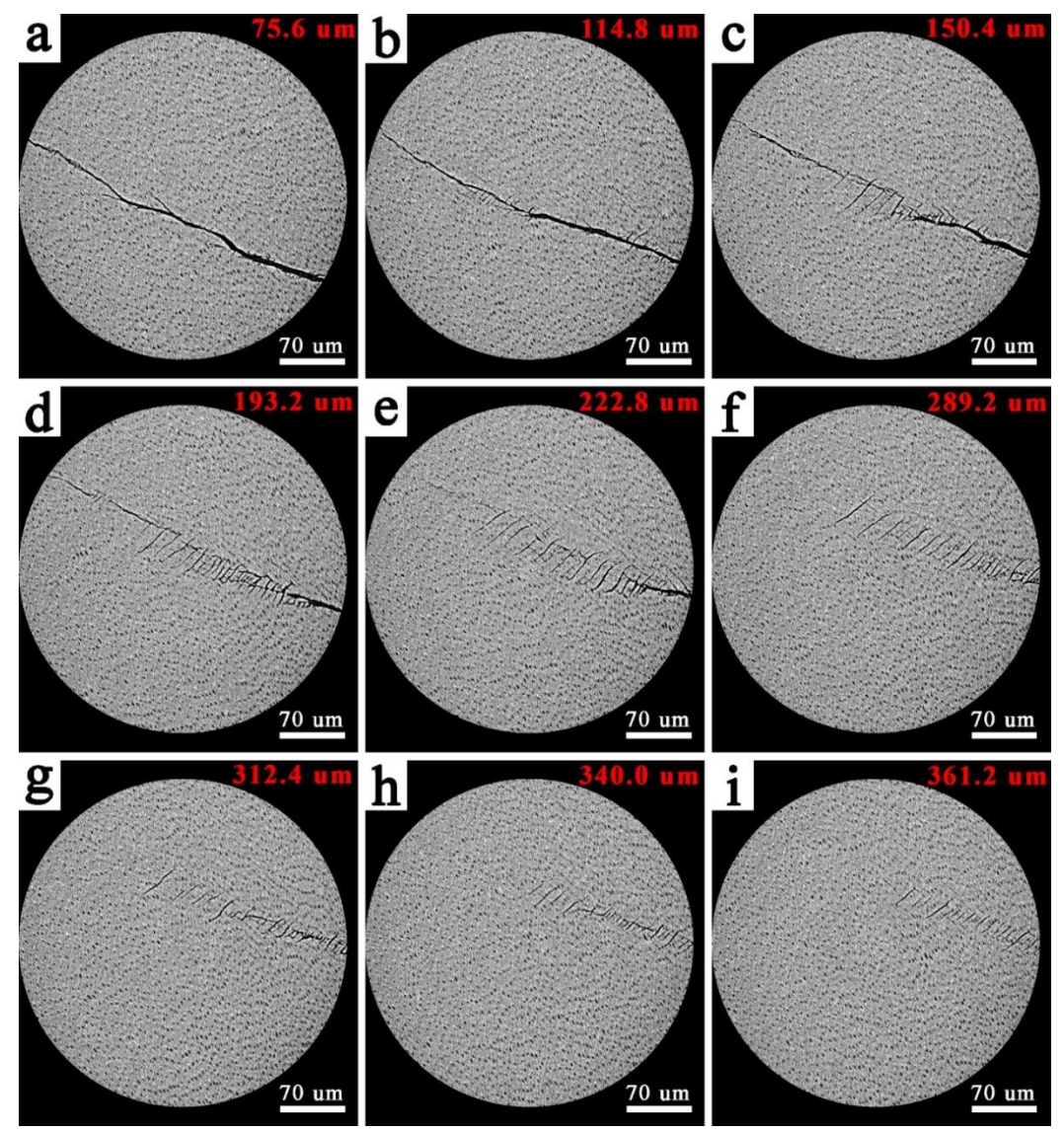


Fig. 7. The reconstructed cross-section slices of the main crack tip area of sample 5 at high resolution (indicated black circle at Fig. 3(f)). Red numbers indicate the layer depth: (a) 75.6 μm; (b) 114.8 μm; (c) 150.4 μm; (d) 193.2 μm; (e) 222.8 μm; (f) 289.2 μm; (g) 312.4 μm; (h) 340.0 μm; (i) 361.2 μm

Furthermore, besides the crack pattern, X-ray computed tomography enables studies of the overall microstructure of the samples 1 to 5. A varying number of "pores" was detected at low resolution within the sample series, c.f. (Fig. 8). As the dentinal tubules are not visible at low resolution, the "pores" can be clearly detected without mixing them with the dentinal tubules. The number of individual "pores" in sample 1 is about 900, which is significantly larger than in all other samples; samples 2, 4 and 5 show less than 50 and sample 3 has no more than 5 "pores" In the literature, such "pores" are referred to as "micro-canals" or "giant dentinal tubules" [22]. The "pores" found in the samples 1 to 5 are mostly ranging in size between 6 μ m and 20 μ m (sphere equivalent diameter) with the mean diameter of about 10 to 12 μ m, however, also outliers with about 30 up to 50 μ m were found. These outliers are two or more smaller but merged "pores". The detection of "pores" in sample 4 and 5 is challenging due to the dominant crack pattern. The influence of "pores" on the crack evolution is not determined from this sample loading series. Cracks may hit and destroy a "pore" and hence, "pores" will not be

detected anymore. However, "pore" examples were found in sample 5 where the crack avoids hitting the "pores". It is also possible that "pores" will close while compressed. To clarify this, in- or ex-situ X-ray computed tomography from the same sample exposed to loading steps needs to be performed. Nevertheless, X-ray computed tomography proves to be a valuable tool to preinvestigate the quality of tooth samples in advance of any future experimental testing.

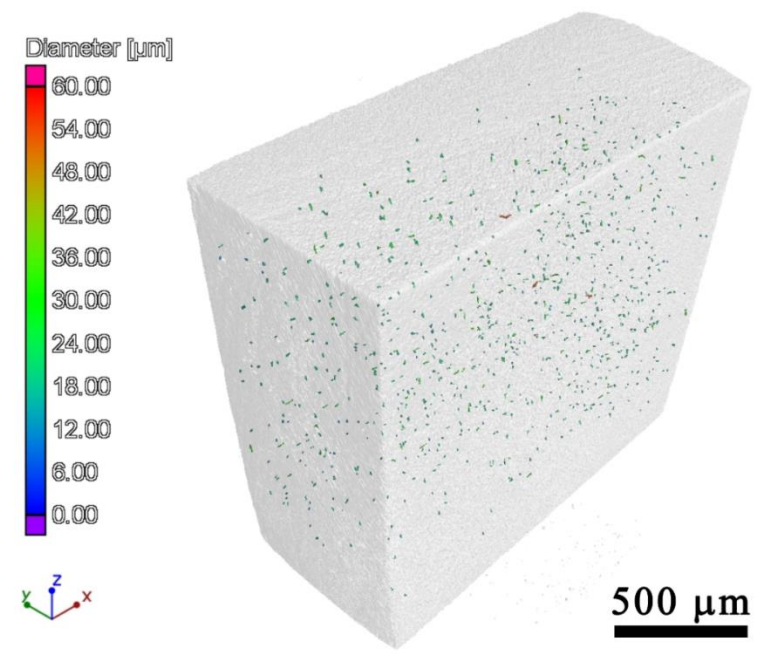


Fig. 8. The 3D visualization of the pore size distribution in sample 1. Color code refers to the pore size equivalent diameter

Discussion

The deformation behavior of compressed dentin samples, when the linear dependence of strain on stress at the initial stage of loading changes to nonlinear at high stresses, is typical for human dentin and elastic-plastic bodies under compression [2]. X-ray computed tomography has shown that the fracture process starts before reaching the compression strength. There are no observed cracks up to the middle of the irreversible deformation of dentin under compression (15 %). Therefore, the considerable elastic and irreversible deformation is not caused by the accumulation of the cracks, at least there is no such evidence at 0.4 µm resolution. Hence, human dentin is able to withstand considerable elastic and irreversible deformation due to its microstructure, but for an implementation it is necessary to create certain conditions. The main one is the reduction of tensile stresses. It was shown by the compression of dentin in liquid nitrogen that the ability to irreversible deformation of dentin is provided by means of the plasticity of collagen fibers and porosity of intertubular dentin [23]. Elastic deformation is realized due to the elasticity of collagen. At high stress loads, when the crack nucleation is starting, intensive deformation occurs in the plastic zone in front of the crack tip. It is clear that highly mineralized cuff withstands less deformation compared to intertubular dentin. During loading and further deformation of dentin, cracking of the peritubular cuff occurs. Since the deformation in the plastic zone is higher than the average deformation for the specimen, the fracture of the peritubular dentin is occurred in front of the tip of the main crack. The tiny cracks nucleate in peritubular cuff [11]. Increasing the deformation leads to an increase in the angle of opening of tiny cracks and their length in peritubular dentin. After that, one of the tiny cracks in the peritubular cuff joint with the tiny crack in the nearest dentin tubular and so on as a result D. Zaytsev, A. Funk

the satellite crack is formed. Therefore, the crack path lies through the dentinal tubules due to this mechanism of crack growth [9].

The crack growth mechanism under compression is similar to the mechanisms of tensile or bending loadings [10,24]. The main crack grows due to the junction with the satellite cracks that are situated in front of it and lie along its growth path (Fig. 9(a)). However, the microcracks are inclined (~ 60°) to the trajectory of the main crack, which was formed when the deformation exceeded deformation at the compression strength (Fig. 7(e)). At that, the growth of the main crack is not taking place due to the junction with the micro-cracks even though the main crack goes through them (Fig. 7(d)). The nucleation of micro-cracks occurs in the plastic zone in front of the tip of the main crack (Fig. 9(b)). This may be due to the accumulated damage in the peritubular dentin in the plastic zone of the main crack that indicates the existence of intense deformation there [25]. The damaged areas of the peritubular dentin are stress concentrators where it is easier for cracks to arise. Similar micro-cracks were observed earlier, where it was defined as "ladder-like" bands that consist of an array of cracks oriented orthogonal to the main band trajectory of the crack [26]. The band texture consists of segments of dentin separated by orthogonal cracks at regular intervals of about 20 µm. Shifting and torsion of these segments is thus an energy dissipation mechanism, slowing the crackdown and preventing catastrophic failure [26].

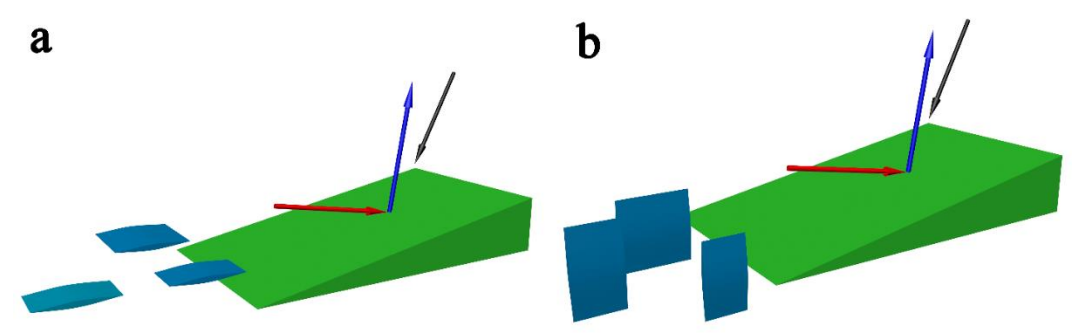


Fig. 9. The schemes of crack grow in human dentin under compression stress: (a) the scheme for crack grows in sample 4; (b) the scheme for crack grows in sample 5. The green wedge is the main crack whereas blue areas are satellite cracks (sample 4) or micro-cracks (sample 5). The red arrows indicated compression stress. The blue arrows indicated tensile stress and the black arrows indicated the direction of dentinal tubules

Stress accommodation of mechanical energy in the sample under the loading is realized due to two channels: deformation and free surface formation (crack nucleation). Deformation of the material in the plastic zone reduces the energy of the crack and can lead to its stop. The nucleation of cracks in front of the main crack tip also decrease its energy. Although the microcracks in sample 5 do not join the main crack, micro-cracks are reducing the main crack's energy and suppressing its growth. The micro-cracks act as a shield for the main crack tip and hence, extrinsically toughen the material. Therefore, the nucleation of the micro-cracks is the additional channel of stress accommodation to ligament bridging and crack deviation of the main crack. The samples do not break apart after the compression test due to this channel of stress accommodation as, on the contrary, it takes place under bending and tension. The cracks deviation from the plane of maximum driving force the stress intensity experienced at the crack tip is reduced, thereby providing an additional source of toughening [24]. The formation of a large number of stable cracks in the sample reduces its energy. Due to the sample that contained the cracks can be compressed several times without destruction and decreasing the ability to the elastic deformation [13].

Despite the fact that the crack growth occurs through the dentinal tubules, a strong dependence of the crack trajectory on the orientation of the dentinal tubules was not obtained.

Usually, the relationship between the crack trajectory and the orientation of the dentinal tubules is difficult to evaluate under compression as the orientation, density and diameter of the dentinal tubules in the sample of such volume is nonhomogeneous. There is a significant increase in tubule density and tubule diameter with increasing distance from dentin enamel junction in the tooth [27]. It has been reported that dentinal tubules possess sigmoid "S" shape distribution in coronal dentin [28,29]. Therefore, the dentinal tubules in the samples have different orientations relative to the direction of the compression. Scanning of the areas at the tip of the crack at high resolution showed that the orientation, density and diameter of the dentinal tubules is uniform in a given volume (Figs. 4 and 5). However, in both cases (samples 4 and 5) the angles of inclination of the main cracks and the satellite cracks to the dentinal tubules were different. Therefore, the crack growth trajectory is determined by the scheme of deformation and the shape of the sample, and not by the orientation of the dentinal tubules. On the other hand, the fracture behavior of elephant dentin depends on the orientation of dentinal tubules under indentation where imprint depth was small and comparable to the diameter of dentinal tubules [30]. Besides, the deformation and the fracture behaviors of dentin are anisotropic at some other tests such as share test, bending and diametric compression [24, 31-33]. It is possible that in those tests the main deformation is realized in a plane whereas under compression the entire sample volume is involved in deformation process under compression.

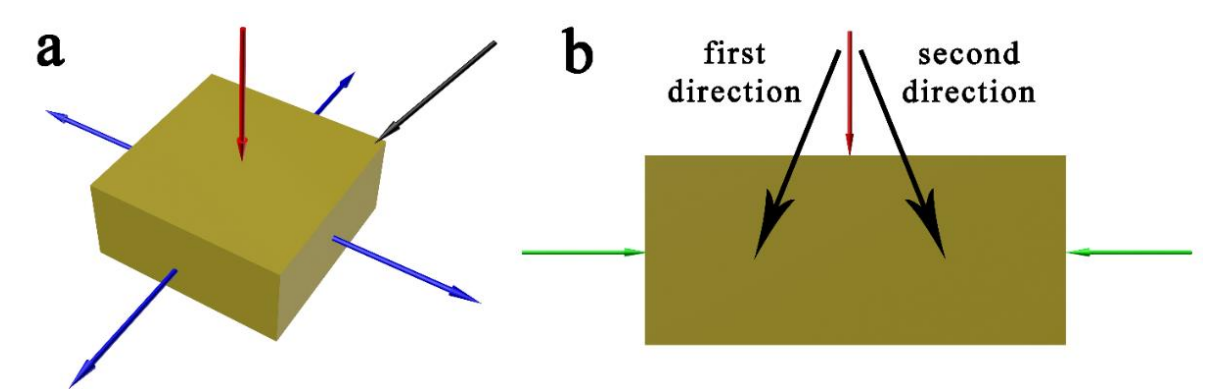


Fig. 10. The schemes forces and stresses acting on the sample under compression: (a) common view of the sample; (b) cross-section of the sample. The red arrows indicated compression stress. The blue arrows indicated tensile stress and the green arrows indicated the direction of the friction forces. The black arrow indicated the direction of dentinal tubules

The reason of the nucleation of the micro-cracks in the plastic zone of the main crack is caused by the scheme of loading and the shape of the sample. Two forces act on the sample when it is compressed: one is directed along the compression axis – the loading force (along Z, Fig. 1), and the second is the friction force between the sample and the compression plate. The friction forces are perpendicular to the compression force and lie in the X-Y plane in Fig.1 (Fig. 10(a)). Therefore, the vector sum of the loading force and friction forces acts on the sample under compression. The friction forces are directed toward the center of the sample or opposite to tensile stress insomuch as the sample expands under compression. The friction forces are maximal in the directions of the diagonals of the sample since it has a square crosssection. Two forces act on the sample if we consider the cross-section in the Z-Y Plane (Fig. 1) of the sample (Fig. 10(b)). Indeed, it can be seen that in the cross-section of sample 5, two directions of crack growth are active (Fig. 3(f)). The first direction is inclined at an angle of 30° to the upper compression surface, and the second direction is inclined at an angle of 30° to the lower compression surface (Fig. 3(f)). The cracks grow in the planes of maximum driving forces where tensile stresses are maximal. At that, the crack moves from one surface to another, and the secondary crack begins at the crack exit point on the sample surface (Fig. 3(f)). The microD. Zaytsev, A. Funk

cracks appear in the second direction for a crack moving in the first direction and *vice versa*, a crack moving in the second direction has micro-cracks in the first direction. Hence, the satellite cracks in two directions are formed in the plastic zone in front of the crack tip under the action of two forces where the damaged zone is formed. At low loads, the damaged zone is not large enough for secondary satellite cracks or micro-cracks to nucleate there. There is a damage zone formed inside the plastic zone. The damage zone is situated ahead of the main crack tip and its shape is not circular. The width of the damage zone is $\sim 60 \, \mu m$ and its length is $\sim 120 \, \mu m$ according to the size of the area of the micro-cracks (Figs. 5(b) and 7(e)). The damage zone can be determined as the pre-fracture zone. Micro-cracks do not nucleate under tension and bending since there is no effect of friction forces.

Conclusion

The considerable elastic and irreversible deformation is not caused by the accumulation of the cracks at least visible at 0.4 μm resolution up to the middle of the irreversible deformation of the dentin under compression. The cracks appear right before reaching the compression strength. The mechanism of crack growth under compression is similar to the crack growth under tensile test or three-point bending. The main crack grows due to the junction with the satellite cracks that are situated in front of it and lie along its growth path. However, the microcracks that are inclined ($\sim 60^{\circ}$) to the trajectory of the main crack appear when the deformations exceed the deformation at the compression strength. The growth of the main crack is not realized due to the junction with the micro-cracks. However, it is suggested that the microcracks decrease the energy of the main cracks and suppress their growth. These micro-cracks are an additional channel of stress accommodation due to which the samples do not break apart after the compression test as, on the contrary, it takes place under bending and tension.

References

- 1. Waters NE. Some mechanical and physical properties of teeth. Symp. Soc. Exp. Biol. 1980;34: 99–135.
- 2. Zaytsev D. Correction of some mechanical characteristics of human dentin under compression considering the shape effect. *Mater. Sci. Eng. C.* 2015;49: 101–105.
- 3. Zaytsev D, Ivashov AS, Mandra JV, Panfilov P. On the deformation behavior of human dentin under compression and bending. *Mater. Sci. Eng. C.* 2014;41: 83–90.
- 4. Arola DD, Reprogel RK. Tubule orientation and the fatigue strength of human dentin. *Biomaterials*. 2006;27: 2131–2140.
- 5. Staninec M, Nguyen H, Kim P, Marshall GW, Ritchie RO, Marshall SJ. Four-point bending evaluation of dentin-composite interfaces with various stresses. *Med. Oral. Patol. Oral. Cir. Bucal.* 2008;13: 81–84.
- 6. Giannini M, Soares CJ, Carvalho RM. Ultimate tensile strength of tooth structures. *Dent. Mater.* 2004;20(4): 322–329.
- 7. Fuentes V, Ceballos L, Osorio R, Toledano M, Carvalho M, Pashley DH. Tensile strength and microhardness of treated human dentin. *Dent. Mater.* 2004;20: 522–529.
- 8. Nishitani Y, Yoshiyama M, Tay FR, Wadgaonkar B, Waller J, Agee K, Pashley DH. Tensile strength of mineralized/demineralized human normal and carious dentin. *J. Dent. Res.* 2005;84(11): 1075-1078.
- 9. Yahyazadehfar M, Ivanchik J, Majd H, Zhang BAnD, Arola D. On the mechanics of fatigue and fracture in teeth. *Appl. Mech. Rev.* 2014;66(3): 1–19.
- 10. Kruzic J, Nalla RK, Kinney JH, Ritchie RO. Mechanistic aspects of in vitro fatigue-crack growth in dentin. *Biomaterials*. 2005;26(10): 1195–1204.
- 11. Imbeni V, Nalla RK, Bosi C, Kinney JH, Ritchie RO. In vitro fracture toughness of human dentin. *Journal of Biomedical Materials Research Part A.* 2003;66A(1): 1–9.

- 12. Zaytsev D, Panfilov P. On some features of the shape effect in human dentin under compression. *Mater. Sci. Eng. C.* 2014;45: 205–209.
- 13. Zaytsev D, Grigoriev S, Panfilov P. Deformation behavior of human dentin under uniaxial compression. Int. J. Biomater. 2012;2012: 854539.
- 14. Kinney JH, Nalla RK, Pople JA, Breunig TM, Ritchie R. Age-related transparent root dentin: mineral concentration, crystallite size, and mechanical properties. Biomaterials. 2005;26(16): 3363–3376.
- 15. Gudkina ZV, Argunova TS, Gutkin MYu. Nondestructive 3D-evaluation of human dentin by microtomography using synchrotron radiation. J. Phys.: Conf. Ser. 2019;1410: 012066.
- 16. Kinney JH, Marshall SJ, Marshall GW. The mechanical properties of human dentin: a critical review and re-evaluation of the dental literature. Crit. Rev. Oral. Biol. Med. 2003;14(1): 13–29.
- 17. Feldkamp LA, Davis LC, Kress JW. Practical cone-beam algorithm. J. Opt. Soc. Am. A. 1984;1(6): 1–2.
- 18. Buzug, TM. Computed Tomography From Photon Statistics to Modern Cone-Beam CT. Berlin; Springer; 2008.
- 19. *ImageJ wiki software*. Available from: www.imagej.net. (Accessed 14.12.2021)
- 20. Thermo Fisher scientific. Available from: www.thermofisher.com. (Accessed 14.12.2021)
- 21. Volume Graphics. Available from: www.volumegraphics.com. (Accessed 14.12.2021)
- 22. Sumikawa DA, Marshall GW, Gee L, Marshall SJ. Microstructure of primary tooth dentin. Pediatr. Dent. 1999;21(7): 439-444.
- 23. Zavtsev D, Panfilov P. Influences of the sample shape and compression temperature on the deformation behavior and mechanical properties of human dentin. Mater. Sci. Eng. C. 2014;43: 607–613.
- 24. Nalla RK, Kinney JH, Ritchie RO. Effect of orientation on the in vitro fracture toughness of dentin: the role of toughening mechanisms. *Biomaterials*. 2003;24(22): 3955–3968.
- 25. Cheboksartseva MA, Zaytsev D, Ivashov AS, Mandra JV, Zholudev S. On the Possibility of Describing the Microstructure of Human Dentin as Soft Matrix Filled by Solid Particles. J. Phys. Conf. Ser. 2021;1945: 012057.
- 26. Fleck C, Burke M, Ganzosch G, Müller C, Currey JD, Zaslansky P. Breaking crown dentine in whole teeth: 3D observations of prevalent fracture patterns following overload. Bone. 2020;132: 115178.
- 27. Montoya C, Arola D, Ossa EA. Time depend deformation bevavior of dentin. Arch. Oral Biol. 2017;76: 20-29.
- 28. Nanci A. Ten cate's oral histology: Development, structure, and function. 7th ed. St. Louis MO: Mosby; 2008.
- 29. Zaslansky P, Zabler S, Fratzl P. 3D variations in human crown dentin tubule orientation: A phase-contrast microtomography study. Dent. Mater. 2010;26(1): 1–10.
- 30. Lu X, Fernandez PM, Bradley RS, Rawson SD, O'Brien M, Hornberger B, Leibowitz M, Tozzi G, Withers PJ. Anisotropic crack propagation and deformation in dentin observed by four-dimensional X-ray nano-computed tomography. Acta Biomaterialia. 2019;96: 400–411.
- 31. Watanabe LG, Marshall GW, Marshall SJ. Dentin shear strength: Effects of tubule orientation and intratooth location. Dent. Mater. 1996;12(2): 109–115.
- 32. Zaytsev D, Ivashov AS, Panfilov P. Anisotropy of the mechanical properties of human dentin under shear testing. Materials Letters. 2015;138: 219–221.
- 33. Lertchirakarn V, Palamara JEA, Messer HH. Anisotropy of tensile strength of root dentin. J. Dent. Res. 2001;80(2): 453-456.

THE AUTHORS

Zavtsev Dmitry (10) e-mail: dmitry.zaytsev@urfu.ru

e-mail: alexander.funk@bam.de

Alexander Funk (10)

Estimation of breakdown pressure in laboratory experiments on hydraulic fracturing

Submitted: July 18, 2022

Accepted: July 31, 2023

Approved: September 22, 2022

E.V. Novikova 1-3 , M.A. Trimonova 1 1, N.V. Dubinya 1 2,3, S.B. Turuntaev 1, E.V. Zenchenko 1

¹ Sadovsky Institute of Geosphere Dynamics of the Russian Academy of Science, Moscow, Russia ²O.Yu. Schmidt Institute of Physics of the Earth RAS, Moscow, Russia ³ Moscow Institute of Physics and Technology, Dolgoprudny, Russia ⊠ helenvn97@gmail.com

Abstract. Hydraulic fracturing is one of the most common methods used to study stress-strain state of hydrocarbon reservoir being developed. The process of fracture initiation and propagation is affected by initial stress state in the rock and tensile strength of the rock. Moreover, fracturing fluid filtered through the walls of the well into the well surrounding rock mass also affects the process of fracture propagation. The purpose of this work is to determine the best method for assessing the fracture breakdown pressure according to laboratory experiments. The experiments on hydraulic fracturing were carried out on a special laboratory setup that allows to create loading conditions on a model sample that are close to real conditions at a real field being developed. Some of the known methods based on analysis of the dependencies of borehole pressure on time were used for laboratory data processing.

Keywords: hydraulic fracturing; stress-strain state; breakdown pressure; backstress effect; laboratory experiments; data processing

Acknowledgements. The research was carried out within the state assignment of Ministry of Science and Higher Education of the Russian Federation (theme No 122032900167-1).

Citation: Novikova EV, Trimonova MA, Dubinya NV, Turuntaev SB, Zenchenko EV. Estimation of breakdown pressure in laboratory experiments on hydraulic fracturing. *Materials* Physics and Mechanics. 2023;51(5): 52-65. DOI: 10.18149/MPM.5152023_6.

Introduction

Hydraulic fracturing is one of the most common methods used to study the stress-strain state of a hydrocarbon reservoir under development [1,2]. The hydraulic fracturing process involves a fracture initiation in the oil-saturated reservoir under development by pumping pressurized fluid into the reservoir through a specially drilled well. The resulting fracture is of interest to the researcher since it allows to estimate the values of the principal stresses acting in the undeformed formation [3].

Fracture initiation and propagation are influenced by stress distribution in the reservoir under development [4–6]. Therefore, there are various methods to determine the values of the main stresses acting in the formation using the analysis of borehole data. Some of the methods are based on the analysis of the pressure-time dependence function obtained from the well during hydraulic fracturing. For the first time, such an approach was described in the work [7].

In addition to the initial stress-strain state of the medium, it is necessary to know the formation breakdown pressure to carry out hydraulic fracturing properly and for successful oil/gas field development [8]. This pressure can be defined as the pressure needed for tensile fracture initiation at a given depth, more precisely, at the depth of hydraulic fracturing. The paper considers one of the existing methods of theoretical assessment of formation breakdown pressure by analyzing pressure-time curves obtained during hydraulic fracturing. However, the main objective of the study was to evaluate the impact of some effects on the magnitude of formation breakdown pressure.

In particular, the authors of the work have shown that in addition to the existing stress distribution in the formation, so-called reverse stress (backstress) has a significant effect on fracture initiation. This is an additional stress of the fracturing fluid pumped into the formation and filling the porous medium of the near-well zone, which prevents fracture propagation [9–14].

A series of laboratory experiments on hydraulic fracturing was conducted within the framework of the current study. As a result, time-dependent pressure relationships for each experiment were obtained and further processed. Backstress and formation breakdown pressure were theoretically calculated for each of the experiments. The obtained theoretical values of the formation breakdown pressure were compared with the known values from the borehole data of the laboratory experiments.

Theoretical part

The study is generally aimed at understanding mechanical processes in a small zone near the wellbore, where hydraulic fracture initiation occurs. The well and fracture initiated after fluid injection as well as its propagation in the well surrounding rock masses are the main objects of the research. There are several approaches for estimating the hydraulic formation breakdown pressure [8,14,15].

The distribution of horizontal stresses in well surrounding rock masses was obtained from the modification of the classical Kirsch problem solution for stress concentration around a circular hole [16]. This distribution was consequently used to evaluate formation breakdown pressure for a formation. Fracture initiation occurs whenever minimum principal stress becomes tensile and its modulus exceeds the unconfined tensile strength (UTS) of the rock mass.

The problem of determining the formation breakdown pressure was solved under different boundary conditions. Therefore, it is possible to formulate four cases with different conditions.

Case 1. In the first case, the fracture occurs in a homogeneous nonporous medium, which is considered impermeable to the fracturing fluid. In this case, $\sigma_H = S_H$, $\sigma_h = S_h$ is true for effective stresses, since there is no pore pressure distribution in the formation. Compressive stresses are considered as positive hereafter, $S_H \ge S_h$.

The formula for estimating the formation breakdown pressure has the form:

$$P_w^* = 3S_h - S_H + UTS, \tag{1}$$

with fracturing fluid pressure P_w^* , in-situ horizontal stresses S_h and S_H , acting far from the well. P_w^* corresponds to pressure at well resulting into fracture initiation or formation breakdown pressure (FBP).

Case 2. In the second case, the fracture occurs in a homogeneous porous medium, which is considered impermeable to the fracturing fluid. Since the pore pressure distribution is now present in the medium, the Terzaghi representation [15] was used for effective stresses: $\sigma_H = S_H - P_0$, $\sigma_h = S_h - P_0$, $S_H \ge S_h$.

Then the formula for estimating the formation breakdown pressure has the form:

$$P_{w}^{*} = 3S_{h} - S_{H} - P_{0} + UTS,$$
 with pore pressure P_{0} . (2)

Case 3. In the third case, the fracture occurs in a homogeneous porous medium, which is considered permeable to the fracturing fluid. In this case, in addition to the distribution of pore pressure in the environment, it is necessary to take into account the process of filtration of the fracturing fluid from the well into the formation $\alpha \frac{1-2\nu}{1-\nu} (P_W - P_0)$, with Biot's coefficient α [18] and Poisson 's ratio ν . Moreover, it is necessary to take into account the condition of the presaturation of the medium. The Terzaghi representation [17] was also used for effective stresses: $\sigma_H = S_H - P_0$, $\sigma_h = S_h - P_0$, $S_H \ge S_h$.

Then, the formula for estimating formation breakdown pressure takes the form:

$$P_{w}^{*} = \frac{3S_{h} - S_{H} + UTS - \alpha \frac{1 - 2\nu}{1 - \nu} P_{0}}{2 - \alpha \frac{1 - 2\nu}{1 - \nu}}.$$
(3)

Case 4. However, when using the Terzaghi representation, it is assumed that a fracture forms instantly as soon as the annular effective stress of the Terzaghi directly on the wall of the borehole exceeds the uniaxial tensile strength UTS. However, in this case, the influence of changing pore pressure on the well wall is not considered. Therefore, it was proposed by Schmidt [19] to rewrite the equations for effective stresses in the form: $\sigma_H = S_H - \beta P_0$, $\sigma_h = S_h - \beta P_0$, $S_H \ge S_h$, where β – pore pressure coefficient ($0 \le \beta \le 1$). In this case, it is also assumed that the fracture occurred in a homogeneous porous medium, which is considered permeable to the fracturing fluid. Here, as in the previous case, the process of filtration of the fracturing fluid from the well into the formation $\alpha \frac{1-2\nu}{1-\nu}(P_W - P_0)$ and the condition of pre-saturation of the medium are taken into account.

The formula for estimating the formation breakdown pressure has the form:

$$P_W^* = \frac{3S_h - S_H + UTS - \alpha \frac{1 - 2\nu}{1 - \nu} P_0}{1 + \beta - \alpha \frac{1 - 2\nu}{1 - \nu}}.$$
(4)

Experimental part

Laboratory experiment on hydraulic fracturing. A series of laboratory experiments were conducted to simulate the process of fracture formation in the area of the well in which the fluid is injected. A state-of-art setup was used (Fig. 1), which makes it possible to simulate the process of hydraulic fracturing. The design consists of two steel discs and a wide ring-wall between them. The lower disk and the ring-wall together form a working chamber, which has the following characteristic dimensions: diameter – 43 cm, height - 6.6 cm. The model sample of the formation is separated from the upper disk of the setup by a rubber membrane. There is a gap between the top lid of the setup and the membrane, which is filled with water under constant pressure to simulate lithostatic pressure in the reservoir model. Horizontal loading on the model sample is carried out by pumping gas or fluid into flat copper chambers located along the inner surfaces of the side walls of the working chamber. A more detailed description is provided in the work [20]. In this study, the setup is considered as a layered medium, i.e. a permeable layer, in which the fracture propagation occurs, surrounded by impermeable walls of the setup.

The laboratory experiment on hydraulic fracturing itself is carried out in several stages. Initially, a mixture of gypsum and cement is poured into the working chamber of the setup. After drying of the modeling material, a model sample is formed. The dimensions of the working chamber of the experimental setup determine the dimensions of the model sample. The resulting porous sample is then saturated with a solution of gypsum in water. After that, the setup is closed, loading of the model sample is done and the fracturing fluid, more precisely mineral oil, is injected into the preliminary prepared well at a constant flow rate. It is important to note that the horizontal stresses used in further calculations are the calculated horizontal

stresses acting in the central region of the sample. They take into account both the applied horizontal loads and the friction between the sample and the metal covers.

The central well is a brass tube (diameter 16 mm), which is hermetically inserted into the lower cover of the setup. The upper end of the tube is closed with a screw plug. The tube has a vertical slot in the middle part, into which a thin brass gauze folded in half is inserted. The brass gauze serves as a seed for the fracture. The size of the gauze petals is 8×8 mm. The corners of the petals are cut off by about 2 mm. The tube has the ability to rotate freely around the vertical axis so that it is possible to orient the fracture perforation in a given direction.

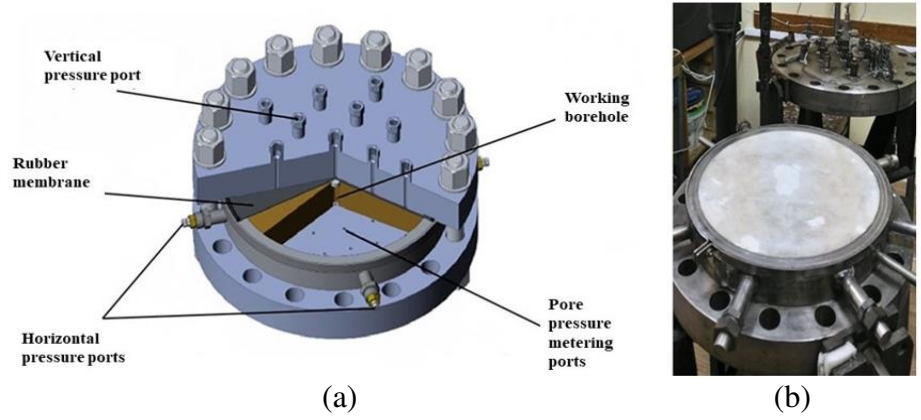


Fig. 1. A schematic illustration of the experimental setup (a), and an actual photo of the setup (b)

A series of laboratory experiments on hydraulic fracturing was carried out in the course of the study. As a result, two types of hydraulic fractures can be formed: vertical fractures (along the vertical well) and horizontal fractures (perpendicular to the well). In this series, experiments with vertical fractures were considered. An example of the obtained pressure-time curves for this type of fracture is presented below (Fig. 2).

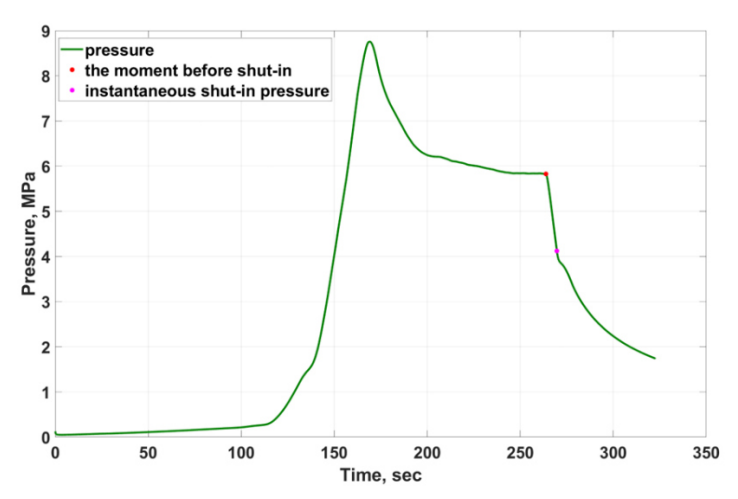


Fig. 2. An example of the dependence of pressure on time obtained in a laboratory experiment on the creation of a vertical fracture of a hydraulic fracturing

It is also important to note that prior to conducting laboratory experiments on hydraulic fracturing, the modelling materials were additionally studied. The modelling materials and fluids were selected in such a way that the propagation of a hydraulic fracture in a laboratory experiment was similar to its propagation in a real field. Similarity criteria were used to achieve the similarity of processes in laboratory and real models [20,21].

A mixture of gypsum and cement was found to be a suitable material for modelling the formation and mineral oil as the fracturing fluid. The numerical values of the material characteristics are presented in the table below (Table 1).

Table 1. Some properties of the modelling material and fluid used in the laboratory experiments

Fracturing fluid viscosity μ , Pa·s	0.12
Injection rate q , cm ³ /s	0.17 - 0.37
Young modulus E, Pa	4×10 ⁹
Poisson's coefficient v	0.25
Model sample permeability k , m^2	2×10 ⁻¹⁵
Model sample porosity φ	0.4

Determination of uniaxial tensile strength. One of the characteristics of the material used, which has been given special attention in this work, is the single-axis tensile strength. This parameter plays a major role in the framework of the conducted studies since the criterion for fracture formation was considered to be the moment when the local tensile stress in the stress concentrations area exceeds the ultimate tensile strength of the material in magnitude.

Therefore, an additional series of laboratory tests was initially carried out to determine the uniaxial tensile strength by applying the "Brazilian" method [22,23].

Samples from a model material with a diameter of 40 mm and a length of 42 mm were used in this series of experiments. The sample was placed between parallel steel plates during the manual press test. The tensile strength for such a series of experiments was calculated by the formula $\sigma_p = K \frac{P}{S}$, where $K=2/\pi$ when loaded with plates, P is the breaking force, S is the product of the length of the sample by its diameter. The results of the tests by the "Brazilian" method are shown in Table 2.

Table 2. The results of the tests by the "Brazilian" method

Sample number	Sample diameter d , mm	Sample height <i>h</i> , mm	Breaking force <i>P</i> , kN	Tensile strength UTS, MPa
1	40	42.2	1.7	0.6
2	40	42.2	2.6	1.0
3	40	42.2	2.0	0.8
4	40	42.2	2.1	0.8
5	40	42.2	1.8	0.7
6	40	42.2	2.3	0.9

Based on the calculations obtained, the value of the tensile strength can be considered equal to 0.8 MPa.

According to some sources [24,25], the tensile strength can be determined by knowing the re-opening pressure of the hydraulic fracture. Another series of laboratory experiments was carried out to clarify the obtained tensile strength. In this case, all experiments were carried out in two stages. The first stage was a standard laboratory experiment on hydraulic fracturing, which is described above. The second stage involved re-conducting hydraulic fracturing to expand the existing fracture.

However, after processing the pressure drop curves, it was detected that the uniaxial tensile strength of the material varies in the framework of laboratory experiments. According to the sources [24–26], it is no longer necessary to overcome the tensile strength of the medium in the course of repeated fracturing, because the fracture already exists. Therefore, repeated fracturing is considered to be another applicable method for determining the tensile strength by subtracting the breakdown pressure of the reopened fracture from the breakdown pressure of

the primary fracture. Two such two-stage experiments were conducted. The loading parameters of the samples and the results of the tensile strength calculations are shown in Table 3.

Table 3. Results of defining the tensile strength using two-stage laboratory experiments on hydraulic fracturing

_ 3						
Expansion of a vertical	stage 1	experimental formation breakdown pressure	8.80	MPa		
fracture	stage 2	age 2 experimental formation reopening pressure				
		Tensile strength	2.40	MPa		
Expansion of a vertical	stage 1	experimental formation breakdown pressure	7.69	MPa		
fracture	stage 2	experimental formation reopening pressure	5.96	MPa		
		Tensile strength	1.73	MPa		

The corrected tensile strength value is 2.07 MPa. The corrected tensile strength value is used in further calculations for the formation breakdown pressure because it is considered more correct under the conditions of hydraulic fracturing.

Results

Experimental data processing. In the course of this study, a series of six standard one-stage laboratory experiments on the formation of a vertical hydraulic fracture was carried out. The formation breakdown pressure was estimated for all four cases described, taking into account the characteristic parameters of the experiments (Tables 1, 2). The values of the formation breakdown pressure were obtained after analyzing the curves of pressure versus time, which were recorded using sensors during laboratory experiments on hydraulic fracturing. The pattern of the obtained experimental pressure-time curves corresponds to the classical characteristic pattern of hydraulic fracturing pressure curves, which was described in [27].

These curves have a characteristic pattern. Provided that the fluid is pumped at a constant rate, there is a linear increase in pressure over time in the beginning, which is violated at the first appearance of leaks, which is sometimes considered the moment of fracture initiation. The point of maximum pressure on the graph corresponds to the moment of fracture formation. Thereafter, there is a pressure drop to a value called fracture propagation pressure. Further, there is a rapid pressure drop after stopping fluid injection into the well to the fracture closure pressure. Thus, experimental formation breakdown pressures were determined from these pressure curves. The results are shown in Table 4: each experiment was carried out with its own vertical and horizontal loads forming far-field stresses S_h and S_H (equal to each other) and vertical stress S_V stated in the table.

Table 4. A comparison table of the values of the hydraulic formation breakdown pressure obtained experimentally and calculated theoretically

000000000000000000000000000000000000000		••••••••••••••••••••••••••••••••••••••		
Experiment	Q,	Horizontal stress	Vertical stress	FBP, MPa
number	cm ³ /s	$(S_h = S_H)$, MPa	S_V , MPa	(experimental)
1	0.17	2.01	6.6	8.76
2	0.37	2.01	7.1	12.55
3	0.20	1.32	4.8	7.07
4	0.20	1.12	4.6	10.96
5	0.20	1.29	4.7	7.74
6	0.20	1.50	5.1	13.46

The formation breakdown pressure was estimated under different assumptions (four cases), taking into account the characteristic parameters of each of the experiments (Table 4). All formulas (1) - (4) given in the theory are valid in the case of initiation of a vertical fracture in an infinite homogeneous formation. Ideally, it is assumed that the fracture formation process occurs on a vertical well with an open borehole.

The experiments presented in this paper differ from the ideal theory in the finite size of the sample along the radius, the restriction of the sample from above and below by metal plates, and the fact that the well is cased. However, the cased well does not contradict ideal conditions, because perforations are made in it in the direction of fracture development, which seamlessly connects the well with the sample. It is important to note that the horizontal stresses given in the work represent the calculated horizontal stresses acting in the central region of the sample. They take into account both the applied horizontal loads and the friction between the sample and the metal covers. Therefore, the use of formulas (1) - (4) in the processing of experimental data can be considered sufficiently conditioned and correct.

The results of theoretical estimates of formation breakdown pressure are presented in Table 5. Theoretical estimates of formation breakdown pressure were made for each experiment.

Table 5. Experimental values of formation breakdown pressure and theoretical estimates were made for different boundary conditions and taking into account different values of uniaxial tensile strength

		Theoretical FBP, MPa							
E	Experimental <i>FBP</i> ,	UTS = 0.8 MPa			UTS = 2.07 MPa				
Experiment number			Case						
MI	MPa	1	2	3	4	1	2	3	4
		1	4	3	$(\beta = 0)$	1	2	3	$(\beta = 0)$
1	8.76	4.82	4.27	2.98	8.56	6.09	5.54	3.80	10.94
2	12.55	4.82	3.77	2.82	8.12	6.09	5.04	3.65	10.50
3	7.07	3.44	2.82	2.05	5.90	4.71	4.09	2.88	8.28
4	10.96	3.04	2.24	1.74	5.00	4.31	3.51	2.57	7.38
5	7.74	1.29	2.58	1.96	5.64	4.65	3.85	2.79	8.02
6	13.46	1.50	3.20	2.30	6.60	5.07	4.47	3.12	8.98

As can be seen from the data obtained (Fig. 3), the best results are obtained by the approach to calculating the formation breakdown pressure (with modified expressions for effective stresses) proposed by Schmidt. It is also obvious that the use of the adjusted uniaxial tensile strength contributes to a significant reduction in the difference between the theoretically calculated values of the formation breakdown pressure and the experimental ones.

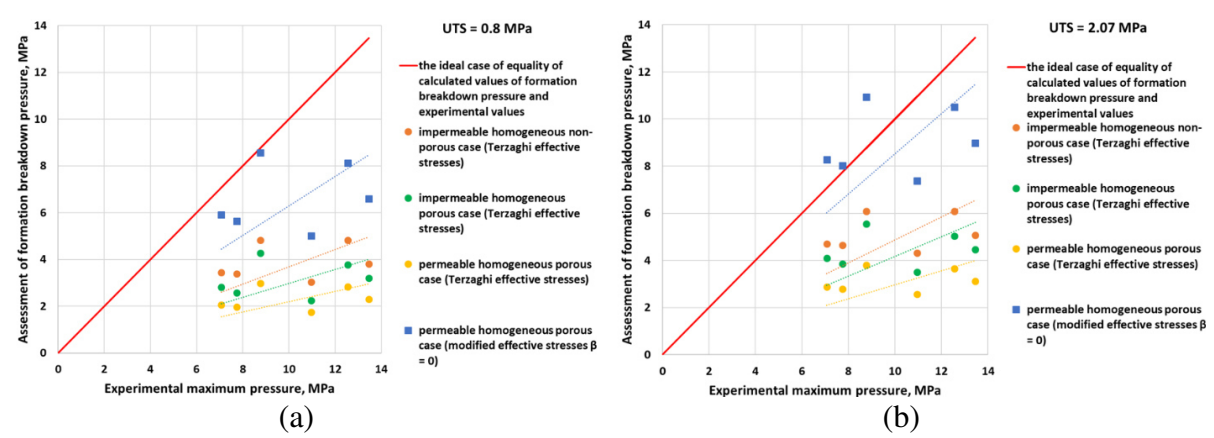


Fig. 3. Comparison of the results of calculations of the formation breakdown pressure under different boundary conditions and different values of uniaxial tensile strength *UTS*:

(a) UTS = 0.8 MPa; (b) UTS = 2.07 MPa

Analysis of calculated values of formation breakdown pressure. The obtained experimental values of the formation breakdown pressure allow us to evaluate the influence of various parameters on the theoretical assessment of the formation breakdown pressure. In some cases, the following normalized:

$$FBP_n = \frac{FBP_{\text{theor}}}{FBP_{\text{exp}}},\tag{5}$$

theoretically evaluated formation breakdown pressure FBP_{theor} is normalized by the 'true' corresponding experimental measurement FBP_{exp} . This particular indicator was chosen due to both parameters being positive in all experiments and a general tendency of FBP_{exp} exceeding FBP_{theor} . It is clear from formula (5) that the best match between theoretical and experimental formation breakdown pressures is achieved if $FBP_n = 1$.

Various factors affecting FBP evaluation can be analyzed using the reported experimental results, especially the mechanical properties of the studied medium. The state of the medium is characterized by stresses S_h and S_H , as well as by pore pressure P_0 , in particular, the pore pressure coefficient β ; other notable properties of the medium are uniaxial tensile strength UTS and parameters – Biot's coefficient α , Poisson's ratio ν .

Let's consider the influence of the parameter β on the formation breakdown pressure. Equation (4) assumes that an increase in this parameter leads to a corresponding nonlinear decrease in the formation breakdown pressure: at the maximum possible value $\beta = 1$ equation (4) becomes the same as equation (3), and we expect that the estimate obtained for such a case will be the same as from equation (1), where the process of radial filtration of fluid from the well into the medium and the pressure drop in the medium are not considered. Figure 4 confirms these expectations as it presents different *FBP* estimates, where all parameters, except for β , remain constant.

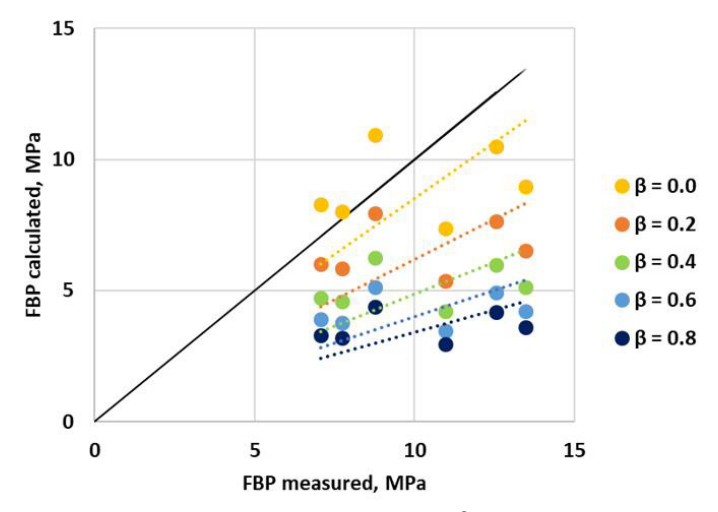


Fig. 4. Calculated FBP vs. measured FBP for a set of β parametrs – other properties and state of the medium remain unchanged. Theoretical estimations were in the conditions of the case 4

Parameter β was claimed to depend on rock porosity – it was suggested as close to unity for highly porous rocks and vanish for rocks with vanishing porosity. To our understanding, this parameter can be altered due to the redistribution of fluid in the well surrounding rock masses: filtration of hydraulic fracturing fluid into the environment surrounding the well reduces the effective porosity and permeability after replacing the reservoir fluid with a fracturing fluid with a relatively lower viscosity. A circular layer around the well can be formed around the well during the leak-off preceding fracture initiation. This layer can be quite thin – an analysis of its size and evolution during fluid filtration deserves a distinct study – but since tensile failure occurs near the wellbore, whenever this layer has a non-zero size, the effective

stresses determined by the parameter β have to be used in the tensile failure law. This leads to an increase in effective stresses and a corresponding increase in the pressure in the well required to initiate tensile failure.

Figure 5 demonstrates the dependency of the formation breakdown pressure on Biot's coefficient. Figure 5 shows calculated *FBP* (not normalized) is plotted versus measured value. Equation (4) is used for the measurement of the *FBP* values for a set of Biot's coefficients between 0.0 and 1.0 (the natural range of Biot's coefficients for saturated media). Poisson's ratio remains unchanged – it stays equal to 0.25. It can be seen that an increase in Biot's coefficient leads to the growth of the slope of the calculated vs measured *FBP* curve. As it only exceeds 1 for the greatest Biot's coefficient, a certain preliminary conclusion can be drawn: the effect of the process of radial fluid filtration from the well into the medium grows for high Biot's coefficients. Keeping in mind that Biot's coefficient remains in a positive correlation with the permeability of rocks [26] one can conclude that error in *FBP* evaluation due to this effect is larger for highly permeable rocks. This conclusion, however, is not as clear as it could seem.

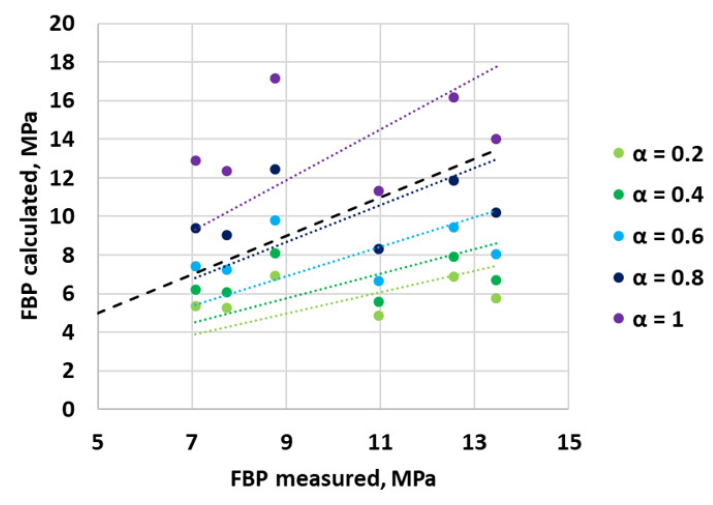


Fig. 5. Calculated *FBP* vs. measured *FBP* for a set of Biot's coefficients – other properties and state of the medium remain unchanged. Theoretical estimations were in the conditions of the case 4

Figure 6 represents normalized formation breakdown pressure *FBPn* as a function of measured *FBP* as well. The usage of *FBPn* instead of *FBP* makes it possible to see the rate at which Poisson's ratio alteration affects the discrepancy between measured and true values. Biot's coefficient remains equal to 0.7 in this case.

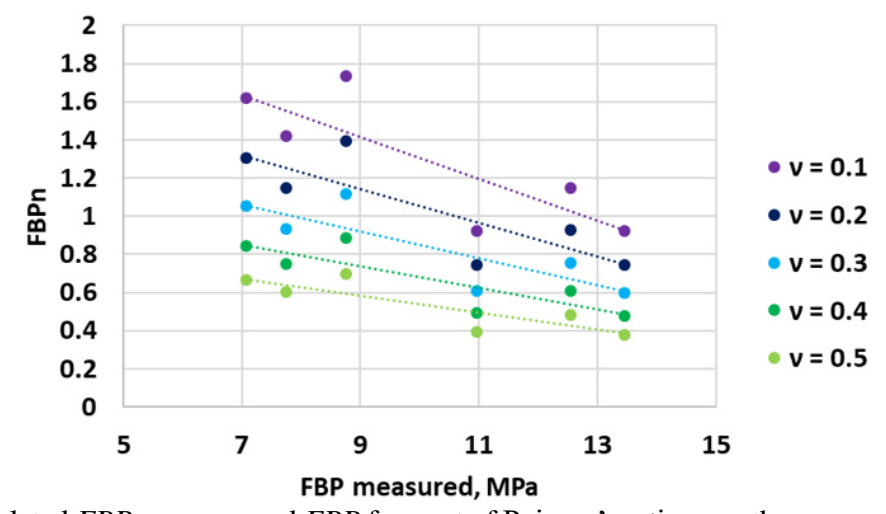


Fig. 6. Calculated *FBP* vs. measured *FBP* for a set of Poisson's rations – other properties and state of the medium remain unchanged. Theoretical estimations were in the conditions of the case 4

An increase in Posson's ratio leads to a decrease in the average *FBPn* as well as alters the slope of the *FBPn* vs. *FBP* measured curve. Under ideal conditions, *FBPn* would not depend on measured *FBP* and stayed at a constant value of 1. Interestingly enough, while larger Poisson's ratios lead to larger discrepancies between measured and calculated values, the slope decreases, so the dependency on measured *FBP* weakens.

Figures 5 and 6 only deal with one parameter affecting the petroelastic coefficient each. These findings can be summed up in a form of Fig. 8 presenting the series of curves where averaged FBPns – or, in other words, average slopes of calculated FBP vs. measured FBP dependencies – are plotted as functions of Biot's coefficient and Poisson's ratio. Biot's coefficient is on the horizontal axis, while Poisson's ratio remains constant along each line of the corresponding color according to the legend. Both mechanical properties are taken from naturally possible ranges: Biot's coefficient α remains between 0.0 and 1.0; Poisson's ratio v is between 0.0 and 0.5.

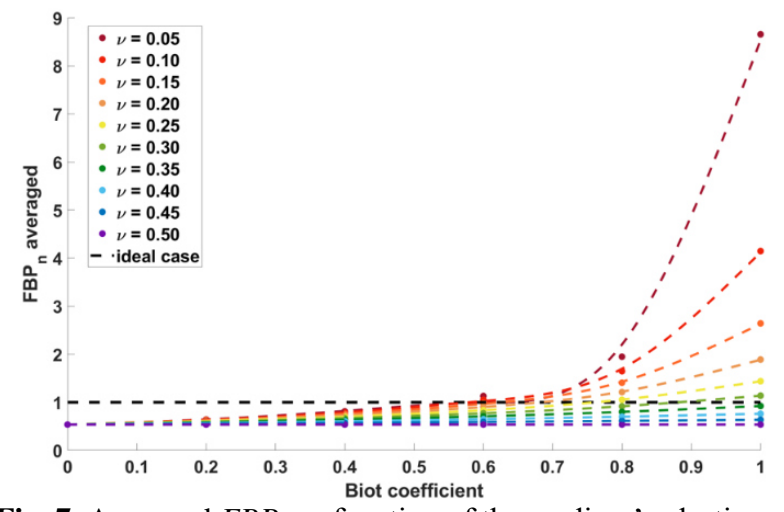


Fig. 7. Averaged FBP_n as function of the medium's elastic properties

The analysis of the influence of the mechanical properties of the medium on the discrepancy between the experimentally measured and theoretically calculated values of the formation breakdown pressure is presented. To sum up, both the state of the environment and its properties have a certain impact on the *FBP* assessment: generally, the higher the permeability and compressive stresses are, the lower discrepancy between the measured and calculated formation breakdown pressure. The Bio coefficient and Poisson's ratio affect the calculated *FBP* in a non-linear way: the calculated *FBP* increases with larger Bio coefficients and smaller Poisson's coefficients (Fig. 7).

Discussion

In the discussion, we propose to consider such an effect as backstress and its possible impact on the theoretical assessment of formation breakdown pressure. The backstress effect has previously been investigated in the context of hydraulic fracture closure pressure [13]. Recent works in which the backstress effect is discussed in the most complete and detailed manner belong to the authorship of Baykin and Golovin [9–12]. When considering the fracture closure pressure, backstress was introduced as additional stress caused by the fracturing fluid filtered out of the fracture.

We propose to consider this effect concerning the process of fracture formation. The material of the near-well area is strengthened when fracturing fluid saturates the pores. This process can be mathematically described by creating additional pressure of the fluid on the

walls of the well, which in turn leads to an increase in the hydraulic formation breakdown pressure (Fig. 8).

In the context of the task under consideration, namely, the hydraulic fracture initiation and propagation in well surrounding rock masses with fracturing fluid injection at a constant rate, the authors of these papers propose to calculate backstress in well surrounding rock masses using the following equation:

$$\sigma_b = 2\eta (FBP - P_0), \quad \eta = \frac{\alpha(1-2\nu)}{2(1-\nu)},$$
(6)

where η is a poroelastic coefficient, α is Biot's coefficient, and v is Poisson's ratio. This coefficient deserves extra attention. There are reported studies [9–12,14,19], for backstress being given by equation (6). This equation is proposed for the case of one permeable layer representing a hydrocarbon reservoir being between two impermeable layers preventing fracturing fluid from filtrating into upper and lower layers [13]. In this paper, the application of such an assumption to calculations is considered correct, since the laboratory experimental setup can be represented as a layered medium, where the model material acts as a permeable layer and the steel upper and lower covers act as impermeable layers of the medium surrounding the permeable one.

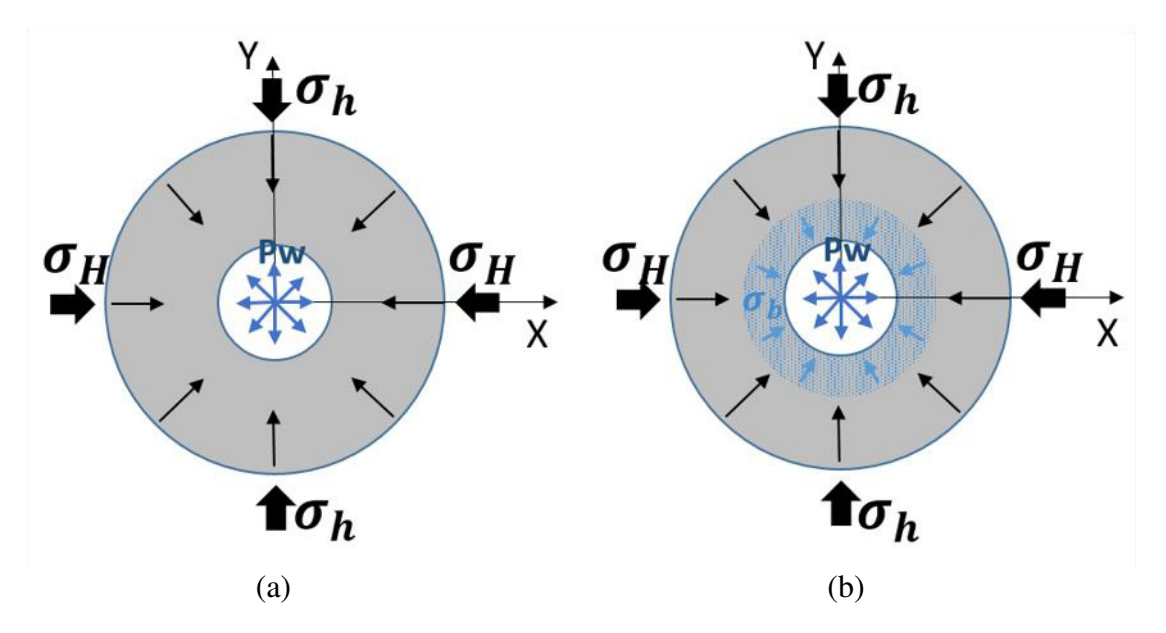


Fig. 8. Schematic representation of the stress distribution in the reservoir with the well into which the fluid is injected

The increase in formation breakdown pressure is since fracture formation criterion alters due to hydraulic fracture initiation in a medium. Thus, taking into account the additional compressive stress acting externally on the borehole walls, which will be referred to as backstress σ_b , it is possible to rewrite the expression for the formation breakdown pressure FBP as follows:

$$FBP = 3S_h - S_H + UTS + \sigma_b. (7)$$

It is interesting to note that after substituting (6) into equation (7), the expression for the formation breakdown pressure will have the form:

$$FBP = \frac{3S_h - S_H + UTS - \alpha \frac{1 - 2V}{1 - V} P_0}{1 - \alpha \frac{1 - 2V}{1 - V}}.$$
(8)

The form of equation (8) coincides with equation (4), provided that $\beta = 0$. Thus, the backstress effect can replace the total impact of the process of filtration of the fracturing fluid

from the well into the formation $\alpha \frac{1-2\nu}{1-\nu}(P_w-P_0)$ and the condition of saturation of the medium. Figure 9 shows a comparison of the results of the formation breakdown pressure estimation calculated by formulas (4) and (8).

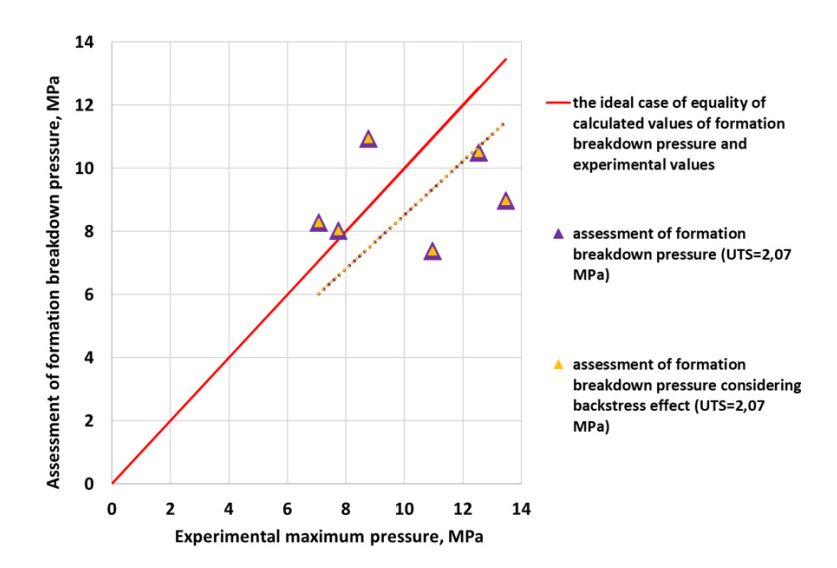


Fig. 9. Comparison of experimental and theoretical values of formation breakdown pressure during hydraulic fracturing

Conclusion

The current study deals with laboratory modeling of hydraulic fracture initiation and propagation. While there are evident problems with rescaling laboratory data to field scale, there is still a positive side: properties of the studied material and its state are known for sure if the controlled experiment is carried out in a laboratory. This provides an opportunity to study interrelationships between various parameters controlling fracture initiation and growth. The current study was aimed at understanding formation breakdown pressure – a parameter essential for hydraulic fracturing procedures.

The data from six laboratory experiments on hydraulic fracturing were analyzed in the work. In the course of all experiments, pressure dependences on time in the well during hydraulic fracturing were obtained, according to which experimental values of formation breakdown pressures were determined. These values were compared with theoretically calculated values according to four theories. According to the first theory, the formation breakdown pressure was calculated without taking into account fluid filtration. The second theory, when calculating the formation pressure, took into account the saturation condition of the medium impervious to the fracturing fluid from the well. According to the third theory, both the saturation of the medium and the filtration of fluid from the well were taken into account. The fourth theory is some improvement of the third one, which takes into account the gradual penetration of the fracturing fluid into the medium through the pore pressure coefficient (beta). The best agreement with the experimental data was shown by the latest theory at $\beta = 0$. In general, β tends to zero with the vanishing porosity of the medium. On the one hand, the porosity of the material is quite large (about 40 %), but when filling the impacted zone with the fracturing fluid, the porosity, in fact, becomes disappearing for the fluid saturating the sample. Consequently, the use of the pore pressure coefficient β , tending to 0, becomes a fairly reasonable step. In addition, an interesting fact was demonstrated in the discussion. There was a proposal to investigate the backstress effect at the moment of fracture formation. Previously, backstress was only used in the context of the connection of minimum stress and fracture

closure pressure. It was proposed to replace the condition of saturation of the medium and the condition of penetration of the fracturing fluid from the well with backstress, considering it in the equation for the formation breakdown pressure for the simplest case (unsaturated and impermeable medium). It turned out that in this case, the equation for the formation breakdown pressure completely coincided with the equation that takes into account both the saturation of the medium and the filtration of the fracturing fluid at $\beta = 0$. Thus, the authors summarize that under experimental conditions, the best coincidence of the calculated formation breakdown pressures with the experimental values was shown by the backstress theory.

References

- 1. Ljunggren C, Chang Y, Janson T, Christiansson R. An overview of rock stress measurement methods. *International Journal of Rock Mechanics and Mining Sciences*. 2003;40(7-8): 975–989.
- 2. Zoback MD. Reservoir Geomechanics. NY: Cambridge University Press; 2010.
- 3. Zoback MD, Mastin L, Barton C. In-situ Stress Measurements In Deep Boreholes Using Hydraulic Fracturing, Wellbore Breakouts, And Stonely Wave Polarization. In: *Proc. of ISRM International Symposium, Stockholm, Sweden, August 1986.* 1986.
- 4. Afanasyev IS, Nikitin AN, Latypov ID, Haidar AM, Borisov GA. Hydrofracturing crack geometry prediction. *Oil Industry Journal*. 2009; 62–66. (In-Russian)
- 5. Berchenko IE, Detournay E. Deviation of hydraulic fractures through poroelastic stress changes induced by fluid injection and pumping. *International Journal of Rock Mechanics and Mining Sciences*. 1997;34(6): 1009–1019.
- 6. Hagoort J, Weatherill B, Settari A. Modeling the Propagation of Waterflood-Induced Hydraulic Fractures. *Society of Petroleum Engineers Journal*. 1980;20(04): 293–303.
- 7. Hubbert M, Willis DG. Mechanics of Hydraulic Fracturing. Transactions. 1957;210(01): 153–168.
- 8. Zhang J, Yin S. Fracture gradient prediction: an overview and an improved method. Pet Sci. 2017;14: 720–730.
- 9. Golovin SV, Baykin AN. Influence of pore pressure on the development of a hydraulic fracture in poroelastic medium. *International Journal of Rock Mechanics and Mining Sciences*. 2018;108: 198–208. 10. Baykin AN, Golovin SV. Non-symmetry of a hydraulic fracture due to the inhomogeneity
- 10. Baykin AN, Golovin SV. Non-symmetry of a hydraulic fracture due to the inhomogeneity of the reservoir. ArXiv [Preprint] 2016. Available from: doi.org/10.48550/arXiv.1610.09471.
- 11. Baykin AN, Golovin SV. Application of the fully coupled planar 3D poroelastic hydraulic fracturing model to the analysis of the permeability contrast impact on fracture propagation. *Rock Mech Rock Eng.* 2018;51: 3205–3217.
- 12. Baykin AN, Golovin SV. Modelling of hydraulic fracture propagation in inhomogeneous poroelastic medium. *J. Phys. Conf. Ser.* 2016; 722: 012003.
- 13. Cleary MP. Analysis of mechanisms and procedures for producing favourable shapes of hydraulic fractures. In: *SPE Annual Technical Conference and Exhibition, Dallas, Texas, September 1980.* 1980. p. SPE-9260-MS.
- 14. Detournay E, Cheng A-D, Roegiers J-C, McLennan JD. Poroelasticity considerations in in situ stress determination by hydraulic fracturing. *International Journal of Rock Mechanics and Mining Sciences & Geomechanics Abstracts*. 1989;26(6): 507-513.
- 15. Haimson BC, Fairhurst C. In-Situ Stress Determination At Great Depth By Means Of Hydraulic Fracturing. In: *The 11th U.S. Symposium on Rock Mechanics (USRMS), Berkeley, California, June 1969.* 1969. p. ARMA-69-0559.
- 16. Kirsh E.G. Die Theorie der Elastizitat und die Bedurfnisse der Festigkeitslehre. *Zantralblatt Verlin Deutscher Ingenieure*. 1898;42: 797–807.
- 17. Paterson MS. Experimental Rock Deformation: The Brittle Field. Springer;2005.
- 18. Biot MA. Mechanics of deformation and acoustic propagation in porous media. *J. Appl. Phys.* 1962;33: 1482–1498.
- 19. Schmitt DR, Zoback MD. Poroelastic effects in the determination of the maximum horizontal principal stress in hydraulic fracturing tests—A proposed breakdown equation

employing a modified effective stress relation for tensile failure. *International Journal of Rock Mechanics and Mining Sciences & Geomechanics Abstracts*. 1989;26(6): 499–506.

- 20. Trimonova M, Baryshnikov N, Zenchenko E, Zenchenko P, Turuntaev S. The Study of the Unstable Fracure Propagation in the Injection Well: Numerical and Laboratory Modeling. *SPE Russian Petroleum Technology Conference. Moscow, Russia, October 2017.* p.SPE-187822-MS.
- 21. de Pater CJ, Cleary MP, Quinn TS, Barr DT, Johnson DE, Weijers L. Experimental verification of dimensional analysis for hydraulic fracturing. *SPE Production & Facilities*. 1994;9: 230–238.
- 22. Bell FG. ENGINEERING GEOLOGY. Rock Properties and Their Assessment. In: Selley RC, Cocks LRM, Plimer IR. (Eds.) *Encyclopedia of Geology*. Oxford: Elsevier; 2005. p.566-580.
- 23. Iofis MA, Kasparian EV, Turchaninov IA. *Fundamentals of Rock Mechanics*. Leningrad: Nedra; 1989. (In-Russian)
- 24. Rutqvist J, Tsang CF, Stephansson O. Uncertainty in the maximum principal stress estimated from hydraulic fracturing measurements due to the presence of the induced fracture. *International Journal of Rock Mechanics and Mining Sciences*. 2000;37(1-2): 107–120.
- 25. Zhang J, Roegiers JC. Discussion on "Integrating borehole-breakout dimensions, strength criteria, and leak-off test results, to constrain the state of stress across the Chelungpu Fault, Taiwan". *Tectonophysics*. 2010;492(1-4): 295–298.
- 26. Bredehoeft JD, Wolff RG, Keys WS, Shuter E. Hydraulic fracturing to determine the regional in situ stress field, Piceance Basin, Colorado. *Geol Soc Am Bull*. 1976;87(2): 250–258. 27. Gaarenstroom L, Tromp RAJ, Jong M de, Brandenburg AM. *Overpressures in the Central North Sea: implications for trap integrity and drilling safety*. 1993.

THE AUTHORS

Novikova E.V.

e-mail: helenvn97@gmail.com

Dubinya N.V. 👵

e-mail: Dubinya.NV@gmail.com

Zenchenko E.V.

e-mail: zenchevi@gmail.com

Trimonova M.A. 🗓

e-mail: trimonova.ma@gmail.com

Turuntaev S.B. @

e-mail: s.turuntaev@me.com

Prediction of mechanical properties of elastomeric materials using neural networks

Submitted: January 27, 2023

Approved: May 23, 2023

Accepted: July 11, 2023

S.V. Fomin [□] , V.S. Rostovtsev [□] , V.U. Meltsov [□] , E.S. Shirokova [□]

Vyatka State University, Kirov, Russia

☐ rubber@vyatsu.ru

Abstract. The article is devoted to the use of neural networks for predicting the mechanical properties of rubber. Rubbers include, as a rule, more than one and a half dozen components. Each of the components has a complex and ambiguous effect on the complex of material properties. When developing new compositions, this significantly complicates and lengthens the solution of material science problems by traditional methods of composition selection. These problems can be effectively solved using machine learning techniques. The authors have developed approaches to the use of neural networks for predicting the mechanical properties of rubber from a known composition. In this article, neural network models have been created and optimized, which make it possible to predict the mechanical properties of elastomeric materials with high accuracy.

Keywords: elastomers; rubbers; physical and mechanical properties; convolutional neural network; hyperparameter optimization; neural network technologies; python language; keras library

Citation: Fomin SV, Rostovtsev VS, Meltsov VU, Shirokova ES. Prediction of mechanical properties of elastomeric materials using neural networks. *Materials Physics and Mechanics*. 2023;51(5): 66-78. DOI: 10.18149/MPM.5152023_7.

Introduction

Due to a unique set of properties – a combination of good physical and mechanical characteristics, elasticity, energy absorption ability, minimal compressibility, etc. – elastomers as structural materials are used in a large number of applications, such as seals, elements for absorbing vibrations and shocks, load-bearing structures [1,2]. The most common elastomers are rubbers, which are materials based on rubbers that acquire their operational properties as a result of the technological vulcanization of so-called raw rubber mixtures. Raw rubber compounds, in turn, are a mixture of many components. During vulcanization, individual polymer rubber molecules are "stitched" into a three-dimensional structure due to cross-links formed, most often, due to interacting with special components – vulcanizing agents. The composition of rubber compounds is very diverse and usually includes the following groups of ingredients [1,2]:

- rubber, it is an amorphous or partially crystallizing polymer, which is the basis of rubber and determines its basic set of properties;
- vulcanizing group, that is a group of components introduced into the rubber mixture to form cross-links between rubber molecules during vulcanization;
- fillers, which are a group of components introduced into the rubber mixture mainly to improve mechanical properties (reinforcing fillers), or reduce the cost (inert fillers);

- plasticizers, which are a group of components introduced primarily to facilitate processing of rubber compounds, as well as to expand the temperature range of rubber operation;
- age resistors, which are a group of components introduced into the composition of rubber compounds to protect them against chemical and physical aging and, accordingly, to increase the operation duration of final products;
- technological additives, which are the components introduced to facilitate technological processing of rubber mixtures;
- other components, which may provide certain narrowly specific properties. For example, components which provide electrically conductive properties of rubbers, or protect them from the effects of fire, microorganisms, etc.

To the greatest extent, the basic properties of rubbers are determined by the type of rubber, the type and content of the components of the vulcanizing group, fillers, plasticizers. At the same time, there are tens, if not hundreds, of thousands of brands of ingredients. To obtain rubbers with a given set of properties, it is necessary to correctly select the compounds of the composition – the components used and their ratio.

It should be noted that a set of characteristics of the material is significantly influenced by the conditions for obtaining rubbers. The conditions of vulcanization – temperature and duration – have the greatest influence. If vulcanization parameters are selected incorrectly, the vulcanized grid of cross-links is formed incompletely, or rubber degrades thermally. Both processes negatively affect the properties of final products.

As a rule, when developing compositions of rubber compounds with specified technological and operational characteristics, quite a lot of developer experience and accumulated empirical knowledge are required. No wonder that many professionals in rubber compounding consider their activities to be more art than engineering. It is significant that even the discovery of the rubber vulcanization itself turned out to be the result of a huge number of experiments on mixing rubber with various components. Charles Goodyear [2] spent more than ten years searching for a vulcanizing agent and, to a certain extent, accidentally discovered sulfur vulcanization. Of course, modern rubber compositions differ significantly from those used in the middle of the XIX century when C. Goodyear experimented, but empirical experience is still of great importance while obtaining the material with the specified properties.

The authors of this paper claim that problems of predicting properties of rubbers according to a known composition (a direct problem) and selecting the composition for a given set of properties (an inverse problem) can be successfully solved using modern computing.

As noted in [3], traditionally, the quantitative structure-property relationship (QSPR) model is used as a core of the descriptor model, which allows predicting properties of a material of interest based on certain input characteristics. But at the same time, the authors [3] note that it is extremely difficult to use traditional methods of linear and nonlinear correlation for these purposes due to complex relationships between inputs and outputs of the model. To predict properties, Machine Learning (ML) is much more promising.

Machine learning is a branch of Artificial Intelligence (AI). Its purpose is to create models trained on the basis of past data and situations. In recent decades, ML methods are rapidly developing due to the increased computing power of modern computers and a large amount of experimental data accumulated. ML is successfully applied to predict properties of materials in a variety of areas. Here are some examples of successful application of ML methods for materials research: predicting physical and mechanical properties of alloys [4,5], properties of inorganic materials [6], electronic forbidden zones of perovskite materials [7], catalytic activity [8,9], acid dissociation constants [10], designing organometallic sorbents [11], properties of polymer dielectrics [12], materials for producing organic light-emitting diodes (OLED) [13],

superconductors [14], photovoltaic materials [15], polymer electrolyte membranes (PEM) for fuel cells [16].

When using ML methods, it is not necessary to build complex theoretical regression models based on fundamental conservation laws and thermodynamics. In materials science, as a rule, such relations, if they exist, are extremely complicated and poorly describe the real relationship between the structure and properties. This makes it difficult to predict properties of complex materials, and it is almost impossible to solve the inverse task of selecting a composition for a given set of characteristics. However, when using ML, these difficulties almost disappear.

To solve materials science problems, when applying ML for predicting properties of materials, it is extremely important to acquire, accumulate, and systematize a large amount of experimental data to successfully train the artificial intelligence. To date, the world has accumulated a large amount of data on various materials – metals and alloys, plastics, medicines, minerals, fibers, etc. [17].

As rubbers are used to produce many critical products (e.g., automobile, aviation pneumatic tires, etc.), and their quality affects a person's life and well-being, it is necessary to predict their characteristics. Field tests are usually extremely costly, in terms of financial, labor, time, and material resources. ML methods applied can increase productivity and speed of achieving results. We have not found any research literature on the use of ML methods for predicting properties of rubbers or other elastomeric materials.

Materials and Methods

Due to the fact that more than 70 % [18,19] of the elastomers are consumed by the tire industry, the objects of the study were general-purpose rubbers traditionally used in this area: isoprene (IR, NR), butadiene (BR), styrene butadiene and methylstyrene butadiene (SBR-30). It should be noted that the proposed approach, due to its versatility, can also be extended to special-purpose elastomers: nitrile butadiene (NBR), ethylene-propylene (EPDM), fluoroelastomers (FKM) and others.

As a vulcanizing system, a combination of sulfur and sulfonamide accelerators (CBS, MBS) was used. This vulcanizing system provides optimal vulcanization kinetics: an induction period during vulcanization, which is sufficient for the composition to spread in shape; a high rate of vulcanization and a wide plateau, which makes it possible to prevent the reversion of properties.

Carbon black of various grades, dispersion, and specific surface area were used as fillers. Carbon black of the applied grades belongs to the group of reinforcing fillers that improve physical and mechanical characteristics of rubbers [1]. Some rubber mixtures contained inert fillers (chalk, kaolin, etc.) introduced to facilitate processing and reduce the cost of materials. They affected physical and mechanical properties insignificantly.

Petroleum oils were used as plasticizers: the PN-6sh petroleum plasticizer, which is a mixture of mainly aromatic hydrocarbons, paraffin oil (MP), which is a mixture of linear hydrocarbons.

These ingredients were selected due to their wide distribution, availability, convenient processing, and stable properties.

When the artificial neural network was trained, other components of rubber mixtures affected physical and mechanical properties of rubbers insignificantly.

Rubber mixtures for the control sample were prepared using laboratory mixing rollers according to the following mixing mode: rubber was plasticized; zinc oxide and stearic acid were introduced; fillers were introduced; plasticizers were introduced; components of the vulcanizing group were introduced. The mixing temperature was 60-70 °C.

Rubber mixtures were vulcanized in a hydraulic vulcanization press at 160 °C. Vulcanization lasted for 9 minutes.

To obtain a sample of input data, the results of tests of industrially produced rubbers were also used, in which samples were obtained under different conditions. This fact was taken into account when describing the input parameters.

Experimental tests of rubber properties were carried out according to the requirements of GOST 270-75. Rubber. A method for determining elastic and strength properties at elongation.

The computation was done using the MATLAB (developed by the MathWorks), as well as with the help of the program developed by the authors in the freely distributed Python programming language and ready-made libraries of this language.

Results and Discussion

Preparing data for computer modeling. In this paper, it was necessary to take into account types and contents of rubbers, the vulcanizing group, carbon black, plasticizer as input parameters (descriptors) for the neural network. The effect of the other components was considered insignificant. Obviously, it is most convenient to represent the input parameters in the form of numerical values.

The number of all components was calculated per 100 parts by weight of rubber. This made it possible to simplify the model by excluding one input parameter – rubber content, which was always equal to 100 parts by weight.

The most difficult task was to describe the structure of the ingredients used so that it could be processed on a computer. Chemists usually apply structural formulas of organic substances, for polymers, structural formulas of monomeric units are used. This is a general principle for the chemical sciences to use molecular descriptors optimized for human perception. However, the neural network required the search for numerical quantities that adequately described the structure of the components.

To describe the structure of rubbers and petroleum plasticizers, a basic thermodynamic indicator – the solubility parameter (δ) – can be used. It is fundamentally important to know solubility parameters when solving many applied problems. This parameter is often used to decide if mutual solubility of multicomponent systems [20-25], including rubber-plasticizer systems, is possible. Values of solubility parameters for various compounds, including polymers, can be found in reference books on chemical and physical and chemical properties of substances.

For low molecular weight compounds, such as petroleum plasticizers, the solubility parameter can be determined experimentally [26]. In this case, it is calculated as follows:

$$\delta^2 = \frac{\Delta E_0}{V},\tag{1}$$

where $\Delta E_0 = \Delta H_0 - RT$ is the evaporation energy, ΔH_0 is the latent heat of the liquid evaporation, R is the gas constant, T is the absolute temperature, V is the molar volume.

For polymers, the δ parameter is difficult to determine experimentally since it is impossible to experimentally determine their evaporation energy: polymers cannot be converted to a gaseous state without being decomposed. For polymers, solubility parameters are determined based on the maximum swelling in a group of solvents with the known solubility parameter, using the results of indirect measurements [27], or computational schemes [28-31].

In this paper, the solubility parameters for petroleum plasticizers and for rubbers were obtained by computation using the method of group contributions according to the method described in [28].

In addition, for rubber, an important factor affecting physical and mechanical properties of rubbers is its ability to crystallize: the higher the degree of crystallinity, the higher the physical and mechanical parameters. In this research, it was assumed that the fraction of the crystalline phase is constant since the samples for testing were obtained under standard

conditions. Considering this, the ability of rubbers to crystallize was described by a binary input parameter taking either "1" (for rubbers that can crystallize) or "0" (for rubbers that cannot crystallize) value.

For carbon black, the iodine number was used as a numerical value characterizing its properties. This parameter, numerically equal to the amount of iodine adsorbed by carbon black, characterizes the surface of carbon black particles. The iodine number is determined according to GOST ISO 1304-2013 Ingredients of rubber mixtures. Carbon black. Determining the iodine adsorption value.

Vulcanization process parameters – temperature and duration – are numerical values. As input parameters of the model, they were used unchanged.

Thus, taking into account the above, a list of input parameters that characterize the composition of rubbers and, accordingly, affect the structure and properties of the material was formed. The list is given below (Table 1).

Table 1. List of input parameters for computer modeling

Component in	Input parameter									
rubber compound	Name	Measurement unit	Variable type	Notation						
Rubber	Rubber (rubber mixture) solubility parameter	$\frac{J^{1/2}}{m^{3/2}}$	Numerical	Input1						
Kubbei	Rubber crystallization capacity	-	Binary	Input2						
Vulcanizing	Content of vulcanizing agent	Part by weight per 100 parts by weight of rubber	Numerical	Input3						
group	Content of vulcanization accelerator	Part by weight per 100 parts by weight of rubber	Numerical	Input4						
Filler	Content of carbon black	Part by weight per 100 parts by weight of rubber	Numerical	Input5						
	Iodine number of carbon black	$\frac{\text{mg of iodine}}{g}$	Numerical	Input6						
Plasticizer	Content of plasticizer	Part by weight per 100 parts by weight of rubber	Numerical	Input7						
Plasticizer	Plasticizer (mixture of plasticizers) solubility parameter	$\frac{J^{1/2}}{m^{3/2}}$	Numerical	Input8						
Process	Vulcanization temperature	°C	Numerical	Input9						
parameters	Vulcanization time	Min.	Numerical	Input10						

Setting the output parameters of rubber. As previously noted, physical and mechanical properties of rubbers were used as output parameters. From a large variety, it was necessary to identify those characteristics that would be important from the point of view of operational properties of elastomeric materials, easy to determine and give a relatively low error, and would correlate with changes in input parameters well. The list of output parameters is given below (Table 2).

Table 2. List of output parameters for modeling

Rubber properties	Measurement unit	Parameter notation
Tensile strength	MPa	Output1
Stress at 300 % elongation	MPa	Output2
Elongation at break	%	Output3

Results of neural network modeling. The computer modeling scheme is presented below (Fig. 1). Rubber samples with various types of rubber, fillers, and component contents were manufactured and tested. The total number of examined samples was 36. In addition, data on the compositions of industrially produced rubbers were processed, which made it possible to obtain 84 samples. Such a sample size is insufficient for training a neural network. At the same time, many sources (e.g., [17]) note the importance of obtaining correct, accurate, and sufficient data.

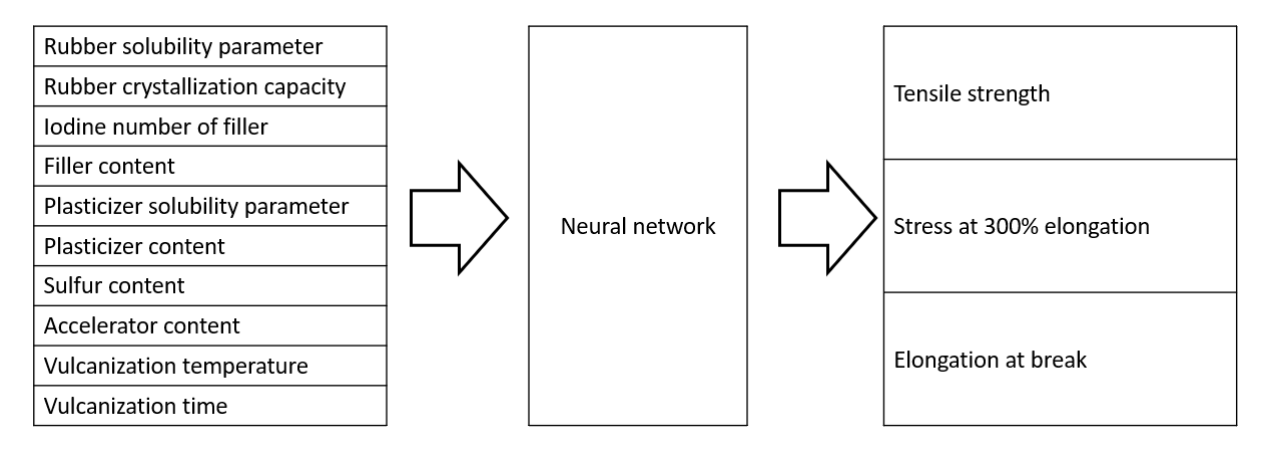


Fig. 1. Computer modeling scheme

We used the augmentation method [32–35] to expand the training sample. Data augmentation methods are widely used to improve the performance of deep learning neural networks. In the process of augmentation, training examples are modified in such a way that the number of these examples is sufficient to create deep learning neural networks. In this work, a ready-made CTGAN neural network model was used. It was trained on the available data. The CTGAN model allows to specify which columns are discrete and which are continuous. The parameters that describe the type of rubber, plasticizer or filler were taken discrete. The parameters characterizing the content of the plasticizer and filler, as well as the output parameters, were taken continuous. After the generation of new data, the data generated during the augmentation were processed, namely:

- 1. rounding was performed. The plasticizer's and filler's content were rounded up to integers. Output values were also rounded to integer values;
- 2. removal of duplicates, if any;
- 3. checking the generated data for out of limits.

As a result, it was possible to obtain 2,564 samples.

All the data were divided at the ratio of 70-15-15: 70 % were considered the training sample of the neural network, 15 % – as the test sample and 15 % – as the validation one.

At the first stage, the possibility to use neural networks to solve the task was fundamentally assessed, and neural network optimal parameters were also selected.

While training a neural network, there is a random factor which can lead to a change in the results produced by the trained neural network during retraining. To minimize the randomness factor, each computational experiment was carried out three times, the result obtained was averaged.

At the initial stage, the neural network of the multilayer perceptron architecture was used. At this stage, we set the tasks to evaluate the fundamental possibility of using neural network modeling methods to predict the properties of elastomers based on the known composition of rubber compounds, as well as to select the neural network parameters, which, in turn, included:

- determining optimal number of neurons in layers, with default activation and learning functions;
- selecting optimal activation functions for each layer;
- selecting optimal learning functions.

As a parameter for optimizing the neural network parameters, the mean squared error was used calculated by the formula:

$$MSE = \frac{\sum_{i=0}^{n} (y_{ex} - y)^2}{n},$$
(2)

where y_{ex} is the result obtained from the neural network; y is the reference result taken from the training sample; n is the number of predicted parameters.

The parameters were optimized using the default "tansig" activation functions in the input layer, "purelin" – in the hidden layer, and the "trainlm" training function – in the output layer. Neural network modeling at this stage was carried out using the MATLAB (developed by The MathWorks).

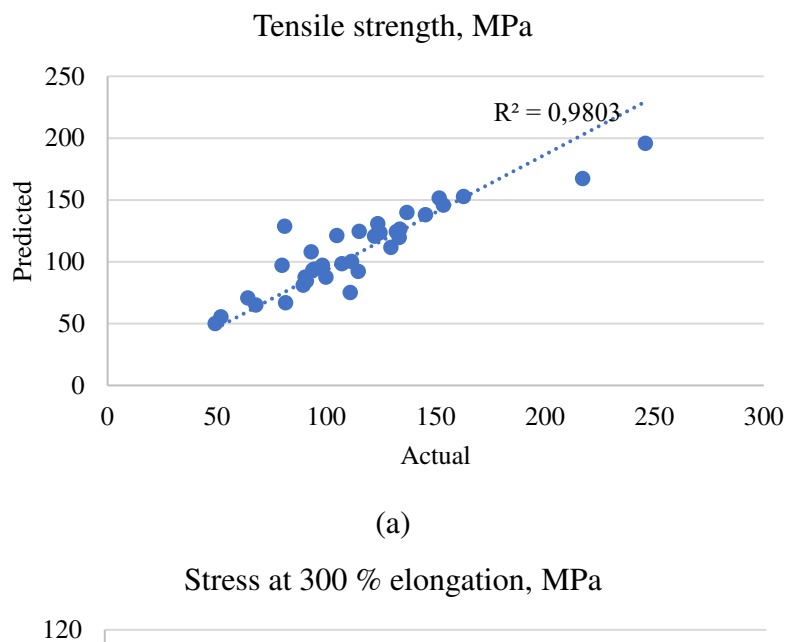
According to the results of the computational experiments, it was found that if the above activation and learning functions are used, the optimal number of neurons in the input layer is 16; in the hidden layer - 16, in the output layer - 32. With these parameters, in this series of computational experiment, the minimum value of MSE = 239.5230 was obtained for the neural network of the multilayer perceptron architecture.

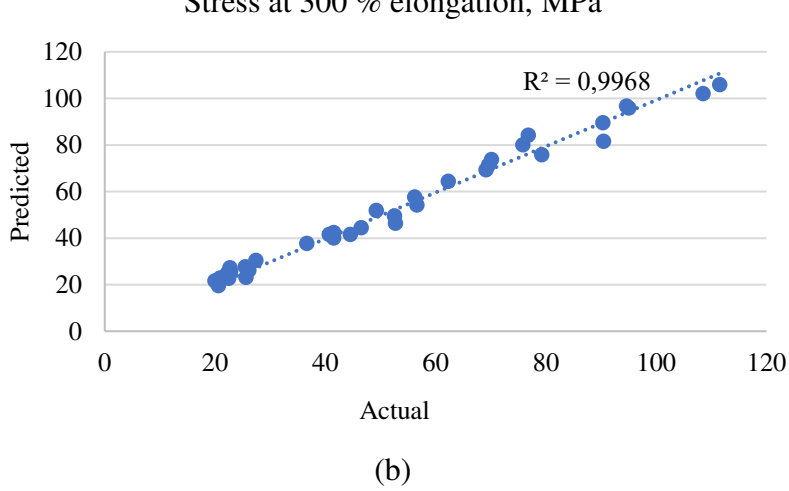
Figure 2 shows the results of validating the physical and mechanical properties selected as output parameters. The trend line is drawn provided that the point intersects with the coordinates (0.0).

In Fig. 2, the data for two output parameters ("stress at 300 % elongation" and "elongation at break") show a high level of approximation accuracy when comparing experimentally determined and predicted neural network properties. For the output "tensile strength" parameter, the approximation accuracy is less than 0.75, which does not provide a sufficiently good level of modeling. Taking into account the fact that tensile strength is an extremely important physical and mechanical characteristic for elastomeric materials, the authors found it necessary to test neural networks of a different architecture.

In order to continue predicting operational properties of rubbers in accordance with the modeling scheme shown above (Figure 1), a program in the freely distributed Python language based on the principles of convolutional neural network architecture was developed [36]. The developed program makes it possible to perform pre-processing of the sample for training; to select the architecture of the convolutional neural network and the corresponding hyperparameters. To make selecting hyperparameters for the TensorFlow library automatic, the Keras Tuner was used. With the help of this tool, when searching for hyperparameters, we iterated:

- the 'relu', 'sigmoid', 'tanh', 'elu', 'selu' activation functions;
- the 'adam', 'rmsprop', 'SGD' learning functions;
- the number of neurons in the input layer (from 32 to 256 in increments of 16);
- the number of neurons in the hidden layer (from 32 to 256 in increments of 16).





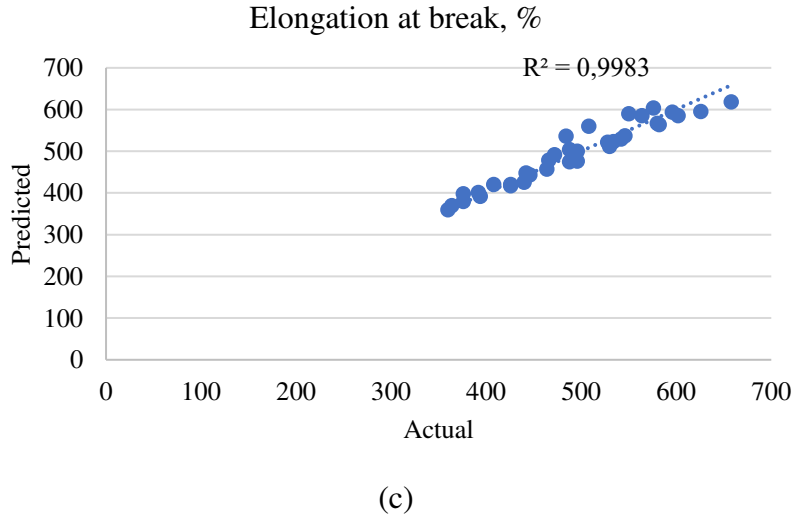


Fig. 2. Results of validating properties selected as output parameters: (a) tensile strength, MPa; (b) stress at 300 % elongation, MPa; (c) elongation at break % for the neural network of the multilayer perceptron architecture

In each case, the neural network was trained up to 8,000 epochs. As a result, it was found that the smallest error was obtained when the "relu", "elu", "selu" activation functions were used. A large prediction error was observed when the 'sigmoid', 'tanh' activation functions, as well as the "SGD" training function were used in the experiment. After a series of experiments, the "sigmoid", 'tanh' activation functions and the 'SGD' learning function were excluded from the possible iteration options.

The optimal number of iterations was determined using the validation sample. After 20,000 iterations, the error in the validation sample stopped decreasing; it even increased slightly, which proves the effectiveness of retraining. Therefore, after 20,000 iterations, the learning process was completed. To assess the quality of the neural network, cross-validation was used. The mean squared error obtained during cross-validation was 768,778.

According to the results of the computational optimization experiment, it was found that to solve the problem of predicting rubber properties, the best results should be provided by the neural network with the following parameters:

- three (input, hidden, and output) layers;
- 224 neurons in the input layer;
- 208 neurons in the hidden layer;
- 3 neurons in the output layer;
- the 'selu' activation function used for the input and hidden layers;
- the 'rmsprop' training function used;
- 20,000 iterations.

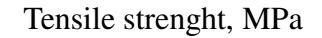
The program in the freely distributed Python language for predicting properties of rubbers using optimized hyperparameters and convolutional neural network architecture made it possible to obtain the MSE of 153.9453, against 239.5230, using the MATLAB for the neural network of the multilayer perceptron architecture, which proves the fact that the data augmentation was effective, and the neural network hyperparameters were properly selected.

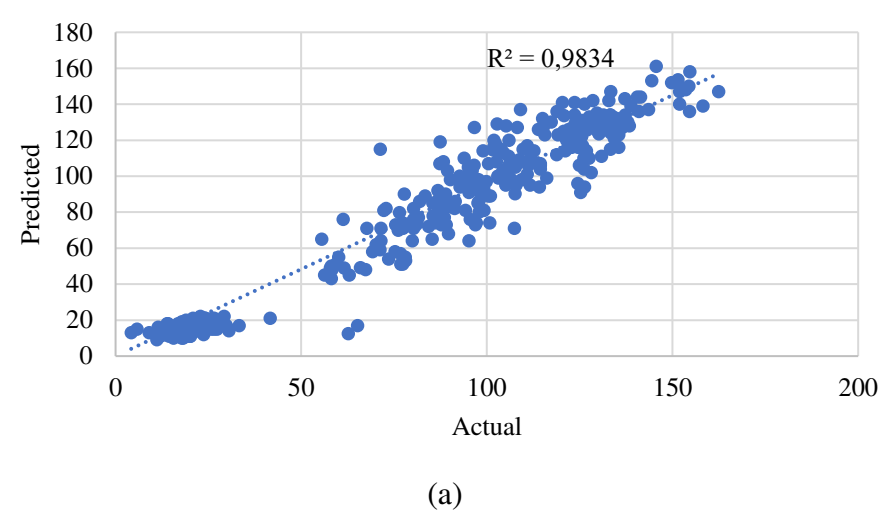
Figure 3 shows the results of validating the physical and mechanical properties selected as output parameters. The trend line, as in the previous case, is drawn provided that the point intersects with the coordinates (0.0).

According to the presented data, a significantly higher level of approximation is obtained for the convolutional neural network architecture for the output "tensile strength" parameter. At the same time, an acceptable level of approximation is also obtained for the remaining properties, albeit slightly lower than for the neural network of the multilayer perceptron architecture. Tensile strength is predominantly considered the most important physical and mechanical property, and most other properties correlate with it. This underlines the importance of the result achieved.

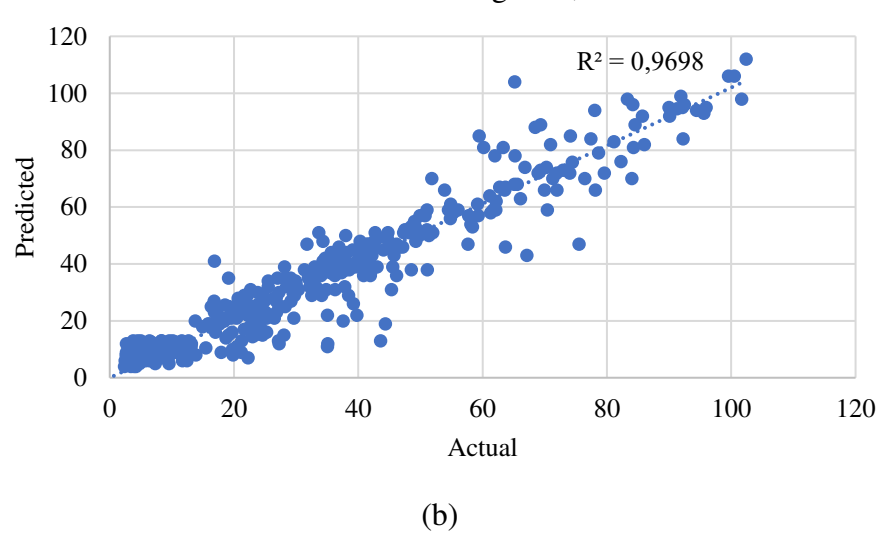
Based on the results of experimental modeling, hyperparameters of the convolutional neural network were selected to predict rubber quality indicators [37].

As a result, the architecture of the convolutional neural network with two convolutional layers, three fully connected layers, and the 3×4 input matrix was chosen. At the last stage, we automatically selected the hyperparameters for the best architecture [35] which automatically selects ten characteristics of the convolutional neural network: activation functions of convolutional and fully connected layers, the number of filters in convolutional layers, the number of neurons in fully connected layers, regularization functions after each layer, the optimization function.





Stress at 300 % elongation, MPa



Elongation at break, %

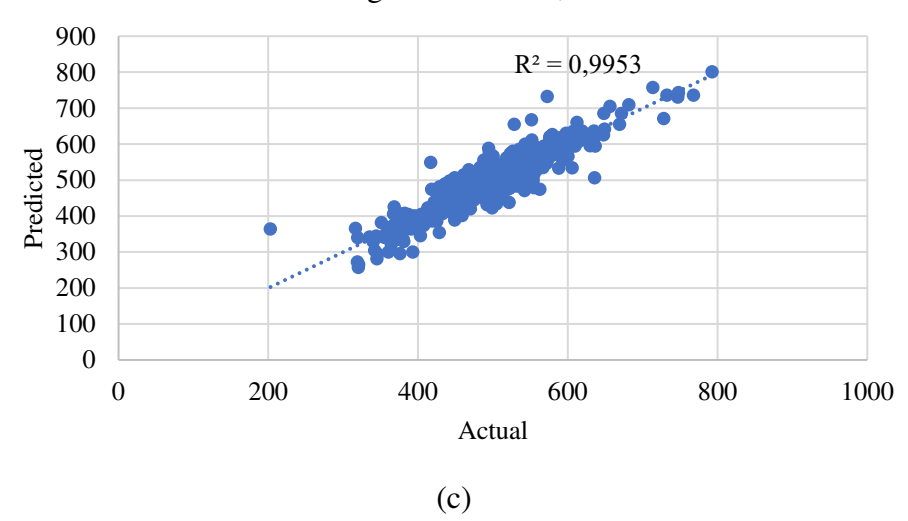


Fig. 3. Results of validating properties selected as output parameters: (a) tensile strength, MPa; (b) stress at 300% elongation, MPa; (c) elongation at break % for convolutional neural network architecture

Conclusions

Thus, based on the research results, the following conclusions can be drawn:

- 1. we substantiated the use of computer modeling of performance characteristics of elastomeric materials;
- 2. we substantiated the approaches to compiling the list of input parameters for neural network modeling, which includes the content and type of key components, as well as technological parameters of vulcanization of rubbers;
- 3. we proved the effectiveness of computer augmentation methods for expanding the training sample of laboratory test data. Using augmentation methods, the training sample was expanded to 2,564 samples and ensured the accuracy of experimental modeling;
- 4. we optimized neural network architecture and hyperparameters for modeling properties of elastomeric materials, depending on their composition and parameters of the vulcanization process;
- 5. we highlighted that the use of the convolutional neural network makes it possible to predict, with high accuracy, physical and mechanical properties of elastomeric materials based on butadiene, isoprene, butadiene (methyl) styrene rubbers filled with carbon black obtained during sulfur vulcanization with sulfonamide accelerators.

References

- 1. Gent AN. (ed.) *Engineering with rubber: how to design rubber components*. 3rd ed. Munich: Carl Hanser Verlag GmbH & Co. KG; 2012.
- 2. Klingender RC. (ed.) Handbook of specialty elastomers. Boca Raton: CRC Press; 2008.
- 3. Zhou T, Song Z, Sundmacher K. *Big Data Creates New Opportunities for Materials* Research: A Review on Methods and Applications of Machine Learning for Materials Design. *Engineering*. 2019;5(6): 1017–1026.
- 4. Agrawal A, Deshpande PD, Cecen A, Basavarsu GP, Choudhary AN, Kalidindi SR. Exploration of data science techniques to predict fatigue strength of steel from composition and processing parameters. *Integrating Materials and Manufacturing Innovation*. 2014; 3(1): 90–108.
- 5. Karak SK, Chatterjee S, Bandopadhyay S. Mathematical modelling of the physical and mechanical properties of nano-Y₂O₃ dispersed ferritic alloys using evolutionary algorithm-based neural network. *Powder Technology.* 2015; 274: 217–226.
- 6. Sumpter B, Vasudevan R, Potok T, Kalinin SV. A bridge for accelerating materials by design. *npj Computational Materials*. 2015;1: 15008.
- 7. Pilania G, Mannodi-Kanakkithodi A, Uberuaga B, Ramprasad R, Gubernatis JE, Lookman T. Machine learning bandgaps of double perovskites. *Scientific Reports*. 2016;6: 19375.
- 8. Jinnouchi R, Asahi R. Predicting catalytic activity of nanoparticles by a DFTaided machine-learning algorithm. *The Journal of Physical Chemistry Letters*. 2017;8(17): 4279–4283.
- 9. Madaan N, Shiju NR, Rothenberg G. Predicting the performance of oxidation catalysts using descriptor models. *Catalysis Science & Technology*. 2016;6(1): 125–33.
- 10. Zhou T, Jhamb S, Liang X, Sundmacher K, Gani R. Prediction of acid dissociation constants of organic compounds using group contribution methods. *Chemical Engineering Science*. 2018;183: 95–105.
- 11. Aghaji MZ, Fernandez M, Boyd PG, Daff TD, Woo TK. Quantitative structure–property relationship models for recognizing metal organic frameworks (MOFs) with high CO₂ working capacity and CO₂/CH₄ selectivity for methane purification. *European Journal of Inorganic Chemistry*. 2016;2016(27): 4505–4511.
- 12. Sharma V, Wang C, Lorenzini RG, Ma R, Zhu Q, Sinkovits DW, Boggs SA, Ramprasad R. Rational design of all organic polymer dielectrics. *Nature Communications*. 2014;5: 4845.
- 13. Gómez-Bombarelli R, Aguilera-Iparraguirre J, Hirzel TD, Duvenaud D, Maclaurin D, Blood-Forsythe MA, et al. Design of efficient molecular organic light-emitting diodes by a

- high-throughput virtual screening and experimental approach. *Nature Materials*. 2016;15(10): 1120–1127.
- 14. Stanev V, Oses C, Kusne AG, et al. Machine learning modeling of superconducting critical temperature. *npj Computational Materials*. 2018;4: 29.
- 15. Olivares-Amaya R, Amador-Bedolla C, Hachmann J, Atahan-Evrenk S, Sánchez-Carrera RS, Vogt L, Aspuru-Guzik A. Accelerated computational discovery of high-performance materials for organic photovoltaics by means of cheminformatics. *Energy & Environmental Science*. 2011;4: 4849–4861.
- 16. Wang Y, Seo B, Wang B, Zamel N, Jiao K, Adroher X-C. Fundamentals, materials, and machine learning of polymer electrolyte membrane fuel cell technology. *Energy and Al.* 2020;1: 100014.
- 17. Butler KT, Davies DW, Cartwright H, et al. Machine learning for molecular and materials science. *Nature*. 2018; 559: 547–555.
- 18. Dick JS. Rubber Technology: Formulation and Testing. 2010.
- 19. Reznichenko SV, Morozov YL. *The Big Handbook of the Rubberman. Part 1. Rubbers and Ingredients*. 2012.
- 20. Gyulmaliev AM, Zekel LA, Dandaev AU, Batov AE, Kadieva MK, Magomadov EE, Kadiev KM. A simple method for estimating solubility parameter of small molecules and polymeric materials. *Russian Journal of Applied Chemistry*. 2021;94(1): 55–63.
- 21. Kostochko AV, Valishina ZT, Shipina OT, Akhmadullin IN. Mathematical model of compatibility in the cellulose nitrate-solvent system. *Bulletin of Kazan Technological University*. 2013;14: 55–58.
- 22. Shirokova ES. Mass transfer of plasticizer in elastomeric composite materials and their adhesive properties. Diss. of Cand. Sc. in Chemistry. 2009. (In-Russian)
- 23. Khamzina LF, Treskova VI, Nikitina LE, Garaeva MR, Strekalova GR., Shipina OT. Structural organization and heat resistance of composites based on microcrystalline cellulose. *Bulletin of Technological University*. 2020;23(6): 68–72.
- 24. Olabisi O, Robeson LM, Shaw MT. Polymer-Polymer Miscibility. NY: Academic Press; 1979.
- 25. Gerasimov VK. *Thermodynamic analysis of amorphous exfoliation of polymer polymer systems. Diss. Doctor of Chemical Sciences.* Moscow: Institute of Physical Chemistry and Electrochemistry; 2013. (In-Russian)
- 26. Knunyants IL. (ed.) *Chemical Encyclopedia. 4th Ed.* Moscow: Sovetskaya Entsiklopedia; 1995. (In-Russian)
- 27. Rabek Y. Experimental methods in polymer chemistry. Moscow: Mir; 1983.
- 28. Van Krevelen DW. *Properties of polymers their correlation with chemical structure; their numerical estimation and prediction from additive group contributions.* 4th ed. Amsterdam: Elsevier; 2009.
- 29. Askadsky AA, Matveev YI. *Chemical structure and physical properties of polymers*. Moscow: Chimia; 1983. (In-Russian)
- 30. Askadsky AA, Kondrashchenko VI. Computer materials science of polymers. Atomic and molecular level. Moscow: Nauchny Mir; 1999. (In-Russian)
- 31. Hansen CM. The universality of the solubility parameter. *Industrial & Engineering Chemistry Process Design and Development*. 1969; 8 (1): 2–11.
- 32. Rostovtsev VS, Bakulin AA. Fomin SV, Shirokova ES. Modeling quality indicators of elastomeric products using convolutional neural network. In: *Materials of the reports of the 85th Scientific and Technical Conference of the teaching staff, researchers, and postgraduates (with international participation) on February 1-13, 2021*. Minsk: Belarusian Technological University; 2021. p.230-232. Available from: https://elib.belstu.by/handle/123456789/40836.

- 33. Cheremisinova ON, Rostovtsev VS. Certificate of state registration of computer programs. *Program for automatic selection of hyperparameters of convolutional neural network: computer program.* Copyright holder Vyatka State University. No. 2021610729; dated 27.01.2021.
- 34. Rostovtsev VS, Cheremisinova ON. Improving the quality of image recognition by selecting parameters of convolutional neural network. In: *Materials of the reports of the 52nd International Scientific Conference of the Eurasian Scientific Association (June 2019)*. Moscow: Eurasian Scientific Association, 2019;6(52): 114–118.
- 35. Cheremisinova ON, Rostovtsev VS. Methods of automated hyperparameters tuning of a convolutional neural network. *Neurocomputers*. 2021;2: 26–34.
- 36. Rostovtsev VS, Bakulin AA. Certificate of state registration of computer programs. *A program for modeling the characteristics of chemical production output based on a convolutional neural network.* Copyright holder the Vyatka State University. No. 2021611858 dated 29.01.2021. app.No. 2021610789 dated 29.01.2021.
- 37. Fomin SV, Shirokova ES, Rostovtsev VS, Meltsov VY, Bakulin AA. Using convolutional neural networks when modeling chemical product quality indicators. In: *Materials of Interuniversity International Congress "Higher School: Scientific research". (Moscow, February 4, 2021).* Moscow: Infiniti Publishing House, 2021. p.151–156. (In-Russian)

THE AUTHORS

Fomin S.V.

e-mail: rubber@vyatsu.ru

Meltsov V.U.

e-mail: meltsov@vyatsu.ru

Rostovtsev V.S.

e-mail: rostovtsev@vyatsu.ru

Shirokova E.S. (10)

e-mail: usr06779@vyatsu.ru

The numerical simulation of the post-welding stress-strain state of thinsheets welded joints of EP718 alloy

Submitted: April 27, 2023

Approved: May 12, 2023

Accepted: June 6, 2023

A.Yu. Medvedev, A.E. Medvedev [□] , A.F. Shaikhulova [□] , R.V. Nikiforov, O.V. Murugova, V.R. Galimov

Abstract. The paper presents the development of a numerical thermal deformation model of two-pass pulsed arc GMA (Gas Metal Arc) welding of a thin-sheet welded joint made of EP718 alloy using the ANSYS package, considering the distribution of temperature fields from a consumable electrode during transverse vibrations. Experimental verification of the calculation results showed that the developed thermal deformation model of two-pass GMA welding makes it possible to predict the stress-strain state of a thin-sheet welded joint with an error of 10 %, sufficient for engineering calculations. Residual stresses von Mises after welding according in the weld does not exceed 840 MPa (0.8 σB). The thermal deformation model of two-pass GMA pulsed arc welding developed during research can be used to assess the stress-strain state of a welded structure of complex spatial geometry with a large number of welds.

Keywords: deformation simulation during welding; heat-resistant alloy; EP718; thermal cycles during welding; ATOS deformation measurement.

Acknowledgements. Ministry of Science and Higher Education of the Russian Federation within the framework of the state assignment of "Metals and Alloys under Extreme Impacts" Laboratory of Eurasian Center of Excellence (agreement No. 075-03-2023-119/1).

Citation: Medvedev AY, Medvedev AE, Shaikhulova AF, Nikiforov RV, Murugova OV, Galimov VR. The numerical simulation of the post-welding stress-strain state of thin-sheets welded joints of EP718 alloy. *Materials Physics and Mechanics*. 2023;51(5): 79-89. DOI: 10.18149/MPM.5152023_8.

Introduction

Gas turbine engine body parts are subject to high requirements for strength and rigidity - they should provide freedom from temperature deformations of individual elements included in the body and provide simplicity and convenience in their manufacture and assembly. Usually, such highly loaded elements are made of heat-resistant nickel-based alloy KhN45MVTYuBR (EP718).

Its use for the manufacture of welded structures is complicated by the tendency to form hot cracks of various nature, not only in the weld metal, but also in the near-affected zone (NAZ), as well as grain growth and softening of the metal in the NAZ [1–8,10] One of the reasons for the increased susceptibility to cracking of the EP718 alloy in the NAZ is the high level of residual welding stresses [9]. To solve the abovementioned issues, the electron beam welding (EBW) and manual argon arc welding with a non-consumable electrode with filler wire (TIG) are used for welding the considered alloy in aircraft and engine building. The EBW technology (due to the high concentration of heat in the source) makes it possible to

form a fine-grained weld structure, but its widespread use is complicated by the following aspects: it requires laborious preparation of edges; it is difficult to apply on curved paths of welds.

Manual welding with filler material is carried out at low speeds in 3 or more passes when filling a groove with a metal thickness of 4–5 mm. This leads to repeated heating of the metal in the weld zone and the NAZ, and, as a result, the accumulation of residual stresses and an increase in the grain size. Based on the available foreign recommendations, welding of butt joints with a thickness of 4 mm from an analogue alloy of Inconel 718 can be carried out by a multilayer GMAW with a constant arc with a heat input of at least 400 kJ / m per pass of 2 mm at a welding speed of at least 24 m/h, a multilayer GMAW pulsed arc with a heat input of at least 360 kJ/m per pass of 2 mm at a welding speed of at least 15 m/h. Based on foreign data and our own experience, the use of fusion welding (consumable electrode in an inert gas) with transverse vibrations will provide a reduction in heat input up to 30 % compared to a multilayer GMAW pulsed arc, will reduce the grain growth rate, the drop in ductility in the temperature ranges of brittleness and the minimum level of residual stresses in the NAZ. When welding alloy EP718, welding wire 08Kh20N57M8V8T3R (EP533) is used. Table 1 shows the chemical composition of the EP718 alloy and EP533 welding wire [1,10,12].

It is impossible to predict residual stress and deformations of a welded assembly with many welds and with complex spatial geometry using traditional analytical calculations. The only possibility is to use powerful CAE systems, which allow simulating the stress-strain state of the welded structure after welding. The Mechanical module of the ANSYS package has this functionality.

Thus, the development of numerical models of the stress-strain state of a welded structure with complex spatial geometry after GMA welding is an urgent task, but it is extremely time-consuming and cumbersome without the stage of some simplifications. The selection of parameters of the numerical model is much easier to carry out on a somewhat simplified thermal deformation model of welding of the flat samples, which allows to quickly correct the mode parameters, followed by interpolation of the results to a more complex geometry.

Materials and Experimental methods

Material and welding technique. In the present study the base metal EP718 and welding wire EP533 alloy was used. The chemical composition of the alloy is presented in Table 1.

Table	Table 1: Chemical composition of Li 710 and y and Li 333 welding whe [1,3]															
A llove		Chemical composition, wt. %														
Alloys	C	Si	Mn	Cr	Ni	W	Mo	Mg	Nb	Al	Ti	Fe	В	P		Others
EP718	EP718 <0.1 <0.3 <0	3 < 0.6 14-	43-	2.5-	4-5 2	0.001-	0.8-	0.9-	1.9-	1.9- 2.4 Remain \(\le 0.008 \le 0.010	<0.010	<0.015	Zr≤0.02;			
L1 / 10		_0.5 _0.0	16	47	3.5	1 3.2	0.5	1.5	1.4	2.4	rcmam	_0.000	_0.010	_0.013	Ce≤0.3	
EP533	≤0.1	≤0.3	≤0.5	19- 22	Ост.	7-9	7-9	-	-	Σ3.3	≤3.0	≤0.005	< 0.015	≤0.01	≤0.1	-

Table 1. Chemical composition of EP718 alloy and EP533 welding wire [1,3]

The geometrical parameters of the welded joint corresponded to type C18 according to GOST 14771. Edge preparation for welding was carried out by milling. Plates with dimensions of $100 \times 100 \times 5$ mm were welded in 2 passes by GMA-welding. Sheet blanks from the EP718 alloy had a thickness of 5 mm as delivered. Filler wire - EP533 Ø1.2 mm in hardened state. Welding was carried out with transverse oscillations of the burner relative to the weld trajectory in 2 passes. The nominal gap between the welded plates was 1.0 mm. The preparation of the edges to be welded was carried out on a milling machine. Before welding, tacking was used along the ends of the plates, followed by a selection to a height of 1.0 ± 0.5 mm.

Figure 1 shows the macrostructure of a two-pass weld made with filler wire EP533 (Fig. 1,(a)), and the appearance of the front side of the weld after the first (Fig. 1(b)) and second passes (Fig. 1(c)).

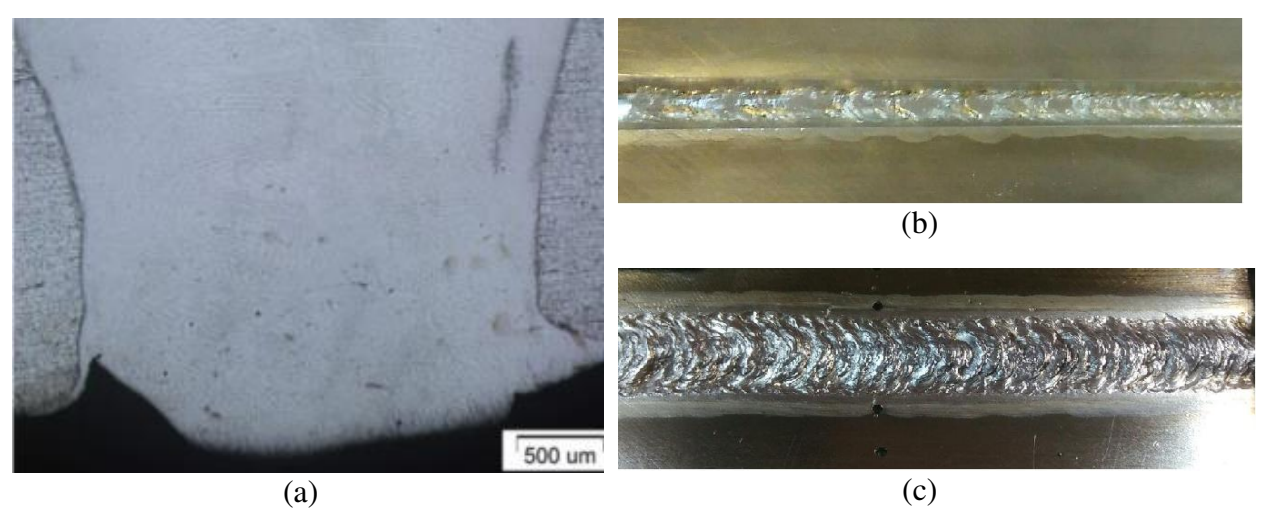


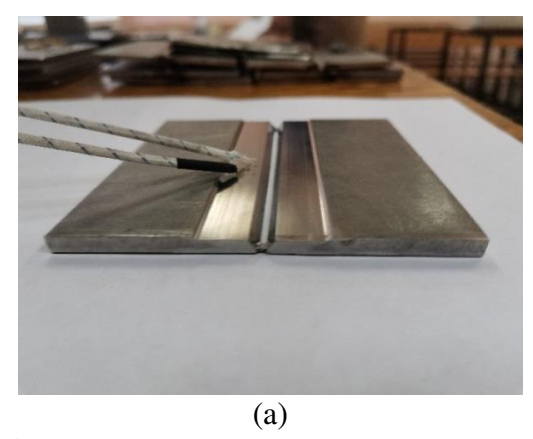
Fig. 1. Macro section of a 2-pass weld made with filler wire EP533 (a) and the appearance of the front side of the weld after the first (b) and second passes (c)

The fusion line is clearly visible on the macrostructure (Fig. 1(a)). Thanks to the use of transverse oscillations of the burner, it was possible to achieve a minimum height of the facing bead of the seam, as can be seen in Fig. 1(c). At the same time, the conducted microstructural studies and X-ray inspection of welded joints did not reveal defects in the weld and HAZ. Figure 1(a) shows the microstructure of the NAZ after the 1st pass. The microstructure of the NAZ is a partially remelted layer cold-worked as a result of milling, the grain size of which is 5–7 times smaller than the grain size of the base metal and is 5–10 μ m. In this case, the length of the NAZ does not exceed 50–100 μ m [20,21].

On the first pass of the weld (Fig. 1(b)), there is a large proportion of disoriented crushed structure, the presence of which can be caused using transverse oscillation technique, during which the molten metal is constantly mixed or thermomechanical vibration of the melt during pulsed arc welding. At the same time, the volume of the molten weld pool under specific conditions is significantly less than in argon-arc welding with a non-consumable electrode. In the second pass, the weld structure is more equiaxed, which is most likely due to an increase in the rigidity of the welded joint after the 1st pass and a large space for free temperature deformation between the welded edges [8,9,12].

Thermocouples were welded to the outer surface of the welded sample by capacitor welding: the first thermocouple was installed at a 1 mm from the edge, second at a 3 mm. Thermocouples were located on the line perpendicular to the joint. Thermal cycles during the welding process were recorded using a CENTER 511 digital 4-channel temperature meter. Figure 2 shows the places for installation of "K-type" thermocouples on a welded sample (Fig. 2(a)) and equipment for welding sheet blanks (Fig. 2(b)).

Longitudinal shrinkage of welded specimens was measured using the ATOS Compact Scan portable 3D scanner for full-size digitization and geometry control. ATOS is a precision measurement system for digitizing geometric objects. The measurement accuracy of ATOS Compact Scan is ≈ 0.1 mm. The measurements were taken after welding the root and facing passes.



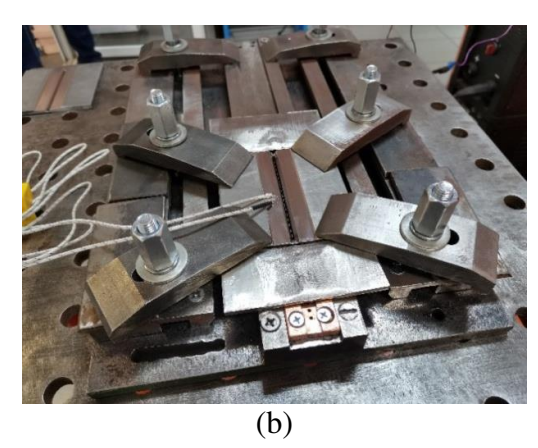


Fig. 2. Places for installation of "K-type" thermocouples on a welded sample $100 \times 100 \times 4$ mm (a) and equipment for welding sheet blanks (b)

Numerical simulation. The ANSYS/Mechanical package was chosen as a tool for numerical simulation. The calculation was carried out using the internal programming language APDL. The solution of the problem of modeling the stress-strain state of plates after welding was carried out in 2 stages: first, the thermal problem of simulating heating by a moving source was solved, and the resulting temperature field at the nodes of the model was converted into a stress and strain field at the second stage.

To describe the temperature field T(x, y, z, t) in flat samples, a differential nonlinear heat conduction equation was used [3]:

$$c\rho(T)\frac{\partial T}{\partial t} = \frac{\partial}{\partial x} \left(\lambda \frac{\partial T}{\partial x}\right) + \frac{\partial}{\partial y} \left(\lambda \frac{\partial T}{\partial y}\right) + \frac{\partial}{\partial z} \left(\lambda \frac{\partial T}{\partial z}\right),$$
where $\rho(T)$ is the density, kg/m³.

The dependence of the thermophysical properties of steel on temperature $\rho(T)$, $\lambda(T)$, c(T) was taken in accordance with the calculations of the OPENCALTHAD program for the average chemical composition of the EP718 alloy, since there is no information on the properties of the alloy in the scientific literature. At temperatures above 1200 °C, the internal ANSYS algorithm approximates linearly the values of the property function over the last temperature interval.

The 3D model of the simulated sample consisted of two parts. First part is a plate with the size of $100 \times 100 \times 4$ mm having a groove of 30° of incline. Underneath it a copper lining is placed with a size of $100 \times 30 \times 6$ mm, having a groove of 6 mm width and 1 mm depth. Element type - Solid 70, 8-node hexahedral. The size of the finite elements near the joint is 0.3 mm, gradually increases from 1.3 to 7 mm towards the ends of the plate.

The boundary conditions for heat transfer were set from the outer and inner surfaces of the plate. Heat radiation was calculated by the equation (2):

$$q_{2r}(T) = \varepsilon C_0 \left(T^4 - T_C^4 \right), \tag{2}$$

where C_0 is the Stefan-Boltzmann constant, $C_0 = 5.67 \times 10^{-8} \text{ W/(m}^2 \text{deg}^4)$; ε is the integral coefficient of radiant heat transfer of nickel; T is the body surface temperature, ${}^{\circ}\text{C}$; T_C is the ambient temperature, ${}^{\circ}\text{C}$.

Convective heat transfer was determined by the equation (3):

$$Q(T) = Ah(T - T_C), (3)$$

where Q is the heat flux density during convection, W/m²; h is the heat transfer coefficient, W/m² °C; A is the surface area, m²; T – body surface temperature, °C; T_C – ambient temperature, °C. The coefficient of convective heat transfer was determined according to the data of [11] following the dependence: $h = 0.68 \cdot 10^{-2} \text{T}$ at 0 < T < 500 °C and h = 0.231 T-82.1 at T > 500 °C. The initial temperature T and the ambient temperature T_C were set to be 20 °C in the calculations.

The boundary conditions of the contact "weld sample - copper lining" were considered as the sum of thermal conductivities of the air gap α_{air} between the microprotrusions of the contacted materials and the metal contact α_{M} . As a result of calculations, the following values of contact thermal conductivity $\alpha_{air}(T)=9100+28T$ were obtained [8].

The welding mode parameters were taken from full-scale experiments. During the welding of the root pass, the heat input was 147 kJ/m, during the welding of the facing pass, it was 150 kJ/m [4-8]. To model the heating source, the Goldak double semi-ellipsoid model was used, the scheme of which is presented in Fig. 3 [8,9].

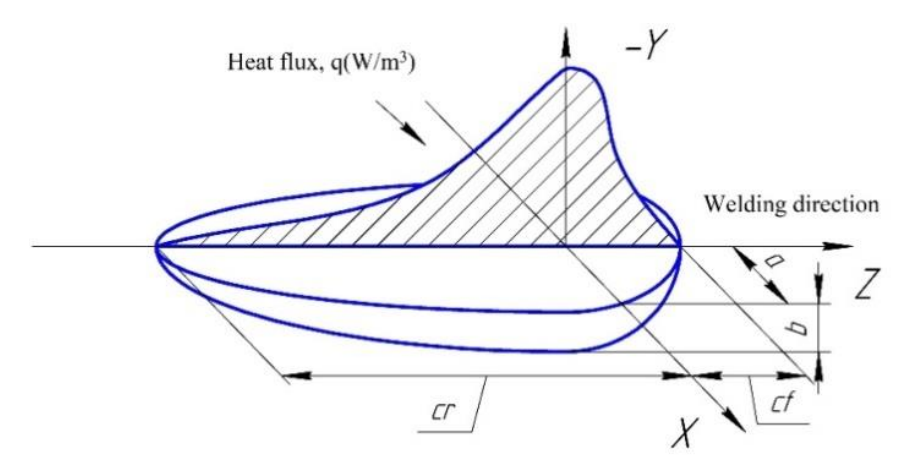


Fig. 3. Goldak's double semi-ellipsoid model [8,9]

For a point inside the first semi-ellipsoid, located in front of the weld pool, the heat flux was determined by the equation (4):

$$q(x,y,z) = \frac{6\sqrt{3}(f_f Q)}{abc_f \pi \sqrt{\pi}} exp\left(\frac{-3x^2}{a^2} - \frac{3y^2}{b^2} - \frac{3z^2}{c_f^2}\right), x \ge 0,$$
(4)

where f_f is the part of the heat flow in the front part of the bath; a, b, c are the semiaxes of the ellipsoid.

For points (x, y, z) inside the second semi-ellipsoid at the back of the weld pool, the heat flux was described by the equation (5):

$$q(x, y, z) = \frac{6\sqrt{3}(f_r Q)}{abc_r \pi \sqrt{\pi}} exp\left(\frac{-3x^2}{a^2} - \frac{3y^2}{b^2} - \frac{3z^2}{c_r^2}\right), x < 0,$$
(5)

where f_r is the heat flow to the back of the weld pool.

In the calculations, $f_r/f_r = 1/3$ was taken, and the effective heating efficiency was taken as 0.8.

The specific heat flux was adapted to the equation of uniform motion along a sinusoid, simulating the transverse vibrations of a welding torch:

$$q = Q \cdot exp\left(-3\left(\left(\frac{Z-v \cdot t}{r_1}\right)^2 + \left(\frac{Y}{r_2}\right)^2 + \left(\frac{X-Tsin(A \cdot t)}{r_3}\right)^2\right)\right),\tag{6}$$

where Q is the input power, W; t is the time, s; V is the source velocity, m/h; r_i – ellipsoid semiaxes, m; T – period, s⁻¹; A is the amplitude, mm. The values of T=1.5 mm and r=2.2 mm were taken.

Results and Discussion

Analysis of the simulation results. Figure 4 shows the distributions of temperature fields from a movable heating source of the type of a double Goldak's semi-ellipsoid. Verification of the results of simulation of the thermal problem during welding was carried out by comparing thermal cycles from the nodes of the finite element mesh, corresponding to the places where "K-type" thermocouples are fixed on the welded sample, as shown in Fig. 2.

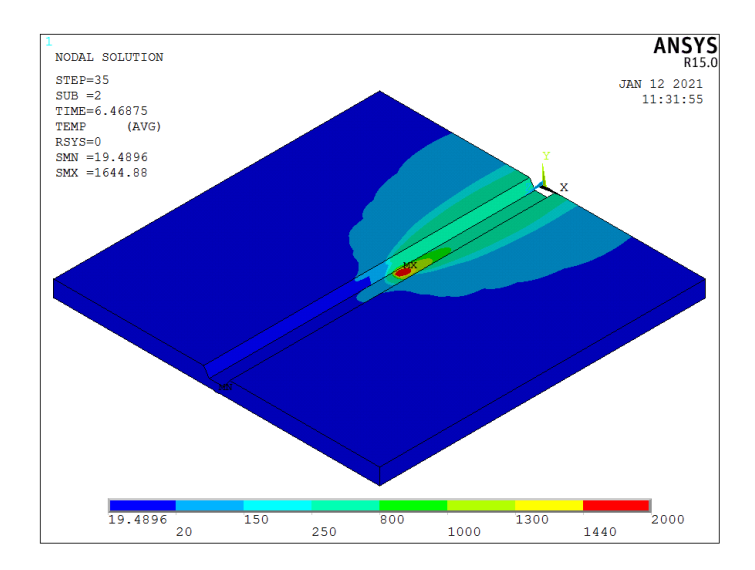


Fig. 4. Distributions of temperature fields from a moving source heating type double semi-ellipsoid Goldak: 1^{st} pass: t=6,47 s

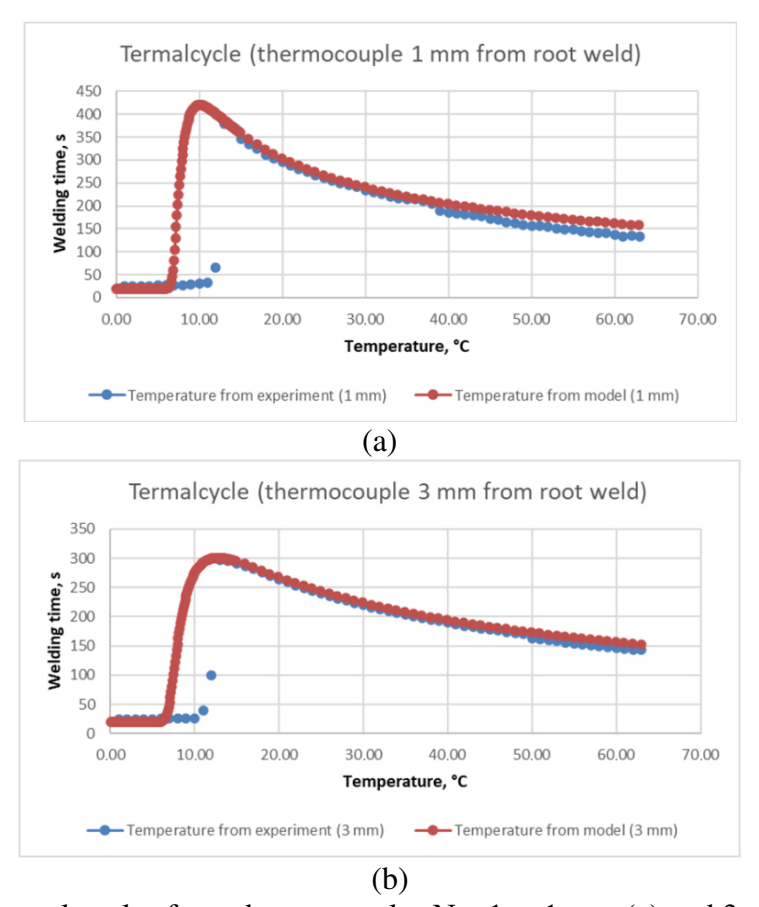
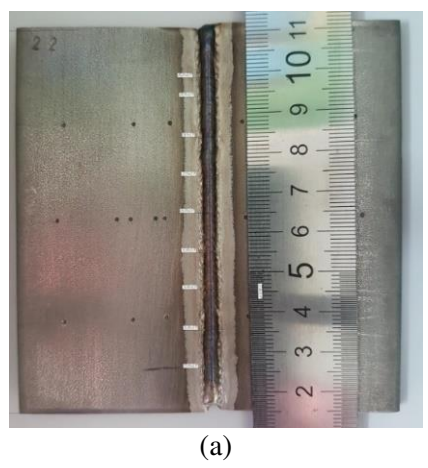


Fig. 5. Thermal cycles from thermocouples No. 1 at 1 mm (a) and 3 mm (b) for root

Figure 5 shows thermal cycles from thermocouples and nodes of a finite element mesh during simulation after the first welding pass, a detailed analysis of thermal cycling of welded specimens is presented in [5,6].

The thermal cycles from the numerical thermal model of welding reflect the actual heating during 2-pass fusion welding of the EP718 alloy with an error of no more than 7% compared to the experimental data.



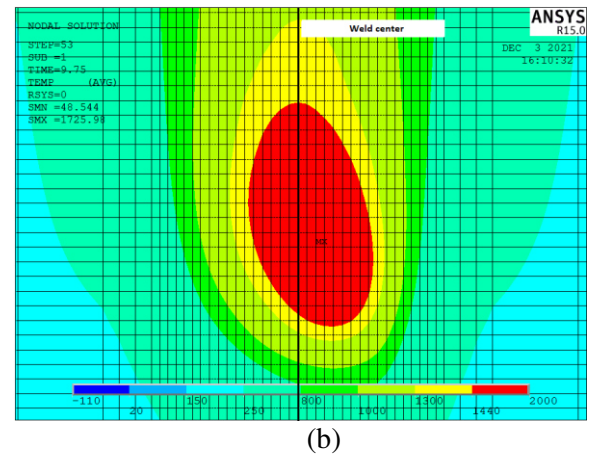


Fig. 6. The width of the weld after a two-pass GMA-welding with transverse vibrations (a) and an example of the penetration zone when modeling the second weld of a GMA-welding with transverse vibrations (b)

Figure 6 shows the measurement of the width of the penetration zone after the second pass of the robotic GMA-welding by measuring the dimensions and bringing them to the desired scale in the KOMPAS 3D program using 9 points along the axis of the weld.

As shown in Fig. 6(b), the width of one element in the weld zone is 0.46 mm, as the source advances to the melting temperature, the conditional weld zone heats up by 15.5 elements in width, which corresponds to 7.13 mm in the width of the penetration zone.

Figure 7 shows a range graph comparing the results of measuring the width of the penetration zone for samples after statistical processing using the least squares method along the median with significance quantiles Q25% and Q75%.

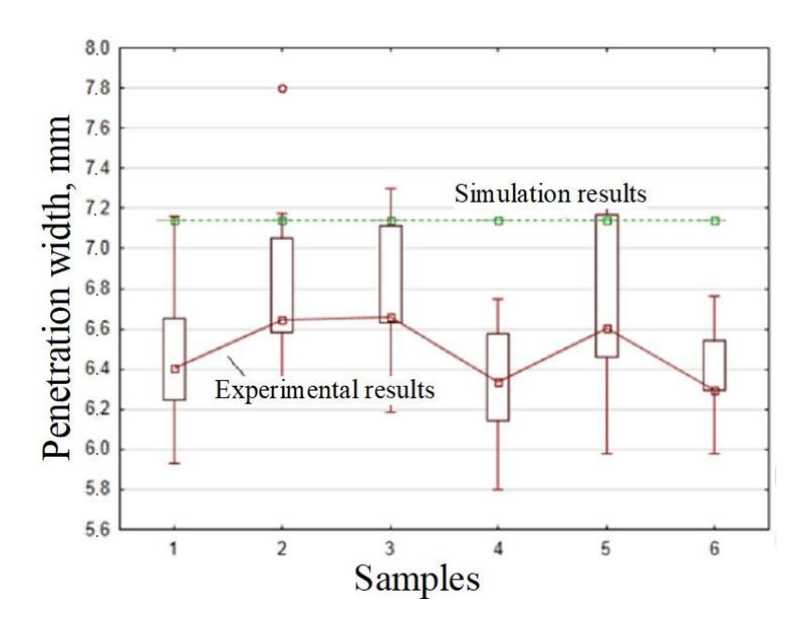


Fig. 7. Range diagram of weld width measurement results

As the comparison of the experimental and modeling data in Fig. 1 demonstrates, the developed numerical temperature model of the 2-pass GMA-welding of the EP718 alloy makes it possible to predict the size of the penetration zone with an error of 9 % compared to the experimental data.

Welded joint deformation and stress analysis. A mathematical model of plasticity behaviour with isotropic hardening (MISO) was used. The mechanical properties were taken according to the OPENCALTHAD method data on the average chemical composition of the EP718 alloy and EP533 wire, since there is no information on the mechanical properties of the alloys in the scientific literature. However, the simulated mechanical properties are almost identical to those of Inconel 718 [14,16–19,24].

The strain hardening curves modeled for the EP718 alloy using the OPENCALTHAD method, are almost identical to the strain hardening curves of the Inconel 718 alloy presented in [11,13].

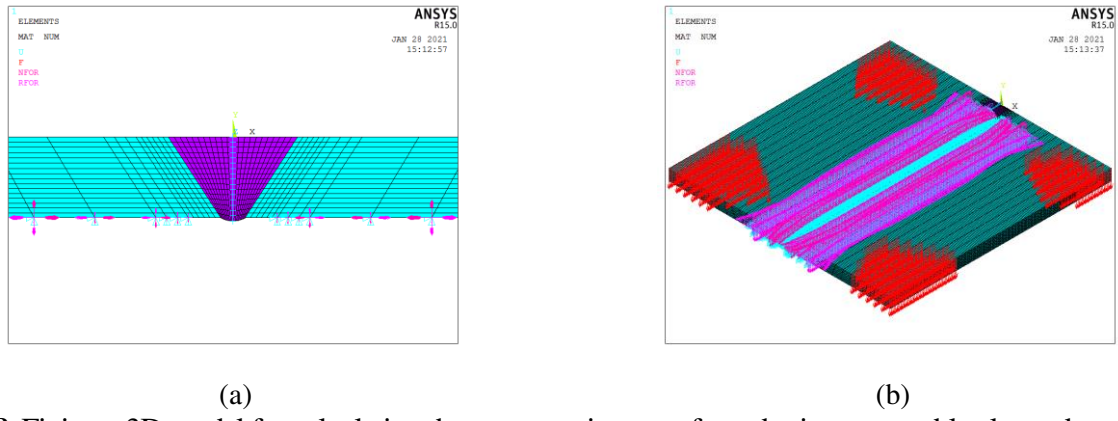


Fig. 8. Fixing a 3D model for calculating the stress-strain state after robotic consumable electrode welding: (a) Fixing along the OX and OY axes, (b) Imitation of clamps for clamping a sample in a tooling

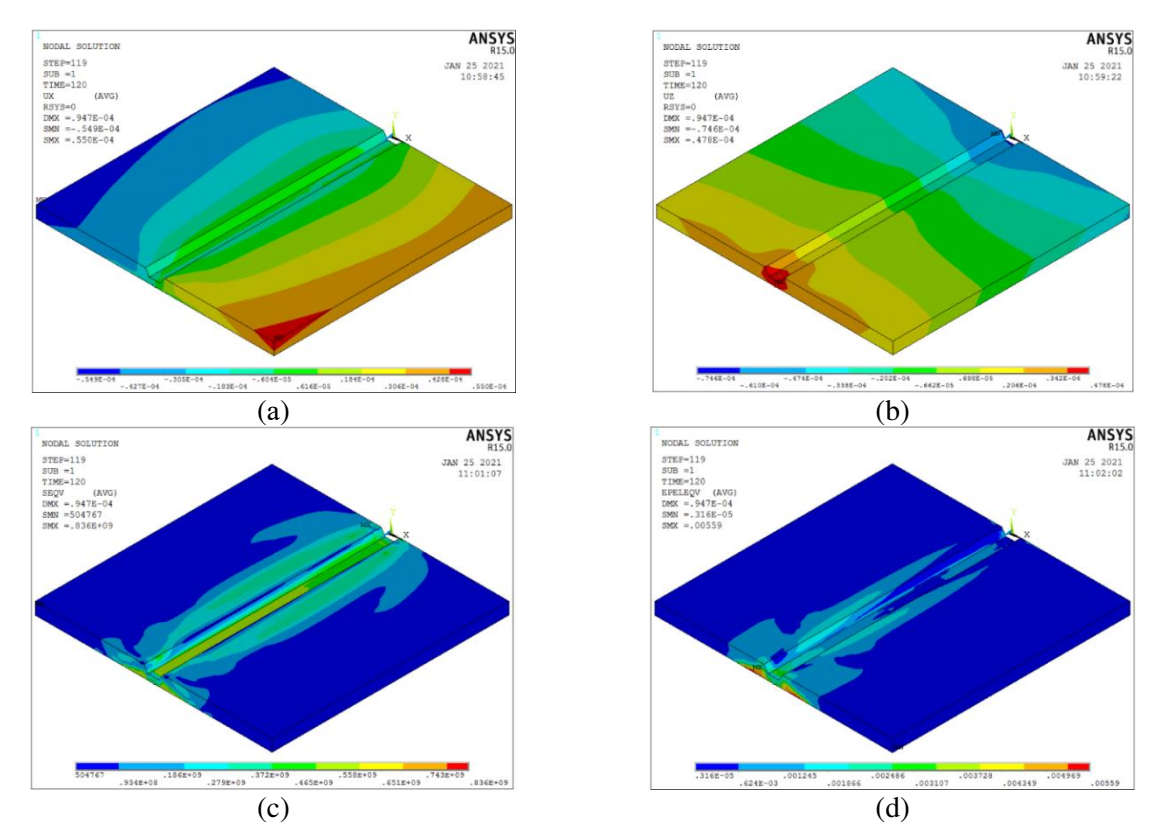


Fig. 9. The results of simulation of displacements (a,b) and residual welding stresses (c,d) during GMA welding of the butt joint of EP718 alloy after the 1st pass

The scheme of fixing the plate in the tooling for calculating deformations is presented in Fig. 8. Fastening along the OX axis is carried out by fixing the movements of nodes along the line in the middle of the plate; along the OY axis – by supporting along the area of contact of the sample with a copper lining and by applying the force of $\approx 20~kg$ for each of the 4 clamps (200 N / number of nodes on the surface). Figure 9 shows the results of modeling the stress-strain state of butt joints from sheet EP718 after the 1st pass.

The simulation results are summarized in Table 2. After the first pass, the equivalent stress level is 836 MPa ($\approx 0.6~\sigma_B$) and decreases to the level of 783 MPa ($\approx 0.56~\sigma_B$), while the transverse shrinkage increases to 0.055 from 0.157 mm after the first pass, which is primarily caused by an increase in the stiffness of the samples after the first pass and the heat input during welding, as well as a decrease in the free volume for plastic deformation between the edges in the second pass. The level of plastic deformation increases from 0.0056 to 0.063 % also due to an increase in the heat input during welding.

Table 2. Simulation results of the stress-strain state of butt joints made of sheet EP718

Condition	Transverse shrinkage, mm	Longitudinal shrinkage, mm	Maximum equivalent stresses, MPa	Maximum equivalent strains, %	
After first pass	0.055	0.048	836	0.0056	
After second pass	0.157	0.125	783	0.063	

Verification of the deformation problem using ATOS. The verification of the stress-strain model (section 3.3) was performed using the ATOS. The ATOS system is a coordinate-measuring topometric system for determining the geometric parameters of surfaces of complex shape. One of the samples with marking points in the ATOS Compact Scan system is shown in Fig. 10(a) - the displacement of points corresponds to the transverse shrinkage of the sample. Figure 10(b) demonstrates a 3D model in ANSYS with points corresponding to the location of the markings on the welded samples.

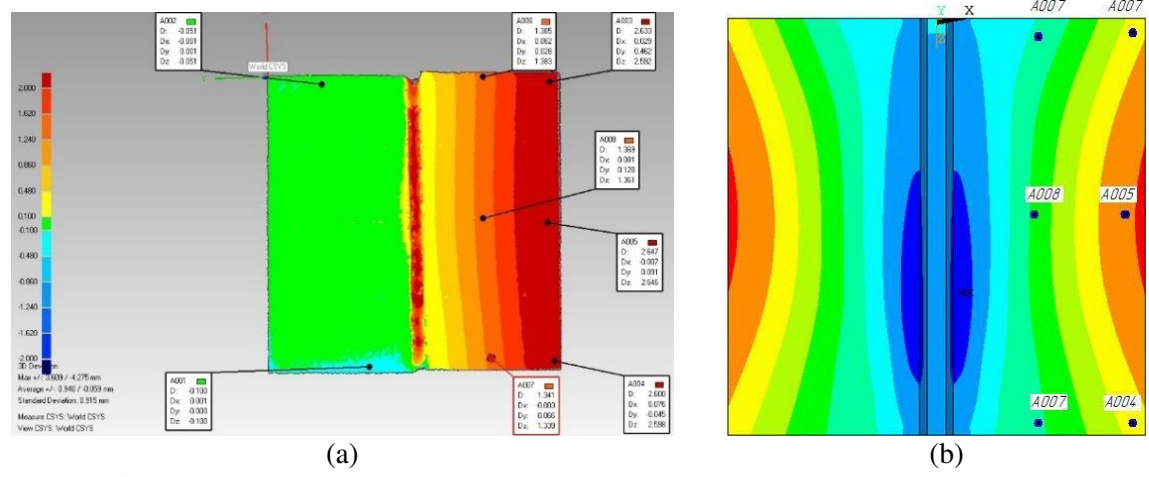


Fig. 10. Movement of points on the outside of the weld after the second pass, measured with ATOS (a) and the corresponding points on the 3D model in ANSYS

The developed numerical thermal deformation model of 2-pass GMA-welding of the EP718 alloy makes it possible to predict deformations with an error of no more than 10% compared to experimental data. And the mechanical properties in the elastic and plastic deformation region for EP718 alloys and EP533 wire, modelled by the OPENCALTHAD method, are suitable for use in the developed thermal deformation model [11,13].

In a number of studies, the same 3D scanning method was used with the ATOS 2 system to evaluate the deformations of welded joints of bimetals obtained by explosion

welding (EXW). Data analysis showed that the scanning accuracy is sufficient not only to assess not only the deformations of welded joints, but also to detect external defects with a size of 0.25 mm [14]. The paper [15] considers the 3D scanning method as one of the options for assessing the deformation of welded joints obtained by arc welding methods - TIG / GMA. However, there are no data on measurement errors in the work.

Verification of the thermal and deformation models with sufficient accuracy for engineering calculations provided the formation of a knowledge base for finite element modeling of the thermal deformation state of a flat sample during and after robotic welding, which makes it possible to synthesize a similar welding model of a real aircraft engine assembly with a large number of welds.

Conclusions

- 1. A thermal model of welding has been developed that reflects the actual heating during 2-pass fusion welding of butt-welded joints 4 mm thick from the EP718 alloy with transverse oscillations of the burner with an error of no more than 7 % compared with the experimental data.
- 2. A thermal deformation model of 2-pass GMA-welding of EP718 alloy of 4 mm thick butt-welded joints with transverse torch oscillations was developed, which makes it possible to predict deformations with an error of no more than 10% compared with experimental data. Verification of residual deformations of welded samples was carried out using the ATOS system.
- 3. Based on the results of numerical simulation of 2-pass GMA-welding of butt-welded joints 4 mm thick from alloy EP718, it was found that the level of equivalent residual stresses according to von Mises in the weld does not exceed 840 MPa $(0.8 \sigma_B)$.
- 4. The thermal deformation model of 2-pass GMA-welding developed during research can be used to assess the stress-strain state of a welded structure of complex spatial geometry with a large number of welds, provided that the parameters of the heating source and the parameters of the finite element mesh of the 3D model of the structure are constant.

References

- 1. Sorokin LI. Filler materials for welding heat-resistant nickel alloys (review). Part 1. *Welding Production*. 2003;4: 4-16. (In-Russian)
- 2. Agilan M, Krishna SC, Manwatkar SK, Vinayan EG, Sivakumar D, Pant B. Effect of Welding Processes (GTAW & EBW) and Solutionizing Temperature on Microfissuring Tendency in Inconel 718 Welds. *Materials Science Forum.* 2012;710: 603–607.
- 3. TU 14-1-1059-74. Sheets from alloy grades KhN45MRTYBR-VD(EP718-VD), KhN45MVTYBR-ID(EP718-ID). Specifications. (In-Russian)
- 4. Nikiforov RV. Improving the technology of TIG-welding of butt joints from thin-sheet corrosion-resistant steels, taking into account thermal deformation processes in the product. Cand. Tech. Sciences Thesis 05.02.10. Moscow; 2014. (In-Russian)
- 5. Atroshchenko VV, Nikiforov RV, Murugova OV. Development of technology for robotic consumable electrode welding of KhN45MVTYuBR alloy joints. *Welding and Diagnostics*. 2020;4: 46–49. (In-Russian)
- 6. Medvedev AU, Nikiforov RV, Galimov VR, Murugova OV, Savichev MP, Bolshakov BO. Peculiarities of the formation of the near-weld zone microstructure during robotic welding of a heterogeneous nickel-based alloy. *Materials. Technologies. Design.* 2021;3(1): 40–47. (In-Russian)
- 7. Nikiforov RV, Murugova OV. Application of robotic GMA-welding for nickel alloys in aircraft engine building. *Youth Bulletin of USATU*. 2020;1(22): 109–111. (In-Russian)
- 8. Nikiforov RV, Murugova OV. Analysis of residual stresses after welding of structures of complex spatial geometry with curved trajectories of welds. *Youth Bulletin of USATU*. 2020;2(23): 101–105. (In-Russian)

- 9. Deng D, Murakawa H. Numerical simulation of temperature field and residual stress in multi-pass welds in stainless steel pipe and comparison with experimental measurements. *Computational Materials Science*. 2006;37(3): 269–277.
- 10. Sorokin LI. On the formation of hot cracks in the seam at welding of heat-resistant alloys. *Welding Production*. 1997;4: 12–18. (In-Russian)
- 11. John N. DuPont, John C. Lippold, Samuel D. Kiser. Welding metallurgy and weldability of nickel-base alloys. A John Wiley & Sons Inc.; 2009.
- 12. Sorokin LI. Stresses and cracks during welding and heat treated heat resistant nickel alloys. *Welding Production*. 1999;12: 11–16. (In-Russian)
- 13. Ramkumar KD, Mulimani SS, Ankit K, Kothari A, Ganguly S, Effect of grain boundary precipitation on the mechanical integrity of EBW joints of Inconel 625. *Materials Science and Engineering: A.* 2021;808: 140926.
- 14. Jerold JP, Dev AM. Comprehensive Analysis of TIG Welded Inconel–718 Alloy for Different Heat Input Conditions. *International Journal of Engineering and Technology*. 2018;(3.6): 206–209.
- 15. Urminsky J, Marônek M, Jáňa M, Morovič L. Analysis of Weld Joint Deformations by Optical 3D Scanning. *Acta Polytech.* 2016;56(1): 76–80.
- 16. The ABC's of Arc Welding and Inspection. Tokio, Japan: Kobe Steel, LTD; 2011.
- 17. Benoit A, Jobez S, Paillard P, Klosek V & Baudin T. Study of Inconel 718 weldability using MIG CMT process. *Science and Technology of Welding and Joints*. 2011;16(6): 477–482.
- 18. Isaev LS. Simulation of heat transfer processes during laser welding of dissimilar metals using an intermediate insert. *Bulletin of Samara State Technical University*. *Technical Sciences*. 2016;4(52): 123–129. (In-Russian)
- 19. Brochu M. Thermal stability of a Stellite/steel hardfacing interface during long-term aging. In: *Proc. of 13th International Conference on Fracture, Beijing, China, June 16-21, 2013.* 2013. p.1–10.
- 20. Gregori A. Welding and Deposition of Nickel Superalloys 718, Waspaloy and Single Crystal Alloy CMSX-10. *Welding in the World*. 2007;51(11–12): 34–47.
- 21. Devendranath Ramkumar K, Jagat Sai R, Santhosh Reddy V, Gundla S, Harsha Mohan T, Saxena V, Arivazhagan N, Effect of filler wires and direct ageing on the microstructure and mechanical properties in the multi-pass welding of Inconel 718. *Journal of Manufacturing Processes*. 2015;18: 23–45.
- 22. Tkacheva AV, Abashkin EE. Impact of forced cooling of the joint zone and thermal effect on the distribution values of residual stress generated by arc welding. *Materials Physics and Mechanics*. 2022;50(3): 509–517.
- 23. Mimmi A, Merzoug M, Ghazi A, DellalN. Mechanical behavior of structures welded with friction stir lap welding process. *Materials Physics and Mechanics*. 2023;51(2): 151–163.

THE AUTHORS

Medvedev A.Yu.

e-mail: medvedev.ayu@ugatu.su

Shaikhulova A.F. 🗓

e-mail: shaihulova@inbox.ru

Murugova O.V.

e-mail: murugova.oxana@mail.ru

Medvedev A.E.

e-mail: medvedevandreyrf@gmail.com

Nikiforov R.V.

e-mail: nikiforov_svarka@mail.ru

Galimov V.R.

e-mail: houndedreaper@mail.ru

Simplistic model for the investigation of mechanical stability parameters of pyrochlore structured solids

Submitted: January 19, 2023

Accepted: September 6, 2023

Approved: May 15, 2023

Abstract. Herein, we present a simplistic theoretical model for the calculation of bulk modulus, shear modulus and Young's modulus. These parameters indicates that investigated materials show stability or instability in nature. A stable material may be used in many applications like thermoelectric, photovoltaic, etc. In this paper, we have found all the materials have good stability. We have proposed a simple relation with plasmon oscillation theory. The calculated values are in better agreement with their experimental and reported values, and even for many pyrochlore compounds, these are revealed for the first time, and have great potential for technological applications of thermal barrier coatings (TBC) in aerospace, construction, nuclear reactors, and supercritical boiler industries.

Keywords: bulk modulus; shear modulus; Young's modulus; rare earth pyrochlores

Citation: Bhati R, Yadav DS, Gupta RC, Verma AS. Simplistic model for the investigation of mechanical stability parameters of pyrochlore structured solids. *Materials Physics and Mechanics*. 2023;51(5): 90-98. DOI: 10.18149/MPM.5152023_9.

Introduction

During the last few years, increasing attention has been given to the theoretical study of physical, chemical and elastic properties of cubic phase $A_2^{+3}B_2^{+4}O_7$ pyrochlore oxide solids because of their important role in thermal barrier coatings (TBC) for gas turbine energies, superconductivity, fast ion conductors, catalyst design, dielectrics, nuclear waste encapsulation, high-temperature stability, boiler, thermoelectric and optoelectronic applications. These materials have thermal efficiencies, high melting temperatures, low thermal conductivities and low cost [1-6]. Pyrochlore materials are of great technical importance and have fundamental interest in aerospace, construction, and solid oxide fuel cells [7-10]. The REP (rare earth pyrochlores) has composition $A_2^{+3}B_2^{+4}O_7$, here A and B are metallic cations of the geometry trivalent, tetravalent, or divalent, pentavalent, respectively [11-14]. Pyrochlore complexes (stannate, titanate, zirconate, hafnate) are of face centered cubic (FCC) structure with a generic formula $A_2^{+3}B_2^{+4}O_7$. This system has unit cell with space group Fd-3m/227 and eight formula units (Z=8) with 88 ions; among them 16 A⁺³cations, 16B⁺⁴cations and 56 O^{-2} anions [15]. In this geometry, Ti^{+4} cations occupy the 16c (0, 0, 0) position, the A^{+3} cations are at the Wyckoff positions 16d (1/2, 12, 1/2), and O^{-2} anions reside at the 8b (3/8, 3/8, 3/8) and 48f (x, 1/8, 1/8) positions. In the conformation of pyrochlore $A_2^{+3}B_2^{+4}O_7$, A-site cations (atomic radius of ~100 pm) are coordinated with six 48f 0^{-2} and two 8b 0^{-2} ; whereas B cations (atomic radius of 60.5 pm) are coordinated with six $48f O^{-2}$ anions. In the stereotype of pyrochlore structure

(x= 0.3125); The B and A atoms are coordinated by typical octahedra and skewed cubes, respectively. The B-site polyhedral deformed into a trigonal antiprism (when x rose to 0.375) and the rare earth A-site polyhedral changed to regular cubes. The stable structure pyrochlore is obtained when $1.46 \le r_A/r_B \ge 1.78$ (r_A and r_B denote the radii of A^{+3} and B^{+4} cations, respectively) [15]; while the fluorite structure is stable when $r_A/r_B < 1.46$.

The rare earth stannate were synthesized using the solid state methods by Kennedy et al. [16]. They ascertained structural parameters and found $x48f0^{-2}$ decreases monotonically with increasing lattice parameters. In further course of time Liu et al. studied structural stability, theoretical elastic stiffness, and thermal conductivity of $La_2T_2O_7(T = Ge, Ti, Sn, Zr, and Hf)$ [17]. They showed that comparatively weak bonds of La-O in La₂T₂O₇ contribute a predominant role in assessing the thermal, mechanical properties; and structural stability. Later, Chernyshev et al. [18] have used ab-initio calculations to study the elastic properties of rare earth titanate. Kushwaha [19] has studied the thermodynamic, vibrational and mechanical properties of RE₂Ti₂O₇ (RE = Sm, Gd, Dy, Ho, Er, Yb) pyrochlores using suggested eight parameter bondbending force constant model. Feng et al. [20,21] have performed experimental and theoretical methods for calculating the thermal conductivity, chemical bonding, structural, and mechanical properties of Ln₂Zn₂O₇ (Ln = La, Pr, Nd, Sm, Eu, and Gd) by applying the LSDA+U methods and in RE₂Sn₂O₇ using DFT (density functional theory) and ultrasonic resonance methods. Again, Liu et al. [22,23] have executed the first principles approach to investigate structural and mechanical properties of rare earth stannate and titanate pyrochlores. Many other researchers [24–27] have evolved various theories to analyze the structural, mechanical, thermal, and chemical properties of ideal REP; such as bond angle, bond length, lattice parameters, elastic moduli, volume expansion coefficient, and linear thermal expansion coefficient (TEC). Due to hardships fetched by experimental processes and their high cost, as well as intricacies in obtaining accurate values of the above discussed parameters; researchers have moved to calculate these parameters by theoretical methods using a series of approximations, but such a method has always been complex [17,27]. In past years, many theoretical calculations based on empirical relationships have become the crucial part of the material research. Mostly, empirical formula has been found to be simple, easy to use and provide better results for physical parameters. Consequently, empirical formulae have accepted as the methods of choice for computational solid state researches.

In earlier researches, authors used the plasmon oscillation theory of solids to successfully develop empirical relationships for electronic, structural, and mechanical properties of zinc blende and rock salt structured solids and ternary chalcopyrite semiconductors [28–30]. These results validate the relevance plasmon oscillation theory, as it determines various characteristics of quantum aspects; until now this has remained closer to accuracy. Plasmon energy relies on the quantity of valance electrons, which varies as a metal form a compound. Empirical correlations sometimes don't produce incredibly exact findings for each unique substance; though, they may still be helpful, nevertheless, the plasmon energy dependent elastic properties of REP have been investigated. Thus, noticing the accuracy in previous researches provided by plasmon oscillations theory [31–33]; this study is focused to offer a different and more accurate explanation for the shear modulus (G), bulk modulus (B), and Young's moduli (E) of ternary compounds with cubic pyrochlore structure. As far as, it is acknowledged, besides a few earlier studies on this phenomenon, there have not been any studies on the impact of conduction delectrons in REP (effect of conduction d-electrons) [6,34]. Whether, this occurrence is common among rare-earth pyrochlores is a crucial question. Hence, d-electrons effect persists in REP. In this respect, results of this investigation will have a favourable impact on further studies of physical and chemical properties; as well as promotes the applications REP in many diverse fields of material research.

The objectives of this study were to estimate the elastic properties of REP $A_2^{+3}B_2^{+4}O_7(A=La\to Lu \text{ and }Y;\text{ and }B=Sn,Ti,Zr,Hf)$ applying the valance electron plasmon oscillation theory of solids.

Scientific backgrounds and results and discussion

The tendency of material to deform elastically when a deforming force is applied is described by elastic characteristics including bulk, shear, and Young's moduli; which are employed as measures of a material's mechanical strength. Kamran et al. suggested a semi-empirical formula of shear modulus based on ionicity fraction of bonding for diamond like and zinc-blende covalent crystals [35]. Li et al. [36] have proposed that the bond ionicity of compounds, and electronegativity of atoms A and B can be used to express the shear modulus (G) of zinc-blende structured solids as given below:

$$G = K_1 (\chi_A \chi_B)^{K_2} (1 - f_i)^{K_3}, \tag{1}$$

where K_1 , K_2 , and K_3 are constants.

Cohen [37,38] has arrived at equations for bulk and shear moduli as the second order partial differential equation of total energy E with respect to some suitable deformation parameter at the equilibrium state:

$$G = \frac{1}{\Omega} \frac{\partial^2 E}{\partial \delta^2} \Big|_{\delta = \delta_o},\tag{2}$$

$$B = \Omega \frac{\partial^2 E}{\partial \Omega^2} \Big|_{\Omega = \Omega_o}, \tag{3}$$

where δ and Ω are dimensionless parameters and volume, respectively. Thus, in order to create the equations for the bulk and shear moduli, it is evident that the energy derivatives must first be estimated in terms of the chemical bonding parameters.

Forst and Ashby [39] have suggested the empirical equations for Young's modulus (E) and shear modulus (G) in order to establish correlations among the elastic properties of polycrystalline solids and their melting temperature T_m .

$$E = 100 K_B T_m / \Omega, \tag{4}$$

$$G = 44 K_B T_m / \Omega, \tag{5}$$

where K_B is Botzmann's constant, T_m is melting temperature of compound and Ω is volume of unit cell.

They have improved their correlation (5) on shear modulus by analyzing the variation in numerical coefficient. These coefficients were determined based on the crystal structure and chemical bonding of the material class. This coefficient was constant for every category of material and varied from 20 to 95 for alkali metals to basic oxides with the crystal structure α -A₂O₃ (corundum). Applying this notion, concept of iso-mechanical group was developed by them. When combined with the suitable empirical normalization, this group of materials exhibits that mechanical and transport properties are quite comparable or identical.

Verma et al. [40,41] have proposed the following empirical relationships of lattice thermal conductivity K and bulk modulus B for ternary tetrahedral semiconductors as the function of the bond length and product of ionic charges.

$$K = T_m (Z_A Z_B Z_C)^{0.845} d^{-5}, (6)$$

$$B = (Z_A Z_B Z_C)^S V d^{-5}, \tag{7}$$

where V and S are constants for chalcopyrite solids and depends upon crystal lattice, T_m -melting temperature, and Z_A , Z_B , Z_C are the ionic charges on the A, B and C elements.

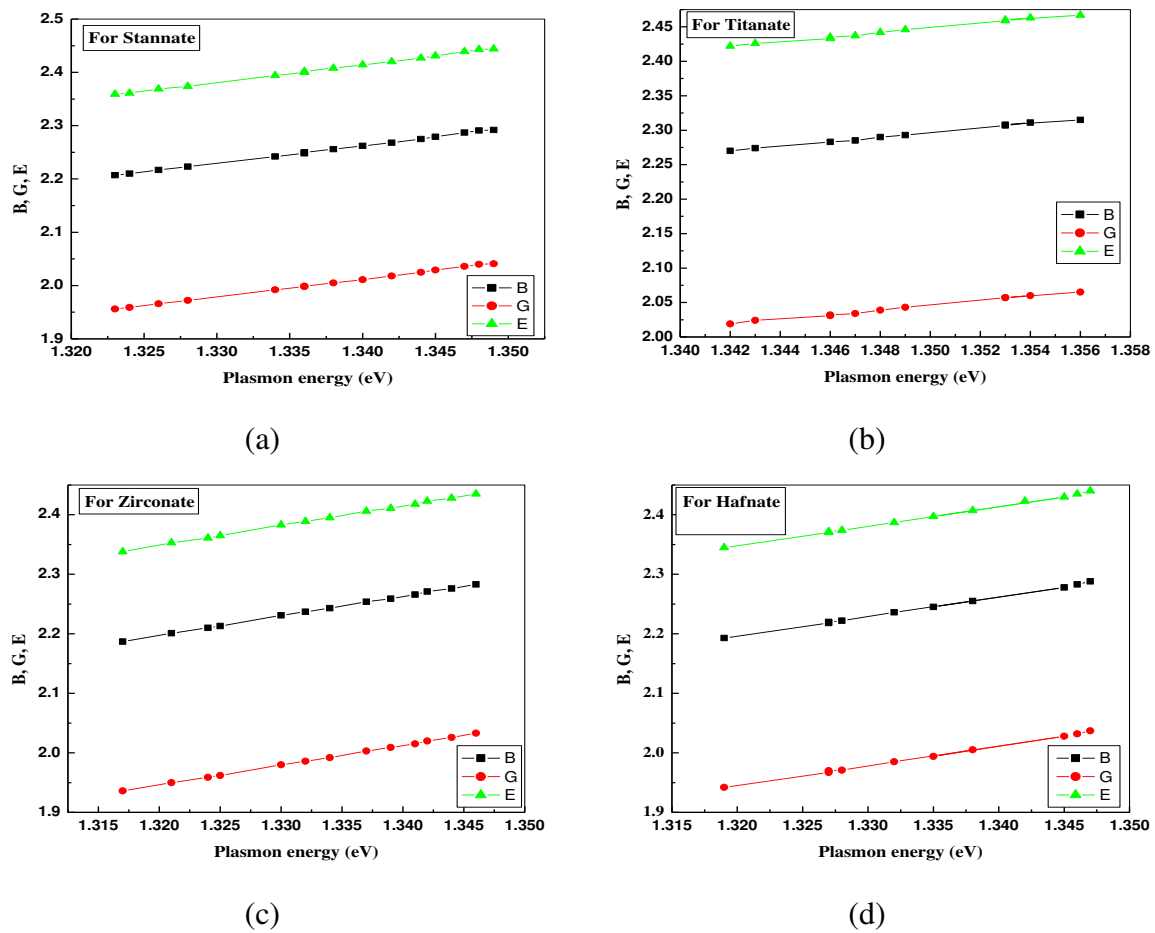


Fig. 1. Plot of elastic constants (B, G, E) versus plasmon energy on log-log scale for rare earth pyrochlores for stannate (a), titanate (b), zirconate (c), and hafnate (d)

Ionic charge is modified when a metal makes a compound because it depends on the amount of valance electrons and the plasmon energy therein. Here, the calculated results are reported in Fig. 1. The results show that bulk modulus (*B*), shear modulus (*G*), and Young's modulus (*E*) illustrate a linear relationships; lie on a straight line; and increasing trend when draw on a log-log scale against the plasmon energy of the compounds. Many authors have found that drastically lowered plasmon energy can be used to get better agreement with experimental values of electronic, mechanical, static and dynamic characteristics of binary solids, ternary chalcopyrite semiconductors, and rare earth mono-chalcogenides [40–42]. Now, we may extend relationships (1)-(5) as the function of plasmon energy with minor modifications for cubic structured rare earth pyrochlores, and consequently we get the better agreement between experimental and theoretical data.

$$B = \zeta (\hbar \omega_p)^{\mu}, \tag{8}$$

$$G = \kappa (\hbar \omega_p)^{\eta}, \tag{9}$$

$$E = \varsigma (\hbar \omega_{\rm p})^{\eta}, \tag{10}$$

where ζ , κ , ς , μ , and η are constants varies with the group of materials. The constants ζ , κ , ς have values 0.006254, 0.00335 and 0.004247 GPa/ eV, respectively. The exponents μ and η have values 3.35 and 3.344, respectively. The plasmon energy ($\hbar\omega_p$) of these compounds was estimated elsewhere [42].

Table 1. Calculated values of bulk, shear and Young's moduli of tin based rare earth

pyrochlores with the available theoretical and experimental data

pyrochlores	with the							ı			
		E	Bulk modul	us	Sh	ear modul	us	Yo	Young modulus		
		~ .	B, GPa		~ .	G, GPa	1	E, GPa			
$A_2B_2O_7$	$\hbar\omega_p(eV)$	Cal. Eq.	Theo.	Expt.	Cal. Eq.	Theo.	Expt.	Cal. Eq.	Theo.	Expt.	
		(9)			(10)			(11)			
La ₂ Sn ₂ O ₇	21.05	161.06	155.75 ^a , 182.30 ^a 190.00 ^q	188.90 ^d	90.37	95.00 ^q		228.40	245.00 ^q		
Ce ₂ Sn ₂ O ₇	21.09	162.08	160.81a		90.95			229.86			
Pr ₂ Sn ₂ O ₇	21.20	164.92	158.51a		92.55			233.89			
Nd ₂ Sn ₂ O ₇	21.28	167.00	162.73 ^a , 187.4 ^a	199.2 ^d	93.72			236.86			
Sm ₂ Sn ₂ O ₇	21.57	174.71	163.24 ^a , 187.50 ^a	193.77 ^d	98.07			247.84			
$Eu_2Sn_2O_7$	21.66	177.15	128.18 ^a		99.45			251.32			
Gd ₂ Sn ₂ O ₇	21.68	177.70	166.37 ^a , 176.60 ^a	192.77 ^d	99.75	89.00 ^r		252.10	226.00 ^r		
$Tb_2Sn_2O_7$	21.77	180.17	167.99a		101.15			255.62			
$Dy_2Sn_2O_7$	21.86	182.66	168.36a		102.56			259.17			
$Ho_2Sn_2O_7$	21.96	185.46	169.46a		104.14			263.16			
Er ₂ Sn ₂ O ₇	22.07	188.58	170.36 ^a , 188.7 ^a	193.50 ^d	105.89			267.60			
$Tm_2Sn_2O_7$	22.13	190.29	170.69a		106.86			270.04			
Yb ₂ Sn ₂ O ₇	22.24	193.46	127.69 ^a , 172.63 ^a	192.23 ^d	108.65			274.56			
Lu ₂ Sn ₂ O ₇	22.30	195.21	176.07a		109.64			277.05			
Y ₂ Sn ₂ O ₇	22.32	195.79			109.97			277.88			
La ₂ Ti ₂ O ₇	21.980	186.03	176.72 ^b , 199 ^t		104.45	99.00 ^t		263.97	253.00 ^t		
Sm ₂ Ti ₂ O ₇	22.051	188.04	184.29 ^b , 206.00 ^h		105.59	108.00 ^h		266.83	277.00 ^h		
Eu ₂ Ti ₂ O ₇	22.161	191.73	140.60 ^b		107.36			271.31			
Gd ₂ Ti ₂ O ₇	22.180	191.73	186.91 ^b , 186.00 ^c , 206.00 ^e 200.00 ^h		107.67	107.00 ^h		272.09	272.00 ^h		
Tb ₂ Ti ₂ O ₇	22.212	192.65	187.87 ^b , 207.00 ^e	199±1 ^g 204.00 ^f	108.19			273.41			
Dy ₂ Ti ₂ O ₇	22.293	195.00	188.91 ^b , 208.00 ^e , 194.00 ^h	197.00 ^f	109.52	105.00 ^h		276.76	267.00 ^h		
Ho ₂ Ti ₂ O ₇	22.346	196.55	189.83 ^b , 209.00 ^e	213±2g 200.00f	110.40	104 ^h		278.97	264.00 ^h		
Er ₂ Ti ₂ O ₇	22.556	202.78	191.0 ^b , 209.00 ^e		113.91	101.00 ^h		287.84	256.00 ^h		
Tm ₂ Ti ₂ O ₇	22.615	204.55	190.69 ^b , 210.00 ^e		114.91			290.37			
Yb ₂ Ti ₂ O ₇	22.568	203.14	210.00°, 178.00 ^h		114.11	97.00 ^h		288.36	246.00 ^h		
Lu ₂ Ti ₂ O ₇	22.683	206.61	191.89 ^b , 211.00 ^e	181.00 ^f	116.07			293.30			

aRef. [23], bRef. [22], cRef. [45], dRef. [20], Ref. [18], fRef. [45], sRef. [46], bRef. [19], Ref. [21], iRef. [47], kRef. [48], hRef. [49], mRef. [50], Ref. [25], Ref. [24], rRef. [51], dRef. [17], Ref. [52], Ref. [53], Ref. [54].

The utility of relations (8)-(10) lies in the fact that they just need plasmon energy of the of rare earth pyrochlores as input values instead experimental data. A full explanation of the elastic properties of rare earth stannate, zirconate, titanate and hafnate has been given elsewhere [18–28]. Explicitly, an analogue evolves among the ternary pyrochlores, this may be used to calculate the elastic properties from their plasmon energy $(\hbar\omega_p)$. Equations (8)-(10) are the

expression of elastic properties for cubic structured rare earth pyrochlores. In this paper we employ equations (8)-(10) to study the elastic properties of pyrochlores depend upon plasmon energy of the material and presented in Tables 1 and 2. For comparison purposes theoretical and experimental values by earlier researchers are presented in this table. From this table it is evident that calculated values of elastic properties are in good conformity with experimental values as compared to others theoretical findings. From the table it is also clear that experimental and theoretical data is not available for most of the compounds; and the elastic constants values for these pyrochlores are calculated first time in this work. So, these values will be helpful in determining other characteristic values, which find technological applications especially in the TBC industry.

Table 2. Calculated values of bulk, shear and Young's moduli of zirconium based rare earth

pyrochlores with the available theoretical and experimental data

pyrocinores	- With the	Bulk modulus				ear modu		Young's modulus		
			B, GPa	T	G, GPa				E, GPa	1
$A_2B_2O_7$	$\hbar\omega_{p}$, eV	Cal. Eq. (9)	Theo.	Expt.	Cal. Eq. (10)	Theo.	Expt.	Cal. Eq. (11)	Theo.	Expt.
La ₂ Zr ₂ O ₇	20.758	153.73	176.00 ⁱ 192.00 ^m 200.00 ⁿ 179.00 ^o 191.00 ^p 179.00 ^q	175.00 ^j	86.24	87 ⁱ 107 ^m 73 ⁿ 83 ^o 106 ^p 93 ^q	92 ^j	217.97	208 ⁱ 271 ^m 195 ⁿ 214 ^o 268 ^p 237 ^q	186 ^j 175 ^r 239*
$Ce_2Zr_2O_7$	20.964	158.88			89.14			225.29		
$Pr_2Zr_2O_7$	21.088	162.03	155.00 ⁱ	149.00 ^k	90.92	103.00i	100.00 ^k	229.78	224.00 ⁱ	215.00 ^k
Nd ₂ Zr ₂ O ₇	21.135	163.24	164.00 ^r 127.00 ⁱ	131.00 ¹	91.60	88.00 ^r 60.00 ⁱ	86.00s	231.50	224.00 ^r 213.00 ⁱ	219.00s
Sm ₂ Zr ₂ O ₇	21.402	170.21	167.00 ^r 197.00 ⁱ	181.00 ^k	95.53	89.00 ^r 100.00 ⁱ	96.00 ^k 90.00 ^s	241.44	226.00 ^r 252.00 ⁱ	231.00s
Eu ₂ Zr ₂ O ₇	21.491	172.59	149.00 ⁱ	140.00 ^k	96.87	67.00 ⁱ	72.00 ^k	244.82	243.00i	229.00 ^k
Gd ₂ Zr ₂ O ₇	21.583	175.06	165.00 ⁱ	156.00 ^s 175.00 ^t 158.00 ^l	98.27	88.00 ^r 63.00 ⁱ	89.00 ^t 80.00 ^s 66.00 ^l	248.34	224.00 ^r 214.00 ⁱ	238.00 ^t 205.00 ^s
Tb ₂ Zr ₂ O ₇	21.743	179.42			100.73			254.56		
Dy ₂ Zr ₂ O ₇	21.825	181.69			102.01			257.79		
Ho ₂ Zr ₂ O ₇	21.922	184.39			103.53			261.64		
$Er_2Zr_2O_7$	21.998	186.53			104.74			264.69		
$Tm_2Zr_2O_7$	22.084	188.98			106.12			268.17		
$Yb_2Zr_2O_7$	22.187	191.93			107.79			272.38		
La ₂ Hf ₂ O ₇	20.848	155.96	180.00 ^q		87.50	88.00 ^q		221.15	228.00 ^q	
Ce ₂ Hf ₂ O ₇	21.210	165.18			92.69			234.26		
Pr ₂ Hf ₂ O ₇	21.246	166.11			93.22			235.60		
$Nd_2Hf_2O_7$	21.267	166.66			93.53			236.38		
Sm ₂ Hf ₂ O ₇	21.469	172.00			96.54			243.98		
Eu ₂ Hf ₂ O ₇	22.110	189.72			106.54			269.23		
Gd ₂ Hf ₂ O ₇	21.610	175.79	170.00 ^r		98.68	96.00 ^r		249.38	242.00 ^r	
Tb ₂ Hf ₂ O ₇	21.765	180.03			101.07			255.42		
Dy ₂ Hf ₂ O ₇	21.891	183.53			103.04			260.41		
Ho ₂ Hf ₂ O ₇	21.998	186.53			104.74			264.69		
Er ₂ Hf ₂ O ₇	22.094	189.26			106.28			268.58		
$Tm_2Hf_2O_7$	22.183	191.81			107.72			272.22		
Yb ₂ Hf ₂ O ₇	22.254	193.87			108.88			275.14		

^aRef. [23], ^bRef. [22], ^cRef. [45], ^dRef. [20], ^cRef. [18], ^fRef. [45], ^sRef. [46], ^bRef. [19], ⁱRef. [21], ^jRef. [47], ^kRef. [48], ^hRef. [49], ^mRef. [50], ⁿRef. [25], ^cRef. [24], ^pRef. [51], ^qRef. [17], ^rRef. [52], ^sRef. [53], ^mRef. [54].

Concluding remarks

From the discussion in scientific background, it is concluded that plasmon energy of valance electrons in the compound is an important parameter in determining elastic characteristics of rare earth pyrochlores and is a pioneering work. Henceforth, it is found that elastic properties of the materials investigated here present a linear relationship and lie on a straight line when potted on a log-log scale against the plasmon energy. The evaluated values revealed a predictable pattern and agreed with the information provided so far, demonstrating the validity of the proposed approach.

Briefly, a simple model is postulated for the calculation of bulk modulus, shear modulus and Young's modulus of cubic structured rare earth pyrochlores. Furthermore, predictions of this model on elastic properties are reasonably consistent with experimental and theoretical data obtained by using various methodologies. Confidently, this theory will present an important role where experimental data of these elastic properties is not available and to discover new compounds with targeted values of bulk modulus, shear modulus, Young's modulus and Poisson's ratio in a series of a large family of rare earth pyrochlores, which are of utmost technological applications, now-a-days.

References

- 1. Zhang J, Lian J, Fuentes AF, Zhang F, Lang M, Lu F, Ewing RC. Enhanced radiation resistance of nanocrystalline pyrochlore Gd₂(Ti_{0.65}Zr_{0.35})₂O₇. *Applied Physics Letters*. 2009;94(24): 243110.
- 2. Pirzada M, Grimes RW, Minervini L, Maguire JF, Sickafus KE. Oxygen migration in A2B2O7 pyrochlores. *Solid State Ionics*. 2001;140(3-4): 201–208.
- 3. Clarke DR. Materials selection guidelines for low thermal conductivity thermal barrier coatings. *Surface and Coatings Technology*. 2003;163-164: 67–74.
- 4. Park JK, Kim CH, Choi KJ, Park HD, Choi SY. Photoluminescence behavior of Al³⁺, Pr³⁺ doped perovskite La_{2/3}TiO₃ and pyrochlore La₂Ti₂O₇. *Journal of Materials Research*. 2001;16: 2568–2571.
- 5. Dong L, Li Y, Devanathan R, Gao F. Molecular dynamics simulation of the structural, elastic, and thermal properties of pyrochlores. *RSC Advances*. 2016;6(47): 41410–41419.
- 6. Zhang S, Zhang HB, Zhao FA, Jiang M, Xiao HY, Liu ZJ, Zu XT. Impact of isovalent and aliovalent substitution on the mechanical and thermal properties of Gd₂Zr₂O₇. *Scientific Reports*. 2017;7(1): 6399.
- 7. Petrov VP, Chernyshev VA, Nikiforov AE. Structural and vibrational properties of crystals with a rare-earth sublattice: Ab initio calculations. *Solid State Phenomena*. 2018;271: 85–91.
- 8. Sun M, Sui Y, Gao K, Tan C, Dai L, Zhou G, Zhang Y, Wang L. Theoretical analysis of thermal and mechanical properties of Eu₂Hf₂O₇ and Gd₂Hf₂O₇ pyrochlores. *Journal of the Ceramic Society of Japan*. 2019;127(10): 722–727.
- 9. Karthick G, Karati A, Murty BS. Low temperature synthesis of nanocrystalline Y₂Ti₂O₇, Y₂Zr₂O₇, Y₂Hf₂O₇ with exceptional hardness by reverse co-precipitation technique. *Journal of Alloys and Compounds*. 2020;837: 155491.
- 10. Raza A, Afaq A, Kiani MS, Ahmed M, Bakar A, Asif M. First-principles calculations to investigate elasto-mechanical and opto-electronic properties of pyrochlore oxides X₂Zr₂O₇ (X= La, Nd). *Journal of Materials Research and Technology*. 2022;18: 5005–5018.
- 11. Yang J, Shahid M, Zhao M, Feng J, Wan C, Pan W. Physical properties of La₂B₂O₇ (BZr, Sn, Hf and Ge) pyrochlore: first-principles calculations. *Journal of Alloys and Compounds*. 2016;663: 834-841.
- 12. Sayir, Farmer SC, Dynys F. *Advances in Electronics and Eletrochemical Ceramics*. John Wiley and Sons; 2006.
- 13. Anantharaman AP, Dasari HP. Potential of pyrochlore structure materials in solid oxide fuel cell applications. *Ceramics International*. 2021;47(4): 4367–4388.
- 14. Chartier A, Meis C, Crocombette JP, Corrales LR, Weber WJ. Atomistic modeling of displacement cascades in La₂Zr₂O₇ pyrochlore. *Physical Review B*. 2003;67(17): 174102.

- 15. Subramanian MA, Aravamudan G, Rao GS. Oxide pyrochlores—a review. *Progress in Solid State Chemistry*. 1983;15(2): 55–143.
- 16. Kennedy BJ, Hunter BA, Howard CJ. Structural and bonding trends in tin pyrochlore oxides. *Journal of Solid State Chemistry*. 1997;130(1): 58–65.
- 17. Liu B, Wang JY, Li FZ, Zhou YC. Theoretical elastic stiffness, structural stability and thermal conductivity of La₂T₂O₇ (T= Ge, Ti, Sn, Zr, Hf) pyrochlore. *Acta Materialia*. 2010;58(13): 4369–4377.
- 18. Chernyshev VA, Petrov VP, Nikiforov AE, Agzamova PA, Avram NM. Elastic properties of rare earth pyrochlores R₂Ti₂O₇ (R= Gd, Tb, Dy, Ho, Er, Tm, Yb, Lu): Ab initio calculations. *Optical Materials*. 2017;72: 565–570.
- 19. Kushwaha AK. Vibrational, mechanical and thermodynamical properties of RE₂Ti₂O₇ (RE= Sm, Gd, Dy, Ho, Er and Yb) pyrochlores. *International Journal of Modern Physics B*. 2017;31(21): 1750145.
- 20. Feng J, Xiao B, Qu ZX, Zhou R, Pan W. Mechanical properties of rare earth stannate pyrochlores. *Applied Physics Letters*. 2011;99(20): 201909.
- 21. Feng J, Xiao B, Wan CL, Qu ZX, Huang ZC, Chen JC, Zhou R, Pan WJ. Electronic structure, mechanical properties and thermal conductivity of Ln₂Zr₂O₇ (Ln= La, Pr, Nd, Sm, Eu and Gd) pyrochlore. *Acta Materialia*. 2011;59(4): 1742–1760.
- 22. Liu CG, Chen LJ, Yang DY, Wen J, Dong LY, Li YH. The "bimodal effect" of the bulk modulus of rare-earth titanate pyrochlore. *Computational Materials Science*. 2016;114: 233–235.
- 23. Liu CG, Zhang J, Chen LJ, Wen J, Dong LY, Yang DY, Li YH. The structural parameters, structural stability and bulk modulus in RE₂Sn₂O₇ by first-principles calculations. *International Journal of Modern Physics B*. 2017;31(26): 1750184.
- 24. Liu B, Wang JY, Zhou YC, Liao T, Li FZ. Theoretical elastic stiffness, structure stability and thermal conductivity of La₂Zr₂O₇ pyrochlore. *Acta Materialia*. 2007;55(9): 2949–2957.
- 25. Pruneda JM, Artacho E. First-principles study of structural, elastic, and bonding properties of pyrochlores. *Physical Review B*. 2005;72(8): 085107.
- 26. Li H, Tao Q, Li N, Tang R, Zhao Y, Zhu H, Zhu P, Wang X. Pressure-induced structural transition of Y₂Zr₂O₇. *Journal of Alloys and Compounds*. 2016;660: 446–449.
- 27. Farmer JM, Boatner LA, Chakoumakos BC, Du MH, Lance MJ, Rawn CJ, Bryan JC. Structural and crystal chemical properties of rare-earth titanate pyrochlores. *Journal of Alloys and Compounds*. 2014;605: 63–70.
- 28. Yadav DS. Electronic and mechanical properties of rare earth monochalcogenides. *Journal of Alloys and Compounds*. 2012;537: 250–254.
- 29. Yadav DS, Singh DV. Static and dynamical properties of II–VI and III–V group binary solids. *Physica Scripta*. 2011;85(1): 015701.
- 30. Verma AS, Bhardwaj SR. Mechanical and optical properties of A^{II}B^{IV}C₂^V and A^IB^{III}C₂^{VI} semiconductors. *Physica Status Solidi (B)*. 2006;243(12): 2858–2863.
- 31. Verma AS, Gupta RC, Singh K. Empirical Relation for Electronic and Optical Properties of Binary Tetrahedral Semiconductors. *East European Journal of Physics*. 2021;1: 89–92.
- 32. Gupta RC, Verma AS, Singh K. Optoelectronic properties of ternary tetrahedral semiconductors. *East European Journal of Physics*. 2021;1: 80–88.
- 33. Gupta RC, Verma AS, Singh K. Empirical predictions for bulk and shear moduli of zinc-blende structured binary solids. *Journal of Taibah University for Science*. 2022;16(1): 676–682.
- 34. Rittman DR, Turner KM, Park S, Fuentes AF, Yan J, Ewing RC, Mao WL. High-pressure behavior of A₂B₂O₇ pyrochlore (A= Eu, Dy; B= Ti, Zr). *Journal of Applied Physics*. 2017;121(4): 045902.
- 35. Kamran S, Chen K, Chen L. Semiempirical formulae for elastic moduli and brittleness of diamondlike and zinc-blende covalent crystals. *Physical Review B*. 2008;77(9): 094109.
- 36. Li K, Xue D. Empirical calculations of elastic moduli of crystal materials. *Physica Scripta*. 2010;2010(T139): 014072.
- 37. Cohen ML. Predicting useful materials. Science. 1993;261(5119): 307–308.

- 38. Cohen ML. Calculation of bulk moduli of diamond and zinc-blende solids. Physical Review B. 1985;32(12): 7988.
- 39. Atkins AG. Deformation-mechanism maps (the plasticity and creep of metals and ceramics): by HJ Frost and MF Ashby, Pergamon, Oxford; 1982.
- 40. Verma AS, Sarkar BK, Sharma S, Bhandari R, Jindal VK. Models for lattice thermal expansion and thermal conductivity for ternary (A^NB^{2+N}C₂^{7-N}) tetrahedral semiconductors. Materials Chemistry and Physics. 2011;127(1-2): 74-78.
- 41. Verma AS, Bhardwaj SR. Correlation between ionic charge and the mechanical properties of complex structured solids. Journal of Physics: Condensed Matter. 2006;19(2): 026213.
- 42. Yadav DS, Verma AS. Electronic, Optical and Mechanical Properties of AIBVI Semiconductors. International Journal of Modern Physics B. 2012;26(08): 1250020.
- 43. Huang B, Duan YH, Hu WC, Sun Y, Chen S. Structural, anisotropic elastic and thermal properties of MB (M=Ti, Zr and Hf) monoborides. Ceramics International. 2015;41(5): 6831–6843.
- 44. Xiao HY, Weber WJ. Pressure induced structural transformation in Gd₂Ti₂O₇ and Gd₂Zr₂O₇. Journal of Physics: Condensed Matter. 2011;23(3): 035501.
- 45. Luan Y. Elastic properties of complex transition metal oxides studied by Resonance Ultrasound Spectroscopy. University of Tennessee; 2011.
- 46. Scott PR, Midgley A, Musaev O, Muthu DV, Singh S, Suryanarayanan R, Revcolevschi A, Sood AK, Kruger MB. High-pressure synchrotron X-ray diffraction study of the pyrochlores: Ho₂Ti₂O₇, Y₂Ti₂O₇ and Tb₂Ti₂O₇. *High Pressure Research*. 2011;31(1): 219–227.
- 47. Vassen R, Cao X, Tietz F, Basu D, Stöver D. Zirconates as new materials for thermal barrier coatings. Journal of the American Ceramic Society. 2000;83(8): 2023–2028.
- 48. Moriga T, Yoshiasa A, Kanamaru F, Koto K, Yoshimura M, Sōmiya S. Crystal structure analyses of the pyrochlore and fluorite-type Zr₂Gd₂O₇ and anti-phase domain structure. Solid State Ionics. 1989;31(4): 319-328.
- 49. Wu J, Wei X, Padture NP, Klemens PG, Gell M, García E, Miranzo P, Osendi MI. Lowthermal-conductivity rare-earth zirconates for potential thermal-barrier-coating applications. Journal of the American Ceramic Society. 2002;85(12): 3031–3035.
- 50. Gale JD. GULP: A computer program for the symmetry-adapted simulation of solids. Journal of the Chemical Society, Faraday Transactions. 1997;93(4): 629–637.
- 51. Saunders VR, Dovesi R, Roetti C, Causa M, Harrison NM, Orlando R, Zicovich-Wilson CM. CRYSTAL98 user's manual. Torino: University of Torino; 1998.
- 52. Lan G, Ouyang B, Song J. The role of low-lying optical phonons in lattice thermal conductance of rare-earth pyrochlores: A first-principle study. *Acta Materialia*. 2015;91: 304–317.
- 53. Van Dijk MP, De Vries KJ, Burggraaf AJ. Oxygen ion and mixed conductivity in compounds with the fluorite and pyrochlore structure. Solid State Ionics. 1983;9-10: 913-919.
- 54. Shimamura K, Arima T, Idemitsu K, Inagaki Y. Thermophysical properties of rare-earthstabilized zirconia and zirconate pyrochlores as surrogates for actinide-doped zirconia. International Journal of Thermophysics. 2007;28: 1074–1084.

THE AUTHORS

Rekha Bhati 堕

e-mail: rekhabhati782@gmail.com

Dheerendra Singh Yaday (1)

e-mail: dhirendra.867@rediffmail.com

Ajav Singh Verma 🗓

Rajesh Chandra Gupta (10)

e-mail: rajgpt@gmail.com

e-mail: ajay_phy@rediffmail.com

Effect of cobalt and tungsten carbide particles inclusions into the aluminium composite on the hardness and wear properties

Submitted: February 21, 2023

Approved: April20, 2023

Accepted: August 31, 2023

U.B. Gopal Krishna (1) 1 M. B. Vasudeva (1) 1, V. Auradi (1) 1, M. Nagaral (1) 2

¹ Siddaganga Institute of Technology, Karnataka, India

² Hindustan Aeronautics Limited (HAL), Karnataka, India

⊠gopalkrishnaub@gmail.com

Abstract. Using liquid metallurgy route, Al7075 composites comprising 6, 9, and 12 wt. % WC-Co were developed. When testing composites and Al7075, ASTM standards were followed. Increasing the vol. % of the cermet phase enhances the hardness of Al7075-WC-Co composites, according to the experimental data. The produced composites are analyzed using scanning electron microscopic images and energy dispersive microscopy technique before and after the wear. Improvement of 80.23 % on hardness of the composite are observed over the base alloy. For the composite containing 12 wt. % of WC-Co particulates the wear rate is less than the base alloy and other prepared composites.

Keywords: aluminium, tungsten carbide; MMC; hardness; wear

Citation: Gopal Krishna UB, Vasudeva B, Auradi V, Nagaral M. Effect of cobalt and tungsten carbide particles inclusions into the aluminium composite on the hardness and wear properties. Materials Physics and Mechanics. 2023;51(5): 99-106. DOI: 10.18149/MPM.5152023_10.

Introduction

Aluminium metal matrix composite (AMMC) a paradigm shift in the field of automobiles, aerospace, tools, military applications. The key properties like high strength with light weight, capable wear resistance, protective to corrosive environment, better temperature stability made these composite to use in extensive conditions [1–2]. Series of aluminium are exist which are capable of heat treatable, weldable, adapting to elevated temperatures and impact loads. 7075Al with Zn and Mg as major alloy exhibits all those properties and made selecting it as matrix among other aluminium series. Reinforcements like B₄C, WC, Al₂O₃, TiB₂ etc., can be added into the base matrix which enhances the properties stated at maximum level [3-4]. The processing of AMMCs is challenging (wettability concern) in stir casting method, when it processed with the addition of high dense objects as reinforcements [5]. In common, the composites prepared with ceramics as reinforcements exhibit high hardness with poor ductility in nature.WC is a hard ceramic particle reinforcement for Al alloy matrices that is employed in high-temperature applications. With a density of 15.8 g/cc tungsten carbide is a famous refractory metal that is used in fabrication of cutting tools, drill bits, single point cutting tool and extrusion dies. Drill bits and cutting tools composed of WC particles are commonly used in the oil industries [6]. At elevated and room temperatures, the combination of WC and Co particles will have increased characteristics. Low thermal coefficient of thermal expansion and high strength are expected when hard ceramic WC particles reinforced with Co particles for carbide tool products [7]. Since they achieve excellent wear resistance, hot hardness, low coefficient of friction and good chemical stability properties, cermet based composites can be successfully utilized for high speed cutting tool for better surface finishing and high class cutting applications in the current era [8]. Utilization of aluminium based composites in variety © U.B. Gopal Krishna, B. Vasudeva, V. Auradi, M. Nagaral, 2023.

Publisher: Peter the Great St. Petersburg Polytechnic University

of industries can be observed due to its high strength because of the addition of proper reinforcing materials and practical wear resistance, including aviation, architectural, energy sector, vehicle industry, construction, naval, army based products, sports, and recreation. This sparked interest in investigating the effects of adding desirable combinations of WC-Co as reinforcement to the characteristics of Al7075 alloy. Correspondingly the improvement in hardness and wear rate of the composite compared to base alloy can be expected.

Experimental details

Chemical composition of Al 7075 alloy, which is used as a matrix, is shown in Table 1. Al7075 alloy is a significant alloying element that contains zinc, magnesium, and copper. This alloy's properties are based on its strengths and resistance, and it is a major alloy used in aircraft applications (Landing gear, wing body, brakes etc). In comparison to other aluminum alloysseries, as the 7 series aluminum have greater corrosion resistance capacity, they have made their way into structural applications.

Table 1. Chemical composition of Al7075 alloy

Elements	Silicon	Iron	Copper	Manganese	Magnesium	Zinc	Aluminium
Amount in wt. %	0.42	0.51	1.60	0.61	2.51	1.50	Balance

In the current work tungsten carbide (WC) is selected as reinforcement; a well-known cutting tool material with a hardness of 1500 BHN and density of 15.63 g/cc. As previously stated, the reduction in ductility of composites is overcome by adding Cobalt (Co), a soft ductile material with density of 8.90 g/cc, as second reinforcement material. Both WC and Co particulates are fused to cermet form with the help of planetary ball milling operations and used it as combined reinforcements. The presence of cobalt can act as an internal lubricant, improve reinforcement wettability, and increase composite ductility. Following the ball milling operation, the ceramic mixture is sieved, and a particle size of 400 mesh or 37 μ m is chosen as the intermediate particle size.

The composite was produced by adding 6, 9, and 12 wt. % of WC-Co particulate reinforcement to the 7075Al alloy matrix. A quantity of 400 grams of matrix is brought to molten state in crucible (graphite-clay) using resistance furnace. Careful control of temperature is done using a digital temperature controller to an accuracy of \pm 5 °C. When the temperature of the liquid metal reaches 730 °C, solid hexachloroethane (C₂Cl₆) is used to drive out entrapped gases. Constant stirring is maintained at 300 rpm using steel rod coated with zirconia. Into this vortex, preheated WC-Co cermet is introduced. After the addition of reinforcement, constant stirring action is performed for 60 seconds duration to ensure a complete distribution of the reinforcements into the matrix. Later, the well stirred and constant temperature maintained liquid metal mixed with the reinforcements has been poured into a permanent cast iron preheated mould having dimensions of 125 mm length and 15 mm diameter. These prepared composites were characterized microscopically using SEM and EDAX studies. For microstructural characterization, central portions of the castings having size of 5 × 10 ×5 mm were taken and were metallographically polished. The electropolished samples were etched using Keller's reagent.

As-cast samples and composite samples are prepared for wear test operating conditions and hence the samples are prepared with the dimensions of 30 mm length and 10 mm diameter as per ASTM G99 standard. The sliced samples are then metallographically polished to worn out preliminary layers on its end. Using DUCOM pin on disc wear testing machinethe prepared samples are tested. All the samples are tested under dry sliding conditions only. The wear samples are tested for varying load, varying speed and varying distance conditions.

Results and discussions

Microstructure analysis. Composite prepared for 37 μm particle sizes of WC-Co reinforcement are subjected to SEM analysis and corresponding microphotographs are shown in Fig. 1. During casting, the structure of dendrites gets altered, affected by numerous variables, such as discontinuity of the dendrites, thermal conductivity imbalance, lack of dendrite growth between particles and melt. Here the ceramic particles act as an obstruction for dendrite growth which is more prominent when the rate of cooling is high.

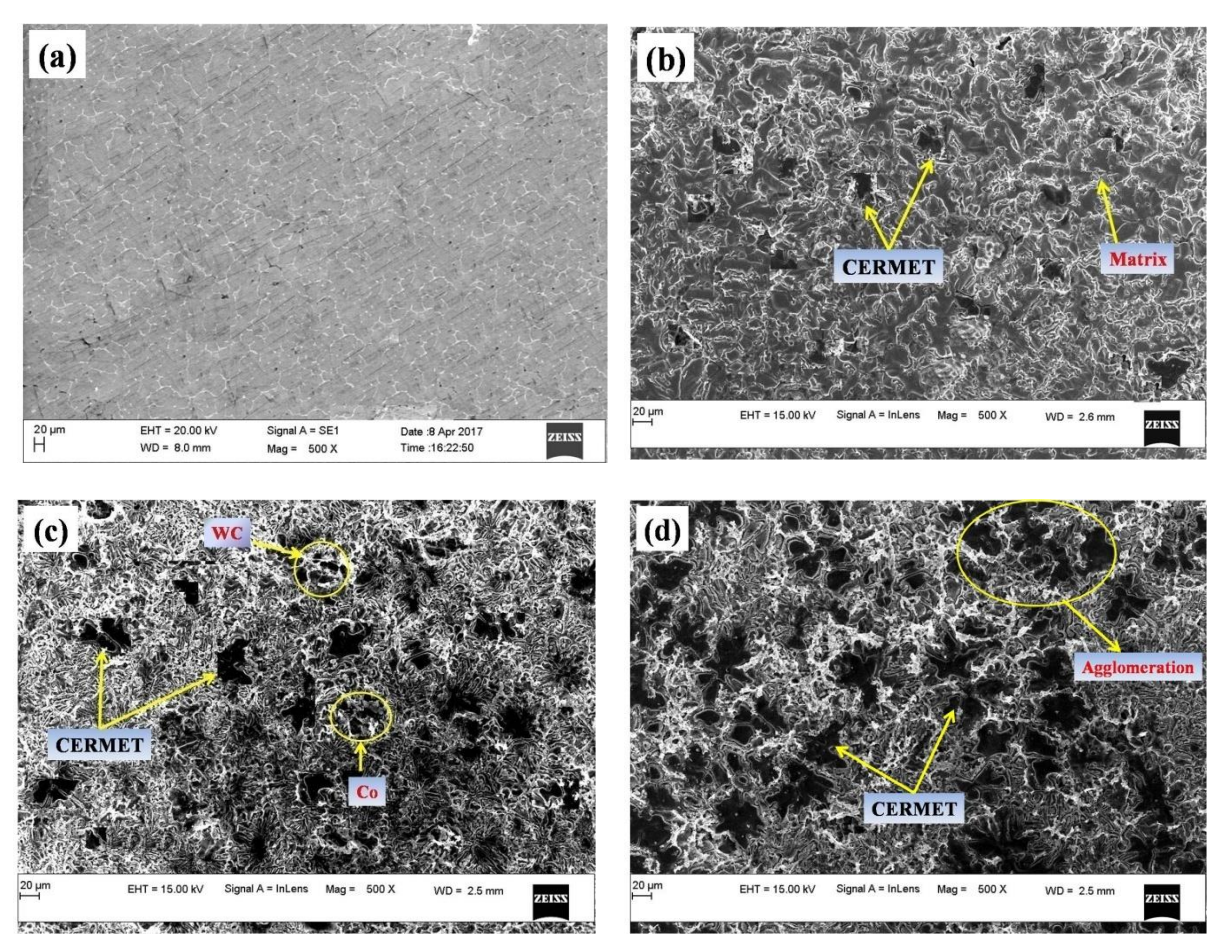


Fig. 1. SEM images of (a) as—castbasealloy, (b) Al7075 + 6 wt. % WC-Co, (c) Al7075 + 9 wt. % WC-Co and(d) Al7075 + 12 wt. % WC-Co composite

Mechanical stirring action disperses the particles consistently as well as reduces settling of the particles during the solidification and shearing of the starting dendritic arms can relate to the dendritic fracture because of the excess stirring action [9,10]. Local solidification takes place due to the variations in the temperature with respect to matrix and reinforcements. Finally, synthesized composite shows the uniform and homogeneous dispersion of WC-Co particles within the alloy matrix.

The strong interface offers excellent properties enhancement for mechanical and tribological zone, as the load transmission occurs. Due to existence of hard ceramic particles which limits the dendrites development and changes the matrix with a progressively refined structure results in improving the strength. As the reinforcement's weight percentage rises, the minimum distance between the particles is seen. Additionally, this might prevent the dislocation from moving.

EDAX analysis. As-cast base alloy Al7075 and Al7075 + 6, 9, and 12 wt. % WC-Co particles added composites underwent an elemental analysis using EDAX analysis. Figure 2 displays the findings. The elemental analysis of the Al7075 + 6, 9, and 12 wt. % WC-Co composite shown in Fig. 2(b-d) confirms the presence of W, Mg, Co, Zn, C, Si in the matrix of the Al alloy.

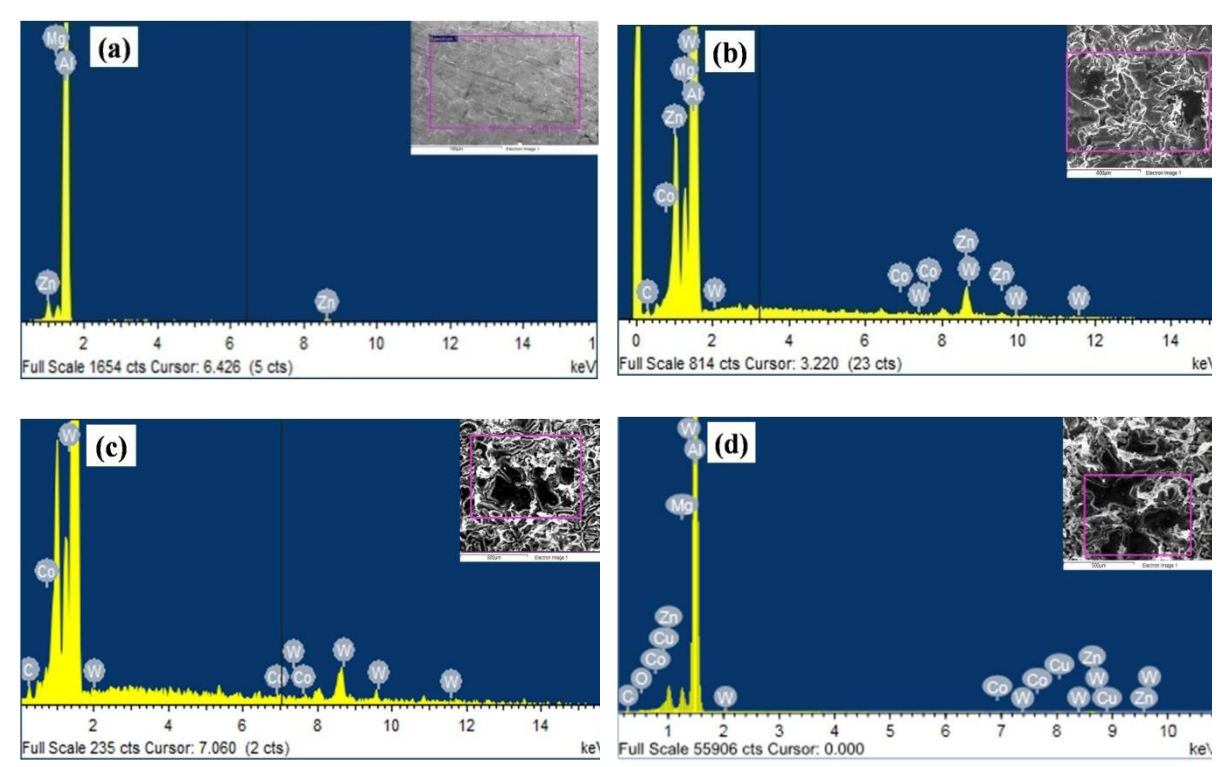


Fig. 2. EDAX spectrum of (a) as - cast Al7075, (b) Al7075 + 6 wt. % WC-Co, (c) Al7075 + 9 wt. % WC-Co and (d) Al7075 12 wt. % WC-Co composite

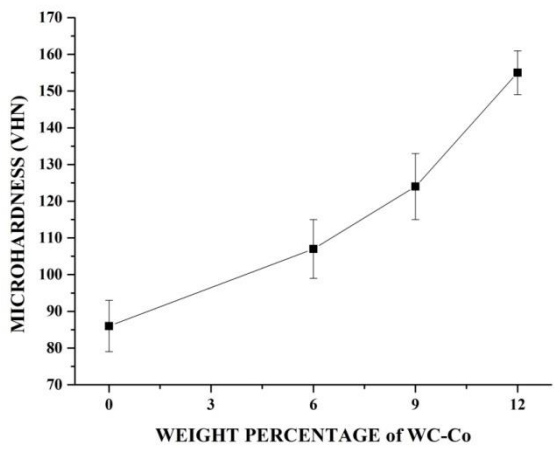


Fig. 3. Microhardness of as-cast Al7075 and Al7075 reinforced with 6, 9 and 12 wt. % of WC-Co particles

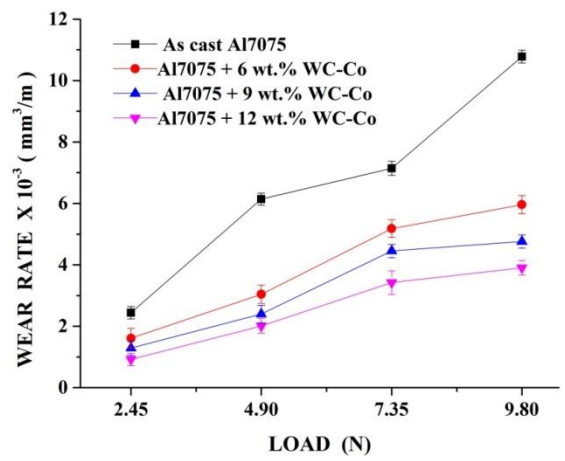
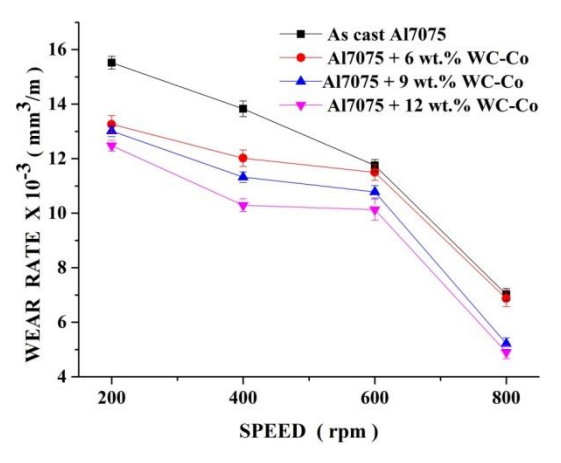


Fig. 4. Impact of variable load on wear rate of the prepared composite keeping sliding speed and sliding distance as constant

Evaluation of hardness of the composite. Vickers microhardness testing is performed on both manufactured composites and as-cast metal. The hardness readings for the Al7075 alloy as-cast and the Al7075 reinforced with WC-Co particles at different weight percentages (6, 9, and 12 wt. %) are shown in Fig. 3. The graph below demonstrates how the toughness of the composite grows significantly as WC-Co particle quantity is increased. Al7075 reinforced with WC-Co composites for 12 wt. % of the particle exhibits a hardness enhancement of around 80.23 % when compared to Al7075 alloy. WC-Co particles greatly improve the hardness of Al7075-WC-Co composites because they are tougher and harder than other materials. This increase in hardness is both evident and predicted. As stated by Velmurugan et al. [11], earlier research has shown that hardness factors are always directly proportional to the hardness of reinforcing particles. Localized matrix deformation during indentation is caused by tougher and

harder micro tungsten carbide and cobalt particles present in the lattice. It is clear that the bulk of composites are harder than the matrix. The hard reinforcing particles, which act as a protection to slide dislocation movement within the matrix, are what give materials their increased hardness [12,13].

Wear rate analysis. Impact of variable load on wear rate. The effects of increasing load on the rate of wear for as-cast Al 7075 and Al 7075 + 6, 9, and 12 wt. % of WC-Co particulate composite with varied loads are tested by maintaining the speed (400 rpm) and sliding distance (500 m) consistent (2.45, 4.90, 7.35, and 9.8 N). Figure 4 demonstrates that for all composite materials, the wear rate rises with increasing load and falls with decreasing load. The alloy Al7075 has the highest rate of wear when it is cast. Ramesh et al. [14] claim that, as the applied force is increased, both the as-cast Al and composite specimens experience increased wear loss. Furthermore, the data definitely shows that at a specific transition load, incremental volumetric wear loss observed in both reinforced and unreinforced materials. Pressure at the pin-on-disc contact grows as load increases. Due to the fact that metals usually contain an oxide layer, the wear analysis for maximum loads results in increased material losses.



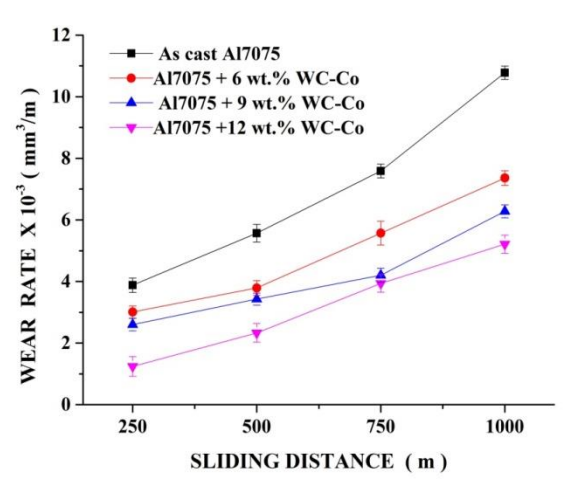


Fig 5. Impact of variable speed on wear rate of the prepared composite keeping constant load and sliding distance

Fig. 6. Impact of variable sliding distance on the wear rate of the prepared composite keeping constant load and speed

Impact of varying speed on wear rate. The impact on the wear rate for the increasing speed on as-cast Al7075 and Al7075 reinforced with WC-Co with 6, 9, and 12 wt. % WC-Co composite is evaluated by keeping the constant load (9.8 N) and constant sliding distance (500 m). Numerous studies have demonstrated that increasing sliding speed/velocity leads to increased wear, especially at higher sliding speeds [15,16]. Figure 5 illustrates how the rate of wear decreases as speed increases and reaches its maximum at lower speeds. At higher speeds, the contact surface might be decreased. The material's surface becomes smoother as temperature rises, which encourages yielding and leads to delamination of the worn surface. As the speed increases, the material deteriorates because of an increase in contact temperature. Debris is eliminated by sliding motion due to wear and weakened bonding at the contact. The WC-Co composite surpasses the base alloy with respect to wear resistance. The thick layer created by solid lubricating coating may fracture at higher sliding speeds. Furthermore, plastic deformation between the mating surfaces is increased due to high temperature caused due to the sliding speed, which boosts the volumetric wear loss and asperity junction density.

Impact of varying sliding distance on wear rate. Al7075 as-cast and Al7075 reinforced with WC-Co at 6, 9, and 12 wt. % wear out more quickly at higher speeds. The evaluation of WC-Co composite uses a load of 9.80 N and a 400 rpm constant speed. Figure 6 makes it plainly evident that, due to the contact surface weakening caused by heat during the experiment, the rate of wear in composite rises with increasing sliding distance. Because of the longer length of contact between the disc and pin

or specimen, temperature conditions vary, in fact getting warmer as the sliding distance rises. The Al7075 matrix alloy and WC-Co reinforcement particulates have enhanced interfacial resistance due to the high surface bond, which hinders particle pull from the Al7075 matrix. Hence, it can be inferred from the aforementioned analysis that the composite reinforcement's greater weight percentage and smaller particle size caused the rate of wear of the samples to be lower than it was for Al 7075 cast ascast. It may be due mostly to the reinforcing particles' in the matrix having a larger contact surface area.

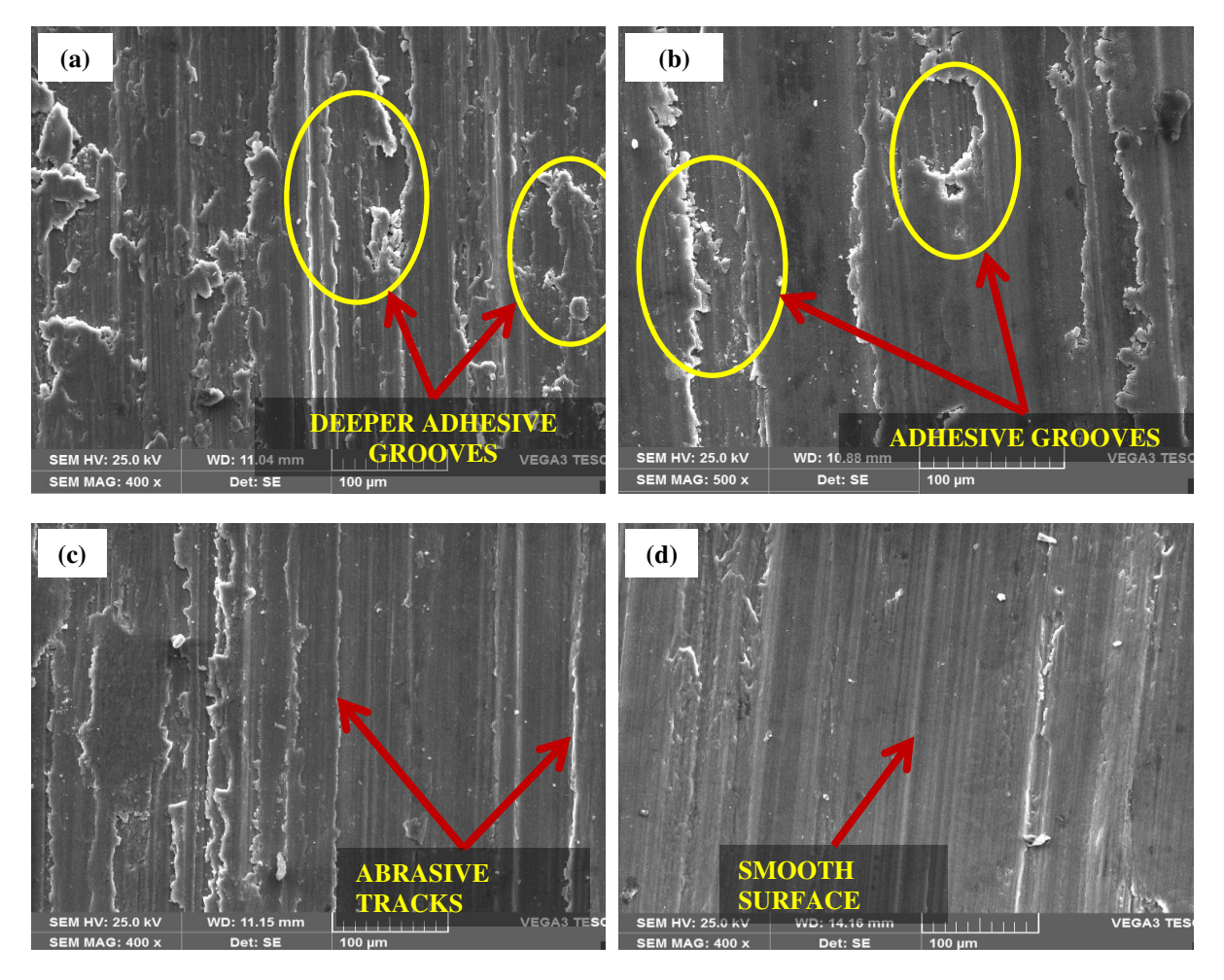


Fig 7. Images showing worn surfaces of (a) as—cast Al7075 alloy, (b-d) Al7075 reinforced with WC-Co at different compositions (6, 9 and 12 wt. %) with a load of 9.8 N, sliding disc speed of 400 rpm and sliding disc distance of 500 m

Worn surface studies. Figure 7 depicts a composite made of WC-Co particles and demonstrates the presence of grooves that are both shallow and sticky. As the weight percentage of the reinforcement grows in the composite, the area that originally formed grooves became smoother. The composite displays stronger wear resistance than the as-cast alloy because there is little material loss and there is a maximum reduction in wear rate. The ease with which the composite surface delaminates depends on both the wt. % of reinforcement and the particle size. In comparison to the alloy as cast, Al7075 reinforced with 12 wt. % WC-Co composite shows very little delaminated area and the formation of grooves, according to a general analysis of the worn surface.

Conclusions

- (1) Use of WC-Co particulates as reinforcement in preparation of Al composites is successful.
- (2) Studies utilising SEM and EDAX analysis have shown that the reinforcements in the matrix system are distributed fairly uniform.
- (3) Al7075 reinforced with WC-Co composites for 12 wt. % of the particle exhibits a hardness enhancement of around 80.23 % when compared to Al7075 alloy.
- (4) Wear rate effect of the composite under different load, speed and distance shows good wear resistance compared to base alloy.

References

- 1. Bharath V, Nagaral M, Auradi V, Kori SA. Studies on Dry Sliding Wear Characteristics of Ceramic Al₂O₃ particulate Reinforced 6061Al Matrix Composites. *Advanced Materials Research*. 2014;985: 319–325.
- 2. Rao RN, Das S. Effect of sliding distance on the wear and friction behavior of as cast and heat-treated—SiCp composites. *Materials and Design*. 2011;32(5): 3051–3058.
- 3. Bhansali KJ, Mehrabian R. Abrasive Wear of Aluminum-Matrix Composites. *Journal of Metals*. 1982;34: 30–34.
- 4. Jebin VD, Shivalingappa D, Rino JJ. Wear behavior of Al6063-Alumina Metal Matrix composite. *International Journal of Science and Research*. 2013;2: 446–449.
- 5. Oh SY, Cornie JA, Russel KC. Wetting of ceramic particulates with liquid aluminium. Part II. Study of Wettability. *Metall Trans A*. 1989;20: 533.
- 6. Xiao TD, Tan X, Yi M, Peng S, Peng F, Yang J, Dai Y. Synthesis of Commercial-Scale Tungsten Carbide-Cobalt (WC/Co) Nanocomposite Using Aqueous Solutions of Tungsten (W), Cobalt (Co), and Carbon (C) Precursors. *Journal of Materials Science and Chemical Engineering*. 2014;2(7): 47605.
- 7. Wang XJ, Wang NZ, Wang LY, Hu XS, Wu K, Wang YQ, Huang YD. Processing, microstructure and mechanical properties of micro SiC particles reinforced magnesium matrix composites fabricated by stir casting assisted by ultrasonic treatment processing. *Materials and Design*. 2014;57: 638–645.
- 8. Ibrahim IA, Mohamed FA, Lavernia EJ. Particulate Reinforced MMCs-A Review. *Journal of Material Science*. 1991;26: 1137–1156.
- 9. Kuruvilla AK, Bhanuprasad VV, Prasad KS, Mahajan YR. Effect of different reinforcements on Composite-strengthening in aluminium. *Bull. Mater. Sci.* 1989;12(5): 495–505.
- 10. Mohanavel V, Rajan K, Kumar SS, Vijayan G, Vijayand MS. Study on mechanical properties of graphite particulates reinforced aluminium matrix composite fabricated by stir casting technique. *Materials Today Proceedings*. 2018;5(1): 2945–2950.
- 11. Velmurugan C. The Tribological Studies on the Heat treated hybrid aluminium metal matrix composites. *International Journal of Mechanical and Production Engineering Research and Development*. 2008;8(7): 790–800.
- 12. Srikanth BG, Amarnath G. Microstructure and tribological behaviour of aluminium reinforced with tungsten carbide particulate and flyash metal matrix composites. *International Journal of Research in Engineering and Technology*. 2015;04(05): 567–572.
- 13. Suresh S, Moorthi NSV. Process development is stir casting and investigation on microstructures and wear behaviour of TiB2 on Al6061 MMC. *Proceedia Engineering*. 2013;64: 1183–1190.
- 14. Dasgupta R, Meenai H. SiC particulate dispersed composites of an Al–Zn–Mg–Cu alloy: Property comparison with parent alloy. *Materials Characterization*. 2005;54: 438–445.
- 15. Kumar GBV, Swamy ARK, Ramesha A. Studies on properties of as cast Al6061-WC-Gr hybrid composites. *Journal of Composite Materials*. 2011;46(17): 2111–2122.
- 16. Srivastava S, Mohan S. Study of wear and friction of Al-Fe metal matrix composite produced by liquid metallurgical method. *Tribol Industry*. 2011;33(3): 128–137.

- 17. Jadhav PR, Sridhar BR, Nagaral M, Harti JI. Mechanical behavior and fractography of graphite and boron carbide particulates reinforced A356 alloy hybrid metal matrix composites. Advanced Composites and Hybrid Materials. 2020;3: 114–119.
- 18. Boppana SB, Dayanand S, Murthy BV, Nagaral M, Telagu A, Kumar V, Auradi V. Development and mechanical characterisation of Al6061-Al₂O₃-graphene hybrid metal matrix composites. Journal of Composites Science. 2021;5(6): 155.
- 19. Nagaral M, Deshapande RG, Auradi V, Boppana SB, Dayanand S, Anilkumar MR. Mechanical and wear characterization of ceramic boron carbide-reinforced Al2024 alloy metal composites. Journal of Bio-and Tribo-Corrosion. 2021;7: 19.
- 20. Bharath V, Auradi V, Nagaral M, Boppana SB. Experimental Investigations on Mechanical and Wear Behaviour of 2014Al–Al₂O₃ Composites. *Journal of Bio-and Tribo-Corrosion*. 2020:6: 45.
- 21. Nagaral M, Auradi V, Kori SA, Shivaprasad V. Mechanical characterization and wear behavior of nano TiO2 particulates reinforced Al7075 alloy composites. Mechanics of Advanced Composite Structures. 2020;7(1): 71–78.
- 22. Dayanand S, Boppana SB, Auradi V, Nagaral M, Udaya Ravi M, Bharath. Evaluation of Wear Properties of Heat-Treated Al-AlB₂ in-situ Metal Matrix Composites. Journal of Bio-and Tribo-Corrosion. 2021;7: 40.
- 23. Kumar R, Deshpande RG, Gopinath B, Harti J, Nagaral M, Auradi V. Mechanical Fractography and Worn Surface Analysis of Nanographite and ZrO2-Reinforced Al7075 Alloy Aerospace Metal Composites. *Journal of Failure Analysis and Prevention*. 2021;21: 525–536.
- 24. Vencl A, Bobic I, Arostegui S, Bobic B, Marinkovic A, Babic M. Structural, mechanical and tribological properties of A356 aluminium alloy reinforced with Al2O3, SiC and SiC+ graphite particles. Journal of Alloys Compounds. 2010;506(2): 631–639.
- 25. Umanath K, Selvamani ST, Palanikumar K, Raphael T, Prashanth K. Effect of sliding distance on dry sliding wear behavior of Al6061-SiC-Al₂O₃ hybrid composite. In: *Proceedings of* International Conference on Advances in Mechanical Engineering. 2013. p.749–775.
- 26. Harti JI, Prasad TB, Nagaral M, Jadhav P, Auradi V. Microstructure and dry sliding wear behavior of Al2219-TiC composites. *Materials Today Proceedings*. 2017;4(10): 11004–11009.
- 27. Alaneme KK, Odoni BU. Mechanical properties, wear and corrosion behavior of copper matrix composites reinforced with steel machining chips. Engineering Science and Technology. 2016;19(3): 1593-1599.
- 28. Guo MLT, Tsao CYA. Tribological behavior of aluminium SiC-nickel coated graphite hybrid composites. Materials Science and Engineering A. 2002;333(1-2): 134–145.
- 29. Huang K, Lin X, Xie C, TM Y. Microstructure and wear behaviour of laser-induced thermite reaction Al₂O₃ ceramic coating on AA7075 aluminum alloy. Journal of Materials Science and Technology. 2007;23(2): 201-206.

THE AUTHORS

U.B. Gopal Krishna 🗓

e-mail: gopalkrishnaub@gmail.com

V. Auradi 🗓

e-mail: vsauradi@gmail.com

B. Vasudeva 🗓 e-mail: bva@sit.ac.in

Madeva Nagaral 🗓

e-mail: madev.nagaral@gmail.com

Effect of Al addition on the mechanical properties of $Zr_{50}Cu_{50-x}Al_x$ ($0 \le x \le 50$) bulk metallic glass

Submitted: March 3, 2023

Approved: March 20, 2023

Accepted: April 10, 2023

V. Guder 📵 🛚

Trakya University, Edirne, Turkey

⊠ vildanguder@trakya.edu.tr

Abstract. The evolution of microstructural and mechanical properties of ternary Zr-Cu-Al metallic glass under tensile loading was investigated by molecular dynamics simulations using embedded atomic potentials to describe interactions between atoms in the system. Special attention was paid to the variation of these properties according to the Al content in the $Zr_{50}Cu_{50-x}Al_x$ ($0 \le x \le 50$) system. The results showed that there is no systematic relationship between the elastic properties and the amount of Al, but the local structure of the system is significantly affected during the tensile load. The elastic modulus and yield stress were found to be maximum at 40 and 20 %, respectively. It was also revealed that the addition of Al decreased the fraction of Al-centered <0,0,12,0> polyhedra, and increased the fraction of the same polyhedra around Cu and Zr.

Keywords: molecular dynamics simulations; elastic modulus; voronoi polyhedral; mechanical properties; ZrCuAl metallic glass

Citation: Guder V. Effect of Al addition on the mechanical properties of $Zr_{50}Cu_{50-x}Al_x$ ($0 \le x \le 50$) bulk metallic glass. Materials Physics and Mechanics. 2023;51(5): 107-114. DOI: 10.18149/MPM.5152023_11.

Introduction

Zr-based bulk metallic glasses (BMGs), which are among the BMG that have attracted great attention due to their physical, mechanical and chemical properties, have attracted attention due to their high glass-forming ability (GFA) [1–3]. Properties such as ease of formability, low Elastic Modulus, high elastic strain and yield strength make BMGs very useful for structural applications. It is known that suppression of crystal nucleation and enhancement of GFA can be achieved by the addition of a third element [4,5]. The ternary Cu-Zr-Al systems have a large supercooled liquid region and high mechanical strength [6]. It has been observed that the addition of Al to the Cu₅₀Zr₅₀ system caused significant plastic deformation and increased the GFA [4–7]. Zr₃₀Cu₆₀Al₁₀ shows better GFA, higher stiffness and strength [8]. The ductility is observed as a result of nucleation of shear bands for Cu_{47.5}Zr_{47.5}Al₅ BMG, while brittleness is observed as a result of rapid propagation of shear bands by fracturing an amorphous phase for Cu₄₆Zr₄₇Al₇BMG [7]. The improved GFA and high viscosity value due to the denser liquid structure of (Cu₅₀Zr₅₀)₉₅Al₅ alloy compared with the Cu₅₀Zr₅₀ alloy is reported [9]. For $Zr_{50}Cu_{50-x}Al_x$ systems, it has been found that the alloys of $x \le 20$ have the best GFA and Al is the active element in controlling GFA [10]. Al content cause amorphization and more pronounced amorphization has been observed for Zr₅₀Cu₄₄Al₆ and Zr₅₀Cu₄₀Al₁₀ alloys [11]. For $Cu_{50}Zr_{50-x}Al_x$ alloys, the range is $0 \le x \le 4$ for non-eutectic alloys, while the range to eutectic composition is 5≤x≤11. Cu₅₀Zr₄₇Al₃ alloy has the best GFA, lowest brittleness index and highest fracture strength [12]. The glass transition temperature (T_g), the initial crystallization

V. Guder

temperature (T_x) and supercooled liquid region, hardness and Elastic Modulus increase with increasing Al concentration for $(Cu_{50}Zr_{50})_{100-x}Al_x$ (x=0–12). Cheung and Shek have reported that the hardness was smallest for $Cu_{50}Zr_{50}$ and greatest for $(Cu_{50}Zr_{50})_{90}Al_{10}$ [13]. The T_x , yield and fracture strength increase with increasing Al content for $(Cu_{50}Zr_{50})_{100-x}Al_x$ (x=0-6) metallic glass wires [14]. It has been found that T_g , fracture strength and hardness decreased, and Elastic Modulus, Debye temperature and shear modulus increased with the addition of Al for $Cu_{50}Zr_{50}$ [15]. The crystal nucleation in the system is suppressed with the addition of 7 % of Al to the $Cu_{50}Zr_{50}$ amorphous system [19]. It is seen that the studies on Zr-Cu-Al described above are mostly limited to the addition of Al content in small amounts. In this study, the influence of mechanical and structural properties in a wide range of Al amounts for $Zr_{50}Cu_{50-x}Al_x$ ($0 \le x \le 50$). The results are discussed in detail in terms of the local environment and atomic localization.

Method

A Large – scale Atomic-Molecular Massively Parallel Simulator (LAMMPS) served as an open-source code [16] was used to investigate effects of Al addition on the mechanical properties of Zr₅₀Cu_{50-x}Al_x (0≤x≤50) bulk metallic glass during tensile process. The reliability of the MD simulation strongly depends on the interatomic potential, which can better explain the atomic interactions of the system. Embedded atom method (EAM) potential was used for the Zr-Cu-Al system, which was successful in simulating existing binary and ternary metallic glasses [17,18]. In order to construct a ternary Zr₅₀Cu₄₀Al₁₀ crystalline system, the simulation box was taken as body-centered cubic (BCC) with 31250 atoms and the lattice constant was taken as 3.283 Å. The snapshot of the initial model is given in Fig. 1(a). After the energy minimization, the system was heated from 50 to 2050 K with a heating rate of 0.5 K/ps using an isothermal-isobaric ensemble with a constant number of particles, pressure and temperature (NPT). The time step was 0.001 ps. The snapshot of the model system in the liquid state is given in Fig. 1(b). The liquid model obtained for Zr₅₀Cu₄₀Al₁₀ alloy was used to construct the initial configuration of $Zr_{50}Cu_{50}$, $Zr_{50}Cu_{45}Al_5$, $Zr_{50}Cu_{35}Al_{15}$, $Zr_{50}Cu_{30}Al_{20}$, $Zr_{50}Cu_{25}Al_{25}$, $Zr_{50}Cu_{20}Al_{30}$, $Zr_{50}Cu_{15}Al_{35}$, $Zr_{50}Cu_{10}Al_{40}$, $Zr_{50}Cu_{5}Al_{45}$ and $Zr_{50}Al_{50}$ liquid systems by changing the Al concentration. After adjusting the atom labels to guarantee the composition of alloys, these systems were subjected to a 100 ps equilibration at 2050 K and cooled to 300 K with a cooling rate of 0.1 K/ps applying the periodic boundary conditions through x-, y- and zdirections. Obtained amorphous systems for Zr₅₀Cu₄₀Al₁₀ and other compositions are shown in Fig. 1(c) and Fig. 2.

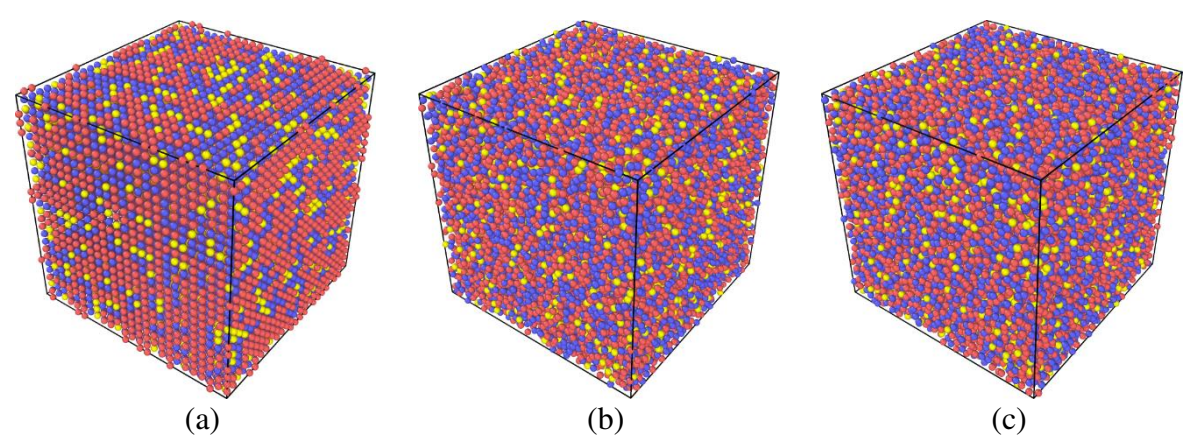


Fig. 1. MD simulation snapshots (a) initial crystalline (b) liquid (c) amorphous for Zr₅₀Cu₄₀Al₁₀ system. The red, blue and yellow spheres represent Zr, Cu and Al atoms, respectively

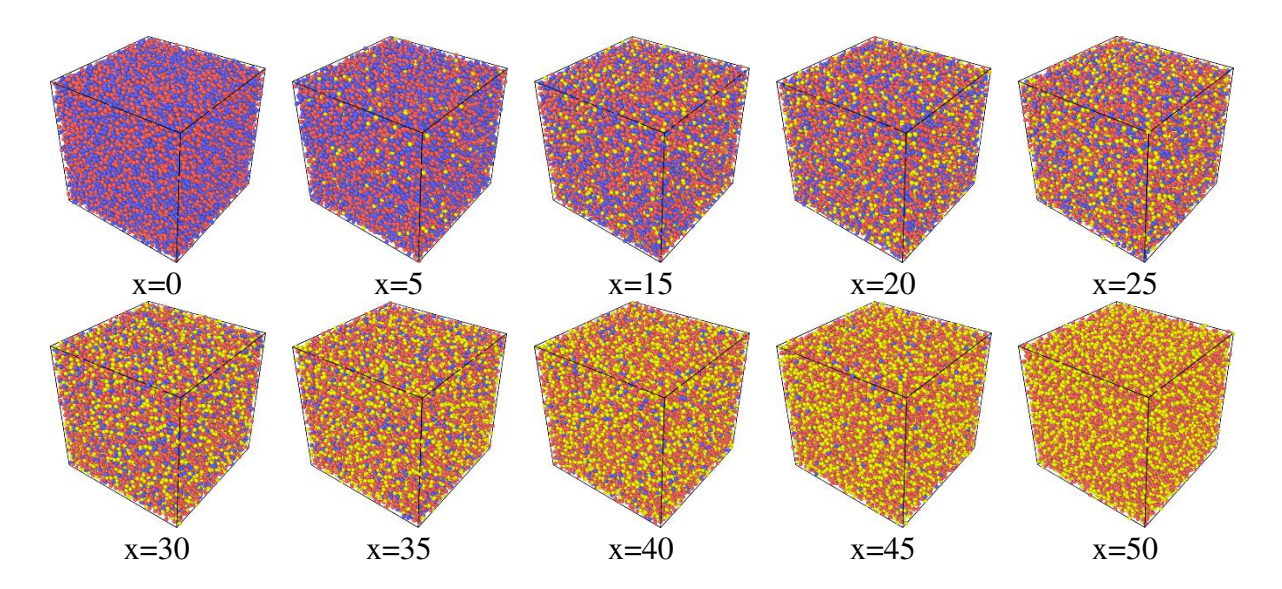


Fig. 2. MD simulation snapshots for amorphous $Zr_{50}Cu_{50-x}Al_x$ ($0 \le x \le 50$) systems. The red, blue and yellow spheres represent Zr, Cu and Al atoms, respectively

Before loading, each amorphous system has been relaxed with 100 ps under the microcanonical ensemble of NVE (N atomic number, V volume, E total energy) to obtain an equilibrium state at 300 K. For all amorphous systems, uniaxial stress was applied along the z-direction. During the tensile deformation, the periodic boundary conditions were applied along the three directions of Cartesian coordinates. In this method, while the periodic length in the z-direction increases with the applied strain rate, the other two directions (ie x- and y-) are allowed to change to keep the pressure in these directions equal to zero. The temperature was kept at 300 K based on the Nose-Hoover thermostat, each amorphous system was elongated by 10 % during the tensile deformation at the strain rate of 0.0001 ps⁻¹ with the isothermal-isobaric (NPT) ensemble.

Results and Discussions

The stress-strain curves guide to investigate of the effects of Al addition on the mechanical properties of Zr₅₀Cu_{50-x}Al_x (0≤x≤50) bulk metallic glass. Figure 3(a) shows that stress-strain curves for Zr₅₀Cu_{50-x}Al_x bulk metallic glass during tensile deformation. The region in which the atoms maintain their regular lattice arrangement is called the elastic region. The stress and strain at the boundary of the elastic region correspond to the yield stress and yield strain, respectively. In this study, the stress corresponding to the strain value of 0.04 in which the linearity of the stress-strain curve deteriorates has called yield stress. For amorphous systems, stress-strain curves show smooth transition behaviour after the elastic region, indicating that the small deformation region is enlarged and spread throughout the system and the deformation is homogeneous. The highest value of the stress in the stress-strain curve during all tensile deformation is called the ultimate stress. The ultimate stress for Zr₅₀Cu₅₀ is 1.85 GPa which agrees with experimental data (1.88 GPa) [7]. Figure 3(b) shows that the variation of yield stress depending on Al amount for Zr₅₀Cu_{50-x}Al_x (0≤x≤50) bulk metallic glass. The yield stress increases from x=0 to x=10 and decreases sharply at x=15. A maximum value at x=20 is followed by zigzag behavior. In this case, Zr₅₀Cu₃₀Al₂₀ has the highest strength. The value of yield stress is almost the same for $Zr_{50}Cu_{50}$ and $Zr_{50}Al_{50}$, $Zr_{50}Cu_{45}Al_5$ and $Zr_{50}Cu_5Al_{45}$, Zr₅₀Cu₄₀Al₁₀ and Zr₅₀Cu₁₀Al₄₀. The yield stress for Zr₅₀Cu₄₀Al₁₀ is 1.91 GPa which is a fair agreement with experimental data (1.86 GPa) [19].

V. Guder

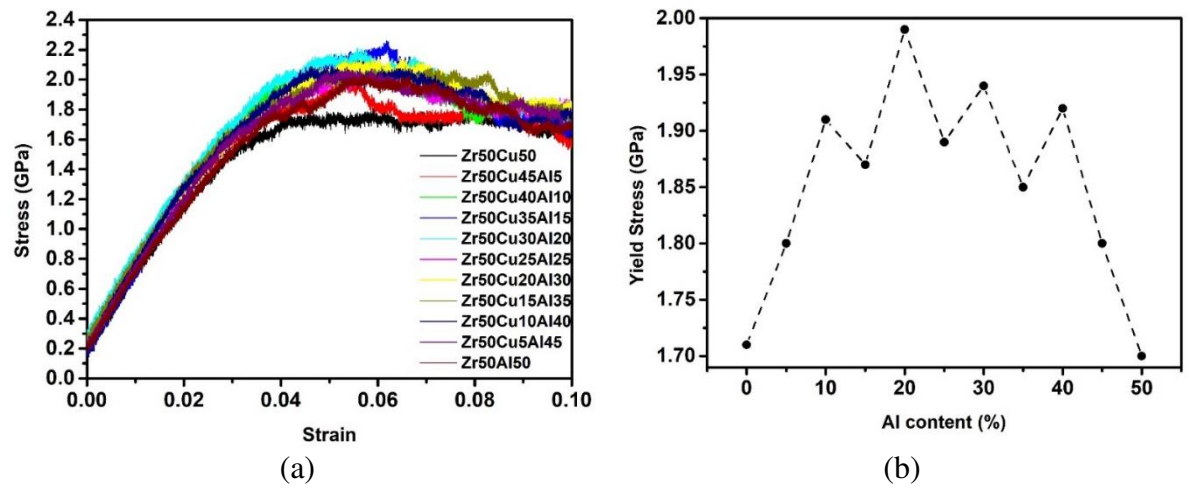


Fig. 3. For Zr₅₀Cu_{50-x}Al_x (0≤x≤50) bulk metallic glass (a) stress-strain curves (b) yield stress variation depending on Al concentration

Elastic modulus is known as a measure of elastic deformation under applied tensile loading and is calculated from the slope of stress-strain curves up to a strain value of 0.015 in present work. Figure 4 shows that elastic modulus variation depending on Al content for $Zr_{50}Cu_{50-x}Al_x$ ($0 \le x \le 50$) bulk metallic glass. There is no clear relationship between Al concentration and Elastic Modulus. In the range of Al amount studied in this study, the Elastic Modulus of $Zr_{50}Cu_{50}$ is minimum which reflects its flexible nature while the elastic modulus of $Zr_{50}Cu_{10}Al_{40}$ is maximum which is a sign of a stiffer material. Table 1 lists elastic modulus values for $Zr_{50}Cu_{50-x}Al_x$ (x=0,10). Elastic modulus values obtained in this study are compatible with the literature. However, the Elastic modulus obtained by molecular dynamics simulation is different from that obtained from the experimental study due to the small size of the metallic glasses used in MD simulation and ignoring the defects and cracks in the sample during simulations.

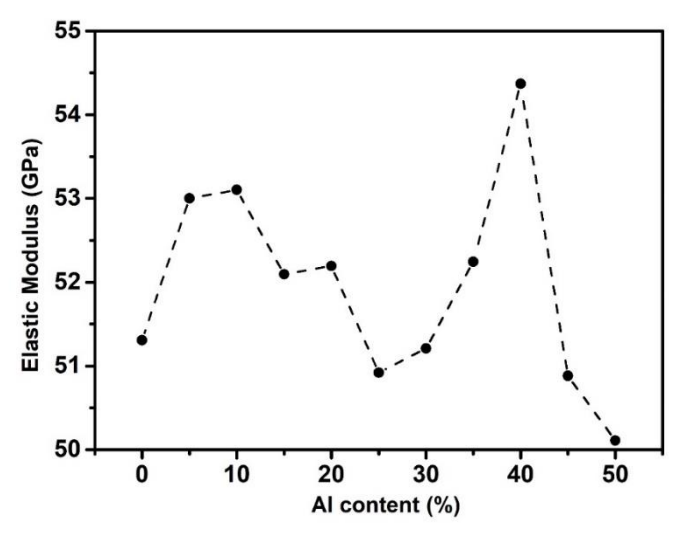


Fig. 4. Elastic modulus variation depending on Al concentration for Zr₅₀Cu_{50-x}Al_x (0≤x≤50) bulk metallic glass

Table 1. Elastic Modulus values for $Zr_{50}Cu_{50-x}Al_x$ (x=0,10)

	This work, GPa	Exp., GPa	Other, GPa
Zr ₅₀ Cu ₅₀	51.3	-	55 ^a
$Zr_{50}Cu_{40}Al_{10}$	53.1	88 ^b	59°

^a[20], ^b[19], ^c[8]

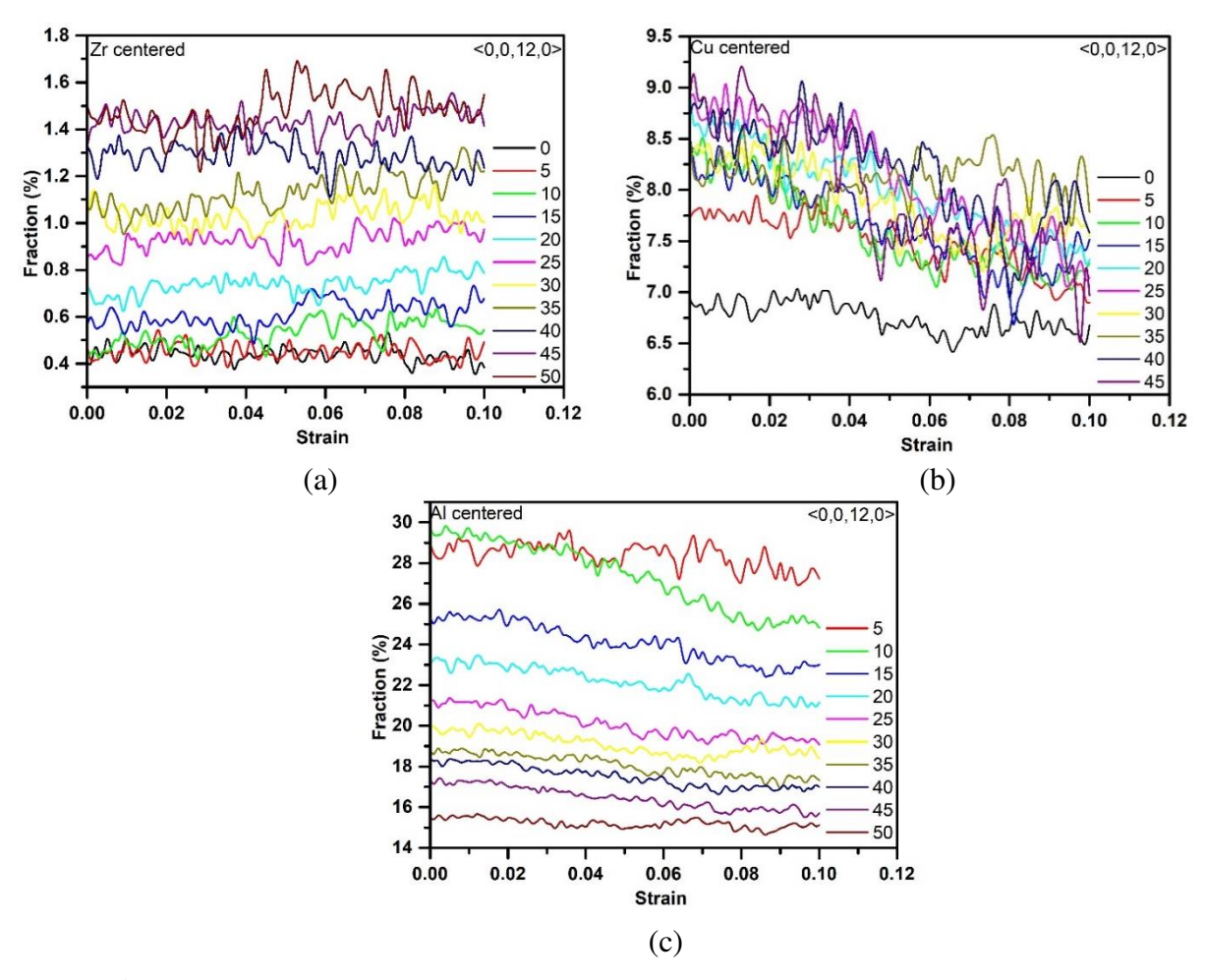


Fig. 5. The variation of (a) Zr (b) Cu (c) Al centered <0,0,0,12> VPs with strain for $Zr_{50}Cu_{50-x}Al_x$ ($0 \le x \le 50$) BMGs

The Voronoi tessellation method [21,22] gives us detailed information about the local atomic structure of the system and the variation of local clusters during the tensile process. In the Voronoi tessellation method, the polyhedra in the system are defined by connecting each atom with an index $\langle n_3, n_4, n_5, n_6 \rangle$ where n_i is the number of faces with i vertices of the VP. In this study, ideal icosahedral (ico) and icosahedra-like (ico-like) VPs were categorized according to reference [23,24]. Ideal ico is defined by <0,0,12,0> VP while ico-like are presented by $\langle 0,2,8,x \rangle$, $\langle 0,0,12,x \rangle$ and $\langle 0,1,10,x \rangle$ VPs (x=2-6). Figure 5 shows that the variation of (a) Zr (b) Cu (c) Al centered <0,0,0,12> VPs as a function of strain. Due to the Zr content being kept constant in the system, the <0,0,0,12> VPs fraction around Zr atoms is not affected by strain except for the slight deviation observed in the range between the yield and ultimate strains. While Cu and Al centered <0,0,0.12> VPs are almost unchanged up to the value of yield strain (value of 0.004), these tend to decrease with increasing strain. Before the tensile loading, it is observed that the addition of Al decreases the fraction of Al-centered <0,0,12,0> polyhedra, and increased the fraction of the same polyhedra around Cu and Zr. The fraction of Al centered <0,0,12,0> clusters is higher than that of other constituent atoms. For Zr₅₀Cu₄₀Al₁₀, its value is 29 % which is the maximum before loading. It decreases with strain. The material resists corrosion thanks to the presence of <0,0,12,0> clusters [25]. Al atoms can be considered as the key factor in resisting corrosion of the amorphous system.

Figure 6 shows that the variation of (a) Zr (b) Cu (c) Al centered ico-like VPs with strain for $Zr_{50}Cu_{50-x}Al_x$ ($0 \le x \le 50$). In Figure 5, the ico-like VPs at the relevant atomic centered are represented as follows. Zr centered ico-like is the sum of the fraction of <0,2,8,2>, <0,2,8,3>,

V. Guder

<0,2,8,4>, <0,2,8,5>, <0,2,8,6>, <0,1,10,2>, <0,1,10,3>, <0,1,10,4>, <0,1,10,5>, <0,0,12,0>, <0,0,12,2>, <0,0,12,3> and <0,0,12,4> VPs. Cu centered ico-like is the sum of the fraction of <0,2,8,0>, <0,2,8,1>, <0,2,8,2>, and <0,0,12,0> VPs. Al centered ico-like is the sum of the fraction of <0,2,8,0>, <0,2,8,1>, <0,2,8,2>, <0,2,8,3>, <0,1,10,2> and <0,0,12,0> VPs. Zr centered ico-like VPs are numerous and diverse. It is revealed that the addition of Al decreases the fraction of Al-centered ico-like polyhedra, and increases the fraction of the same polyhedra around Cu and Zr. With increasing strain, Zr and Cu centered ico-like VPs decrease, while Al centered same VPs tend to decrease vaguely.

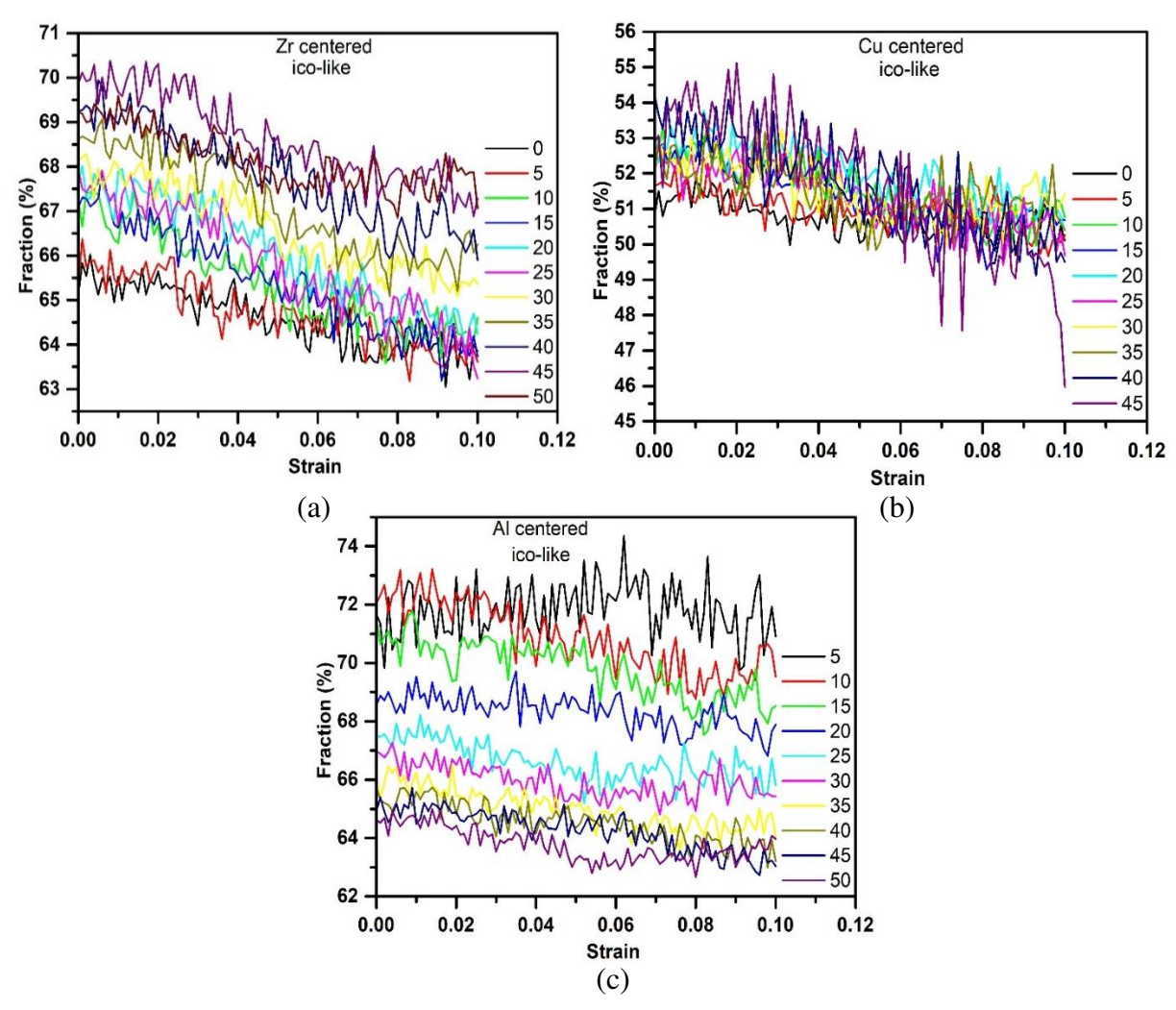


Fig. 6. The variation of (a) Zr (b) Cu (c) Al centered ico-like VPs with strain for $Zr_{50}Cu_{50-x}Al_x$ ($0 \le x \le 50$) BMGs

Conclusion

The evolution of microstructural and mechanical properties of ternary Zr-Cu-Al metallic glass under tensile loading was investigated by molecular dynamics simulations using embedded atomic potentials to describe interactions between atoms in the system. It is observed that $Zr_{50}Cu_{30}Al_{20}$ has the highest strength, while $Zr_{50}Al_{50}$ and $Zr_{50}Cu_{50}$ have the lowest. Additionally, $Zr_{50}Cu_{50}$ is a more flexible material than the other compositions, while $Zr_{50}Cu_{10}Al_{40}$ is a stiffer. The value of yield stress and Elastic Modulus for some $Zr_{50}Cu_{50-x}Al_x$ ($0 \le x \le 50$) alloys are in agreement with the literature. The fraction of ideal-ico clusters around the Al varies between 15 and 29 % and this ratio is higher than other related atoms. Due to the <0,0,0,12> VP constituting the most stable geometric units and forms to the essence of

icosahedral short range, we observed that for BMG, Al atoms dominate the local icosahedral short range. Additionally, Al atoms can be considered as the key factor in resisting corrosion of the amorphous system.

References

- 1. Zhang GQ, Jiang QK, Chen LY, Shao M, Liu JF, Jiang JZ. Synthesis of centimeter-size Agdoped Zr–Cu–Al metallic glasses with large plasticity. *J. Alloys Compd.* 2006;424(1–2): 176–178. 2. Peker A, Johnson WL. A highly processable metallic glass: Zr 41.2 Ti 13.8 Cu 12.5 Ni 10.0 Be 22.5. *Appl. Phys. Lett.* 1993;63(17): 2342–2344.
- 3. Romanov AI, Panov VA, Samsonov MA, Chirkin DE, Bragov AM, Igumnov LA, et al. Study of the deformation and fracture of zirconium alloys under dynamic loading. *Mater. Phys. Mech.* 2020;46(1): 88–98.
- 4. Das J, Tang MB, Kim KB, Theissmann R, Baier F, Wang WH, et al. "Work-Hardenable" Ductile Bulk Metallic Glass. *Phys. Rev. Lett.* 2005;94(20): 205501.
- 5. Yu P, Bai HY, Tang MB, Wang WL. Excellent glass-forming ability in simple Cu50Zr50-based alloys. *J. Non Cryst. Solids.* 2005;351(14–15): 1328–1332.
- 6. Inoue A, Zhang W. Formation, Thermal Stability and Mechanical Properties of Cu-Zr-Al Bulk Glassy Alloys. *Mater. Trans.* 2002;43(11): 2921–2925.
- 7. Baser TA, Das J, Eckert J, Baricco M. Glass formation and mechanical properties of (Cu50Zr50)100–xAlx (x=0, 4, 5, 7) bulk metallic glasses. *J. Alloys Compd.* 2009;483(1–2): 146–149.
- 8. Deb Nath SK. Formation, microstructure and mechanical properties of ternary ZrxCu90-xA110 metallic glasses. *J. Non Cryst. Solids.* 2015;409: 95–105.
- 9. Fan GJ, Freels M, Choo H, Liaw PK, Li JJZ, Rhim WK, et al. Thermophysical and elastic properties of Cu50Zr50 and (Cu50Zr50)95Al5 bulk-metallic-glass-forming alloys. *Appl. Phys. Lett.* 2006;89(24): 241917.
- 10. Celtek M, Sengul S, Domekeli U. Glass formation and structural properties of Zr50Cu50-xAlx bulk metallic glasses investigated by molecular dynamics simulations. *Intermetallics*. 2017;84: 62–73.
- 11. Meng FQ, Tsuchiya K, Yokoyama Y. Crystalline to amorphous transformation in Zr-Cu-Al alloys induced by high pressure torsion. *Intermetallics*. 2013;37: 52–58.
- 12. Cai A, Liu Y, Wu H, Ding D, An W, Zhou G, et al. Phase formation, glass forming ability, mechanical and thermal properties of Cu50Zr50-x Al x ($0 \le x \le 11.0$) glass forming alloys. *Sci. China Mater.* 2015;58(7): 584-594.
- 13. Cheung TL, Shek CH. Thermal and mechanical properties of Cu–Zr–Al bulk metallic glasses. *J. Alloys Compd.* 2007;434–435: 71–74.
- 14. Liao W, Zhao Y, He J, Zhang Y. Tensile deformation behaviors and damping properties of small-sized Cu–Zr–Al metallic glasses. *J. Alloys Compd.* 2013;555: 357–361.
- 15. Wang WH. The elastic properties, elastic models and elastic perspectives of metallic glasses. *Prog. Mater. Sci.* 2012;57(3): 487–656.
- 16. Plimpton S. Fast Parallel Algorithms for Short-Range Molecular Dynamics. *J. Comput. Phys.* 1995:117(1): 1–19.
- 17. Cheng YQ, Ma E, Sheng HW. Atomic Level Structure in Multicomponent Bulk Metallic Glass. *Phys. Rev. Lett.* 2009;102(24): 245501.
- 18. Sheng HW, Kramer MJ, Cadien A, Fujita T, Chen MW. Highly optimized embedded-atommethod potentials for fourteen fcc metals. *Phys. Rev. B.* 2011;83(13): 134118.
- 19. Yokoyama Y, Yamasaki T, Liaw PK, Inoue A. Study of the structural relaxation-induced embrittlement of hypoeutectic Zr–Cu–Al ternary bulk glassy alloys. *Acta Mater.* 2008;56(20): 6097–6108.
- 20. Feng SD, Li L, Chan KC, Qi L, Zhao L, Wang LM, et al. Control of shear band dynamics in Cu50Zr50 metallic glass by introducing amorphous-crystalline interfaces. *J. Alloys Compd.* 2019;770: 896–905.
- 21. Voronoi G. New Parametric Applications Concerning the Theory of Quadratic Forms -

V. Guder

Second Announcement. J. Reine Angew Math. 1908;134: 198–287.

22. Rycroft CH. VORO++: A three-dimensional Voronoi cell library in C++. *Chaos: An Interdiscip J. Nonlinear Sci.* 2009;19(4): 041111.

- 23. Zhang P, Maldonis JJ, Besser MF, Kramer MJ, Voyles PM. Medium-range structure and glass forming ability in Zr–Cu–Al bulk metallic glasses. *Acta Mater.* 2016;109: 103–114.
- 24. Kbirou M, Trady S, Hasnaoui A, Mazroui M. Cooling rate dependence and local structure in aluminum monatomic metallic glass. *Philos. Mag.* 2017;97(30): 2753-2771.
- 25. Park KW, Fleury E, Seok HK, Kim YC. Deformation behaviors under tension and compression: Atomic simulation of Cu65Zr35 metallic glass. *Intermetallics*. 2011;19(8): 1168–1173.

THE AUTHOR

V. Guder 🗓

e-mail: vildanguder@trakya.edu.tr

Effect of the parameters affecting the properties during friction stir welding of AA 5083 H111 alloy

Submitted: September2, 2022

Approved: January 26, 2023

Accepted: May 11, 2023

M. Merzoug ¹⁰ ^{1 ™}, A. Ghazi ², A. Lousdad ¹, N. Benamara ¹,

A. Miloudi ¹, A. Boulenouar ¹

Abstract. This research topic focuses on the friction stir welding (FSW) process. The study focuses on the correlation between the process parameters (feed speed and rotational speed) and the mechanical and microstructural characteristics of the 5083 H111 aluminum alloy sheets 4 mm thick placed end-to-end and welded by a vertical milling machine from. This experimental approach is based on the variation of the depth of penetration of the shoulder of the tool, allowing to contribute to mastering the axial force in order to predict the welding process area for this grade of aluminum by the welding process FSW. Then, tensile and hardness test were done to investigate the mechanical properties of the weld. The optimum process parameters were determined with reference to grain size, ultimate tensile strength and hardness. In addition, microhardness profiles allow to give the importance of the influence of the studied parameters on the different zones of the weld.

Keywords: FSW, aluminum alloys, penetration, pin and fracture surface

Citation: Merzoug M, Ghazi A, Lousdad A, Benamara N, Miloudi A, Boulenouar A. Effect of the parameters affecting the properties during friction stir welding of AA 5083 H111 alloy. *Materials Physics and Mechanics*. 2023;51(5): 116-125. DOI: 10.18149/MPM.5152023_12.

Introduction

Friction stir welding as a relatively new welding technique has gained wide applications in different industries such as aerospace, automotive and maritime [1–3]. This welding technique is essentially based on mechanical process in order to generate a temperature rise in the panels to be assembled. Producing the good quality welds is of great importance in many engineering applications. The maximum temperature created by the friction stir welding (FSW) process ranges from 70 to 80 % of the melting temperature of the welding material [4]. Low heat input during FSW prevents solidification failure and high temperature damage [5]. The development of a sound welds through FSW is more challengeable compared to the other welding techniques due to highly sensitivity to the welding parameters [6]. In a study, the highest tensile strength achieved was about 263 MPa and the defect-free joint was obtained by using the threaded tapered cylindrical pin tool at a rotational speed of 800 rpm [7]. In other study, analysis reveals that the nugget zone (NZ) exhibits recrystallized fine grains with an equiaxed structure as a result of dynamic recrystallization (DRX), resulting in improved mechanical properties of the joint [8,10]. Saravanakumar et al. [11,12] studied that the mechanical properties of the AA5083 UWFSW joint, such as its average ultimate tensile

¹Laboratory of Materials and Reactives Systems, University of Djillali Liabes, Sidi Bel Abbes, Algeria

² Laboratory of Materials and Reactives Systems, University of Mustapha Stambouli, Mascara, Algeria

□m merzoug01@yahoo.fr

strength and hardness, have been greatly improved using a straight hexagonal tool profile, tool rotational speed of 1200 rpm and welding speed of 20 and 40 mm/min.

In dissimilar joining of AA7075T651 retreating side and AA2024T351 advancing side investigated on the radius of pin flute with rotation speed 900 RPM, weld speed 150 mm/min of maximum tensile strength is 424 MPa with an efficiency of 94.3 % tool used threaded pin of flat cone for weld strength and joint strength truncated pin threaded tool is used and hardness of the weld is on soft metal of the heat affected zone [12,13]. Dissimilar joining of aluminum alloys by controlled temperature weld of tensile strength is improved on different clamping materials and backing of specially used for conjunction of weld speed 100 mm/min, rotational speed 900 rpm, tilt angle 30 and tensile strength is 426 MPa, elongation 7.1 % and efficiency of joint strength is 94.8 %. Mehta et al. and Sato et al. [14] studied of 5456-T321 aluminum alloy plates of the lower is 2.5 mm sheet annealed with tools used threaded conical pin, cylindrical conical threaded pin, stepped conical threaded pin, flared triflute pin are used on input parameters of rotational speed 600 rpm and 800 rpm, micro hardness, microstructure on nugget weld, heat affected zone, thermomechanical affected zone with fine grain size 5 μ m with free defect joints with growth of grain are investigated.

In this study, the hardness distribution and mechanical tensile properties of plates welded by FSW with different rotational speeds and welding speeds were investigated to study the effect of welding parameters on mechanical properties and fracture behavior of FSW for aluminum alloy 5083 H111. For all configurations of welding performed, a joint coefficient C_j is evaluated for the qualification of the good mechanical strength of welded joints.

Experimental method

In this investigation, distinct aluminium 5083 H111 sheets were welded using for different parameters. The chemical composition of this aluminium is presented in Table 1 and the mechanical properties of the sheets are presented in Table 2.

Table 1. Chemical composition of 5083 H111 aluminum alloy (BM)

Al	Si	Fe	Cu	Mn	Mg	Cr	Zn	Ti
0.15	0.40	0.40	0.10	0.10	4.90	0.25	0.25	0.15

Table 2. Mechanical properties of 5083 H111 aluminum alloy

E, MPa	YS, MPa	UTS, MPa	A, %	K, J/cm ²	HV	
71008	155	236	16.5	45	88	

A retrofitted milling machine was used for all the FSW experiments. To restrain the thermal expanding and thus bulking behaviour of plates, which could otherwise be encountered during normal FSW conditions, a bolted clamping system was used in all experiments.

Welds were made using a mixing tool, in a high-alloy steel (X210Cr12)with a tensile strength Rm = 870 MPa, a threaded cylindrical pin (7 mm diameter and 3.60 mm in length) and shoulder (25 mm diameter).

The process parameters used in the tests are listed in Table 3. All used sets of welding parameters allowed us to obtain defect-free weld faces. The most visible difference in the joints' appearance was the amount of flash, which increased together with the tool rotation speed. It is impossible to state unequivocally that the welding velocity in the used range (16–400 mm/min) has any impact on the formation of flash. An example photo of the joints produced with the different used welding velocity is presented in Fig. 1. This example illustrates the overall tendency of flash formation. For all tested values of welding velocity the

greatest flashes were obtained in joints produced with a tool rotation speed of 1400 rpm, pointing to the excessive material flow [15,16].

Table 3. Process parameters

ω, rpm	710	1000	1000	1400	2000	
V, mm/min	16	16	40	40	40	
	25	25	80	80	80	
	50	50	100	100	100	
	80	80	200	200	200	
	150	150	400	400	400	

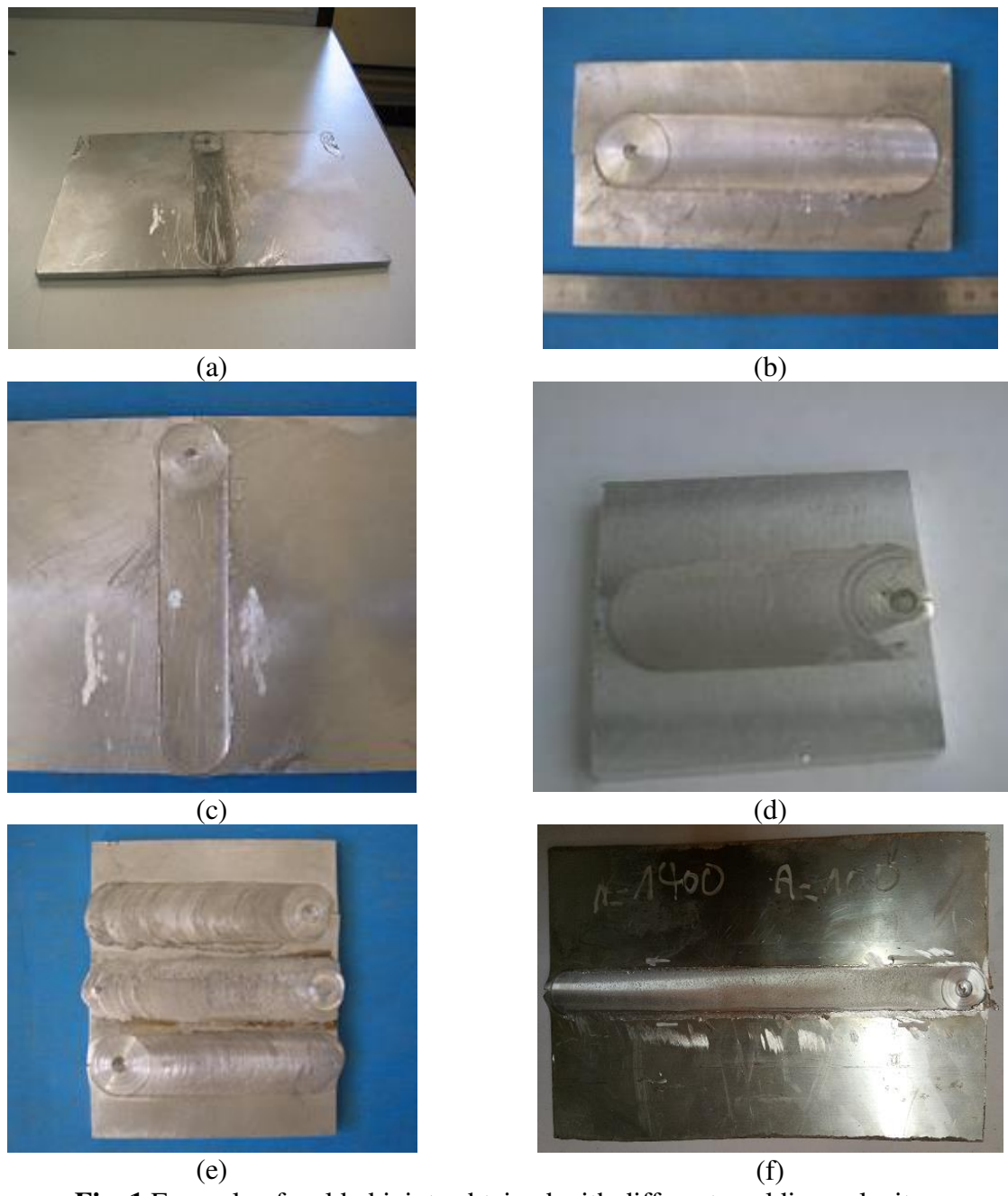


Fig. 1.Example of welded joints obtained with different welding velocity: (a) $\omega = 710$ rpm, V = 80 mm/min; (b) $\omega = 1000$ rpm, V = 80 mm/min; (c) $\omega = 1000$ rpm, V = 150 mm/min; (d) $\omega = 1000$ rpm, V = 16 mm/min; (e) $\omega = 710$, 1000, 1400 rpm, V = 25, 50, 100 mm/min; (f) $\omega = 1000$ rpm, V = 100 mm/min

The cutting operation of samples on the welded plates is shown in the diagram presented in Fig. 2, where the geometric dimensions are expressed in mm according to the American society for testing and materials (ASTM E8M-04) standards [17].

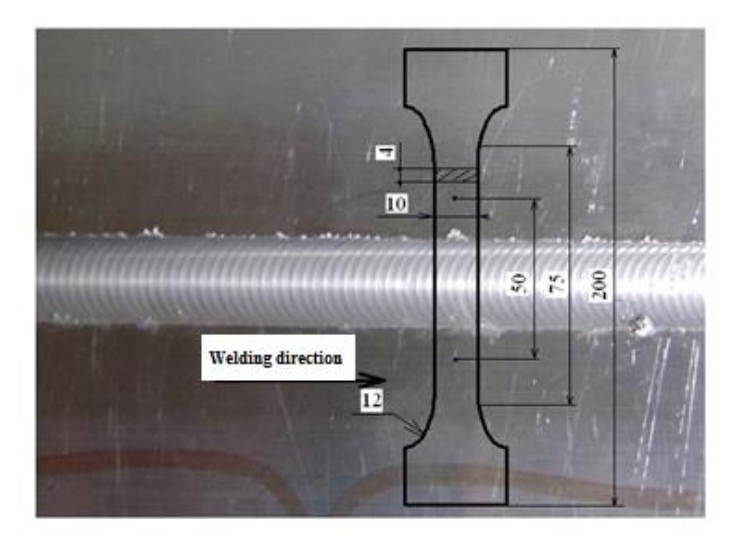


Fig. 2. Specimen preparation for tensile

Tensile tests were performed using a universal INSTRON tensile machine at a crosshead speed of 2 mm/min, controlled by the MTS software, as shown in Fig. 3. The broken tensile specimens after test is illustrated in (Fig. 3(b)).Profiles microhardness at midthickness of the joints; perpendicular to the axis of welding is performed. The measuring sockets are made every millimeter.





Fig. 3.Testing machine INSTRON: (a) tensile test specimen measured by the extensometer; (b) broken tensile specimens after test

Results and Discussions

Radiographic Inspection of Friction Stirs Welds. The results of the radiographic tests conducted on all the similar FSW weld joints produced at rotation speed of 710, 1000, 1400 rpm and transverse speed of 25, 50, 100 mm/min are hereby presented in Table 4. The defects found are mainly lack of penetrations, wormhole or voids. It can be seen from the results table that increasing the transverse speed increases the occurrence of defects. From the results, these weld flash is necessitated by material flow behavior, which is predominantly influenced by the FSW process parameters such as the tool rotational speed [18].

Table 4. Weld photographs and radiographs at different rotational and transverse speed

Table 4. Weld photographs and radiographs at different rotational and transverse speed						
Weld photo	Radiograph	ω, rp m	V, mm/mi n	Observation s		
	3	710 rpm	25 mm/min	Lack of penetrations, hole left		
	2	1000 rpm	50mm/min	Lack of penetrations, crack, incomplete fusion		
		1400 rpm	100 mm/min	Lack of penetrations, wormholedefect, Sufficient mixing		
	0	1000 rpm	150 mm/min	No evidence of root defects was observed on all the welds produced using the 700-rpm rotation speed and the feed rate 150 mm/min. Keyhole observed		

Microhardness profile and microstructure. It is well-known that the hardness profile of the FSW joints with various welding parameters may be a direct indicator of microstructural and global mechanical properties evolution during FSW process [19]. Fig.4 shows the evolution of the hardness variations along the traverse weld section for various welding parameters. Generally, the typical profile of the microhardness of a welded joint FSW is a W shape. Indeed, this type of profile is characterized by two minimum values H_V of microhardness. These two points were located in the TMAZ. In the stirred zone (ZS), the microhardness value increases in comparison with the TMAZ, corresponding to the second minimum. It should be emphasized that the size of the ZS area is governed by the pin diameter, while the TMAZ area is generated by the size of the tool shoulder of the tool.

In addition, Fig. 1 shows that the TMAZ is the weakest region in a welded joint FSW. Whatever the welding parameters there has been a decrease in hardness in the HAZ which is due to the restoration phenomenon. This phenomenon is characterized by the recombination

and rearrangement of dislocations[20]. At the edge zones HAZ and TMAZ the granular structure is completely recrystallized. This recrystallization takes place near the TMAZ where a significant decrease in hardness is detected.

Figure 4 shows that a small welding speed value (40 mm/min, 1000 rpm) gives a small value of the microhardness equal to 33 HV in TMAZ region on both advancing side (AS) and retreating (RS). This 38 % degradation in hardness is mostly characterized in the TMAZ. This is attributed to a combination of high stresses and large strains resulting in the deformation of the grain structure, where re-crystallization did not take place, caused a coarse grain structure [18]. Thus, the roughly homogeneous hardness profiles could have an intimate relationship with the good thermal stability during FSW (Fig. 7). Finally, higher hardness values are attained at the welding speed of 200 mm/min as result of formation of a very fine grain structure. This result is not surprising because a small welding speed generates a high temperature in the seal, which creates a hot welding [21]. Therefore, it is clear that the failure of tensile specimens is often located in the TMAZ region or in a region between TMAZ and HAZ. On the other hand, the hardness values were reduced to a high welding speed because the temperature in the tool is reduced, thus leading to cold welding.

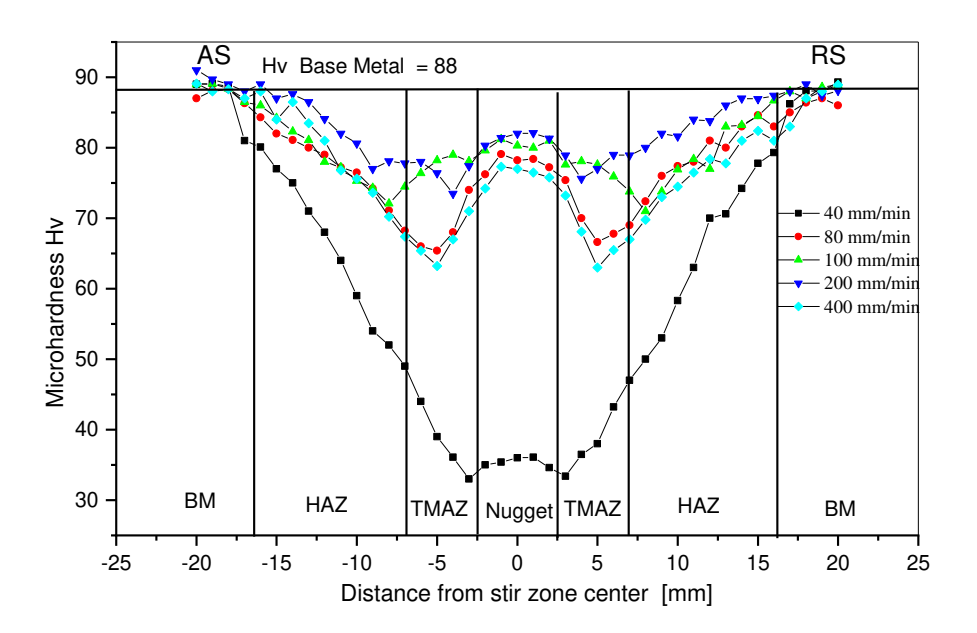


Fig. 4. Variation of the hardness for the rotational speed 1000 rpm

Tensile strength. The material was welded according to the above-mentioned specifications of different welding conditions. Tensile strength of the FSW joints was evaluated by conducting tests in a INSTRON 8516 universal testing machine. For each welded plate, specimens were prepared and tested. The fracture has occurred mostly in the HAZ on the retreating side of the weldment.

At low spindle speeds, frictional heat generation is less, which results in the poor plastic flow of material. Therefore, lower tensile strength was observed. At higher spindle speeds, frictional heat generation is high which enhances the plastic flow of material thus loses the tool material contact. So the poor stirring was obtained. At the highest welding speed of 200 mm/min and lowest welding speed of 80 mm/min, lower tensile strengths were observed.

Figure 5 shows the effects of welding parameters on the mechanical strength of welded joints, which are compared to the yield stress value of the base metal (155 MPa). We define the coefficient of joint efficiency as the ratio between the mechanical assembly and the mechanical properties of the base metal (Table 5). Where Ys is the welded joint tensile elastic limit.

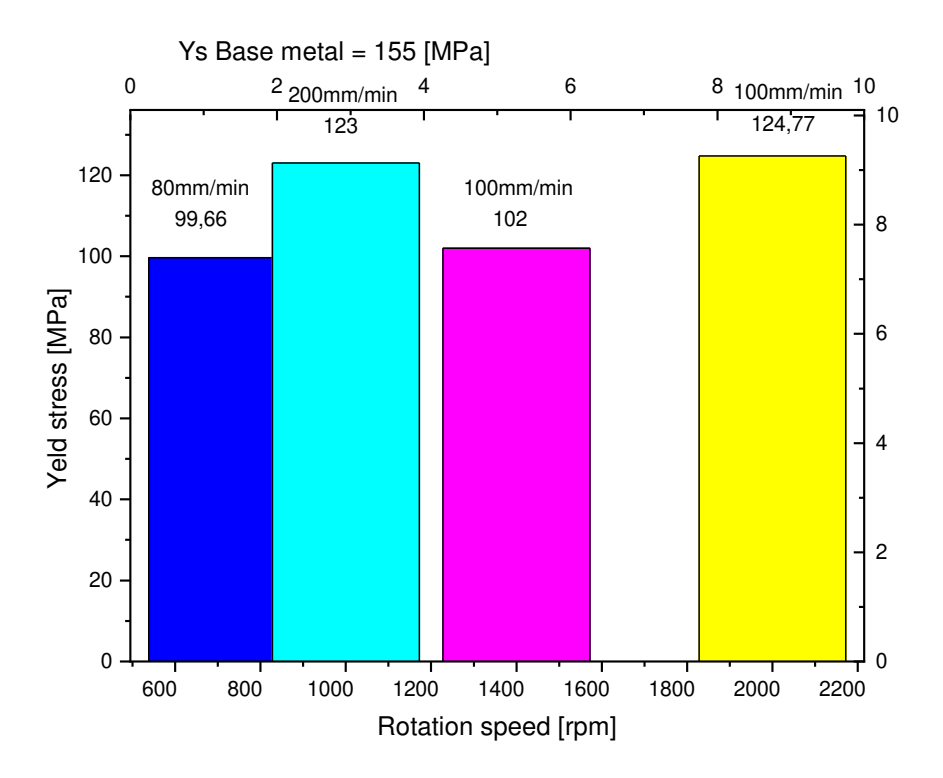


Fig. 5. Variation of the yield strength YS versus rotation speed and welding speed

Table 5. Tensile test results for welded specimens

N° of Sample	ω, rpm	V, mm/min	YS, MPa	UTS, MPa	Efficiency of joints, %	Fracture location
1	710	40	90	139.92	59.29	TMAZ
2	710	80	100	151.63	64.25	TMAZ
3	710	100	90	136.40	57.80	TMAZ
4	710	200	45	71.98	30.50	TMAZ
5	710	400	30	47.64	20.19	Nugget
6	1000	40	35	56.16	23.80	Nugget
7	1000	80	70	115.28	48.85	TMAZ
8	1000	100	110	173.55	73.54	TMAZ
9	1000	200	123	187.26	79.35	TMAZ
10	1000	400	60	95.29	40.38	TMAZ
11	1400	40	33	54.35	23.03	Nugget
12	1400	80	60	85.85	36.38	TMAZ
13	1400	100	105	155.28	65.80	TMAZ
14	1400	200	75	116.91	49.54	TMAZ
15	1400	400	55	83.28	35.29	TMAZ
16	2000	40	20	30.44	12.90	Nugget
17	2000	80	115	181.17	76.77	TMAZ
18	2000	100	123	189.95	80.49	TMAZ
19	2000	200	33	46.94	19.89	Nugget
20	2000	400	28	39.27	16.64	Nugget

This coefficient allows to estimate the reduction in strength due to the welding operation. For aluminum alloys, the coefficient for weld joint by FSW is of the order of 0.6 to 1 [22].

It was found thatultimate tensile strengths(UTS) of the joints were nearly equal a 50 % to those of the BM with the joint efficiency being 20–80%, and they were insensitive to changes in the welding parameter. However, the fracture behavior of the joints varied with the welding parameter. After the tensile test, FSWed specimens had fracture near TMAZ/HAZ at the retreating side. By applying the rolling process, it did not change the location of the fracture [23]. The fracture at the HAZ indicated that it was the weakest point of the welding area. This is because the grains in the HAZ experienced an annealing-like process by heat transfer from the NZ during welding. Hence, the grain size increased, whereas the mechanical properties and hardness decreased [24].

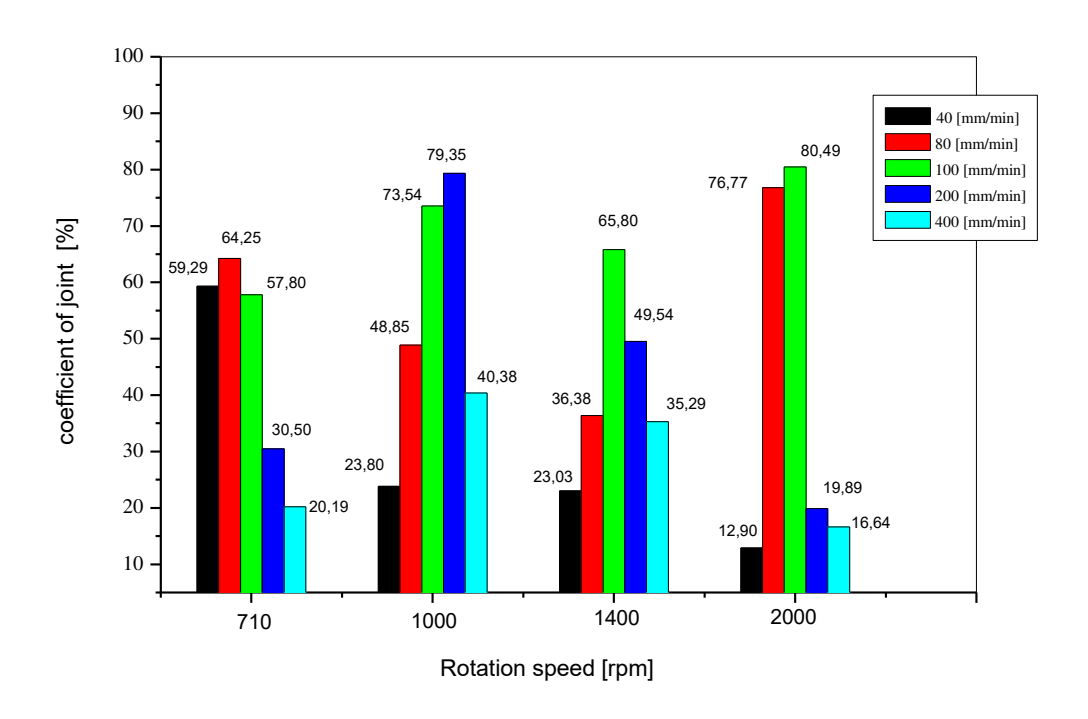


Fig. 6. Variation coefficient of joint versus welding speed for the rotational speed

The Figure 6 shows the variation of the coefficient of the joint for all welding parameters, such as rotational speed and the welding speed. From this figure, we see that the optimal values are obtained in the following ranges:

- 1. [710 rpm, 80 mm/min],
- 2. [1000 rpm, 100 mm/min], [1000 rpm, 200 mm/min],
- 3. [1400 rpm, 100 mm/min],
- 4. [710 rpm, 80 mm/min],
- 5. [1000 rpm, 100 mm/min], [1000 rpm, 200 mm/min],
- 6. [1400 rpm, 100 mm/min],

From these results, one can draw the optimum values for the rotational speed and the welding speeds. The results correspond to the welding speed 100 mm/min gives optimal results that there is a stability.

Macroscopic fracture surface. Fig. 7 shows the fracture surfaces for all configurations of FSW tested in this investigation. The dimple shape on the surface highlights the ductile behaviour of the samples[25]. It is noted that the most homogeneous facies located for the conditions for speed 1000 and 1400 rpm and the welding speed 40 to 200 mm/min. But the

choice of low welding speed leads to an increase in the welding time, therefore ideal for the industry to take welding speed between 100 and 200 mm/min. Therefore, FSW is considered an effective method, and it gives long life welds due to the modification of microstructure which leads to the improvement of mechanical properties [26]. In addition, the heat input reduction leading to reduction in the thickness of TMAZ and HAZ which and reduction in recrystallized grain size, in turn, increases the tensile strength of the joint [27].

The facies of rupture for the speed 2000 rpm present the following observations:

- 1. High heat generation and strong mixing in the shoulder;
- 2. The material is led under the shoulder at the root;
- 3. Appearance of two cores;
- 4. Appearance of a defect of the type "wormhole".

The fracture of the facies for high welding speed 400 mm/min: the minimum boundary layer for steady motion of the material is not reached, lack of material at the root [20].

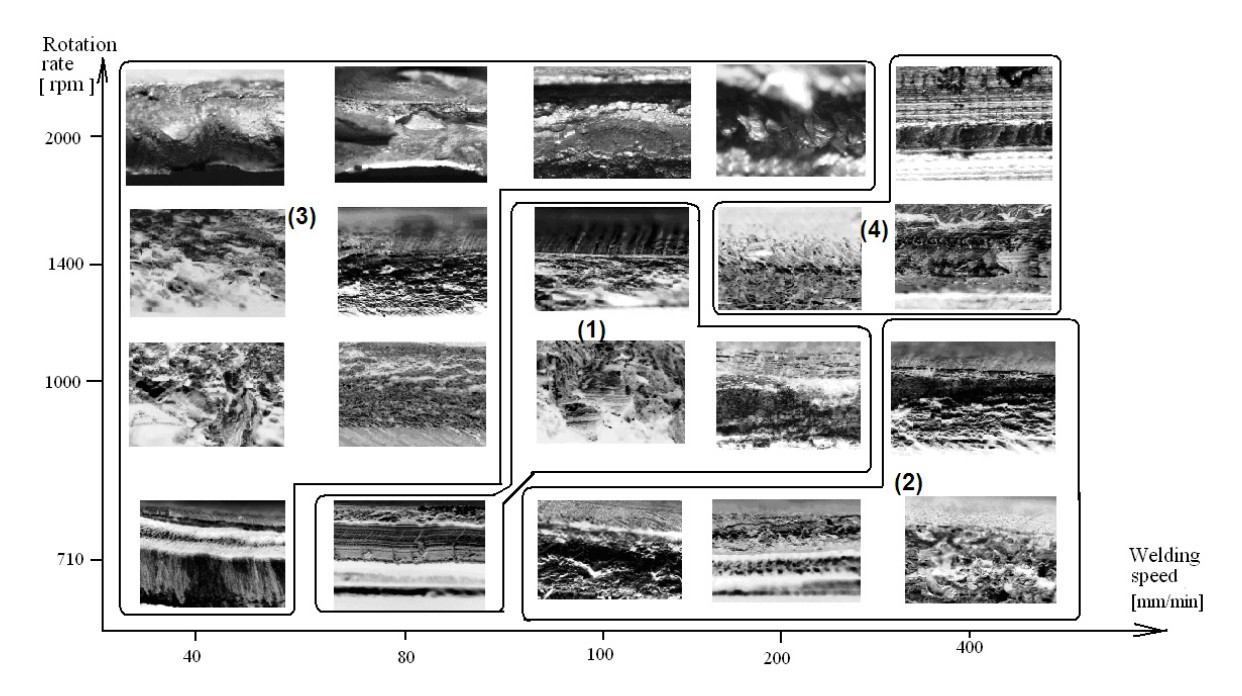


Fig. 7. Fracture surface of the alloy FSW 5083 H111

Conclusions

In this experiment, it is observed that the process parameters like tool design, tool rotational speed, and welding speed are the main parameters to produce the butt joint by friction stir welding. It can be concluded that by varying the process parameters within the range:

- 1. The hardness distribution and mechanical tensile properties of plates welded by FSW with different rotational speeds and welding speeds were investigated to study the effect of welding parameters on mechanical properties and fracture behavior of FSW for aluminum alloy 5083H111;
- 2. Ultimate tensile strengths (UTS) of the joints were nearly equal a 50% to those of the BM,with the joint efficiency being 20-80%;
- 3. Tensile strength increases with increase of tool rotational speed;
- 4. Tensile strength of base material is 155 MPa; it means the joint efficiency is 76 to 80 %;
- 5. The microstructure of the weld zone be dominated by recrystallization caused by the thermal excursion of the unstable base material, resulting in a wide zone of equiaxed grains around the weld line. Increasing the traverse narrows this weld zone.

References

- 1. Akbari M, Abdi Behnagh R. Dissimilar friction-stir lap joining of 5083 aluminum alloy to CuZn34 brass. *Metallurgical and Materials Transactions B*. 2012;43(11): 77–86.
- 2. Behnagh RA, Besharati Givi MK, Akbari M. Mechanical properties, corrosion resistance, and microstructural changes during friction stir processing of 5083 aluminum rolled plates. *Materials and Manufacturing Processes*. 2011;27: 636–640.
- 3. Shojaeefard MH, Behnagh RA, Akbari M, Givi MKB, Farhani F. Modelling and Pareto optimization of mechanical properties of friction stir welded AA7075/AA5083 butt joints using neural network and particle swarm algorithm. *Materials and Design*. 2013;44:190–198.
- 4. Campanelli S L, Casalino G, Casavola C, Moramarco V. Analysis and Comparison of Friction Stir Welding and Laser Assisted Friction Stir Welding of Aluminum Alloy. *Materials*. 2013;6: 5923–5941.
- 5. Saravana R, Linsha P, Harshini N, Rajasekaran T. Numerical Modelling of Thermal Phenomenon in Friction Stir Welding of Aluminum Plates AA5083 Military Grade Aluminium Alloy Joints in Underwater. *AIP Conference Proceedings*. 2022;2460: 070006.
- 6. Saravanakumar R, Rajasekaran T, PandeyC, Menaka M. Mechanical and Microstructural Characteristics of Underwater Friction Stir Welded AA5083 Armor-Grade Aluminum Alloy Joints. *Journal of Materials Engineering and Performance*. 2022;31: 8454–8472.
- 7. AzmiMH, Hasnol MZ, Zaharuddin MFA, Sharif S, Rhee S. Effect of tool pin profile on friction stir welding of dissimilar materials AA5083 and AA7075 aluminium alloy. *Archives of Metallurgy and Materials*.2022;67(2): 465–470.
- 8. Saravanakumar R, Rajasekaran T,Pandey C, MenakaM. Influence of Tool Probe Profiles on the Microstructure and Mechanical Properties of Underwater Friction Stir Welded AA5083 Material. *Journal of Materials Engineering and Performance*. 2022;31: 8433–8450.
- 9. Patil C, Patil H, Patil H. Investigation on Weld Defects in Similar and Dissimilar Friction Stir Welded joints of Aluminium Alloys of AA7075 and AA6061 by X-ray Radiography. *American Journal of Material Engineering and Technology*.2016;4(1): 11–15.
- 10. Saravanakumar R, Rajasekaran T,Pandey C. Optimisation of underwater friction stir welding parameters of aluminum alloy AA5083 using RSM and GRA. To be published in Proceedings of the Institution of Mechanical Engineers, Part E: Journal of Process Mechanical Engineering. [Preprint] 2023. Available from: doi.org/10.1177/09544089231158948.
- 11. Saravanakumar R, Rajasekaran T,PandeyC. Underwater Friction Stir Welded Armour Grade AA5083 Aluminum Alloys: Experimental Ballistic Performance and Corrosion Investigation. To be published in *Journal of Materials Engineering and Performance*. [Preprint] 2023. Available from: doi.org/10.1007/s11665-023-07836-2.
- 12. SalariE, Jahazi M, Khodabandeh A, Nanesa HG. Friction stir lap welding of 5456 aluminium alloy with different sheet thickness: process optimization and microstructure evolution. *International Journal of Advanced Manufacturing Technology*, 2016;82; 39–48.
- 13. Girish G. Effect of tool pin geometry and multi-pass intermittent friction stir processing on the surface properties of aerospace grade aluminium 7075 alloy. To be published in *Journal of Process Mechanical Engineering*. [Preprint] 2023. Available from: doi.org/10.1177/09544089231158948.
- 14. Mehta P K, Badheka J V. Influence of tool design and process parameters on dissimilar friction stir welding of copper to AA6061-T651 joints. *International Journal of Advanced Manufacturing Technology*, 2015;80; 2073–2082.
- 15. Kosturek R, Sniezek L, Torzewski J, Wachowski M. The Influence of Welding Parameters on Macrostructure and Mechanical Properties of Sc-Modified AA2519-T62 FSW Joints. *Manufacturing Review.* 2020;7:28.

- 16. Kosturek R, Torzewski J, Wachowski M, Sniezek L.Effect of Welding Parameters on Mechanical Properties and Microstructure of Friction Stir Welded AA7075-T651 Aluminum Alloy Butt Joints. *Materials*. 2022;15: 5950.
- 17. Chekalil I, Miloudi A, Planche MP, Ghazi A. Prediction of mechanical behavior of friction stir welded joints of AA3003 aluminum alloy. *Frattura ed Integrità Strutturale*. 2020;14(54): 153–168.
- 18. Mumvenge I, Akinlabi Stephen A, Mashinini PM, Fatoba S, Okeniyi J, Esther T, Akinlabi ET. Evaluation of Friction Stir Welds by X-ray Digital Radiographic Non- Destructive Approach. *Materials Science and Engineering*. 2018;413:012035.
- 19. Cavaliere P, Squillace A, Panella F. Effect of welding parameters on mechanical and microstructural properties of AA6082 joints produced by friction stir welding. *Journal of Materials Processing Technology*. 2008;200(1-3): 364–372.
- 20. Edwards P, Ramulu M. Peak temperatures during friction stir welding of Ti–6Al–4V. *Science and Technology of Welding and Joining*. 2010;15(6): 468–472.
- 21. Ahmed MMZ, Ataya S, El-Sayed Seleman M M. Heat input and mechanical properties investigation of friction stir welded AA5083/AA5754 and AA5083/AA7020. *Metals*.2021;11(1): 68.
- 22. Moraitis GA, Labeas GN. Investigation of friction stir welding process with emphasis on calculation of heat generated due to material stirring. *Science and Technology of Welding and Joining*.2010;15(2):177–184.
- 23. Tao Y, Zhang Z, Ni D R, Wang D, Xiao B L, Ma Z Y.Influence of welding parameter on mechanical properties and fracture behavior of friction stir welded Al–Mg–Sc joints. *Materials Science & Engineering A*. 2014;612: 236–245.
- 24. Selamata N M, Baghdadi A H, Sajuria Z. Effect of Rolling on Strength of Friction Stir Welded Joint of Aluminium Alloys. *Jurnal Kejuruteraan SI*. 2018;1(6): 9–15.
- 25. Abdul LN, Sajuri Z, Syarif J. Effect of aluminium content on the tensile properties of Mg-Al-Zn alloys. *Jurnal Kejuruteraan*. 2014;26: 35–39.
- 26. Marhoon II, Al-Kamal AK, Abdulrehman MA. Studying the Mechanical Properties for 5086 Aluminum Alloy Welded Plates by Friction Stir Welding (FSW). *International Conference On Materials Engineering and Science*. 2018;454: 012084.
- 27. Chandan P. Mechanical and Metallurgical Characterization of Dissimilar P92/SS304 L Welded Joints Under Varying Heat Treatment Regimes. *Metallurgical and Materials Transactions A*. 2020;51: 2126–2142.

THE AUTHORS

M. Merzoug (1)

e-mail: m merzoug01@yahoo.fr

A. Lousdad

e-mail: a_lousdad@yahoo.com

A. Miloudi

e-mail: miloudidz@yahoo.fr

A. Ghazi

e-mail: ghaziaek@yahoo.fr

N. Benamara

e-mail: benamara96@yahoo.fr

A. Boulenouar

e-mail: aek_boulenouar@yahoo.fr

Structure and properties of porous glass ceramics from siliceous rocks with the addition of $Mg(OH)_2$

Submitted: April 9, 2023

Approved: April 25, 2023

Accepted: May 29, 2023

A.I. Rodin [□] , A.A. Ermakov [□], I.V. Erofeev [□], V.T. Erofeev [□]

Abstract. Porous glass-ceramic materials are widely used in the construction, reconstruction and repair of objects for various purposes. The article establishes the influence of Mg(OH)₂ and together with Al₂O₃ in the composition of a charge of siliceous rocks and soda ash on the structure and properties of porous glass-ceramic materials. A joint mechanochemical activation of the components was carried out in a planetary ball mill, and then the resulting charge was fired at a maximum temperature of 825 °C. The influence of the type and quantity of additives on the structure and properties of porous glass ceramics was established by thermal analysis (TA), X-ray phase analysis (XRD), etc. From the charge with the addition of Mg(OH)₂ in glass ceramics, instead of wollastonite, diopside is formed, and instead of devitrite, combeite is formed. The influence of the phase composition of the samples on their properties has been established. The developed porous glass ceramics has an apparent density of 135-235 kg/m³, bending and compressive strength up to 1.6 and 4.2 MPa, respectively, a thermal conductivity coefficient of 0.05-0.067 W/m·°C, thermal resistance of 170 °C, maximum operating temperature up to 870 °C, high chemical resistance. The developed materials are superior in many respects to foam glass and other analogues and can be used in the insulation of industrial and civil facilities.

Keywords: glass ceramic; construction material; thermal insulation; siliceous rocks; Mg(OH)₂; compressive strength; thermal conductivity

Acknowledgements. The research was carried out at the expense of the grant of the Russian Science Foundation No. 21-79-10422, https://rscf.ru/project/21-79-10422/

Citation: Rodin AI, Ermakov AA, Erofeeva IV, Erofeev VT. Structure and properties of porous glass ceramics from siliceous rocks with the addition of Mg(OH)₂. *Materials Physics and Mechanics*. 2023;51(5): 127-141. DOI: 10.18149/MPM.5152023_13.

Introduction

Foam glass and porous glass-ceramic materials have a range of unique properties. They are light, durable, do not burn, have good thermal and acoustic insulating properties, high chemical resistance, etc. [1,2]. They are used in the construction, reconstruction and repair of walls of buildings and structures [3]. They insulate the structures of the floor, roof, and facades [2]. These materials have proved efficient in finishing works [4]. Porous glass ceramics are widely used in industry as refractory thermal insulation materials [5], anticorrosive materials [6], acoustic insulation of industrial equipment [7], etc.

Glass-ceramic materials made of solid waste are often used in construction of buildings and structures [7,8]. Numerous studies were aimed at developing compositions and technologies for obtaining porous glass ceramics from different types of industrial waste: ferrous and non-ferrous slags [4,9,10], red mud [11], fly ash [1,2,12,13], etc. A separate group of building materials includes glass ceramics from siliceous rocks (diatomite, tripoli,

© A.I. Rodin, A.A. Ermakov, I.V. Erofeeva, V.T. Erofeev, 2023.

Publisher: Peter the Great St. Petersburg Polytechnic University

This is an open access article under the CC BY-NC 4.0 license (https://creativecommons.org/li-censes/by-nc/4.0/)

opoka) [14–17]. Depending on the raw materials used, porous glass-ceramic materials are obtained using different technologies: by foaming colloidal suspension [18], powder method [1,2], etc. Foaming components are added to the charge to form the porous structure of the resulting glass-ceramic material with such production methods: carbonates [1,2,19], carbon with various additives [3,20], etc. Glass ceramics for construction is obtained from siliceous rocks mainly by the method of alkali activation of components followed by annealing [14,15]. This production method does not require foaming components. This technology yielded good results in the production of granular material. In our early works, we described the specifics of obtaining block-shaped porous glass ceramics from zeolite-containing tripoli [21–23]. Combined mechanochemical activation of dry components (tripoli and soda ash) was carried out at the first stage, and then the resulting charge was annealed at a temperature of no more than 850 °C. The charge foams and crystallizes during annealing. The obtained block-shaped materials have a homogeneous fine structure, low density, relatively high strength, high chemical resistance, elevated service temperature, etc.

The chemical and mineralogical composition of raw materials as well as the production technology have a direct impact on the composition, structure and properties of the resulting glass-ceramic material [15,19]. The chemical and mineralogical composition of the charge components affects the structure and phase composition of glass ceramics, which in turn affect the properties of the finished product. Several studies discovered found that the density of glass ceramics from industrial waste is significantly influenced by the amount of CaO in the composition of the material. The density of the material increases with an increase in CaO fraction [24,25]. The strength properties of glass ceramics improve with an increase in of Al₂O₃ content in the charge composition [26]. A similar effect was also established for an increase of Fe₂O₃ in the composition of the material [27]. The maximum service temperature of glass ceramics sharply decreases with an increased content of Na₂O, Fe₂O₃ and CaO in the charge [28,29]. The reverse effect was established with an increase in Al₂O₃ content in the charge composition [29,30].

We established the influence of chemical and mineralogical composition of charge prepared from siliceous rocks and soda ash on the structure and properties of porous glass-ceramic materials in our earlier studies. A homogeneous fine structure of glass-ceramic materials from siliceous rocks with a high calcite content in the composition was obtained by introducing a small amount of chlorides into the charge [21]. The phase composition of glass ceramics has practically not changed. A large amount of mineral nepheline is produced when porous glass ceramics are prepared from siliceous rocks with a high aluminum oxide content in the charge, increasing the resistance of the material to sudden temperature variations and its maximum service temperature from 850 to 930 °C, but decreasing the chemical resistance of the samples [22]. No results are available in the literature for the combined effect from introducing Mg(OH)₂ and it Al₂O ₃ into charge composition on the structure and properties of porous glass ceramics from siliceous rocks and soda ash.

The goal of the study was to establish the combined effect of magnesium hydroxide and aluminum oxide in the composition of a mechanochemically activated charge from siliceous rocks and soda ash on the structure and properties of porous glass-ceramic materials.

Objectives:

- to determine the combined effect of Mg(OH)₂ and Al₂O₃ on the phase transformations in the charge under heating and the phase composition of annealed porous glass ceramics by thermal analysis (TA) and X-ray diffraction phase analysis (XRD);
- to establish the effect of additives in the charge composition on the macrostructure of porous glass ceramics;

- to determine the effect of phase composition and macrostructure of porous glass ceramic samples on their physico-mechanical and thermophysical properties, as well as chemical resistance.

Methods

Materials. The following components were used for experimental studies: siliceous rocks (zeolite-containing tripoli and diatomite), soda ash, magnesium hydroxide, aluminum oxide and potassium chloride. Characteristics of the components:

- Zeolite-containing tripoli from Engalychevskoye deposit (Russia, Republic of Mordovia) with the following chemical composition: $62.35 \% \, SiO_2$, $11.27 \% \, CaO$, $6.67 \% \, Al_2O_3$, $2.05 \% \, Fe_2O_3$, $1.38 \% \, K_2O$, $0.94 \% \, MgO$, $0.30 \% \, TiO_2$, $0.10 \% \, Na_2O$, $0.18 \% \, P_2O_5$, $0.03 \% \, SO_3$, $0.06 \% \, SrO$, $14.67 \% \, PPP$. Mineralogical composition of the rock: $19.2 \% \, cristobalite$; $19.6 \% \, heulandite$; $8.5 \% \, quartz$; $21.3 \% \, calcite$; $9.9 \% \, muscovite$; $20.0 \% \, amorphous \, phase$. The rock was dried to a moisture content of less than $\leq 2 \% \, and \, crushed$ to a fraction of $< 5 \, mm$.
- Diatomite from Atemarskoye deposit (Russia, Republic of Mordovia) with the following chemical composition: 81.56 % SiO₂, 1.51 % CaO, 5.35 % Al₂O₃, 2.05 % Fe₂O₃, 0.97 % K₂O, 0.89 % MgO, 0.25 % TiO₂, 0.20 % Na₂O, 1.76 % SO₃, 1.46 % PPP. Mineralogical composition of the rock: 10.9 % quartz, 8.1 % muscovite, 80.0 % amorphous phase. The diatomite was dried to a moisture content of ≤ 2 % and crushed to a fraction of ≤ 5 mm.
- Soda ash (Na₂CO₃) with the main ingredient concentration of more than 99 %.
- Magnesium hydroxide (Mg(OH)₂) with the main ingredient concentration of more than 97 %.
- Aluminum oxide (Al₂O₃) with the main ingredient concentration of more than 97 %.
- Potassium chloride (KCl) with the main ingredient concentration of more than 97 %.

Sample compositions and preparation procedure At the first stage, dosing and combined mechanochemical activation of components (siliceous rocks, soda ash, magnesium hydroxide, aluminum oxide and potassium chloride) were carried out in a Retsch PM 400 planetary ball mill. Activation mode: overload inside mill cups was 20 g, duration 30 min. The required number of components for each charge composition is taken in accordance with Table 1.

Table 1. Charge compositions

Commonition	Charge composition, %							
Composition	Zeolite-containing tripoli	Diatomite	Na ₂ CO ₃	$Mg(OH)_2$	Al_2O_3	KCl		
C1	76.5	5.0		_	_			
C2	75.0	5.0		1.5	_			
C3	73.5	5.0		3.0	_			
C4	71.5	10.0		_	_	0.2		
C5	70.0	10.0		1.5	_			
C6	68.5	10.0	10.0	3.0	_			
C7	66.5	15.0	18.2	_	_	0.3		
C8	65.0	15.0		1.5	_			
C9	63.5	15.0		3.0	_			
C10	62.5	15.0		3.0	1.0			
C11	61.5	15.0		3.0	2.0			
C12	60.5	15.0		3.0	3.0	1		

After mechanochemical activation, the charge was annealed in rectangular metal molds with face sizes of $120 \times 120 \times 260$ mm under the following conditions: heating to a temperature of 640 °C at a rate of 6 °C/min, exposure at a temperature of 640 °C for 1 hour, heating to a temperature of 825 °C at a rate of 6 °C/min, exposure at a temperature of 825 °C for 30 min.

The molds with the resulting material were cooled together with the furnace to room temperature. Then they were removed from the furnace and disassembled, and the foamed material was cut into samples of the required sizes and tested.

Analytical methods. The effect of $Mg(OH)_2$ and Al_2O_3 on phase transformations in the charge under heating and the phase composition of the annealed porous glass ceramics were established by thermal analysis methods (differential thermal analysis (DTA) and thermogravimetric analysis (TGA)) and X-ray diffraction analysis (XRD):

- DTA and TGA of charge samples were carried out with the TGA/DSC1 system (Switzerland). The charge in the amount of 20 ± 0.1 mg was poured into an alundum crucible (150 μ l volume) and compacted by tapping the crucible against a table. The sample was placed in the device and heated from 30 to 850 °C at a speed of 10 °C/min. The device recorded changes in the mass and temperature of the sample. The experimental data obtained were processed using the STARe software (Mettler-Toledo, Switzerland).
- XRD of porous glass ceramic samples was carried out on an Empyrean PANalytical diffractometer (Netherlands) using a PIXcel 3D semiconductor detector. Samples of porous glass ceramics were crushed to a fraction of less than 90 μm . XRD patterns were recorded in linear scanning mode with CuK $_{\alpha}$ radiation in the angle range $2\Theta=10-45^{\circ}$. The recording rate was 0.0131 $^{\circ}$ /min, the integration time 150 s. The qualitative phase composition of the samples was determined by the Hanawalt method using an open database on crystallography.

The effect of additives in the charge composition on the macrostructure of porous glass ceramics was established by scanning the surface of the samples at a resolution of 600×600 dpi.

The influence of the phase composition and macrostructure of porous glass ceramic samples on the physical properties (density and porosity), mechanical properties (density under bending and compression), thermophysical properties (thermal conductivity, thermal resistance, maximum service temperature), as well as chemical resistance in water and aqueous solutions of acids and alkalis were established by the following methods:

- The true density of porous glass ceramics (ρ_0 , g/cm³) was determined using a pycnometer on samples crushed to a fraction of < 90 μm. During the experiment, 2 samples of each composition were tested. The arithmetic mean of the test results of the samples was taken as the final result for each composition.
- The open, closed and total porosity of glass ceramics was determined for cubic samples with the face size of 50 ± 5 mm. The testing procedure is described in detail in [22].
- The bending strength of the materials was determined for dry samples shaped as a rectangular prism with the face dimensions of $120 \times 30 \times 30$ mm. The samples were placed horizontally on two cylindrical supports (the diameter of the supports was 6 ± 0.1 mm) located 100 ± 1 mm from each other. A rod (6 ± 0.1 mm in diameter) through which force was applied to the sample was placed over the entire width of the sample at an equal distance from the supports. The force application rate was the same for all samples. The force at which failure occurred in the sample was controlled as a result of the experiment. The bending strength was determined by the standard formula. The arithmetic mean of the test results for three samples of each composition was taken as the final result.
- The compressive strength of porous glass ceramics was determined for cubic samples with a face size of 90 ± 5 mm. The samples were pre-dried and then subjected to a press test. The maximum value of the force at which cracks appeared in the sample or the height of the sample decreased by $10\,\%$ from the initial value was recorded in the experiments. The arithmetic mean of the test results for five samples of each composition was taken as the final result.
- The thermal conductivity of the samples was determined using an MIT-1 portable thermal conductivity meter (Russia) by the probe method. A hole with a diameter of 6 mm and a depth of 50 to 60 mm was drilled in the center of the face in dry cubic samples

 $(90 \times 90 \times 90 \text{ mm})$. Before the test, the prepared samples and the measuring device were kept in the laboratory at a temperature of 24 ± 1 °C for 2 days. During the test, the probe of the device was immersed in the hole and readings were taken. The arithmetic mean of the test results for five samples of each composition was taken as the final result.

The thermal stability of the materials was determined for cubic samples with a face length of 50 ± 5 mm. Cracking in the samples was monitored under abrupt cooling. At the beginning of the experiment, the samples were dried, and then placed for 2 hours in a thermostat with a temperature of 110 °C. After holding at a given temperature, the samples were removed from the thermostat in less than 10 seconds and immersed in a container with water (the water temperature was 20 ± 2 °C). The samples were kept in water for 65 ± 5 s. Cracked samples were removed from the test, and the experiment was repeated with the remaining ones the temperature of the thermostat increased by 10 °C. The experiment was repeated until cracks appeared in all samples. The thermal stability of each sample was calculated by the formula $\Delta T = T_T - T_W - 10$,

where T_T , °C, is the temperature of the thermostat at which the sample was kept; T_w , °C, is the temperature of the coolant in the container; 10 °C is the difference in the thermostat temperatures between the subsequent and the previous test.

The thermal resistance tests adopted the arithmetic mean for four samples of each composition as the final result.

- The maximum service temperature of porous glass ceramics was determined for samples shaped as rectangular prisms with face sizes of $90 \times 40 \times 40$ mm. The variation in sample sizes after heating was monitored. At the beginning of the experiment, the height and width of the samples were measured with an accuracy of 0.01 mm, and then they were mounted vertically in a muffle furnace. The samples in the furnace were heated under the following conditions: heating to a temperature 50 °C less than the set temperature at a rate of 10 °C/min, heating to a set temperature at a rate of 2 °C/min, exposure at a set temperature for 2 hours. The heating rate set was increased by 10 °C and the experiment was repeated if the sample sizes changed by < 1 % after the test. The arithmetic mean of the test results for three samples of each composition was taken as the final result.
- Chemical resistance of materials was determined for samples crushed to a fraction of 0.315-0.630 mm. The change in the mass of the samples after boiling in distilled water, an aqueous solution of acid and alkali was monitored. At the beginning of the experiment, the samples were dried, and then 5 ± 0.0005 g of the sample was poured into a flask. 100 ± 0.5 cm³ of reagent (distilled water, 6N HCl aqueous solution, 1N Na $_2$ CO $_3$ aqueous solution + 1N NaOH aqueous solution) were poured into the flask, which was then connected to a reflux condenser and the reagent was boiled. After 3 hours of boiling, aggressive fluid was poured out of the flask, and the sample was washed with distilled water at least 5 times. Distilled water was filtered through a paper ashless filter. The filter, together with the sample remaining on it, was placed in a ceramic crucible and calcinated in a muffle furnace at a temperature of 800 ± 10 °C for 1 hour. After the sample was dried in a desiccator with CaCl $_2$ to room temperature, it was weighed and the mass variation was determined. The arithmetic mean of the test results for two samples of each composition was taken as the final result.

Results and Discussion

Phase transformations in the charge and the phase composition of porous glass ceramics. The combined effect of $Mg(OH)_2$ and Al_2O_3 on phase transformations in the charge under heating was established by methods of differential thermal analysis (DTA) and thermogravimetric analysis (TGA). The results of the study are presented in Fig. 1.

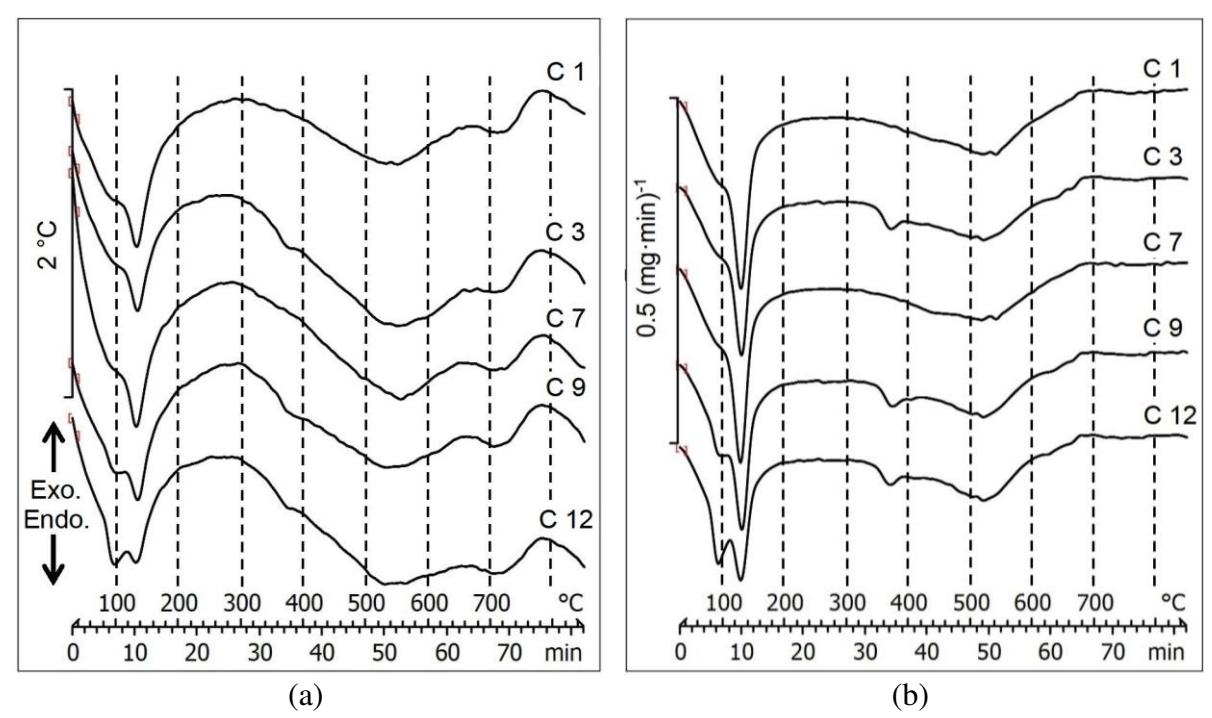


Fig. 1. DTA (a) and TGA (b) curves of charge samples

The data obtained (Fig. 1) can be used to assess the processes occurring in the charge from siliceous rock and soda ash with additives under heating. The endothermic effect in DTA (Fig. 1(a)) and the significant mass loss in TGA (Fig. 1(b)) observed in the curves of all tested samples at temperatures from 100 to 160 °C are likely associated with dehydration of hydrosilicates or sodium bicarbonates formed during grinding of the charge. The release of water from hydrosilicates in this temperature range was also observed by other authors [31]. The following endothermic effect and mass loss of samples C3, C9, C12 in the temperature range from 350 to 380 °C are associated with dehydration of Mg(OH)₂. A smooth endothermic effect in a large temperature range from 300 to 670 °C, accompanied by a significant loss of mass in all samples, is associated with decarbonization of minerals in the charge (calcite, natrite), as well as with the dehydration of minerals of the zeolite group (heulandite) and mica (muscovite). Formation of sodium silicates occurs in this temperature range [15,31]. According to the literature, surface hydroxyl groups are blocked in the micropores simultaneously with the formation of sodium silicates; as the charge is further softened, the micropores produce water vapor and foam it [15,31]. The softening of the charge, accompanied by an endothermic effect in the DTA curves of all tested samples, begins at a temperature of ≈ 680 °C. The reaction proceeds without changing the mass of the samples and ends with an exothermic crystallization effect. The temperature at which crystallization starts in all samples is ≈ 710 °C. The crystallization intensity decreases when the samples are heated above 780 °C.

It was established through thermal analysis of the charge samples that introducing up to 3 % Mg(OH)₂ combined with up to 3 % Al₂O₃ into its composition does not significantly affect the phase transformations in the charge under heating. Figure 2 shows XRD patterns of glass ceramic samples whose compositions are given in Table 1.

Analyzing the XRD patterns of the samples (Fig. 2), we determined the combined effect of $Mg(OH)_2$ and Al_2O_3 on the qualitative phase composition of glass ceramics. All tested samples consist of an amorphous and crystalline phase. The presence of an amorphous phase in the samples is evidenced by a non-monotonic change in the background (halo) in all XRD patterns in the angle range from 17 to 37° (2 θ). The type and amount of additives in the charge composition had no apparent effect on the variation of the amorphous halo. The crystalline

phase in the samples obtained from the charge without $Mg(OH)_2$ and Al_2O_3 additives (C1, C7) consists of quartz [SiO₂, Code: 96-900-9667], wollastonite [CaSiO₃, Code: 96-900-5779], devitrite [Na₂Ca₃Si₆O₁₆, [32]] and anorthoclase [(Na_{0.85}K_{0.15})(AlSi₃O₈), Code: 96-900-0860]. If up to 3 % $Mg(OH)_2$ is added to the charge, wollastonite in the glass ceramics composition is replaced by diopside [Mg_{0.56}Ca_{0.44}SiO₃, Code: 96-900-4210], and devitrite is replaced by combeite [Na₂Ca₂Si₃O₉, Code: 96-900-7718] (XRD patterns C2, C3, C8, C9 in Fig. 2). If diatomite content in the charge is increased from 5 to 15 %, practically no replacement of devitrite with combeite is observed. The effect can be explained by the introduction of chemically active SiO₂ in the amount necessary for crystallization of devitrite into the charge composition with diatomite. Conversely, the absence of this component in the charge composition leads to crystallization of combeite in glass ceramics containing two times less SiO₂. If up to 3 % $Mg(OH)_2$ combined with Al_2O_3 is added to the charge composition (C12), the anorthoclase content in the glass ceramics composition increases slightly. As we established in earlier studies [22], if Al_2O_3 is added to the charge, this leads to an increase of anorthoclase content in the composition of glass ceramics from siliceous rocks.

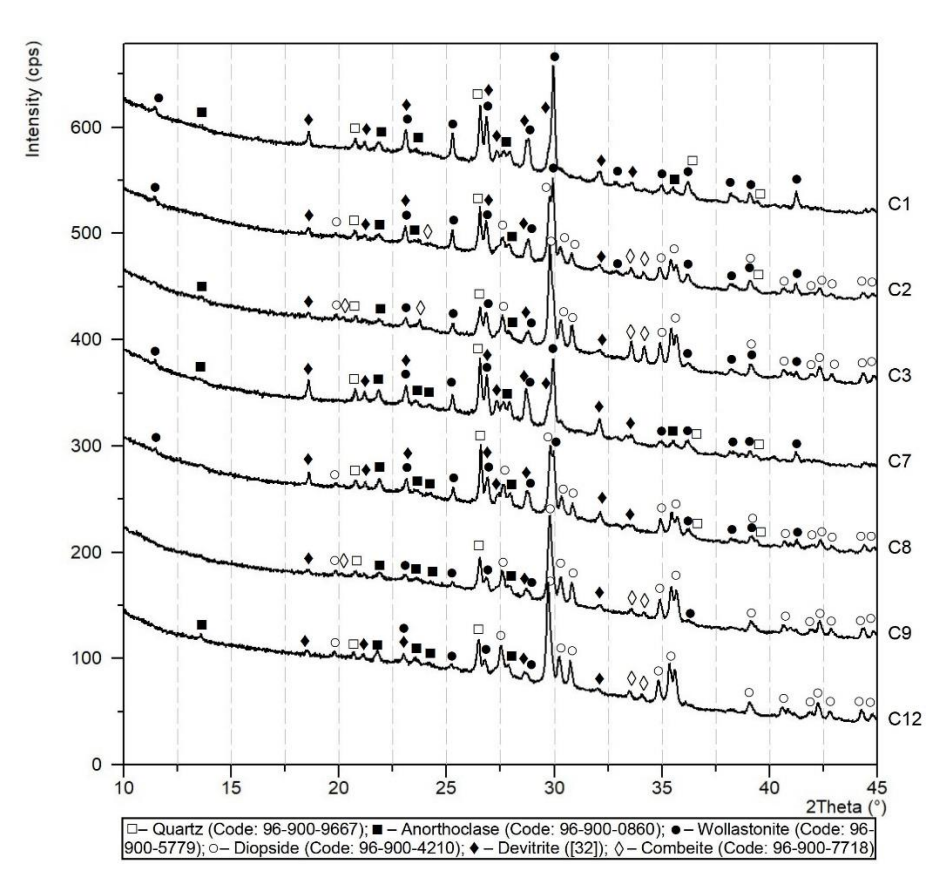


Fig. 2. XRD patterns of glass ceramic samples

Macrostructure of porous glass ceramics. The surface of the porous glass ceramic samples was scanned to illustrate the combined effect of $Mg(OH)_2$ and Al_2O_3 in the charge composition on the macrostructure. Figure 3 shows sample surface scans for all 12 compositions tested in the study.

According to Fig. 3, samples of porous glass ceramics obtained from the charge without $Mg(OH)_2$ additives have a homogeneous fine macrostructure (C1, C4, C7). The diameter of the cells decreases on average from 1.5 to 0.5 mm if 5 to 15 % diatomite is introduced into the charge. If up to 3 % $Mg(OH)_2$ is introduced into the composition of the charge from siliceous rock, this leads to an increase in the pore diameter to 10 mm. Samples C3 and C6 have the most

heterogeneous macrostructure. Analyzing the XRD data of the samples (Fig. 2), we can trace the direct dependence of the increase in the surface macrostructure heterogeneity with an increase in combeite mineral content in the composition. Simultaneously increasing Mg(OH)₂ to 3 % and diatomite to 15 % (C9) in the charge composition allowed to once again obtain a homogeneous macrostructure of glass ceramic samples with a pore diameter of no more than 2 mm. According to XRD analysis (Fig. 2), the combeite mineral content in the C9 sample is insignificant. Introducing Mg(OH)₂ combined with Al₂O₃ into the charge composition had no apparent effect on the surface macrostructure of samples from porous glass ceramics.

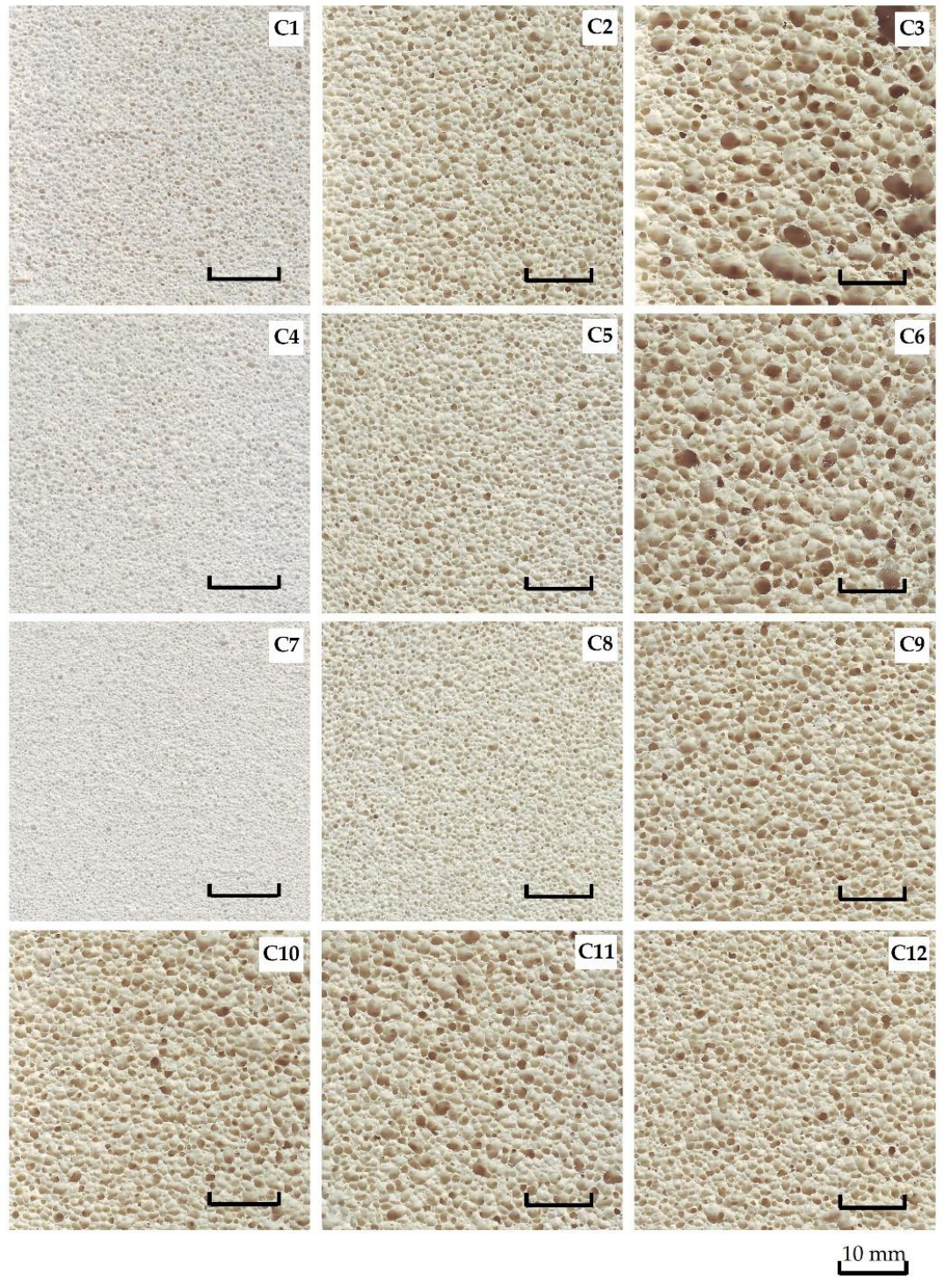


Fig. 3. Surface scan of porous glass ceramic samples

The surface color of samples from porous glass ceramics changed with an increase in Mg(OH)₂ in the charge composition to 3 %. The surface of the samples became more beige instead of light gray (without the Mg(OH)₂ additive). The effect can be associated with an increase in the diopside content in the samples (Fig. 2), as it can have different shades. According to the data given in the literature [4], the color of glass ceramics can also be influenced by the structure of the pores.

Physicomechanical properties of porous glass ceramics samples. Figure 4 shows the dependences of apparent density and porosity of glass ceramics samples on the type and content of additives (Mg(OH)₂, Mg(OH)₂ combined with Al₂O₃, diatomite) to the charge.

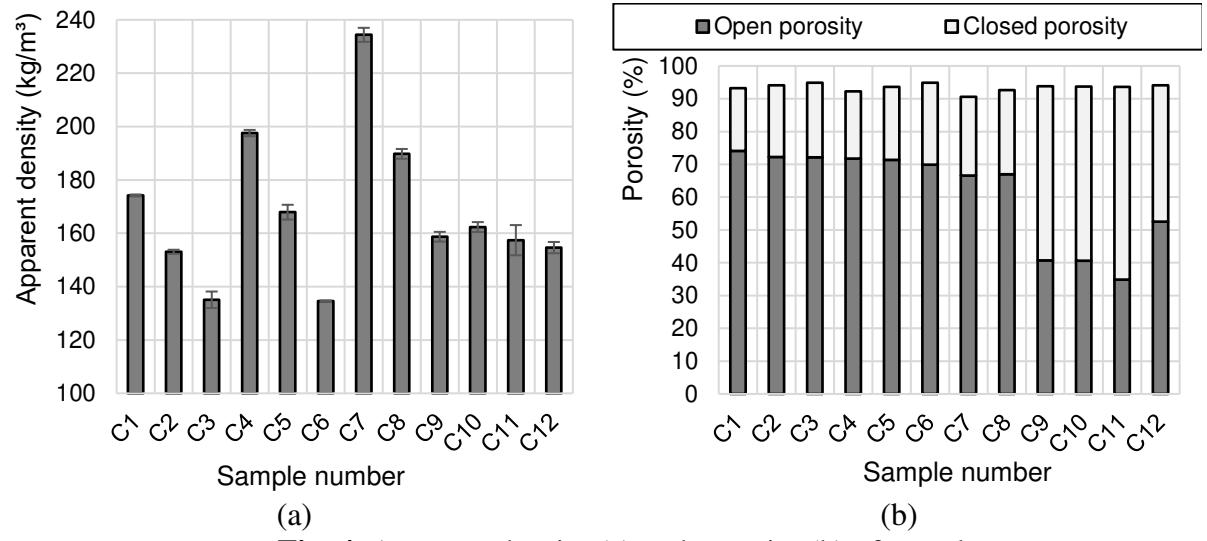


Fig. 4. Apparent density (a) and porosity (b) of samples

The results (Fig. 4(a)) indicate that the apparent density of porous glass ceramics samples decreases almost linearly if $Mg(OH)_2$ content in the charge composition is increased to 3 %. The effect is repeated with an increase in diatomite content in the charge from 5 to 15%. If $Mg(OH)_2$ is added to the charge composition together with Al_2O_3 , the apparent density of glass ceramic samples is further decreased. The highest value of apparent density is reached in samples of composition $C7 \approx 235 \text{ kg/m}^3$). The lowest values of apparent density are reached in samples of compositions C3 and $C6 \approx 140 \text{ kg/m}^3$). However, the samples of these compositions exhibit heterogeneous porosity (Fig. 3). As noted above, this disadvantage can be corrected by introducing amorphous silica into the charge.

According to Fig. 4(b), the total porosity of the tested samples of glass-ceramic materials is in the range from 90.6 to 94.9%. There is an increase in the total porosity of the samples with an increase in the composition of the charge to 3 % Mg(OH)₂. An increase in Mg(OH)₂ in the composition of the charge also contributes to an increase in the number of closed pores in the material. This effect is clearly visible with combined addition of 15 % diatomite to the charge. The number of open pores in the material decreases from \approx 70 to 40 % (C9). This effect is likely associated with a more homogeneous phase composition of the samples, consisting of the dominant mineral diopside and a small amount of quartz, wollastonite, devitrite and combeite minerals.

Introducing up to 2 % $Mg(OH)_2$ combined with Al_2O_3 to the charge composition further reduces open porosity. A further increase in Al_2O_3 increases the number of open pores in the material. An increase in open porosity in glass-ceramic samples from siliceous rocks with added Al_2O_3 was observed in [22]. Figure 5 shows the strength characteristics of porous glass ceramic samples from siliceous rocks.

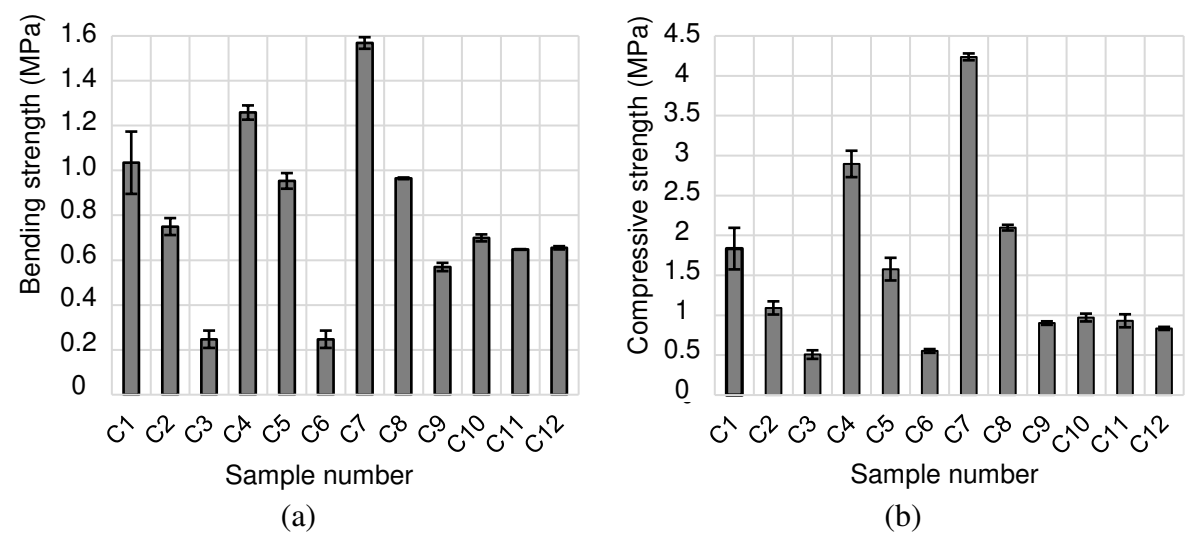


Fig. 5. Bending strength (a) and compressive strength (b) of samples

The analysis carried out (Fig. 5) indicates that bending and compressive strength of samples of porous glass-ceramic materials is linearly related to their apparent density. The apparent density of the samples and, consequently, their strength characteristics decreased as Mg(OH)₂ content in the charge composition was increased to 3 %. The highest value of bending strength (≈ 1.6 MPa) and compression strength (≈ 4.2 MPa) was observed for samples with an apparent density of ≈ 235 kg/m³ (C7), the lowest strengths (≈ 0.25 MPa and ≈ 0.5 MPa respectively) were observed for samples with a density of 135 kg/m³ (C3, C6). It was not possible to establish the influence of the phase composition of porous glass ceramics on their strength characteristics. Introducing up to 3 % Mg(OH)₂ into the composition of the charge from siliceous rocks and soda ash allowed to obtain porous glass ceramic samples whose strength characteristics were superior to foam glass and glass ceramics from industrial waste with the same apparent density [1,2,8,13,28,33].

Thermophysical properties of porous glass ceramic samples. Figure 6 shows the thermal conductivities determined for porous glass ceramic samples. The relationship of thermal conductivity with the apparent density of the samples is shown.

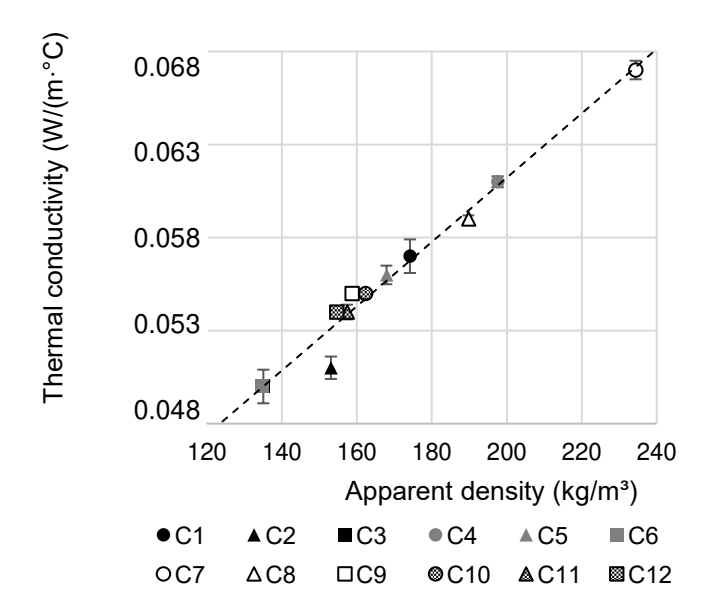


Fig. 6. Thermal conductivity of samples

The results in Fig. 6 point to a linear relationship between the thermal conductivity of porous glass ceramic samples and their apparent density. As the apparent density of glass ceramics is increased from 120 to 240 kg/m³, the thermal conductivity of the samples increases by the following formula:

$$\lambda = 1/6000 \cdot \rho + 0.028,\tag{2}$$

where: λ is the thermal conductivity, W/m °C, ρ is the apparent density of dry material, kg/m³. The approximation accuracy coefficient (R^2) is equal to 0.973.

It was established in the experiments that the lowest thermal conductivity (0.05 W/m·°C) is observed in dry porous glass ceramic samples of compositions C3 and C6. The apparent density of the samples is ≈ 135 W/m³. The highest thermal conductivity (0.067 W/m·°C) is observed in samples of composition C7 (apparent density ≈ 235 kg/m³). We detected no influence of the phase composition of porous glass ceramic samples on their thermal conductivity. The results obtained are in agreement with the data obtained in [34–36].

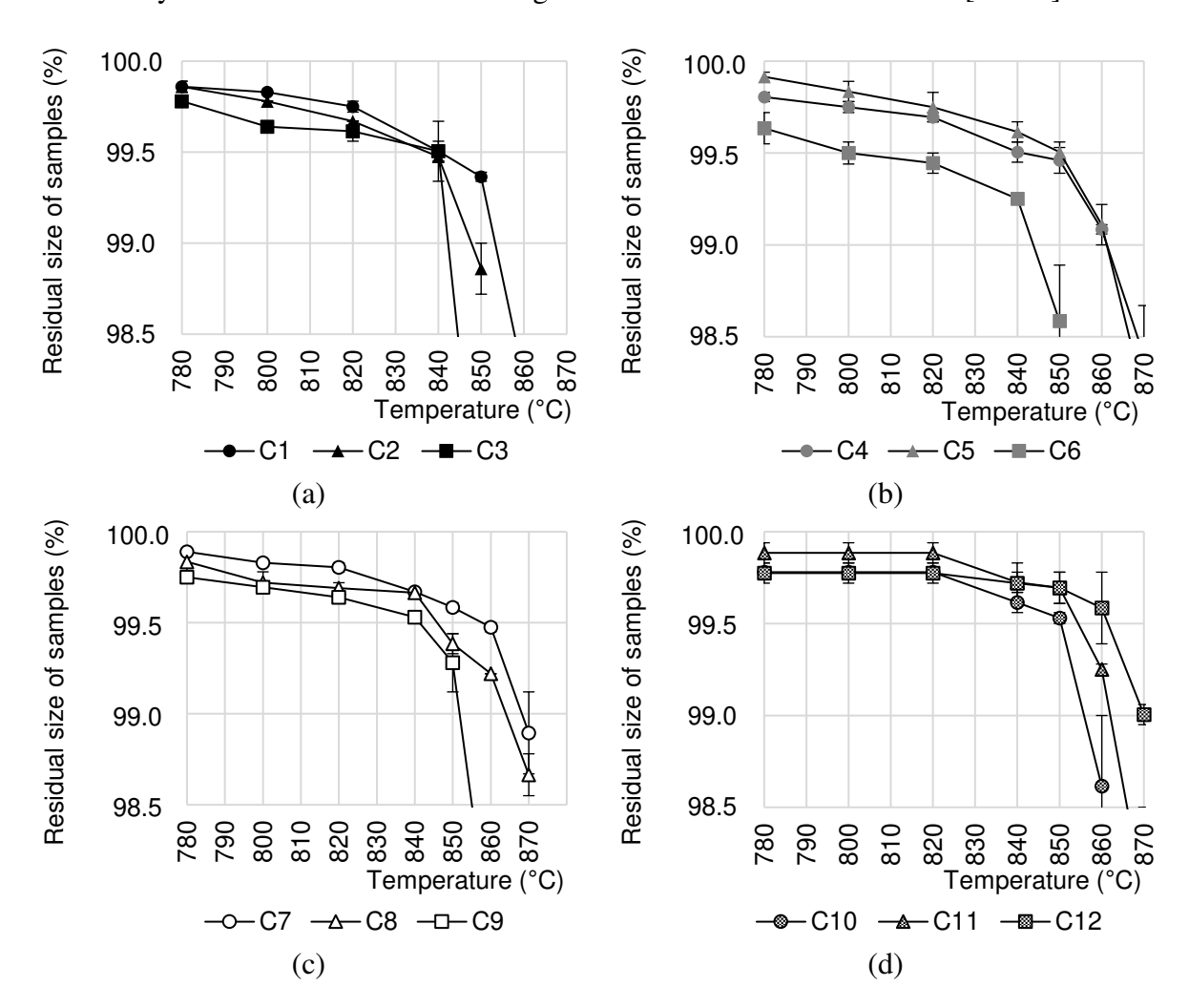


Fig. 7. Final dimensions of samples after exposure for 2 hours at a given temperature (samples from siliceous rock with added diatomite:

5 % (a); 10 % (b); 15 % (c); with added Al₂O₃ (d); C1–C12 are the composition numbers)

According to the data from [22], porous glass ceramics can be used for thermal insulation of industrial equipment. One of the main criteria for using a material as refractory thermal insulation is its maximum service temperature. This criterion is determined by the final size of the sample after exposure at a given temperature for 2 hours. Figure 7 illustrates the effect of

the type and quantity of additives (Mg(OH)₂, Mg(OH)₂ combined with Al₂O₃, diatomite) to the charge composition on the maximum service temperature of glass ceramic materials from siliceous rocks.

It was established in the experiments (Fig. 7) that the phase composition of porous glass ceramic samples has a significant effect on their maximum service temperature. The increased content of mineral combeite in the samples (Fig. 2, C2 and C3) reduces this indicator to 840 °C. If combeite and devitrite contents in the composition were decreased with a simultaneous increase in anorthoclase content, the maximum service temperature of the material increased to 870 °C (C12). This result was achieved by introducing 15 % diatomite, 3 % (Mg(OH)₂ and 3 % Al_2O_3 into the charge from siliceous rock and soda ash. Other studies [22,29,30] also confirmed that adding Al_2O_3 to glass ceramic materials has a positive effect on their resistance to prolonged exposure to high temperatures.

In terms of the maximum service temperature, the developed porous glass-ceramic materials from siliceous rocks (modified with Mg(OH)₂, Al₂O₃ and diatomite) are superior to foam glass and porous glass-ceramics from siliceous rocks obtained by alkaline charge activation [14–17,37]. They can be used as thermal insulation of melting furnaces, boiler equipment, etc.

An equally important requirement for refractory thermal insulation materials is their thermal resistance, which characterizes the ability of the material to withstand abrupt temperature changes [30]. According to experimental data, the thermal stability of the developed samples of porous glass ceramic materials virtually does not depend on the composition (Table 1) and is equal to 170 °C. This indicator is comparable with the test results for foam glass and porous glass ceramics from industrial waste [30], which once again confirms that is possible to use porous glass ceramics as thermal insulation in industrial equipment.

Chemical resistance of porous glass ceramic samples. The effect of the phase composition of porous glass ceramic samples on their chemical resistance is shown in Fig. 8. The criterion for assessing the chemical resistance of the material was the mass loss of crushed samples (fraction of 0.315–0.630 mm) after boiling for 3 hours in various chemical media.

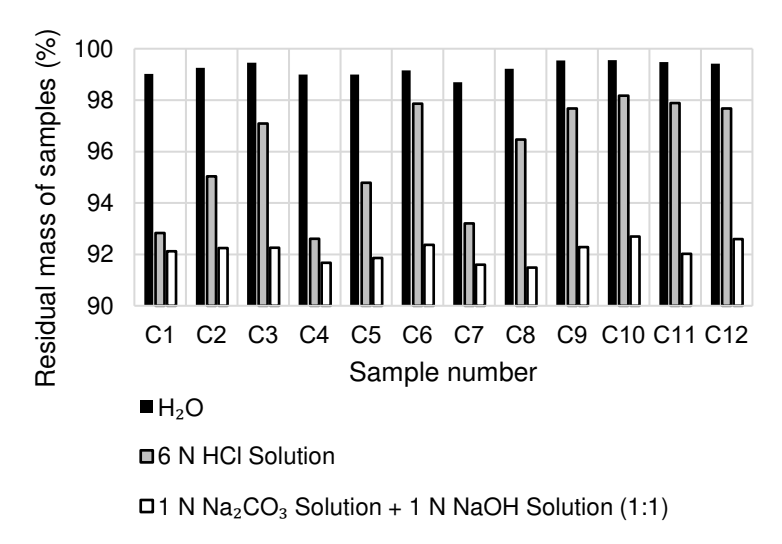


Fig. 8. Residual mass of samples after boiling in chemical media for 3 hours

According to the data obtained (Fig. 8), the developed glass-ceramic materials have high chemical resistance in water. This indicator increases with an increase in the composition of the mineral diopside samples (C3, C6, C9–C12). After boiling for 3 hours, glass ceramic samples with the maximum diopside content in the composition lost approximately 0.5 wt. %. The

results obtained make it possible to recommend the developed materials for applications in wet conditions.

We detected the influence of the phase composition of glass ceramic samples on their chemical resistance in an aqueous solution of HCl (6N). The residual mass of the samples after boiling in hydrochloric acid for 3 hours increased linearly from $\approx 93\,\%$ (C1, C4, C7) to $\approx 97.5\,\%$ (C3, C6, C9) with an increase in mineral diopside content and a consequent decrease in wollastonite in the composition of glass ceramic samples. The results obtained indicate a high chemical resistance of glass ceramics with predominant mineral diopside content. The literature also describes the insolubility of mineral diopside in acids, as well as self-gelation of wollastonite in hydrochloric acid [38].

We could detect no influence of the phase composition of glass ceramics from siliceous rocks on their resistance to alkaline solutions ($Na_2CO_3(1N) + NaOH(1N)$). After the samples were boiled in alkaline solution for 3 hours, their mass decreased by 7.5 – 8.5 %.

Based on our findings, we can argue that porous glass ceramics from siliceous rocks with added Mg(OH)₂, Al₂O₃ and diatomite have high chemical resistance. The results obtained are higher than those for many equivalents [38,39]. As a result, the developed materials can be used as insulation of pipelines, industrial installations, etc.

Conclusions

Porous glass-ceramic materials were obtained from a charge consisting of siliceous rocks, soda ash and additives. $Mg(OH)_2$, Al_2O_3 and diatomite were used as additives. Combined mechanochemical activation of the components was carried out in a planetary ball mill; next, the resulting charge was annealed at a maximum temperature of 825 °C. Thermal analysis and XRD analysis were used to establish the influence of the type and quantity of additives on the structure and properties of porous glass ceramic samples.

Main conclusions:

- Adding up to 3 % $Mg(OH)_2$ combined with up to 3 % Al_2O_3 to the composition of the charge from siliceous rock and soda ash does not significantly affect the phase transformations in the charge under heating. The annealed samples of porous glass ceramics consist of an amorphous and crystalline phase. The crystalline phase of the samples obtained from the charge without $Mg(OH)_2$ and Al_2O_3 additives consists of quartz, wollastonite, devitrite and anorthoclase. If $Mg(OH)_2$ is added to the charge, wollastonite in the composition is replaced by diopside and devitrite is replaced by combeite.
- To obtain a uniform fine structure of glass-ceramic materials from siliceous rock and soda ash with added Mg(OH)₂, it is necessary to minimize the mineral combeite content in the composition of annealed glass ceramics. This problem was solved by introducing diatomite into the charge. If diatomite content in the charge is increased from 5 to 15 %, practically no replacement of devitrite with combeite is observed. Consequently, glass ceramic samples have a homogeneous fine macrostructure with a pore diameter of no more than 2 mm.
- We established the influence of the phase composition of porous glass ceramic samples on their properties. If mineral diopside content in the composition was increased, the open porosity of the samples decreased, while their chemical resistance in water and aqueous hydrochloric acid solution increased. The maximum service temperature of the developed glass-ceramic materials is significantly influenced by the mineral combeite content in their composition. With its increase, the maximum service temperature of the samples decreased.
- The developed porous glass ceramics has an apparent density of $135-235 \text{ kg/m}^3$, bending and compressive strength up to 1.6 and 4.2 MPa, respectively, thermal conductivity of $0.050-0.067 \text{ W/m}\cdot^{\circ}\text{C}$, thermal resistance of 170 °C, maximum service temperature up to 870 °C, high chemical resistance.

- The developed materials are superior in many respects to foam glass and other counterparts and can be used as insulation in industrial and civil facilities.

References

- 1. Fernandes HR, Tulyaganov DU, Ferreira JMF. Preparation and characterization of foams from sheet glass and fly ash using carbonates as foaming agents. *Ceramics International*. 2009;35: 229–235.
- 2. Zhu M, Ji R, Li Z, Wang H, Liu L, Zhang Z. Preparation of glass ceramic foams for thermal insulation applications from coal fly ash and waste glass. *Construction and Building Materials*. 2016;112: 398–405.
- 3. König J, Lopez-Gil A, Cimavilla-Roman P, Rodriguez-Perez MA, Petersen RR, Østergaard MB, Iversen N, Yue Y, Spreitzer M. Synthesis and properties of open- and closed-porous foamed glass with a low density. *Construction and Building Materials*. 2020;247: 118574.
- 4. Cao J, Lu J, Jiang L, Wang Z. Sinterability, microstructure and compressive strength of porous glass-ceramics from metallurgical silicon slag and waste glass. *Ceramics International*. 2016;42(8): 10079–10084.
- 5. Guo H, Ye F, Li W, Song X, Xie G. Preparation and characterization of foamed microporous mullite ceramics based on kyanite. *Ceramics International*. 2015;41(10): 14645–14651.
- 6. Yatsenko EA, Ryabova AV, Goltsman BM. Development of fiber-glass composite coatings for protection of steel oil pipelines from internal and external corrosion. *Chernye Metally*. 2019;12: 46–51. (In-Russian)
- 7. Kyaw O, D'Amore G, Caniato M, Travan A, Turco G, Marsich L, Ferluga A, Schmid C. Innovative thermal and acoustic insulation foam from recycled waste glass powder. *Journal of Cleaner Production*. 2017;165: 1306–1315.
- 8. Hisham NAN, Zaid MHM, Aziz SHA, Muhammad FD. Comparison of foam glass-ceramics with different composition derived from ark clamshell (ACS) and soda lime silica (SLS) glass bottles sintered at various temperatures. *Materials*. 2021;14: 570.
- 9. Khater GA. Glass-ceramics in the CaO–MgO–Al2O3–SiO2 system based on industrial waste materials. *Journal of Non-Crystalline Solids*. 2010;356(52-54): 3066–3070.
- 10. Yatsenko EA, Gol'tsman BM, Kosarev AS, Karandashova NS, Smolii VA, Yatsenko LA. Synthesis of Foamed Glass Based on Slag and a Glycerol Pore-Forming Mixture. *Glass Physics and Chemistry*. 2018;44(2): 152–155.
- 11. Liu T, Li X, Guan L, Liu P, Wu T, Li Z, Lu A. Low-cost and environment-friendly ceramic foams made from lead-zinc mine tailings and red mud: Foaming mechanism, physical, mechanical and chemical properties. *Ceramics International*. 2016;42(1): 1733–1739.
- 12. Romero AR, Toniolo N, Boccaccini AR, Bernardo E. Glass-ceramic foams from 'weak alkali activation' and gel-casting of waste glass/fly ash mixtures. *Materials*. 2019;12: 588.
- 13. Zeng L, Sun H, Peng T, Zheng W. Preparation of porous glass-ceramics from coal fly ash and asbestos tailings by hightemperature pore-forming. *Waste Management*. 2020;106: 184–192.
- 14. Ivanov KS. Associated Synthesis of Microgranular Foam-Glass-Ceramic from Diatomaceous Shales. *Glass and Ceramics*. 2022;79(5-6): 234–238.
- 15. Kazantseva LK, Rashchenko SV. Optimization of porous heat-insulating ceramics manufacturing from zeolitic rocks. *Ceramics International*. 2016;42(16): 19250–19256.
- 16. Chumachenko N, Kizilova D, Hafizov I Studying penetrating ability of alkaline flow solution of caprolactam production in flint aggregate. *MATEC Web of Conferences*. 2018;196: 04016.
- 17. Yatsenko EA, Smolii VA, Gol'tsman BM, Ryabova AV, Klimova LV, Gol'tsman NS. Optimal Fractional Composition of Batch for Synthesis of Foam-Glass Materials Based on Diatomite from the Chernovarskoe Deposit. *Glass and Ceramics*. 2019;75(9-10): 391–393.

- 18. Huo W, Yan S, Wu J-M, Liu J, Chen Y, Qu Y, Tang X, Yang J. A novel fabrication method for glass foams with small pore size and controllable pore structure. *Journal of the American Ceramic Society*. 2017;100(12): 5502–5511.
- 19. Xi C, Zheng F, Xu J, Yang W, Peng Y, Li Y, Li P, Zhen Q, Bashir S, Liu JL. Preparation of glass-ceramic foams using extracted titanium tailing and glass waste as raw materials. *Construction and Building Materials*. 2018;190: 896–909.
- 20. König J, Petersen RR, Iversen N, Yue Y. Application of foaming agent—oxidizing agent couples to foamed-glass formation. *Journal of Non-Crystalline Solids*. 2021;553: 120469.
- 21. Rodin A, Ermakov A, Erofeeva I, Erofeev V. Effect of Chlorides Content on the Structure and Properties of Porous Glass Ceramics Obtained from Siliceous Rock. *Materials*. 2022;15: 3268.
- 22. Rodin AI, Ermakov AA, Kyashkin VM, Rodina NG, Erofeev VT. Porous glass ceramics from siliceous rocks with high operating temperature. *Magazine of Civil Engineering*. 2022;116(8): 11615.
- 23. Erofeev VT, Rodin AI, Bochkin VS, Ermakov AA. Properties of porous glass ceramics based on siliceous rocks. *Magazine of Civil Engineering*. 2021;102(2): 10202.
- 24. Zhou M, Ge X, Wang H, Chen L, Chen X. Effect of the CaO content and decomposition of calcium-containing minerals on properties and microstructure of ceramic foams from fly ash. *Ceramics International*. 2017;43(12): 9451–9457.
- 25. Yang Z, Lin Q, Lu S, He Y, Liao G, Ke Y. Effect of CaO/SiO2 ratio on the preparation and crystallization of glass-ceramics from copper slag. *Ceramics International*. 2014;40(5): 7297–7305.
- 26. Keyvani N, Marghussian VK, Rezaie HR, Kord M. Effect of Al2O3 content on crystallization behavior, microstructure, and mechanical properties of SiO2-Al2O3-CaO-MgO glass-ceramics. *International Journal of Applied Ceramic Technology*. 2011;8(1): 203–213.
- 27. Ren X-Z, Zhang W, Zhang Y, Zhang P-X, Liu J-H. Effects of Fe2O3 content on microstructure and mechanical properties of CaO-Al2O3-SiO2 system. *Transactions of Nonferrous Metals Society of China (English Edition)*. 2015;25(1): 137–145.
- 28. Jia R, Deng L, Yun F, Li H, Zhang X, Jia X. Effects of SiO2/CaO ratio on viscosity, structure, and mechanical properties of blast furnace slag glass ceramics. *Materials Chemistry and Physics*. 2019;233: 155–162.
- 29. Li Y, Zhao LH, Wang YK, Cang DQ. Effects of Fe2O3 on the properties of ceramics from steel slag. *International Journal of Minerals, Metallurgy and Materials*. 2018;25(4): 413–419.
- 30. Costa FPD, Morais CRDS, Pinto HC, Rodrigues AM. Microstructure and physicomechanical properties of Al2O3-doped sustainable glass-ceramic foams. *Materials Chemistry and Physics*. 2020;256: 123612.
- 31. Kazantseva LK, Rashchenko SV. Chemical processes during energy-saving preparation of lightweight ceramics. *Journal of the American Ceramic Society*. 2014;97: 1743–1749.
- 32. Kahlenberg V, Girtler D, Arroyabe E, Kaindl R, Többens DM. Devitrite (Na2Ca3Si6O16) structural, spectroscopic and computational investigations on a crystalline impurity phase in industrial soda-lime glasses. *Mineralogy and Petrology*. 2010;100: 1–9.
- 33. Ji R, Zheng Y, Zou Z, Chen Z, Wei S, Jin X, Zhang M. Utilization of mineral wool waste and waste glass for synthesis of foam glass at low temperature. *Construction and Building Materials*. 2019;215: 623–632.
- 34. Beregovoi VA, Beregovoi AM, Snadin EV. Improvement of Strength Parameters of Foam Ceramics for Energy-Efficient Enclosing Structures. *Solid State Phenomena*. 2020;299: 32–36.
- 35. Beregovoi VA, Sorokin DS, Beregovoi AM. Glass-crystalline materials of a cellular structure, formed by vibration foaming technology. *Defect and Diffusion Forum*. 2021;410: 823–828.
- 36. Erofeev VT, Korotaev SA, Vatin NI. Deformation and Heat-Insulating Characteristics of Light Concrete on Porous Burned Binder Under Heating. *Materials Physics and Mechanics*. 2023;51(1): 33–41.
- 37. Ivanov KS. Extrusion Method for Producing Microgranular Foam-Glass Ceramic from Zeolite Rocks. *Refractories and Industrial Ceramics*. 2021;62(2): 157–161.

- 38. Abdel-Hameed SAM, El-kheshen AA. Thermal and chemical properties of diopside-wollastonite glass-ceramics in the SiO2–CaO–MgO system from raw materials. *Ceramics International*. 2013;29: 265–269.
- 39. Montoya-Quesada E, Villaquirán-Caicedo MA, Mejía de Gutiérrez R, Muñoz-Saldaña J. Effect of ZnO content on the physical, mechanical and chemical properties of glass-ceramics in the CaO–SiO2–Al2O3 system. *Ceramics International*. 2020;46: 4322–4328.

THE AUTHORS

Rodin A.I.

e-mail: al_rodin@mail.ru

Erofeeva I.V.

e-mail: ira.erofeeva.90@mail.ru

Ermakov A.A.

e-mail: anatoly.ermakov97@mail.ru

Erofeev V.T.

e-mail: yerofeevvt@mail.ru

Surface morphology of InGaAs and InP layers after local Zn diffusion from the vapor phase in the MOCVD reactor

Submitted: July 17, 2023

Approved: August 14, 2023

Accepted: September 8, 2023

¹ Ioffe Institute, Saint Petersburg, Russia

Sciences (RAS), Saint Petersburg, Russia

⁵JSC OKB-Planeta, Veliky Novgorod, Russia

⊠ blokh@mail.ioffe.ru

Abstract. The influence of technological parameters during the local Zn diffusion from the metalorganic source DEZn in the MOCVD reactor on the surface morphology of the InGaAs and InP layers was investigated. For a long-term process (more than 120 minutes) of local Zn diffusion into InP through the InGaAs surface layer, erosion of InGaAs surface was observed regardless of the material of the dielectric mask (SiO₂, SiN_x), the method of deposition of the dielectric mask (plasma chemical deposition or chemical vapor deposition) and method of etching of the dielectric mask (plasma chemical etching or liquid chemical etching). The effect of lateral Zn diffusion under the dielectric mask was formed on InGaAs/InP heterostructures has been studied. It was found that the depth of Zn diffusion in lateral direction into InGaAs is several times less than the depth of lateral Zn diffusion into InP layer. At the same time, a decrease in the thickness of the InGaAs surface layer leads to an increase in the depth of lateral diffusion of Zn under the mask due to the mechanism of vertical Zn diffusion from the InP:Zn region into the InGaAs surface layer.

Keywords: zinc diffusion; surface morphology; diethylzinc; indium phosphide; indium gallium arsenide

Acknowledgment. Authors thank RZD for financial support of the fabrication of InGaAs/InP heterostructures for comprehensive studies of the Zn diffusion process.

Citation: Blokhin SA, Levin RV, Epoletov VS, Kuzmenkov AG, Blokhin AA, Bobrov MA, Kovach YN, Maleev NA, Prasolov ND, Kulagina MM, Guseva YA, Zadiranov YM, Nikitina EV, Andryushkin VV, Vasil'ev AP, Voropaev KO, Ustinov VM. Zn diffusion from vapor phase into InGaAs/InP heterostructure using diethylzinc as a p-dopant source. *Materials Physics and Mechanics*. 2023;51(5): 142-151. DOI: 10.18149/MPM.5152023_14.

Publisher: Peter the Great St. Petersburg Polytechnic University

² Alferov University, Saint Petersburg, Russia

³ Connector Optics LLC, Saint Petersburg, Russia

⁴ Submicron Heterostructures for Microelectronics Research and Engineering Center, Russian Academy of

[©] S.A. Blokhin, R.V. Levin, V.S. Epoletov, A.G. Kuzmenkov, A.A. Blokhin, M.A. Bobrov, Y.N. Kovach, N.A. Maleev, N.D. Prasolov, M.M. Kulagina, Yu.A. Guseva, Yu.M. Zadiranov, E.V. Nikitina, V.V. Andryushkin, A.P. Vasil'ev, K.O. Voropaev, V.M. Ustinov, 2023.

Introduction

The Zinc (Zn) diffusion into AIIIBV compounds makes it possible to form local regions with a required depth and a controlled profile of electrically active p-type dopant. That process is widely used for the fabrication of various optoelectronic and photonic devices [1–2] including avalanche photodiodes (APDs) based on InP/InGaAs heterostructures with separate photon absorption regions in InGaAs layer and multiplication of photogenerated charge carriers in the InP layer [3–4]. There are several main approaches to the diffusion process: diffusion in a sealed ampoule [5–6], Zn diffusion from the applied coating [7–8], Zn diffusion through a narrow gap using a planar source [9–10], diffusion from the vapor phase in an open tube [11–12]. Zn diffusion from the vapor phase in an open tube is the most preferable since it simultaneously ensures high uniformity of Zn diffusion over the sample area and reproducibility of the process.

Traditionally, a dielectric mask based on SiN_x is used to carry out the local diffusion process [13–14] because it allows to make diffusion process at elevated temperatures [15–18]. A dielectric mask based on SiO_2 also provides the required impermeability of Zn at moderate temperatures [19–20] and can be used to create an APD based on the $A^{III}B^V$ material system [8,10,21–23]. The choice of dielectric is due not only to the availability of the appropriate dielectric deposition technology but also be related to the features of the dielectric mask formation technology. Thus, several studies have noted the problem of a sharp increase in APD dark counts when using plasma chemical etching to form a surface relief in InP within the photosensitive region necessary to obtain a two-stage front of the distribution of a p-type dopant in a single Zn diffusion process [24]. In fact, the effect of trap-assisted tunneling [25] can be enhanced in comparison with liquid chemical etching of InP [26] apparently caused by defects introduced into InP during the plasma chemical etching process. It can be assumed that the transition from plasma chemical etching to liquid chemical etching during the formation of a dielectric mask may affect the characteristics of the APD.

In this paper we present the results of a study of the local Zn diffusion from the diethylzinc (DEZn) metalorganic source process technological parameters on the surface morphology of InGaAs and InP layers effect and considers the effect of lateral Zn diffusion into InGaAs/InP under a dielectric mask depending on the thickness of the InGaAs surface layer.

Experiment

The InGaAs/InP heterostructures were grown on InP substrates and consisted of undoped InP $3.5~\mu m$ thick layer, an undoped InGaAs 50~nm thick layer, an undoped InAlAs 10~nm thick stop-layer and an undoped InGaAs 250~nm thick surface layer (type I heterostructures). Type II heterostructures were formed from type I heterostructures by sequential selective chemical etching of the InGaAs surface layer and the InAlAs stop-layer. Type III heterostructures were formed from type II heterostructures by selective chemical etching of the InGaAs layer down to undoped InP layer.

The process of Zn diffusion from the vapor phase into InGaAs/InP heterostructures was produced at the MOCVD Aixtron AIX-200 system and DEZn was used as a metalorganic source of Zn with the flow of DEZn ~ 2.5·10⁻⁵ mol/min (a thermostat temperature was 17 °C). The Zn diffusion process was performed at a temperature of 500 °C and a reactor pressure of 50-200 mbar. To prevent deterioration of the InGaAs and InP surface morphology at temperatures above 400 °C a stabilizing flows of AsH₃ and PH₃ was fed into the reactor respectively.

To carry out local Zn diffusion process a dielectric mask was formed on the surface of the studied InGaAs/InP heterostructures using either SiN_x obtained by plasma chemical deposition, or SiO_2 obtained by plasma chemical deposition or by chemical vapor deposition. The required topology of the dielectric mask was formed using contact photolithography followed by plasma chemical etching or liquid chemical etching of the dielectric. To obtain a

two-stage front of a p-type dopant via a single Zn diffusion process a recess with a required shape and etching depth was formed within the dielectric mask window defining the photosensitive area of the APD. The recess was made either by selective chemical etching of the InGaAs layer to the InAlAs stop layer followed by selective removal of the InAlAs stop layer (type I heterostructures) or by chemical etching of InP (type III heterostructures).

After diffusion the studied samples were subjected to ex-situ rapid thermal annealing (RTA) in a nitrogen flow at a temperature of 450 °C for 5 minutes for thermal activation of dopants. To obtain quantitative information about the one-dimensional distribution of electrically active p-type dopants in the InGaAs/InP heterostructure samples after Zn diffusion process electrochemical volt-capacitive profiling (ECV) on the Nanometrics ECVPro electrochemical profiler system was used. The study of the surface morphology of the heterostructures subjected to the local Zn diffusion process was carried out using atomic force microscopy (AFM) on a Veeco Dimension 3100 microscope. Scanning was performed in semicontact scanning mode (when a probe with a certain resonant frequency touches the sample surface) at room temperature and atmospheric humidity of about 20 % using RTESP probes with a radius of 10 nm. Mathematical analysis of the obtained images allows us to determine several metric parameters of the surface topology. The R_{max} parameter represents information about the maximum height difference of the profile within the base (studied) length, while the R_z parameter gives information about the average absolute value of the five highest peaks and five deepest pits within the base length. However, to statistically describe the measured surface roughness the standard deviation of the heights of surface irregularities over the sample area R_q is more useful.

To obtain information about the two-dimensional distribution of electrically active p-type dopants in the studied samples the scanning electron microscopy (SEM) method was used. The position of the diffusion front of the Zn dopant was determined by the contrast boundary in the cross-sectional images of the samples between regions with different types of dopants. SEM images were obtained in the secondary electron mode at low (<5 keV) accelerating voltages.

Results and discussion

Our earlier studies of the Zn diffusion process from the vapor phase into InP through the InGaAs surface layer (type II heterostructures) showed that the minimum temperature of the Zn diffusion process is limited by the precipitation of Zn compounds in the solid phase below 460 °C and by the deterioration of the morphology of the InGaAs surface above 550 °C [27]. At the same time to achieve a necessary Zn diffusion depth (more than 2-2.5 μm with a thickness of undoped InP of about 3-3.5 μm) it is necessary to either extend the process time or increase the reactor pressure (see Fig. 1). However, temperature and pressure have a complex effect on the amount of p-type dopant introduced into InGaAs/InP layers. Thus, an increase in the reactor pressure leads to an increase in the maximum concentration of electrically active p-type dopants in the InP layer, while an increase in the temperature leads to a decrease in the concentration of holes.

Studies of the type I-II heterostructures surface morphology after local Zn diffusion process into InP layer through the InGaAs surface layer using a SiN_x dielectric mask have shown that for short duration (60 minutes) of the Zn diffusion processes the surface roughness of InGaAs:Zn does not exceed $R_q \sim 0.2\text{-}0.3$ nm within a scanning area of $5\times 5~\mu m$, which is at the level of atomic steps of a semiconductor substrate. However, in this case, in order to ensure the required depth of the p-type dopant it is necessary to increase the reactor pressure, which is accompanied by precipitation of Zn compounds in the solid phase [28], the intense defect formation, and the appearance of deep centers in the InGaAs:Zn/InP:Zn diffusion region due to the high concentration of Zn atoms [29–30].

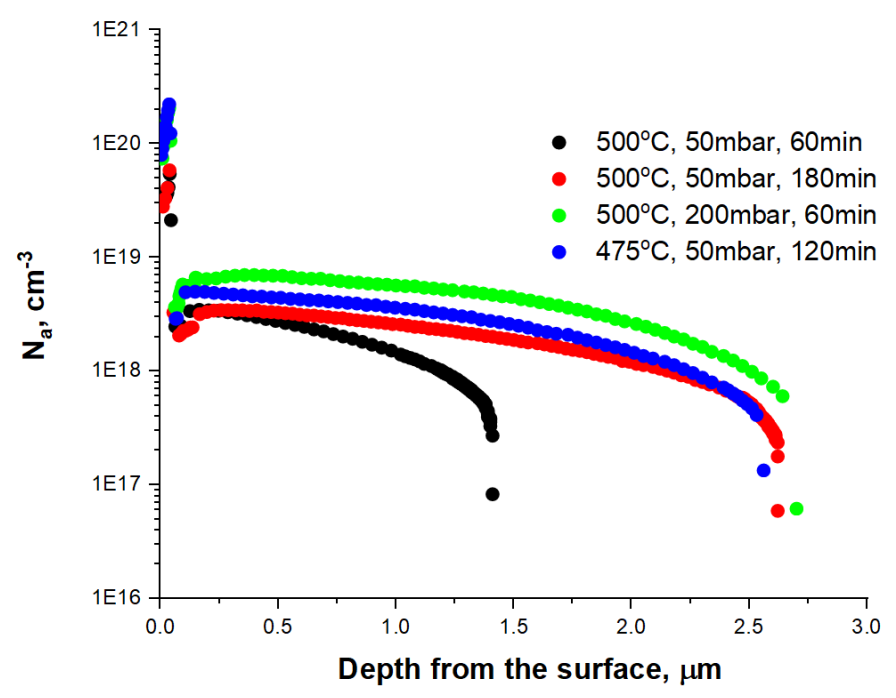


Fig. 1. ECV distribution profiles of electrically active p-type dopant in a type II heterostructure for various technological parameters of Zn diffusion into the InP layer through InGaAs

An increase in the duration of the Zn diffusion process to 180 minutes leads to erosion of the InGaAs:Zn surface (see Fig. 2). AFM measurements indicate a sharp increase in the roughness of the InGaAs:Zn surface to $R_q \sim 2.4$ nm within a scanning area of 5×5 μ m. A further increase in the time only aggravates the erosion of the InGaAs:Zn surface. It should be noted that an increase in the stabilizing flow of group V elements not only does not suppress this negative effect, but also increases the probability of precipitation of Zn compounds in the solid phase. On the one hand, deterioration of the InGaAs:Zn surface morphology (type I and II heterostructures) is not observed in the case of Zn diffusion into InP through the InGaAs layer without using a SiN_x dielectric mask, even for long-term Zn diffusion processes. On the other hand, the attempts made to additionally treat the InGaAs surface within the windows of the dielectric mask, including selective liquid chemical etching of the InGaAs surface layer, does not give a solution of the problem of InGaAs:Zn surface erosion during the local Zn diffusion process. It is possible that the observed dergation of the InGaAs:Zn surface morphology is associated with the modification of the InGaAs surface during plasma chemical deposition and/or plasma chemical etching of the SiN_x dielectric.

To exclude the possible negative effect of plasma chemical etching of the SiN_x dielectric on the InGaAs surface layer, it was proposed to switch to a SiO_2 dielectric mask, for which liquid chemical etching of the dielectric can be used when forming the required topology of the dielectric mask. In addition, it was decided to test two types of SiO_2 dielectric formed by plasma chemical deposition and by chemical vapor deposition. However, AFM studies of heterostructures with the SiO_2 dielectric mask after the local Zn diffusion process into InP through the InGaAs layer showed the retention of the problem of InGaAs:Zn surface erosion during long-term diffusion processes regardless of the type of etching of the dielectric and method of mask formation.

Similar studies of local Zn diffusion process directly into InP (type III heterostructures) have been carried out. It should be noted that the Zn diffusion process into InP layer from the vapor phase using a DEZn source is less studied, apparently due to a lower maximum concentration of a p-type dopant [11,31–32] compared with the case of using dimethylzinc

(DMZn) as an metalloorganic source of Zn [11,33–34]. According to our research, there is a similar behavior of the p-type dopant depth from the process time, temperature, and reactor pressure. However, the maximum concentration of electrically active p-type dopant in the InP layer is 2-3 times lower than the Zn diffusion into InP through the InGaAs layer (see Fig. 3). It can be assumed that the observed difference in the concentration of electrically active p-type dopant is related to the charge of elements diffusing through the interstitial-substitutional mechanism [35–36].

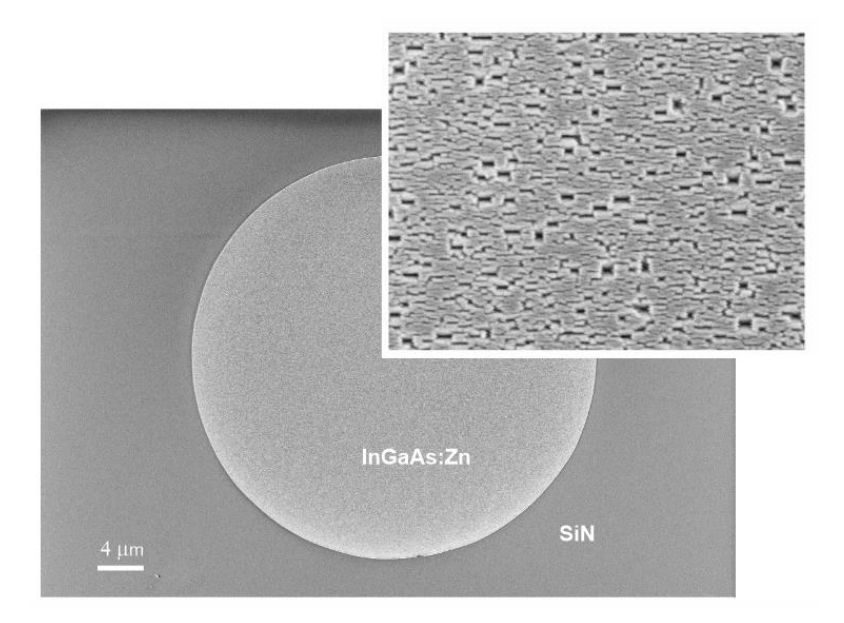


Fig. 2. SEM image (top view) of a sample with local Zn diffusion in InGaAs/InP through a SiN_x dielectric mask (type I heterostructure). The inset shows a SEM image of the sample within the central window. Temperature 500 °C, pressure 50 mbar, process time 180 min

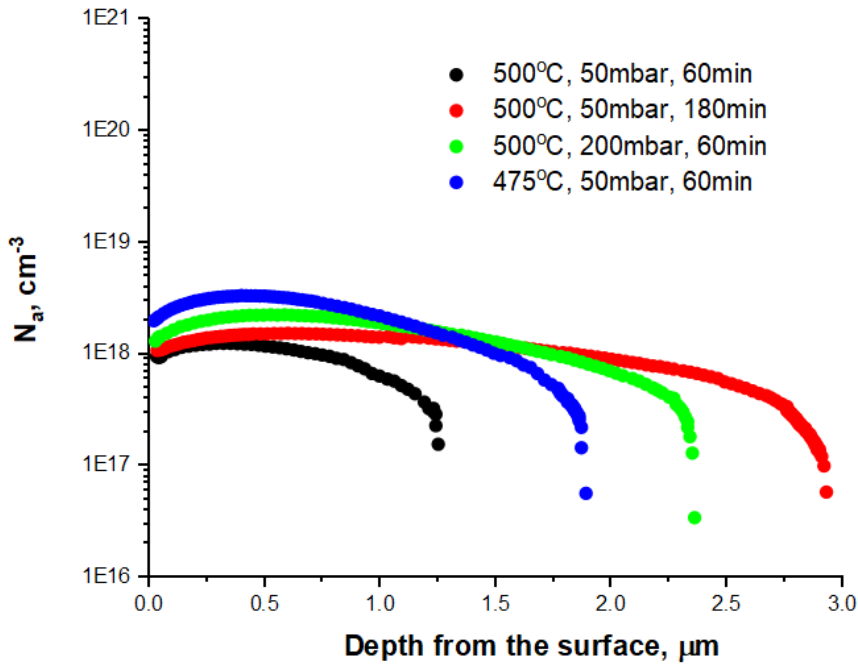


Fig. 3. ECV distribution profiles of electrically active p-type dopant in a type III heterostructure for various technological parameters of Zn diffusion into the InP layer

Studies of the type III heterostructures surface morphology after local Zn diffusion into InP layer during the supply of a stabilizing PH₃ flow did not reveal signs of erosion of the InP surface regardless of the type of dielectric mask and the method of its formation as well as the process time and reactor pressure (see Fig.4). Surface roughness InP:Zn does not exceed $R_q \sim 0.2\text{-}0.3$ nm within a scanning area of $5\times 5~\mu m$. Moreover, there is no precipitation of any Zn compounds in the solid phase unlike the Zn diffusion into InP through InGaAs under identical technological conditions.

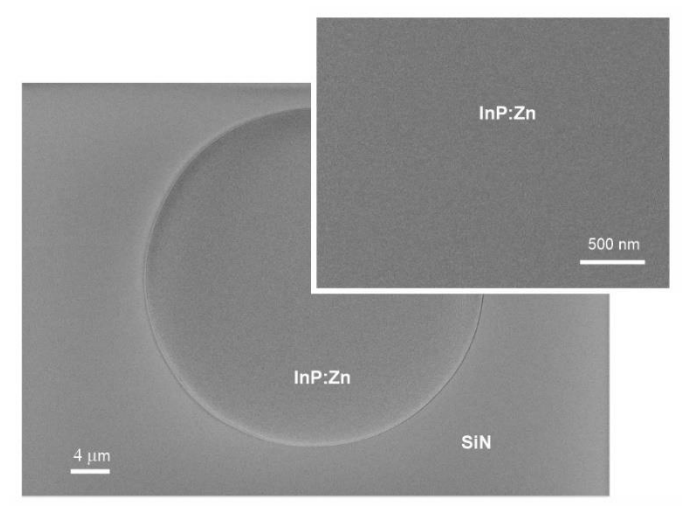


Fig. 4. SEM image (top view) of the sample with local Zn diffusion into the InP through a SiN_x dielectric mask (type III heterostructure). The inset shows a SEM image of the sample within the central window. Temperature 500 °C, pressure 50 mbar, process time 180 min

Thus, on the one hand, the local Zn diffusion into InP layer through InGaAs allows for a high level of doping in the InGaAs surface layer, but it is associated with the problem of erosion of the InGaAs surface during prolongated processes, as well as with the precipitation of Zn compounds in the solid phase at elevated pressures and/or an increase in the stabilizing flow of group V elements. On the other hand, the local Zn diffusion into InP provides a high quality of the InP:Zn surface morphology but is associated with the problem of forming an ohmic contact to the InP:Zn layer. At the same time, to simplify the manufacture of APDs, it is preferable to use InGaAs contact layers to form high-quality ohmic contacts.

One of the possible solutions is to use the effect of Zn diffusion in the direction along the layers of the heterostructure under the dielectric mask [14]. According to our studies of the local Zn diffusion into the InP layer through the InGaAs layer, the lateral Zn diffusion under the dielectric mask depends on the surface concentration of the diffusant: with increasing concentration, the depth of lateral Zn diffusion increases. In the case of a thick surface InGaAs layer (type I heterostructure) the lateral Zn diffusion into the InP layer under the mask reaches 1-1.5 µm (see Fig. 5) for technological modes providing a required depth of Zn diffusion (see Fig. 1). At the same time, the lateral Zn diffusion into the InGaAs layer under the mask varies in the range of 0.4-1.5 µm depending on the thickness of the InGaAs surface layer. Moreover, the morphology of the InGaAs:Zn surface does not deteriorate, because it is protected by a dielectric mask. A decrease in the thickness of the InGaAs surface layer leads to an increase in the effect of lateral Zn diffusion under the mask in the underlying InGaAs/InP layers. The lateral Zn diffusion depth into the InP layer exceeds 2.5 µm for the extreme case (type III heterostructure). Thus, locally preserving a thin near-surface InGaAs layer (20-50 nm) under the protection of a dielectric mask, it is possible to simultaneously provide the p-type doping of this layer due to lateral Zn diffusion from the InP:Zn layer into the InGaAs layer and prevent erosion of the InGaAs:Zn surface (see Fig. 6).

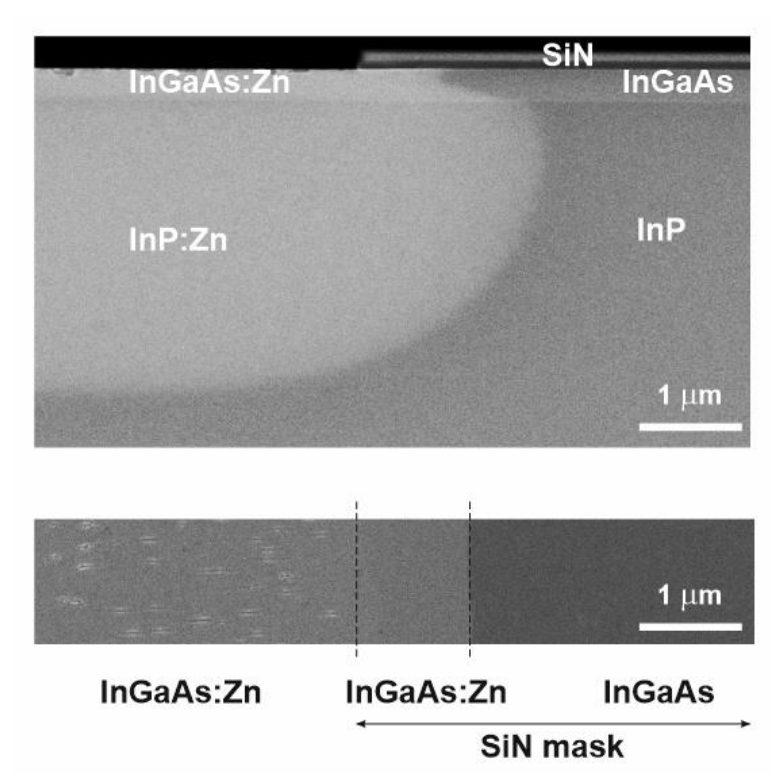


Fig. 5. SEM image of a cross-section of the sample with local Zn diffusion into InGaAs/InP through a SiN_x dielectric mask (type I heterostructure) at the edge of the dielectric mask. The inset shows a SEM image (top view) of the sample on the edge of the dielectric mask after removing the dielectric mask. Temperature 500 °C, pressure 50 mbar, process time 180 min

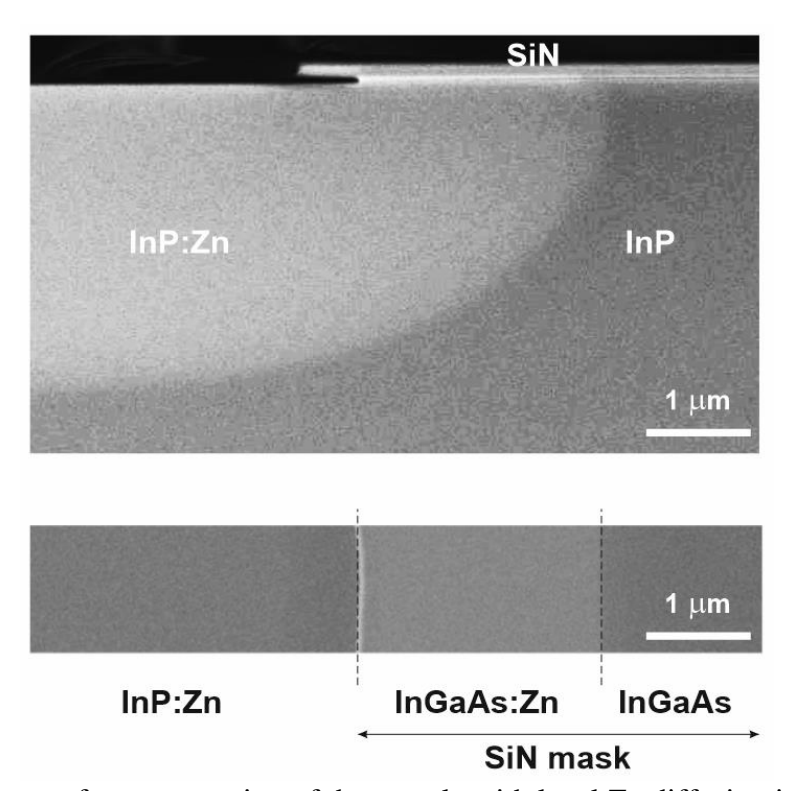


Fig. 6. SEM image of a cross-section of the sample with local Zn diffusion into InGaAs/InP through a SiNx dielectric mask (type II heterostructure) at the edge of the dielectric mask. The inset shows a SEM image (top view) of the sample on the edge of the dielectric mask after removing the dielectric mask. Temperature 500 °C, pressure 50 mbar, process time 180 min

Conclusion

The analysis of local Zn diffusion from the DEZn metalorganic source technological parameters on the morphology of the InGaAs and InP layers surface is presented. It is shown that for long-term processes of Zn diffusion into InP through InGaAs layer erosion of the InGaAs:Zn surface is observed independent of the dielectric mask (SiO₂, SiN_x) material and the method of its formation (plasma chemical deposition or chemical deposition from the vapor phase, plasma chemical etching or liquid chemical etching) and also an increase in the stabilizing flow of group V elements leads to an increase in the probability of Zn compounds precipitation in the solid phase. For short Zn diffusion processes it is necessary to increase the surface concentration of the diffusant (decrease in temperature and/or increase in pressure in the reactor) which is associated with defect formation and the appearance of deep centers in the diffusion region due to the high Zn atoms concentration. In the case of Zn diffusion directly into InP layer these problems are not observed. However, the maximum concentration of holes in the near-surface region does not exceed $3 \cdot 10^{18}$ cm⁻³, which makes it difficult to form ohmic contacts to InP:Zn layer.

The effect of lateral Zn diffusion into InGaAs/InP under a dielectric mask is considered. The influence of the diffusant surface concentration and the thickness of the InGaAs surface layer on the depth of lateral Zn diffusion under the mask was investigated. It was found that the lateral Zn diffusion in InGaAs layer is several times less than the lateral Zn diffusion in InP layer but there is a vertical component of the Zn diffusion from InP:Zn into the InGaAs surface layer. Due to this a decrease in the InGaAs surface layer thickness leads to an increase in the Zn doping depth in the lateral direction.

The studies have shown the fundamental possibility of simultaneously locally forming a necessary p-type dopant distribution profile in InP layer and p-type InGaAs contact layer during a single Zn diffusion process from the vapor phase in the MOCVD reactor without deterioration of the contact surface morphology.

References

- 1. Zhang L, La X, Zhu X, Guo J, Zhao L, Wang W, Liang S. High Speed Waveguide Uni-Traveling Carrier InGaAs/InP Photodiodes Fabricated By Zn Diffusion Doping. *IEEE Journal of Selected Topics in Quantum Electronics*. 2022;28(2): 1–6.
- 2. D'Agostino D, Carnicella G, Ciminelli C, Thijs P, Veldhoven PJ, Ambrosius H, Smit M. Low-loss passive waveguides in a generic InP foundry process via local diffusion of zinc. *Optics Express*. 2015;23(19): 25143.
- 3. Choi H, Park CY, Baek SH, Moon GY, Yun I. Evaluation of the Long-Term Reliability of Open-Tube Diffused Planar InGaAs/InP Avalanche Photodiodes under a Hybrid of Thermal and Electrical Stresses. *Electronics*. 2022;11(5): 802.
- 4. Ceccarelli F, Acconcia G, Gulinatti A, Ghioni M, Rech I, Osellame R. Recent Advances and Future Perspectives of Single-Photon Avalanche Diodes for Quantum Photonics Applications. *Advanced Quantum Technologies*. 2021;4(2): 2000102.
- 5. Ettenberg MH, Lange MJ, Sugg AR, Cohen MJ, Olsen GH. Zinc diffusion in InAsP/InGaAs heterostructures. *Journal of Electronic Materials*. 1999;28(12): 1433–1439.
- 6. Lee K, Yang K. Analysis of InGaAs/InP Single-Photon Avalanche Diodes With the Multiplication Width Variation. *IEEE Photonics Technology Letters*. 2014;26(10): 999–1002.
- 7. Arnold N, Schmitt R, Heime K. Diffusion in III-V semiconductors from spin-on-film sources. *Journal of Physics D: Applied Physics*. 1984;17(3): 443–474.
- 8. Chen Y, Zhang Z, Miao G, Jiang H, Song H. Optimized Selective-Area p-Type Diffusion for the Back-Illuminated Planar InGaAs/InP Avalanche Photodiodes by a Single Diffusion Process. *Physica Status Solidi* (A). 2022;219(2): 2100577.
- 9. Preobrazhenskii VV, Chistokhin IB, Putyato MA, Valisheva NA, Emelyanov EA,

- Petrushkov MO, Pleshkov AS, Neizvestny IG, Ryabtsev II. Single Photon Detectors Based on InP/InGaAs/InP Avalanche Photodiodes. *Optoelectronics*, *Instrumentation and Data Processing*. 2021;57(5): 485–493.
- 10. Petrushkov MO, Putyato MA, Chistokhin IB, Semyagin BR, Emel'yanov EA, Esin MYu, Gavrilova TA, Vasev AV, Preobrazhenskii VV. Zinc Diffusion into InP via a Narrow Gap from a Planar Zn3P2-Based Source. *Technical Physics Letters*. 2018;44: 612–614.
- 11. Jun D-H, Jeong HY, Kim Y, Shin C-S, Park KH, Park W-K, Kim M-S, Kim S, Han SW Moon S. Single-step metal-organic vapor-phase diffusion for low-dark-current planar-type avalanche photodiodes. *Journal of the Korean Physical Society*. 2016;69(8): 1341–1346.
- 12. Chand N, Houston PA. Selective area LPE growth and open tube diffusion in InGaAs/InP. *Journal of Electronic Materials.* 1985;14(1): 9–24.
- 13. Aytac S, Schlachetzki A. Shallow and selective diffusion of zinc in indium phosphide. *Solid-State Electronics*. 1981;24(1): 57–61.
- 14. Zou WX, Vawter GA, Merz JL, Coldren LA. Behavior of SiNx films as masks for Zn diffusion. *Journal of Applied Physics*. 1987;62(3): 828–831.
- 15. Tosi A, Calandri N, Sanzaro M, Acerbi F. Low-Noise, Low-Jitter, High Detection Efficiency InGaAs/InP Single-Photon Avalanche Diode. *IEEE Journal of Selected Topics in Quantum Electronics*. 2014;20(6): 192–197.
- 16. Yun I, Hyun K-S. Zinc diffusion process investigation of InP-based test structures for high-speed avalanche photodiode fabrication. *Microelectronics Journal*. 2000;31(8): 635–639.
- 17. Kim MD, Baek JM, Woo YD, Kim SG, Chung KS, Kim TG. Double Floating Guard-Ring-Type InP/InGaAs Avalanche Photodiodes with Low-Resistance Ohmic Contacts. *Journal of the Korean Physical Society*. 2007;50(6): 1925–1928.
- 18. Pitts OJ, Hisko M, Benyon W, Raymond S, SpringThorpe AJ. Optimization of MOCVD-diffused p-InP for planar avalanche photodiodes. *Journal of Crystal Growth*. 2014;393: 85–88.
- 19. Rezek EA, Wright PD, Holonyak JrN. Planar Zn diffusion in InP. *Solid-State Electronics*. 1978;21(2): 325–329.
- 20. Blaauw C, SpringThorpe AJ, Dzioba S, Emmerstorfer B. CVD-SiO2 and plasma-SiNx films as Zn diffusion masks for GaAs. *Journal of Electronic Materials*. 1984;13(2): 251–262.
- 21. Shuai W, Qin H, Han Y, Liyan G, Ziqing L, Feng X, Fan X. Temperature dependency of InGaAs/InP single photon avalanche diode for 1550 nm photons. *Infrared and Laser Engineering*. 2021;50(11): 20210453.
- 22. Lee K, Lee B, Yoon S, Hong JH, Yang K. A Low Noise Planar-Type Avalanche Photodiode using a Single-Diffusion Process in Geiger-Mode Operation. *Japanese Journal of Applied Physics*. 2013;52(7R): 072201.
- 23. Kim MD, Baek JM, Kim TG, Kim SG, Chung KS. Characterization of double floating guard ring type InP-InGaAs avalanche photodiodes with Au/Zn low resistance ohmic contacts. *Thin Solid Films*. 2006;514(1–2): 250–253.
- 24. Lee K, Yang K. Performance comparison of wet-etched and dry-etched Geiger-mode avalanche photodiodes using a single diffusion process. *Physica Status Solidi* (*C*). 2013;10(11): 1445–1447.
- 25. Itzler MA, Jiang X, Entwistle M, Slomkowski K, Tosi A, Acerbi F, Zappa F, Cova S. Advances in InGaAsP-based avalanche diode single photon detectors. *Journal of Modern Optics*. 2011;58(3-4): 174–200.
- 26. Ninomiya H, Sugino T, Matsuda K, Shirafuji JSJ. Effect of Phosphine on Plasma-Induced Traps in n-InP. *Japanese Journal of Applied Physics*. 1993;32(1A/B): L12-L15.
- 27. Blokhin SA, Levin RV, Epoletov VS, Kuzmenkov AG, Blokhin AA, Bobrov MA, Kovach YaN, Maleev NA, Andryushkin VV, Vasil'ev AP, Voropaev KO, Ustinov VM. Zn diffusion from vapor phase into InGaAs/InP heterostructure using diethylzinc as a p-dopant source. *Materials Physics and Mechanics*. 2023;51(3): 38-45.
- 28. Franke D, Reier FW, Grote N. Post-growth Zn diffusion into InGaAs/InP in a LP-MOVPE reactor. *Journal of Crystal Growth*. 1998;195(1–4): 112–116.

- 29. Guk EG, Kamanin AV, Shmidt NM, Shuman VB, Yurre TA. Dopant impurity diffusion from polymer diffusants and its applications in semiconductor device technology. A review. Semiconductors. 1999;33(3): 265-275.
- 30. Yoon KH, Lee YH, Yeo DH, Kim SJ. The characteristics of Zn-doped InP using spin-on dopant as a diffusion source. Journal of Electronic Materials. 2002;31(4): 244–247.
- 31. Wisser J, Glade M, Schmidt HJ, Heime K. Zinc diffusion in InP using diethylzinc and phosphine. Journal of Applied Physics. 1992;71(7): 3234–3237.
- 32. Vanhollebeke K, D'Hondt M, Moerman I, Van Daele P, Demeester P. Zn doping of InP, InAsP/InP, and InAsP/InGaAs heterostructures through metalorganic vapor phase diffusion (MOVPD). Journal of Electronic Materials. 2001;30(8): 951–959.
- 33. Wada M, Seko M, Sakakibara K, Sekiguchi Y. Zn Diffusion into InP Using Dimethylzinc as a Zn Source. Japanese Journal of Applied Physics. 1989;28(10A): L1700.
- 34. Pitts OJ, Benyon W, Goodchild D, SpringThorpe AJ. Multiwafer zinc diffusion in an MOVPE reactor. Journal of Crystal Growth. 2012;352(1): 249–252.
- 35. Kazmierski C. Zn diffusion in doped InP: Interstitial charge state and apparent activation energy. Journal of Applied Physics. 1988;64(11): 6573-6575.
- 36. Van Gurp GJ, Van Dongen T, Fontijn GM, Jacobs JM, Tjaden DLA. Interstitial and substitutional Zn in InP and InGaAsP. Journal of Applied Physics. 1989;65(2): 553-560.

THE AUTHORS

Blokhin S.A.

blokh@mail.ioffe.ru

Epoletov V.S. (D) vadep@yandex.ru

Blokhin A.A.

Aleksey.Blokhin@mail.ioffe.ru

Kovach Y.N.

yakovachyakov@gmail.com

Prasolov N.D.

Nikpras@mail.ioffe.ru

Guseva Yu.A. 🗓

Guseva.Julia@mail.ioffe.ru

Nikitina E.V. 🗓 nikitina@mail.ru

Vasil'ev A.P. (10)

Vasiljev@mail.ioffe.ru

Ustinov V.M. 🗓 vmust@beam.ioffe.ru Levin R.V. 🗓

Lev@vpegroup.ioffe.ru

Kuzmenkov A.G. (D)

kuzmenkov@mail.ioffe.ru

Bobrov M.A. 🗓

bobrov.mikh@gmail.com

Maleev N.A.

maleev.beam@mail.ioffe.ru

Kulagina M.M. 🗓

Marina.Kulagina@mail.ioffe.ru

Zadiranov Yu.M. 🗓

Zadiranov@mail.ioffe.ru

Andryushkin V.V. (10)

vlad.andryushkin@connector-optics.com

Voropaev K.O. (10)

kirill.voropaev@novsu.ru

Features of the properties of steel with the trip effect under various types of deformation loading

Submitted: April 23, 2023

Approved: May 16, 2023

Accepted: May 29, 2023

A.E. Gulin , A.G. Korchunov , D.V. Konstantinov , M.A. Sheksheev , M. Polyakova □

Nosov Magnitogorsk State Technical University, Magnitogorsk, Russia m.polyakova@magtu.ru

Abstract. Metastable steels, in particular, with the TRIP effect, have advantages over other steels due to the combination of strength and plasticity because of the peculiarities of their microstructure. The article presents the results of a study of the mechanical properties of aluminum-modified TRIP steel. Samples were obtained in the laboratory by traditional method of metallurgical manufacturing. The mechanical properties were investigated by tensile, compression testing methods, as well as by instrumental indentation (Berkovich method). During the tensile tests, the tensile curves of samples with different deformation rates and the values of the proof yield strength under compression were obtained, an experimental hardening curve of TRIP steel modified with aluminum was constructed. The Berkovich method obtained an array of data "load — depth of indentation", which is used to determine the hardness on the Martens scale, indentation hardness, modulus of elasticity, creep during the indentation, as well as the proportion of elastic component work during the instrumental indentation. The results obtained are of great practical importance in the development of technologies for the production of structural products from TRIP steel modified with aluminum.

Keywords: metastable steel; TRIP steel; mechanical properties; hardening curve; additive manufacturing

Acknowledgements. The research was carried out under contract No. 13.2251.21.0107 (№ SIIS "Electronic budget" 075-15-2021-1031) on the topic "Investigation on 3D-printing of Advanced High Strength Steels with TRIP effect for realization of self-adapting aerospace structural elements", funded by the Ministry of Science and Education of the Russian Federation within the joint program for science and technology cooperation and implementation of joint call for Russian-Italian projects for 2021-2023.

Citation: Gulin AE, Korchunov AG, Konstantinov DV, Sheksheev MA, Polyakova M. Features of the properties of steel with the trip effect under various types of deformation loading. *Materials Physics and Mechanics*. 2023;51(5): 152-164. DOI: 10.18149/MPM.5152023_15.

Introduction

The study of metastable austenitic steels was initiated in the middle of the previous century by I.N. Bogachev and R.I. Mints. They proposed and implemented the idea of obtaining metastable solid solutions in alloys based on iron, titanium, copper, undergoing martensitic transformations in the process of testing of mechanical properties and performance. This was fundamentally different from the conventional use of the alloys with metastable solid

© A.E. Gulin, A.G. Korchunov, D.V. Konstantinov, M.A. Sheksheev, M. Polyakova, 2023. Publisher: Peter the Great St. Petersburg Polytechnic University

solutions in the process of manufacturing products. The new concepts allowed the development of highly efficient cavitation-resistant steels [1–4]. It was further established that alloys with metastable austenite have increased wear resistance under waterjet wear [5], abrasive [6], percussion-abrasive [7] effects, dry friction [8] and fatigue loading [9]. A high level of mechanical properties can be obtained in these alloys [10]. This is due to the fact that the development of martensitic transformations occurring in the process of loading consumes a significant part of the energy of external influence and, accordingly, a smaller proportion of energy goes to destruction [11]. In addition, in the process of martensitic transformations, not only hardening occurs, but also relaxation of microstresses, resulting in increased efficiency of micro-volumes of alloys [12].

In studies [13,14], alloys with metastable austenite were considered as adaptive materials in which martensitic transformations play the main role in adapting alloys to external loads. These alloys are synergetic systems capable of self-organization of the structure under the influence of external factors. Most of the present-day studies are devoted to highly alloyed steels and cast irons, in these alloys metastable austenite is the main part of the structure. The works [15–18] summarize the studies of the creation of economically alloyed alloys of various structural classes and purposes, as well as strengthening technologies based on the principle of obtaining multiphase structures, one of which is metastable austenite. To obtain a high level of properties, the quantity and stability of metastable austenite must be controlled by the initial chemical and phase compositions as well as loading conditions. At the same time, it is also important to use a combination of various mechanisms of hardening and resistance to destruction. This approach significantly expands the understanding of the need to obtain metastable austenite in the structure of unalloyed, low- and medium-alloyed steels and cast irons.

Metastable austenite is considered as the most important internal resource of alloys, which allows to significantly improve their properties, reduce or in some cases eliminate completely expensive alloying elements used for the same purpose. The latter plays an important role in resource conservation. Metastable steels, in particular, with the TRIP (transformation-induced plasticity) effect, provide a combination of strength and plasticity due to the peculiarities of their microstructure [19]. As a result, this class of materials is actively used in mechanical engineering, in construction elements, and reinforcing structures of complex shape. The studies [20,21] described the advantages of this type of steel for the automotive industry due to their good plasticity, corrosion, and radiation resistance. The authors of the studies [22,23] demonstrated the advantages of these steels from the point of view of the total weight of the constructions made from them. As a result, the use of TRIP steels made it possible to reduce the weight of vehicles by an average of 10 %, which led to 5.5 % fuel economy in the process of their operation. There are also cases of a decrease in the cost of metal structures made from such steels due to the wide processing possibilities and the lack of need for some traditional reinforcing elements [24].

In the study [25] a review of the world market of TRIP effect steels was made. The authors note that 90 % of the use of TRIP-effect steel falls on the manufacture of vertical and longitudinal beams, reinforcing struts, automobile thresholds and bumper reinforcements. The study [26] considered and proved the wide technological possibilities of welding steels with a TRIP effect by laser, arc and spot welding.

Currently there are not many studies in the field of production of long-dimensional bulk blanks from metastable steels since the idea of producing hardware products from such steels in international periodicals appeared only in 2013-2014. This is due to the formation of a scientific consortium on the basis on one of the largest manufacturers of hardware products in the EU, Metalurgia S.A., part of the MORAVIA STEEL Group (Czech Republic), and the European National Research Center (National Centre for Research and Development). A team

from the Częstochowa Technical University (Technical University of Częstochowa) dealt with theoretical issues of the production of long-numbered volumetric blanks made from TRIP steels: in particular, professors Muskalski Z., Wiewiórowska S., Suliga M.

The studies [27-30] show technological possibilities of obtaining a wire from steel with a TRIP effect and the spheres of its potential application. According to the authors, the unique combination of mechanical properties and fatigue strength, will find the best application in the production of ropes, cables, springs, and fasteners. It is also noted [31] that in the process of drawing the properties of the wire can vary in wide ranges depending on the technological parameters. However, all the results obtained by this team were based mainly on private experiments without phenomenological studying of the macro- and microdynamics of deformation of such steels. In [32], the authors conduct a study of the stress-strain state of the metal in the process of drawing, but the presented models do not consider the microstructure of this type of steel. As the result, it was concluded that disregarding microstructure of metastable steels makes it extremely difficult to create an adequate model with an isotropic material. In such cases simulation methods which make it possible to take into consideration the microstructure changes in different methods of deformational processing show their effectiveness [33].

The potential for the use of metastable steels in additive manufacturing (AM) is extremely extensive due to the huge range of products in this area. In the context of the AM industry, certain points that are contradictory for the field of sheet production, on the contrary, can serve for more flexible management of technological and operational characteristics. For example, the preservation of the remaining austenite in the microstructure makes it possible to increase the wear resistance and operational reliability of the final printed product due to surface hardening. This is fundamentally important for industries such as the aerospace industry where operating conditions are difficult to predict and are characterized by uncontrolled shock, impulse loads, as well as intense wear.

Also, the high potential for the use of metastable steels can be realized already at the design stage of products by controlling the localized hardening of individual elements [34]. For example, it becomes possible to strengthen potentially more loaded elements locally and significantly such as threads, facets, bends, etc. Moreover, almost all industrial processes of manufacturing AM products have a large number of controlled technological parameters (temperature, speed, strain rate, combination of various loading schemes and methods of various physical nature), which allows us to flexibly control the localization of mechanical properties. The previously described experience of using TRIP steels in the fields of passive transport safety allows us to assert the high efficiency of such solutions for the development of the industry.

Thus, the use of TRIP-effect steels beyond the passive safety of cars opens up broad prospects for the creation of self-adapting steel blanks for objects of the aerospace industry. At the same time, these blanks will have technological flexibility that makes it possible to use them for a wide range of products with a high variability of operational characteristics. The features of metastable steels in combination with this type of products will make it possible to create structural elements of critical structures with complex shapes of the entire product and its individual elements. The increased plasticity of metastable steels will make heat treatment optional in separate technological operations, which will also have a positive impact on the cost of production. The ability to adapt to the effects of the operational environment will significantly reduce the wear and the number of repairs of equipment and structures. At the same time, due to the preservation of strength indicators, it will be possible to reduce the weight and metal consumption of mechanisms and structures. Also, the increased plasticity of the workpiece will also reduce the wear of the technological tool in the process of the

production, and its strength properties will allow us to abandon medium and high-carbon steels for individual structural elements.

One of the most well-known review articles in this field [35], which includes more than 500 literary sources, analyzes the features and potential risks of developing additive manufacturing technologies using modern metastable steels. The main conclusion of the authors is the proven fact of the criticality of the purity of metallurgical raw materials for the field of additive manufacturing, which determines the effectiveness and feasibility of certain printing techniques.

At the same time, the initial task in the study of 3D printing for the manufacture of self-adapting structural elements is to select a material of suitable chemical composition and determine its mechanical properties.

Materials and Methods of research

As part of the research work in the foundry laboratory of the Nosov Magnitogorsk State Technical University samples of TRIP steel were manufactured using metallurgical production methods (melting – thermal processing - plastic deformation), the chemical composition of which is given in Table 1. Accuracy of the elements' content corresponded to GOST R 54153. Steel. Method of atomic emission spectral analysis.

Table 1. Chemical composition of TRIP steel modified with aluminum

Fe	С	Si	Mn	P	S	Cr	Ni	Cu	Mo	Ti	V	Al
The basic element	0.37	3.36	2.92	0.015	0.012	0.048	0.040	0.073	0.004	0.005	0.004	0.010

Technological parameters of sample production:

- the total weight of the initial material (charge) is 2 kg;
- total melting time 12 15 minutes;
- melt exposure time for complete homogenization is 2 minutes;
- heat treatment modes: (1) heating and holding at a temperature of 760 ° C for 20 minutes; (2) sharp cooling to a temperature of 400 °C; (3) isothermal exposure at a temperature of 400 °C; (4) the cooling of samples to room temperature in calm air.

All studies of the mechanical properties of samples obtained using the traditional metallurgical technology were carried out in the Research Institute "Nanosteels" of the Nosov Magnitogorsk State Technical University.

Tensile tests were carried out according to GOST 1497-84 on a universal SHIMADZU AG-IC testing machine with a maximum load of 300 kN, which corresponds to accuracy class 1 according to ISO 7500.

After the samples were melted, they were cooled and processed using appropriate processing modes to exclude the possibility of changing the properties of the metal in the process mechanical processing.

The diameter of the samples after the heat treatment was 7.25 mm. The initial even length of the samples was determined by the formula (1) and was 20 mm, (1) where F_0 is the initial cross-sectional area, mm.

$$l_0 = 2.82\sqrt{F_0}. (1)$$

The determination of the conditional yield strength $\sigma_{0.2}^c$ during compression, the compressive strength, the construction of the hardening curve was carried out on cylindrical samples of type III with a diameter of 6 mm and a height of 11.7 mm in accordance with GOST 25.503-97 "Calculations and strength tests. Methods of mechanical testing of metals. Compression testing method".

The determination of hardness and other mechanical properties of the material by local measurement of the load and movement of the indenter was carried out according to GOST R 8.748-2011 (ISO 14577-1:2002) on a dynamic ultramicrohardness tester DUH-210S.

The values of the test load F and the corresponding indentation depth h were recorded during the entire measurement. The samples were subjected to compression tests. An experimental hardening curve was constructed after the compression tests. A triangular diamond tip (Berkovich's indenter) with an angle at the apex of 115 degrees was used as an indenter.

When measuring time-dependent effects, the applied load was kept constant for a certain period of time, and the change in the depth of indentation was measured as a function of the exposure time under load.

The zero point for measurements on the load/depth indentation curve is set for each measurement and corresponds to the first contact of the tip with the ring.

Sets of data values (load — depth of indentation) were used to calculate a number of material properties:

- a) hardness on the Martens scale, determined by the slope of the loading curve on the F-h diagram, HMs;
- b) indentation hardness H_{IT};
- c) modulus of elasticity E_{IT};
- d) creep during indentation C_{IT};
- e) the proportion of the elastic component of the work during instrumental indentation n_{IT} .

Results

The characteristic types of samples after the tensile test and the resulting gravity curve are shown in Figs. 1 and 2.

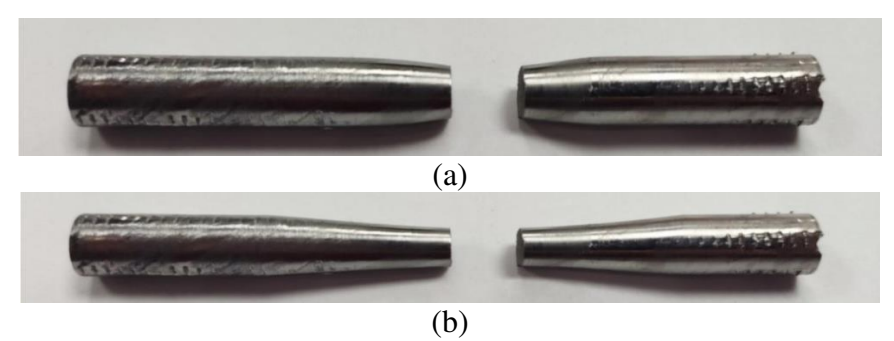


Fig. 1. A characteristic view of samples of TRIP steel modified with aluminum after a tensile test with different deformation rates: (a) minimum deformation rate; (b) maximum deformation rate

The obtained data and the appearance of the samples clearly demonstrate the key feature of the studied steels: the manifestation of the TRIP effect due to the transformation of residual austenite. The studies were carried out with the maximum and minimum possible deformation rates. Thus, with an increase in the deformation rate, all other things being equal, TRIP-effect steel demonstrates a jump-like increase in strength by 15-17 %. The microstructure of the samples shows that there is no pronounced localization of deformation in the process of tensile tests due to the transformation of residual austenite into more durable martensite.

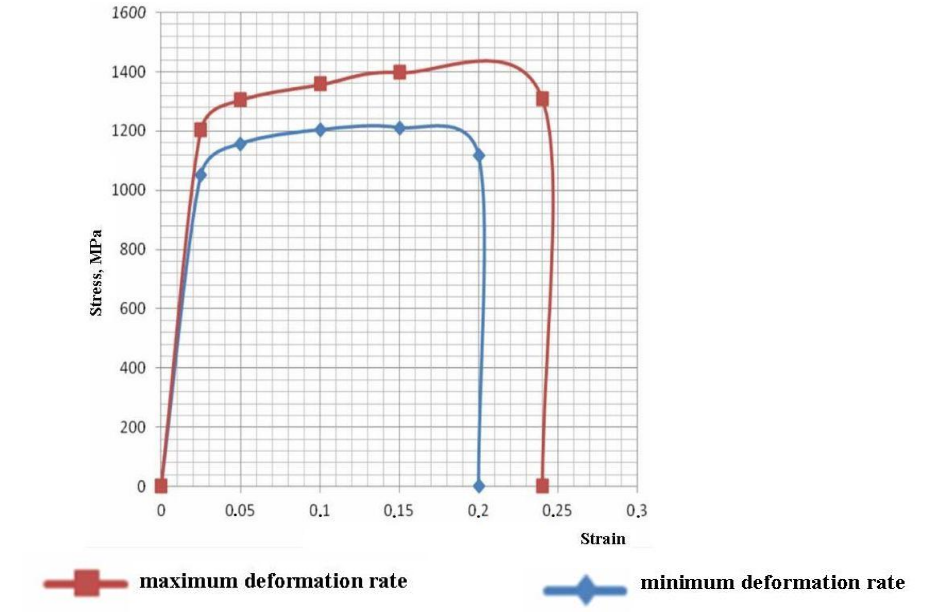


Fig. 2. Gravity curve of TRIP steel modified with aluminium obtained by metallurgical process

During the compression test, the sample is continuously loaded to a stress exceeding the expected value of the conditional yield strength $\sigma_{0.2}$ and a diagram is recorded (Fig. 3) considering the rigidity of the testing machine.

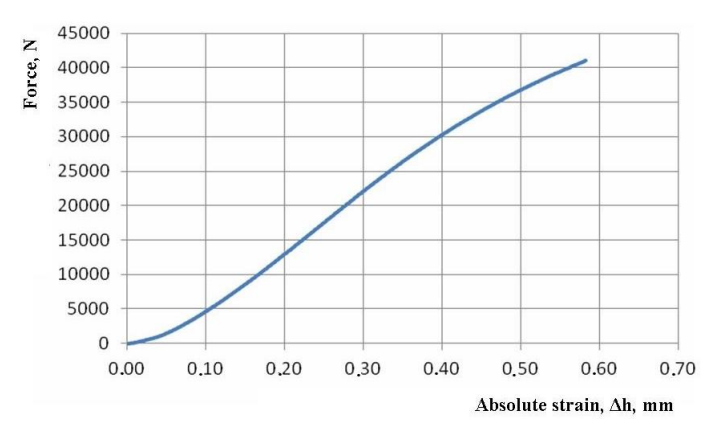


Fig. 3. Diagram of testing a sample of TRIP steel modified with aluminum to determine the conditional yield strength during compression

The diagram determined the load corresponding to the conditional yield strength (physical) in the process of compression $\sigma_{0,2}^c$, calculated by the formula:

$$\sigma_{0,2}^c = \frac{F_{0,2}}{A_0} = 1118.7 \text{ MPa.}$$
 (2)

According to the test results, a diagram was constructed (Fig. 4) and the load corresponding to the conditional yield strength in the process of compression was determined.

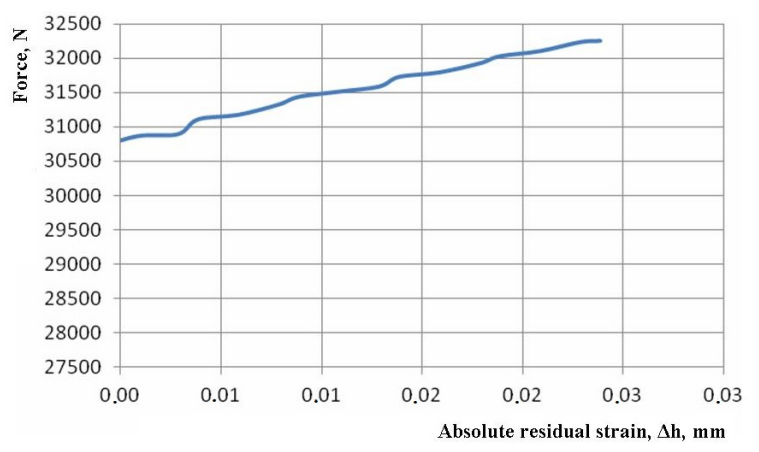
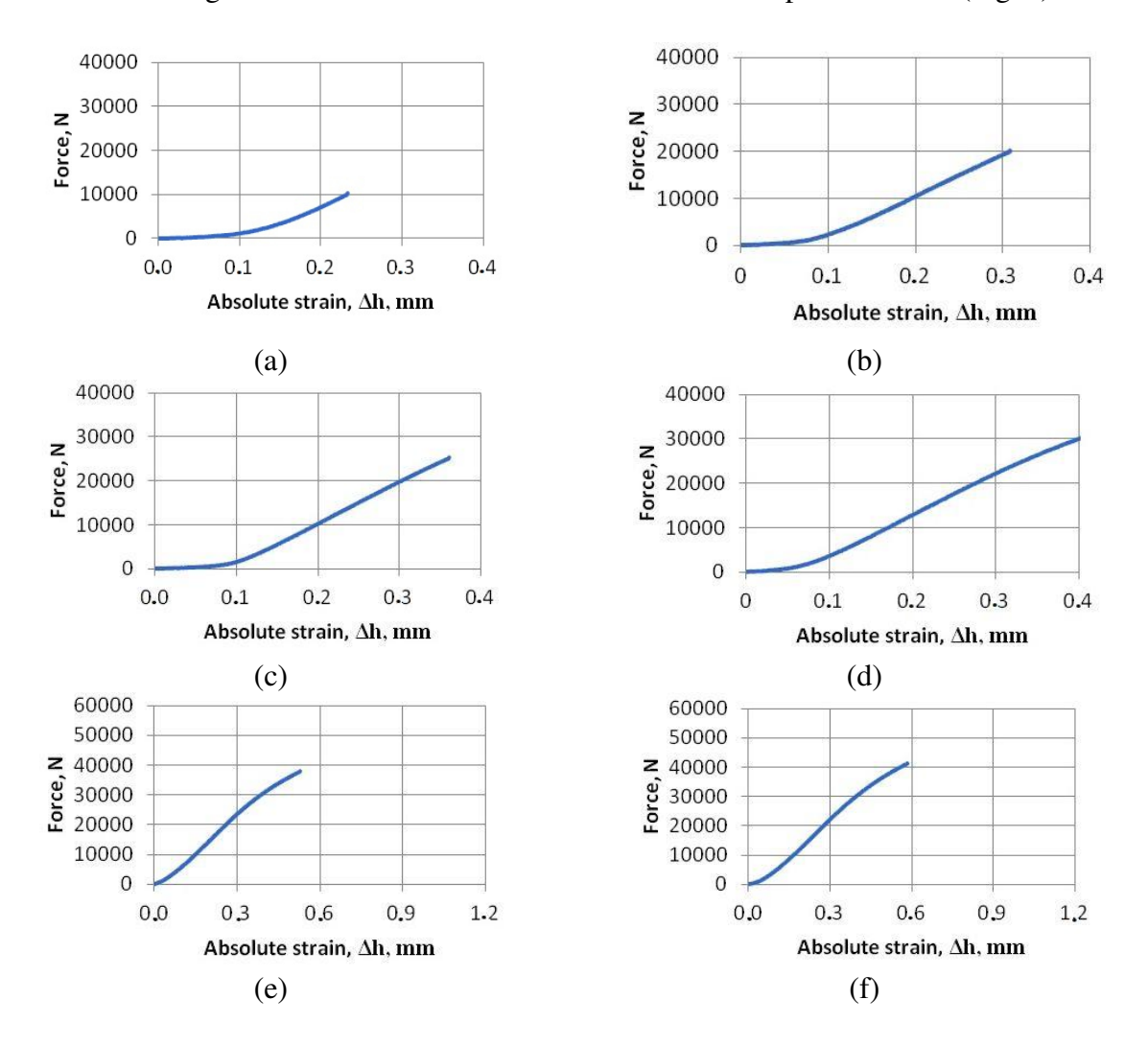


Fig. 4. Test diagram for determining the conditional yield strength during compression of a sample of TRIP steel modified with aluminum

To determine the compressive strength limit σ_s^c , the sample is continuously loaded until destruction. The greatest load preceding the destruction of the sample was taken as the F_{max} load corresponding to the compressive strength σ_s^c calculated by the formula:

$$\sigma_s^c = \frac{F_{max}}{A_0}. (3)$$

To construct the hardening curve, a series of cylindrical type III samples with a diameter of 6 mm and a height of 11.7 mm were tested at several levels of specified loads (Fig. 5).



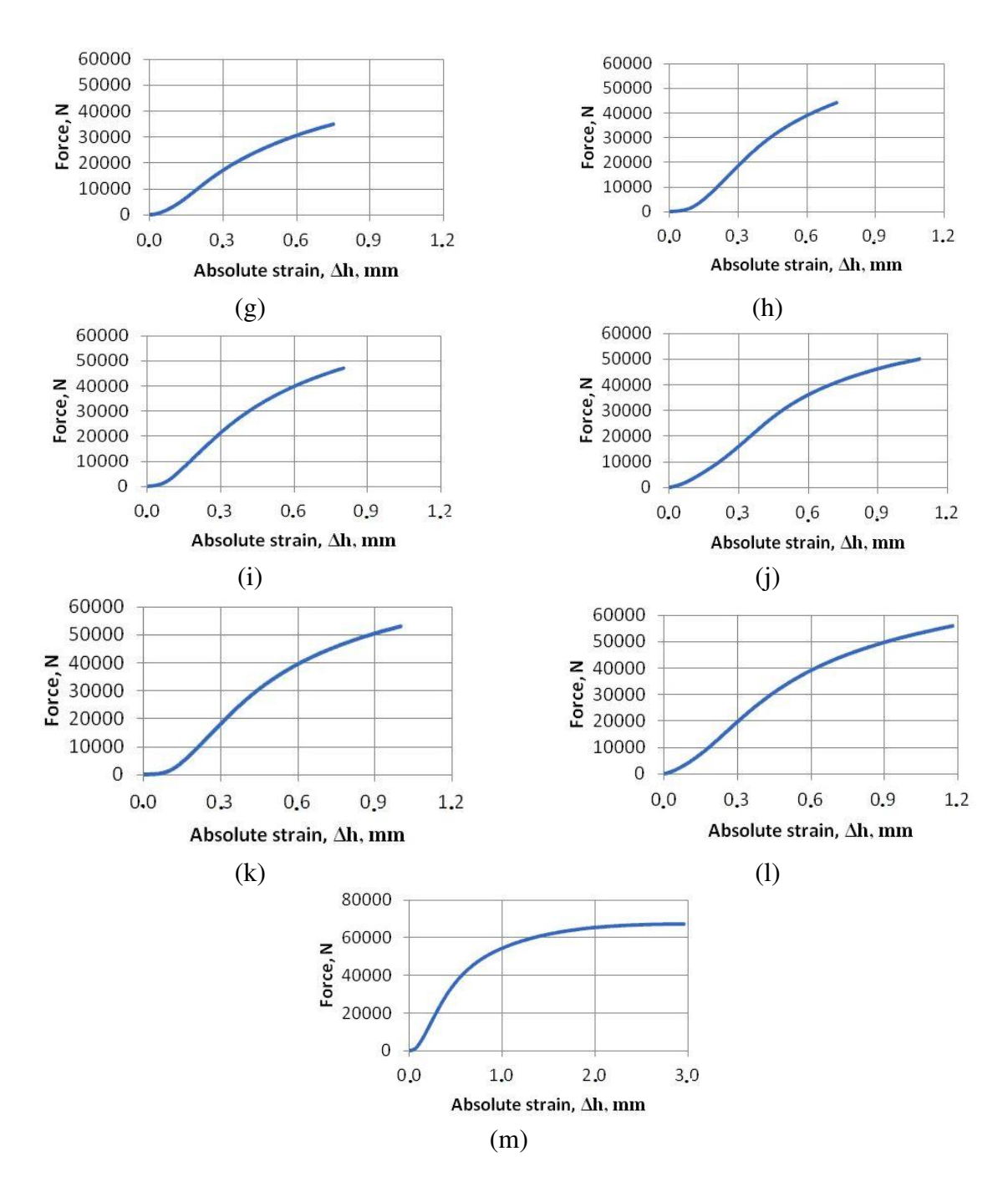


Fig. 5. Test results of a series of samples of TRIP steel modified with aluminum at different load levels: (a-d) change of absolute strain at increase of compression force to 40000 N; (e-l) change of absolute strain at increase of compression force to 60000 N; (m) change of absolute strain at increase of compression force to 80000 N

The obtained results show that with an increase in the deformation degree the increase in the compression force occurs. Samples were slightly shortened without obvious barrel formation. The destruction of the sample happened suddenly with the formation of a crack along the site inclined at an angle of 45° to the axis of the sample, which is typical for brittle materials.

To construct the hardening curve, the flow stress σ_{s1} was determined by the experimental hardening curve with logarithmic strain of the sample ε_l . The log-rhyme deformation ε_l was calculated by the formula:

$$\varepsilon_l = \frac{\ln h_0}{h_k},\tag{4}$$

where h_0 and h_k are the initial and final height of the sample, respectively, mm.

As a result of a series of tests, the data necessary for constructing the hardening curve were obtained (Fig. 6).

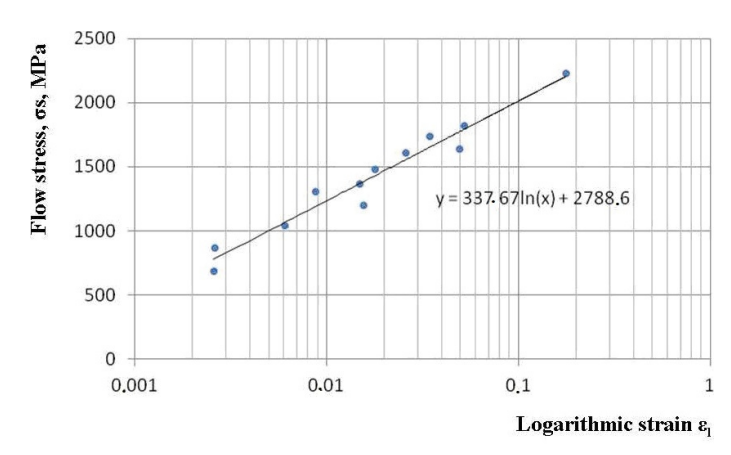


Fig. 6. Experimental hardening curve of TRIP steel modified with aluminum

Further, the approximation of the obtained data was made by constructing a logarithmic trend line with the definition of its equation using standard Microsoft Office tools:

$$\sigma_s = 337.67 \ln \varepsilon_1 + 2788.6.$$
 (5)

This dependence can be used in the design of technological processes. Thus, it can be concluded that in the case of compression, the dynamics of changes in the mechanical properties of TRIP steel modified with aluminum varies somewhat. In the process of compression, deformation processes have a less pronounced localized character, as a result of which the transformation of residual austenite in the microstructure proceeds throughout the entire volume of the sample. This fact is critically important from the perspective of the future potential application of the studied workpieces in areas with a high risk of unpredictable loads, since it is due to the observed effects that the structural element will have an ability to adapt to critical operating conditions.

Figure 7 presents the microstructure of samples under investigation. One can see martensite with 10% of retained austenite in as received state after quenching from the temperature $760\,^{\circ}\text{C}$ with further isothermal aging at $400\,^{\circ}\text{C}$ during 20 minutes. After compression to the fracture of the sample quantity of retained austenite decreases to 5.17%.

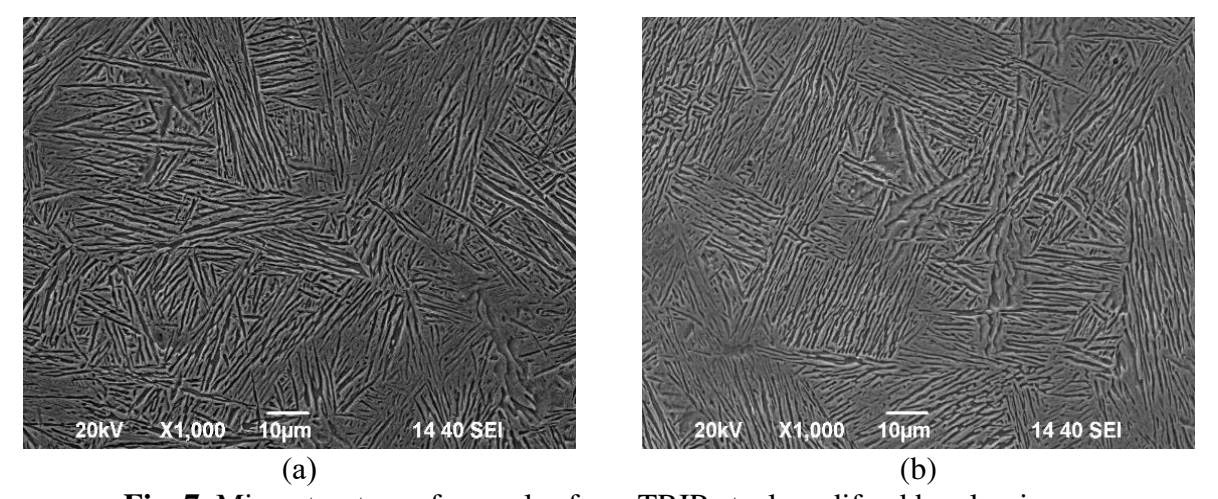


Fig. 7. Microstructure of samples from TRIP-steel modifyed by aluminum: (a) as received state; (b) after compression to fracture

After constructing an experimental compression hardening curve, the obtained samples were used for instrumental indentation. Figures 8 and 9 show the dependences of the indentation force on the depth of penetration of the indenter and the change in the depth of penetration of the indenter in the process of the test for each of the studied samples of aluminum-modified TRIP steel.

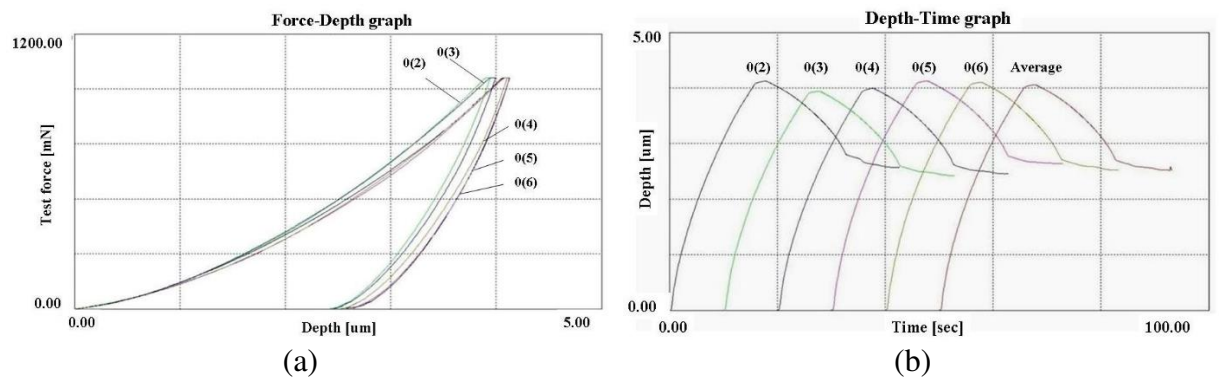


Fig. 8. The dependence of the indentation force on the penetration depth of the indenter (a) and the change in the penetration depth of the indenter (b) in the as-received sample of TRIP steel modified with aluminum

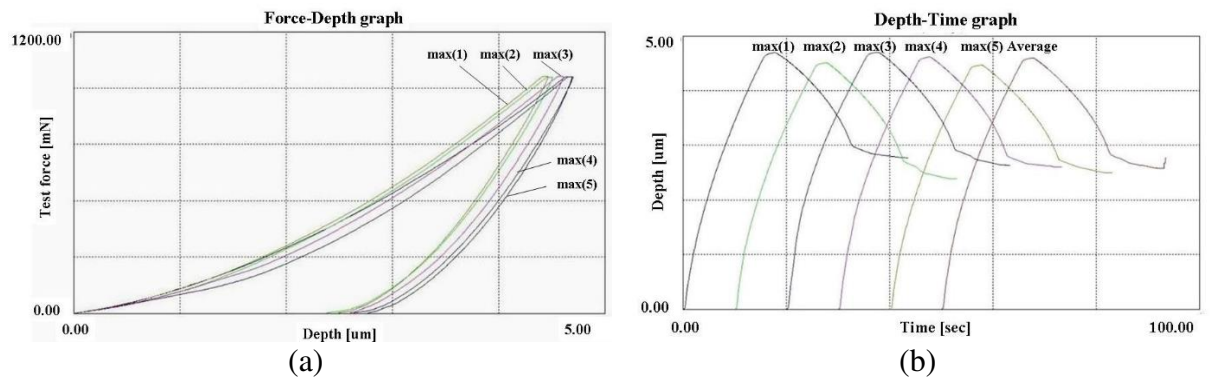


Fig. 9. The dependence of the indentation force on the penetration depth of the indenter (a) and the change in the penetration depth of the indenter (b) in a sample of TRIP steel modified with aluminum during deformation with a force of 67 kN

The results of the study of the properties of TRIP steel modified with aluminum by tool indentation are presented in Table 2 and in Fig. 10. The uncertainty of measurements corresponded to GOST R 8.748-2011 (ISO 14577-1:2002). State system for ensuring the uniformity of measurements. Metallic materials. Instrumented indentation test for hardness and materials parameters. Part 1. Test method.

Table 2. The properties of aluminum-modified TRIP steel determined by tool indentation

F _{max} , kN	$arepsilon_l$	HMT115, MPa	HMs, MPa	H _{IT} , MPa	E _{IT} , N/mm ²	C _{IT} , %	n _{IT} , %
0	0	2320.60	1810.86	3570.08	6.722e+004*	1.53	35.45
25	0.003	2435.40	1915.57	3984.39	6.229e+004*	1.44	36.86
35	0.016	2250.03	1592.18	3686.89	5.708e+004*	1.52	34.83
44	0.018	2800.15	2005.89	4527.21	7.383e+004*	1.57	32.80
53	0.035	2672.35	1967.18	4434.61	6.693e+004*	1.41	36.82
67	0.177	1807.50	1420.38	3059.76	4.282e+004*	1.50	41.39

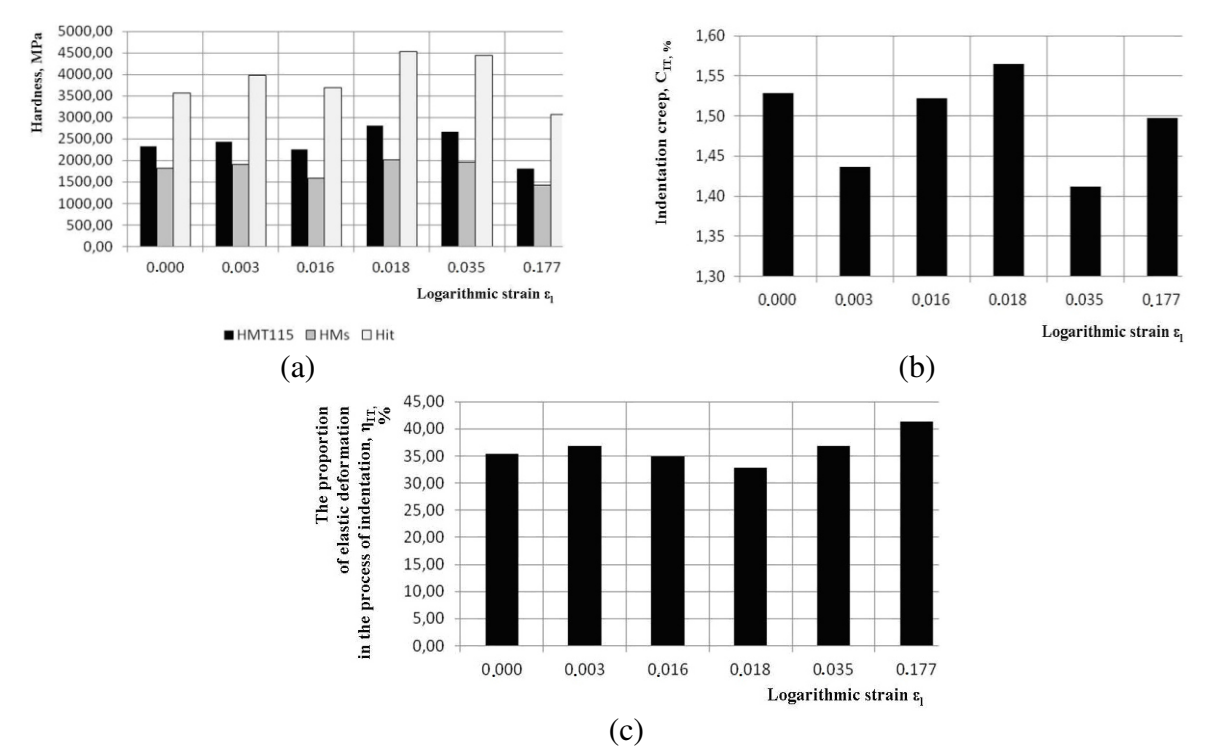


Fig. 10. Dependence of the properties of aluminum-modified TRIP steel on deformation in the process of tool indentation: (a) hardness on the Martens scale, determined by the slope of the loading curve on the F-h diagram HMT115 and HMs; indentation hardness H_{IT};
(b) creep during indentation C_{IT}; (c) the proportion of the elastic component of the work during instrumental indentation n_{IT}

The results obtained allow us to conclude that an increase in the loading rate of the indenter into the surface of the samples leads to a decrease in hardness due to a decrease in the stability of TRIP steel modified with aluminum, to permanent deformation and damage. In this case, there is an increase in the creep of the material and a decrease in the proportion of elastic deformation in the process of indentation.

Conclusions

The use of various methods of studying the properties of TRIP steel modified with aluminum allowed us to obtain a set of data on its behavior under various load application schemes. Stretching curves with a characteristic shape for steels with a TRIP effect are constructed by traditional methods of mechanical testing (tensile and compression testing). The hardening curve of aluminum-modified TRIP steel, as well as its approximation equation, can be used for computer modeling and design of technological processes for the manufacturing of products from this steel. The values of properties obtained by instrumental indentation (by the Berkovich method) are of practical interest for analyzing the behavior of aluminum-modified TRIP steel to predict its behavior when applying various types of external load.

References

- 1. Rajput A, Ramkumar J, Mondal K. Cavitation Resistance of a Cr-Mn Stainless Steel, A Mild Steel, and A High-Carbon Steel Based on Rust Protectivity and Corrosion Behavior. *Journal of Materials Engineering and Performance*. 2022;31: 439–447.
- 2. Santa JF, Blanco JA, Giraldo JE, Toro A. Cavitation erosion of martensitic and austenitic stainless steel welded coatings. *Wear*. 2011; 271(9–10): 1445–1453.

- 3. Bordeasu I, Popoviciu M, Mitelea I, Brânduşa G, Ghiban N. Cavitation erosion resistance of two steels with the same percentage of Chromium and Nickel but different Carbon content. *IOP Conference Series: Materials Science and Engineering*. 2014;57: 012007.
- 4. Zhao L, Hu H, Guo X. Effect of Toughness and Ductility on the Cavitation Erosion of Martensitic Stainless Steel. *Metals*. 2023;13. 154.
- 5. Sharma S, Gandhi B. Erosion Wear Behavior of Martensitic Stainless Steel Under the Hydro-Abrasive Condition of Hydropower Plants. *Journal of Materials Engineering and Performance*. 2020;29: 7544–7554.
- 6. Vargová M, Ťavodová M, Monkova K, Džupon M. Research of Resistance of Selected Materials to Abrasive Wear to Increase the Ploughshare Lifetime. *Metals*. 2022;12(6): 940.
- 7. Bratkovskii E, Shapovalov A, Dema RR. Decreasing the Impact–Abrasive Wear of Steel. *Russian Engineering Research*. 2019;39: 480–484.
- 8. Krbata M, Eckert M, Bartosova L, Barenyi I, Majerik J, Mikuš P, Rendkova P. Dry Sliding Friction of Tool Steels and Their Comparison of Wear in Contact with ZrO2 and X46Cr13. *Materials*. 2020;13: 2359.
- 9. Huating C, Grondin G, Driver RG. *Fatigue resistance of high performance steel*. Structural Engineering Report № 258. 2005.
- 10. Panov D, Chernichenko R, Naumov S, Pertcev AS, Stepanov N, Zherebtsov S, Salishchev
- G. Excellent strength-toughness synergy in metastable austenitic stainless steel due to gradient structure formation. *Materials Letters*. 2021;303: 130585.
- 11. Denkena B, Breidenstein B, Dittrich M-A, Nguyen HN, Fricke LV, Maier HJ, Zaremba D. Effects on the deformation-induced martensitic transformation in AISI 304 in external longitudinal turning. *Advances in Industrial and Manufacturing Engineering*. 2021;2: 100044.
- 12. Uebing S, Brands D, Scheunemann L, Schroder J. Residual stresses in hot bulk formed parts: two-scale approach for austenite-to-martensite phase transformation. *Archive of Applied Mechanics*. 2021;91: 545–562.
- 13. Ennis B, Jimenez-Melero E, Atzema EH, Krugla M, Azeem MA, Rowley D, Daisenberger D, Hanlon D, Lee P. Metastable austenite driven work-hardening behaviour in a TRIP-assisted dual phase steel. *International Journal of Plasticity*. 2016;88C: 126–139.
- 14. Wolf CH, Henkel S, Biermann H. Behaviour of Metastable and Stable Austenitic Stainless Steels Under Planar-Biaxial Load. In: Biermann, H., Aneziris, C. (eds.) *Austenitic TRIP/TWIP Steels and Steel-Zirconia Composites*. Cham: Springer; 2020.
- 15. Vasilyev AA. Sokolov DF, Sokolov SF. Experimental study and modeling of changing mechanical properties in tempering of bainitic-martensitic steels. *Materials Physics and Mechanics*. 2021;47(5): 727–738.
- 16. Vasilyev AA, Sokolov DF, Sokolov SF, Rudskoy AI. Investigation and modeling the austenization kinetics of steels with complex microstructure under continuous heating. *Materials Physics and Mechanics*. 2019;42(4): 423–435.
- 17. Malinov LS, Burova DV, Gomanyuk VD, Yarovaya PA. Increasing the Wear Resistance of Graphitized Steel by Obtaining Metastable Austenite in the Structure. *Journal of Friction and Wear*. 2021;42(2): 91–95.
- 18. Malinov LS, Malinov VL, Burova DV. The wear resistance increasing of low-carbon deposited metal with different manganese content due to the receipt of metastable austenite in the structure. *Welding International*. 2020;34(10-12): 470–474.
- 19. Zackay VF, Parker ER, Fahr D, Bush R. Materials used in automobile manufacture current state and perspectives. *Journal De Physique IV*. 1967;3: 31–40.
- 20. Galan J, Samek L. Advanced high strength steels for automotive industry. *Revista de Metalurgia*. 2012;48: 118–131.
- 21. Kuziak R, Kawalla R, Waengler S. Advanced high strength steels for automotive industry. *Archives of Civil and Mechanical Engineering*. 2008;8: 103–117.
- 22. Bast JL, Lehr J. The Increasing Sustainability of Cars, Trucks, and the Internal Combustion Engine. *Heartland Policy Study*. 2000;95: 1–69.
- 23. Dargay J, Gately D. Income's effect on car and vehicle ownership, worldwide: 1960-2015. *Transport. Res. a Pol.* 1999;33: 101–138.

- 24. Jambor A, Beyer M. New cars—new materials. *Materials & Design*. 1997;18: 203–209.
- 25. Davies G. Magnesium: Materials for automotive bodies. Elsevier. 2003.
- 26. Amirthalingam M. Microstructural Development during Welding of TRIP steels: PhD thesis in Metallurgical and Materials Engineering. Netherlands. 2010.
- 27. Suliga M. The theoretical-experimental analysis of the drawing process TRIP steel wires: PhD thesis in Metallurgical and Materials Engineering. Czestochowa University of Technology, Czestochowa. 2007.
- 28. Wiewiórowska S, Muskalski Z, Ciepiela W. Intensification of the transition of retained austenite to martensite effected by changing the stress state in trip steel wires. *Archives of Metallurgy and Materials*. 2015;60(4): 2729–2732.
- 29. Wiewiórowska S, Muskalski Z. The Application of Low and Medium Carbon Steel with Multiphase TRIP Structure in Drawing Industry. *Procedia Manufacturing*. 2015;2: 181–185.
- 30. Siemiński M, Wiewiórowska S, Muskalski Z. Examination of the effect of variation in stress magnitude on the amount of transformed retained austenite in the structure of TRIP steel wires. *Key Engineering Materials*. 2016;716: 311–316.
- 31. Wiewiórowska S, Muskalski Z. Analysis the influence of drawing process parameters on the amount of retained austenite in trip steel wires. *Metalurgija*. 2013;52: 32–34.
- 32. Muskalski Z, Wiewiõrowska S. Numerical and experimental analysis of the process of drawing wires of TRIP steel with a carbon content of 0.43% C, with single cross-section reductions. *Materialwissenschaft und Werkstofftechnik*. 2015;46: 279–284.
- 33. Konstantinov D, Korchunov A. Multi-scale computer simulation of metal forming processes. *Vestnik of Nosov Magnitogorsk State Technical University*. 2015;1: 36–43.
- 34. Raabe D, Sun B. Current Challenges and Opportunities in Microstructure-Related Properties of Advanced High-Strength Steels. *Metallurgical and Materials Transactions A*. 2020;51: 5517–5586.
- 35. Haghdadi N, Laleh M, Moyle M, Primig S. Additive manufacturing of steels: a review of achievements and challenges. *Journal of Materials Science*. 2021;56: 64–107.

THE AUTHORS

Gulin A.E.

e-mail: walter_chel@mail.ru

Konstantinov D.V.

e-mail: const_dimon@mail.ru

Polyakova M. 🗓

e-mail: m.polyakova@magtu.ru

Korchunov A.G.

e-mail: agkorchunov@mail.ru

Sheksheev M.A.

e-mail: shecsheev@yandex.ru

МЕХАНИКА И ФИЗИКА МАТЕРИАЛОВ

51 (5) 2023

Учредители: Санкт-Петербургский политехнический университет Петра Великого, Институт проблем Машиноведения Российской академии наук Издание зарегистрировано федеральной службой по надзору в сфере связи, информационных технологий и массовых коммуникаций (РОСКОМНАДЗОР), свидетельство ПИ №ФС77-69287 от 06.04.2017 г.

Редакция журнала

Профессор, д.т.н., академик РАН, А.И. Рудской – главный редактор
Профессор, д.ф.-м.н., член-корр. РАН, А.К. Беляев – главный научный редактор
Профессор, д.ф.-м.н. И.А. Овидько (1961 - 2017) – основатель и почетный редактор
Профессор, д.ф.-м.н. А.Л. Колесникова – ответственный редактор
Профессор, д.ф.-м.н. А.С. Семенов – ответственный редактор
Л.И. Гузилова – выпускающий редактор, корректор

Телефон редакции +7(812)552 77 78, доб. 224

E-mail: mpmjournal@spbstu.ru Компьютерная верстка Л.И. Гузилова

Подписано в печать 30.10.2023 г. Формат 60x84/8. Печать цифровая Усл. печ. л. 10,0. Тираж 100. Заказ_____.

Отпечатано с готового оригинал-макета, предоставленного автором в Издательско-полиграфическом центре Политехнического университета Петра Великого. 195251, Санкт-Петербург, Политехническая ул., 29. Тел.: +7(812)552 77 78, доб. 224.

On the exact solution of mixed problems for multicomponent multilayer materials V.A. Babeshko, O.V. Evdokimova, O.M. Babeshko	1-8
Molecular dynamics study of the dissolution of titanium nanoparticles in aluminum G.M. Poletaev, Y.V. Bebikhov, A.S. Semenov, A.A. Sitnikov, V.I. Yakovlev	9-15
A model of the formation of serrated deformation and propagation of Luders bands during the Portevin-Le Chatelier effect in alloys G.F. Sarafanov, Yu.G. Shondin, S. I. Kuznetsov	16-23
Influence of material anisotropy on the interaction between cracks under tension and shear A.V. Savikovskii, A.S. Semenov	24-37
On the crack evolutional in human dentin under uniaxial compression imaged by high resolution tomography D. Zaytsev, A. Funk	38-51
Estimation of breakdown pressure in laboratory experiments on hydraulic fracturing E.V. Novikova, M.A. Trimonova, N.V. Dubinya, S.B. Turuntaev, E.V. Zenchenko	52-65
Prediction of mechanical properties of elastomeric materials using neural networks S.V. Fomin, V.S. Rostovtsev, V.U. Meltsov, E.S. Shirokova	66-78
The numerical simulation of the post-welding stress-strain state of thin-sheets welded joints of EP718 alloy A.Yu. Medvedev, A.E. Medvedev, A.F. Shaikhulova, R.V. Nikiforov, O.V. Murugova, V.R. Galimo	79-89
Simplistic model for the investigation of mechanical stability parameters of pyrochlore structured solids R. Bhati, D.S. Yadav, R.C. Gupta, A.S. Verma	90-98
Effect of cobalt and tungsten carbide particles inclusions into the aluminium composite on the hardness and wear properties U.B. Gopal Krishna, B. Vasudeva, V. Auradi, M. Nagaral	99-106
Effect of Al addition on the mechanical properties of Zr ₅₀ Cu _{50-x} Al _x (0≤x≤50) bulk metallic glass V. Guder	107-114
Effect of the parameters affecting the properties during friction stir welding of AA 5083 H111 alloy M. Merzoug, A. Ghazi, A. Lousdad, N. Benamara, A. Miloudi, A. Boulenouar	115-125
Structure and properties of porous glass ceramics from siliceous rocks with the addition of Mg(OH) ₂ A.I. Rodin, A.A. Ermakov, I.V. Erofeeva, V.T. Erofeev	126-141
Surface morphology of InGaAs and InP layers after local Zn diffusion from the vapor phase in the MOCVD reactor S.A. Blokhin, R.V. Levin, V.S. Epoletov, A.G. Kuzmenkov, A.A. Blokhin, M.A. Y.N. Kovach, N.A. Maleev, N.D. Prasolov, M.M. Kulagina, Yu.A. Guseva, Yu.M. Zadirar Nikitina, V.V. Andryushkin, A.P. Vasil'ev, K.O. Voropaev, V.M. Ustinov	
Features of the properties of steel with the trip effect under various types of deformation loading A.F. Gulin, A.G. Korchunov, D.V. Konstantinov, M.A. Sheksheev, M. Polyakova	152-164



A.E. Gulin, A.G. Korchunov, D.V. Konstantinov, M.A. Sheksheev, M. Polyakova